Chapter 2
Shock Waves in Gases

2.1 Shock Wave Reflections Over Straight Wedges

2.1.1 Introduction

When a shock wave is reflected from a steep wedge, the reflected patter of the incident shock wave, or in short IS, forms a V shaped wave pattern. This pattern is similar to a sound wave reflection from a plane wall and hence is named as a "regular reflection", and in short RR. A head-on-collision of a shock wave with a plane wall is an extreme case of the RR.

When an IS encounters a shallow wedge, it will not reflect from the wedge surface but intersects with the reflected shock wave above the wall surface. A third shock wave which is normal to the wall surface merges with their intersection point resulting in a Y-shaped shock wave pattern. Such a three shock confluence formed a triple point or in short TP and accompanied a slip line. Today, it is known that this pattern is one of typical representations of gas dynamic non-linearity. The reflection pattern is called "Mach reflection", or in short MR. A shock wave propagating perpendicularly along a straight wall is an extreme case of the MR.

If one recalls the history of the survey of shock wave reflections, Ernst Mach was one of pioneers who felt a puzzling feature of MR (Reichenbach 1983). He watched the interaction of two spherical shock waves created by simultaneous spark discharges on a soot covered glass plate. Eventually a V-shaped soot free region was discovered on the glass plate and people named this region as a Mach-V. The Mach-V was created by travelling vortices developed from the triple point, TP and indirectly proved the presence of the Mr. Teopler visualized, for the first time, this unusual shock wave reflection patter which was MR but he failed to claim the pattern as a MR (Krehl and van der Geest 1991).

Although the structure of the TP is not yet fully understood, the third shock wave emanating from the TP to the wedge surface is called a "Mach stem" or a Mach shock, MS. The transition of reflected shock waves between RR and MR is

K. Takayama, *Visualization of Shock Wave Phenomena*,
https://doi.org/10.1007/978-3-030-19451-2_2

governed by the wedge angle, the shock Mach number Ms, and the specific heats ratio γ of the test gas.

An MS is traditionally assumed to be straight and perpendicular to the wedge surface. Figure 1.4 shows a weak shock wave of Ms = 1.158 in atmospheric air reflected from a 7.0° wedge. It is observed that in a case of weak shock wave reflection from shallower wedges, the MS is slightly curved and SL is not observable. The point at which IS, RS and MS intersect is not a triple point but a point on the trajectory of the glancing incidence angle, which will be discussed later. Based on his private preference offered terminology, Birkhoff (1960) named the departure of MS's shape from that of traditional Mach reflection patterns as the von Neumann paradox. Today it is understood that this terminology never means a paradoxical phenomenon but exhibits a feature of weak shock waves, in which the isentropic feature of the state behind weak shock wave reflections are exaggerated. The reflection pattern is shown in grey color as seen in Fig. 2.1. Although we see a dark fringe but miss a straight slip line, SL. This Mach reflection pattern is named as von Neumann Mach reflection or in short vNMR.

Ben-Dor (1979) defined the domain and boundary of the family of Mach reflections in shock tube flows. The pattern shown in Fig. 1.3 is, according to the definition, named as a single Mach reflection SMR. The SMR has a distinct triple point TP and SL emanating from the TP. The reflected shock wave RS is curved, which indicates that the flow behind it is locally subsonic. With increasing the wedge angle, θ_w, the shape of the reflected shock, RS tends to be straightened indicating that the flow behind it is transonic. Then a merger of compression waves behind the straight RS intersects with a curved RS forming a kink point. Then the SMR terminates to become a transitional Mach reflection, TMR. With further increase of the θ_w, the transonic flow region became supersonic, the coalescence of trains of compression waves becomes a shock wave which is named as a secondary shock wave. Then, the kink point turns into a secondary triple point having three shock confluence and a slip line, SL. The second Mach reflection characterizes a

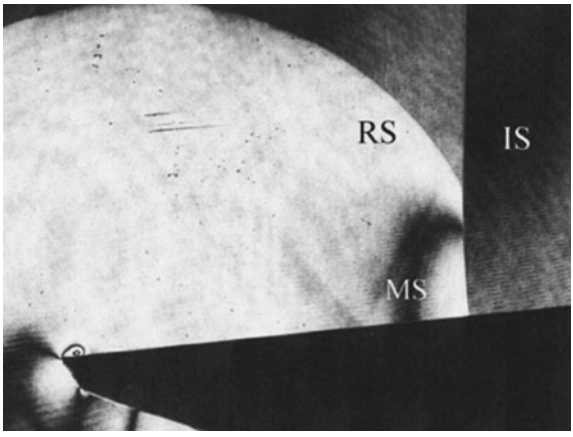

Fig. 2.1 Typical vNMR in a 60 mm × 150 mm shock tube, #87092210, for Ms = 1.158 in atmospheric air at 300 K, wedge angle of θ_w = 7.0°. Notice that no slip line, SL is observable

reflection pattern as a double Mach reflection, DMR. These transitions of reflected shock wave patterns exist only in unsteady flows.

2.1.2 Shock Polar

von Neumann studied systematically, for the first time, reflection of steady oblique shock waves from solid wall. Propagation and reflection of shock waves over wedges were visualized in shock tube experiments. Shock tube flows are essentially non-stationary phenomena but it can be reduced to steady flows by replacing the flow framework to a shock fixed coordinate. Flow conditions in front of and behind a given shock wave are at least locally uniform. The states behind these shock waves are determined by solving the Rankine-Hugoniot relations, R-H relations. Using the R-H relations, von Neumann derived algebraic equations deriving a transition from RR to MR. His analysis showed that a solution for either MR or RR could be determined, given the following set of parameters, ξ, θ_w, and γ. Here, ξ is the inverse strength in the pressure ratio across the shock wave;

$$\xi = (\gamma + 1)/\left(2\gamma \mathrm{Ms}^2 - \gamma + 1\right) \tag{2.1}$$

For a given specific heats ratio γ, the reflected shock transition between MR and RR occurs with continuous change in the parameters ξ, θ_w. Figure 2.1 shows the definition of regions and angles in the frame of the triple point fixed coordinate for Ms = 1.497 # 92090404.

Regions (1) and (2) correspond to the ones in front of the incident shock IS, and the one across it. Regions (3) and (4) designate the one behind the the RS and that behind the MS, respectively. These regions are uniform in the vicinity of the triple point TP. The values of particle velocities' values in the region (3) and (4), obtained while deflected in crossing at the RS and MS, respectively, differ from each other

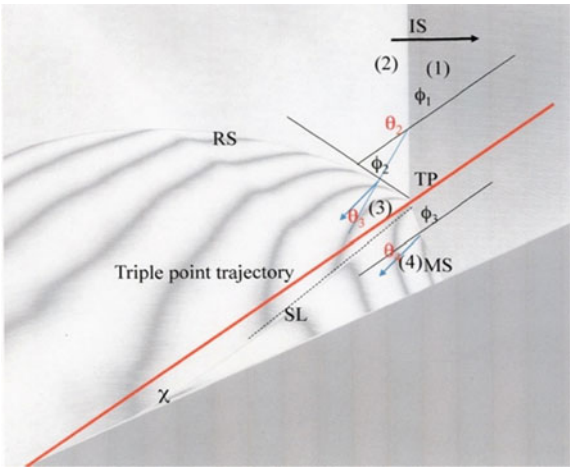

Fig. 2.2 Definition of regions and angles: #92090404, for Ms = 1.497 in atmospheric air at 300.1 K, wedge angle $\theta_w = 25°$

but both have the same direction. This means that the line separating the regions (3) and (4) is a contact discontinuity or a slip line, SL; across it, the pressures are constant, but the densities change discontinuously.

In coordinates fixed to the TP, the conservation of mass, and energy and the equation of motion for the individual shock waves are reduced to those of steady oblique shock waves. Tangential velocity components along the oblique shock should be identically given;

$$U_i \cos\phi_\iota = U_k \cos\left(\phi_j - \theta_k\right) \tag{2.2}$$

where subscripts i, j, and k denote the individual flow regions shown in Fig. 2.2 and are selected: for IS, i = j = 1 and k = 2; for RS, i = j = 2 and k = 3; and for MS, i = k = 1 and j = 4. Angle ϕ is defined, in SMR in Fig. 1.5 as the incident angle of the IS with respect to the trajectory angle of the TP. That is, $\phi_1 = 90^\circ - \theta_w - \chi$, where χ is the trajectory angle of the TP.

This relation is derived based on the assumption that the MS is straight at least in the vicinity of the TP and perpendicular to the wedge surface. For RR, ϕ reduces to the incident angle with respect to the wedge surface,

$$\phi_1 = 90^\circ - \theta_w.$$

Other equations are:

Mass conservation;

$$\rho_I U_i \sin\phi_I = \rho_k U_k \sin\left(\phi_j - \theta_k\right). \tag{2.3}$$

Equation of motion;

$$p_1 + \rho_\iota U_i^2 \sin^2\phi_I = p_k + \rho_k U_k^2 \sin^2\left(\phi_j - \theta_k\right). \tag{2.4}$$

Energy conservation;

$$2h_i + U_i^2 \sin^2\phi_i = 2h_k + U_k^2 \sin^2\left(\phi_j - \theta_k\right). \tag{2.5}$$

Assuming ideal and perfect gases, we define the specific enthalpy as: $h = \gamma p/\{(\gamma - 1)\rho\}$.

The equation of state for ideal gas is

$$p = \rho RT, \tag{2.6}$$

where R is the specific gas constant, that is the universal gas constant divided by the molecular mass of the gas under study. The value of θ_k is, therefore, determined by solving Eqs. (2.3)–(2.6) with known conditions in region (i, j), we have $\theta_k = F(\phi_j, \xi)$, where ξ is the inverse shock wave strength across regions (j) and (k),

$$F(\phi,\xi)=\tan^{-1}\left[(\xi-1)\left\{(\mu-1)M^2-\mu-\xi\right\}^{1/2}/\left\{\left(1-\gamma M^2-\xi\right)(\mu+\xi)^{1/2}\right\}\right], \tag{2.7}$$

where $\mu = (\gamma - 1)/(\gamma + 1)$,

$$\begin{aligned} M &= Ms/\sin\phi \quad \text{for } k=1,3 \\ &= \left\{\left(2/(\gamma-1)+Ms^2\right)\left\{(\mu\xi+1)^{1/2}/\left(\mu\xi+\xi^2\right)^{1/2}-1\right\}\right. \quad \text{for } k=2. \end{aligned}$$

A family of solutions for a given $M_1 = Ms/\sin\phi_1$ and γ is expressed in terms of a pressure, p, and flow deflection angle, θ. A solution curve expressed in a p, θ—plane is known as a shock polar diagram. Shock polar analysis is a useful graphical explanation of wave interactions providing a physical insight into various, not necessarily simple, interactions of shock waves. Kawamura and Saito (1956), for the first time, adopted the shock polar diagram in analyzing shock reflections over wedges. The solution curve, I, for given initial conditions in region (1) is named as an I-polar. Another solution curve which starts from the condition in region (2) on the I-polar and is superimposed on the I-polar is named as a R-polar. The R-polar determines all the possible solutions R for a given ϕ_1 p_2, θ_2.

Depending upon the boundary conditions, all the possible solutions of regions (3) and (4) are described on the R-polar. For determining the state behind the reflected shock wave, boundary conditions have to be specified. In MR, the boundary conditions in the vicinity of TP are that flow vectors in the regions (3) and (4) are parallel to each other and the pressures are identical locally across SL.

That is,

$$p_3 = p_4 \text{ and } \theta_2 \pm \theta_3 = \theta_4. \tag{2.8}$$

In RR, the boundary condition is that the streamline in the region (3) is parallel to the wedge surface:

$$\theta_2 + \theta_3 = 0. \tag{2.9}$$

The second intersection point of the R-polar with the I-polar satisfies the boundary conditions given by Eq. (2.9) (Takayama and Sasaki 1983).

Figure 2.3 shows a shock polar for Ms = 1.50 in air. The ordinate designates pressure p normalized by the initial pressure p_1 and the abscissa designates angle θ in degree. I-polar is drawn for wedge angles ranging from 30° to 60° at every 5° and R-polar is also drawn for individual wedge angles for Ms = 1.50. Intersecting points in the first quadrant of individual I-polar and R-polar provide solutions of pressures, p, and the flow deflection angles, θ, in the vicinity of the TP corresponding to regions (3) and (4).

The reflected shock wave transition between MR and RR occurs theoretically either when the R-polar touches the p-axis or when the R-polar intersects both the I-polar and the p-axis at the same point. The former is called the detachment

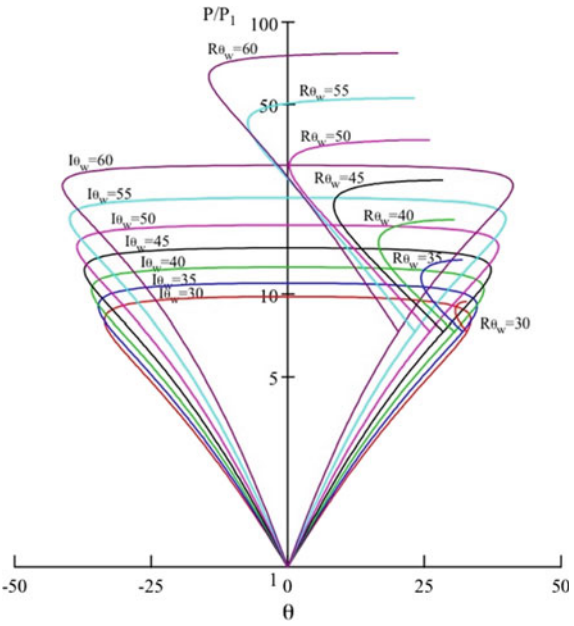

Fig. 2.3 Shock polar for a shock wave of Ms = 1.5 reflecting from wedges of 30° to 60° (Numata et al. 2009)

criterion and latter renamed as the von Neumann criterion (Ben-Dor 1979; von Neumann 1963; Courant and Friedrichs 1948). The detachment criterion satisfies the boundary condition of Eq. (2.8), when $\theta_3 = \theta_{max}$, where θ_{max} is a maximum flow deflection angle, and $\theta_4 = \theta_2 - \theta_3 = 0$. This relationship indicates that the slip line emanating from TP is parallel to the wall.

The von Neumann criterion also satisfies the above-mentioned flow deflection, so that, as will be seen later, the slip line is again parallel to the wedge surface. The wedge angle at which the transition takes place is called the critical transition angle, θ_{crit}. Hence, knowing θ_{crit} and ϕ, the triple point trajectory angle χ is readily obtained if we assume straight and perpendicular MS to the wedge surface.

Figure 2.4 shows experimental results Takayama and Sasaki (1983) for θ_{crit} obtained for concave and convex walls of various radii and initial angles against inverse shock strength ξ. In The experiments were performed in a 30 mm $\times$ 40 mm conventional shock tube and previously obtained results (Smith 1948) were also added. The detachment and von Neumann criteria are also presented. The ordinate denotes θ_{crit} in degree and the abscissa denotes the inverse shock strength ξ.

von Neumann concluded that the criterion for the reflected shock transition depended on the strength of incident shock waves and the detachment criterion was valid for weak shock waves and the von Neumann criterion was applicable to strong shock waves. Von Neumann defined weak and strong shock waves based on the shock polar diagrams (Courant and Friedrichs 1948). For strong shock waves, it is possible that either MR or RR exists in the region between the detachment and the von Neumann criteria. In the shock wave reflection over wedges in shock tubes, the transition consistently follows the detachment criterion, however, as will be

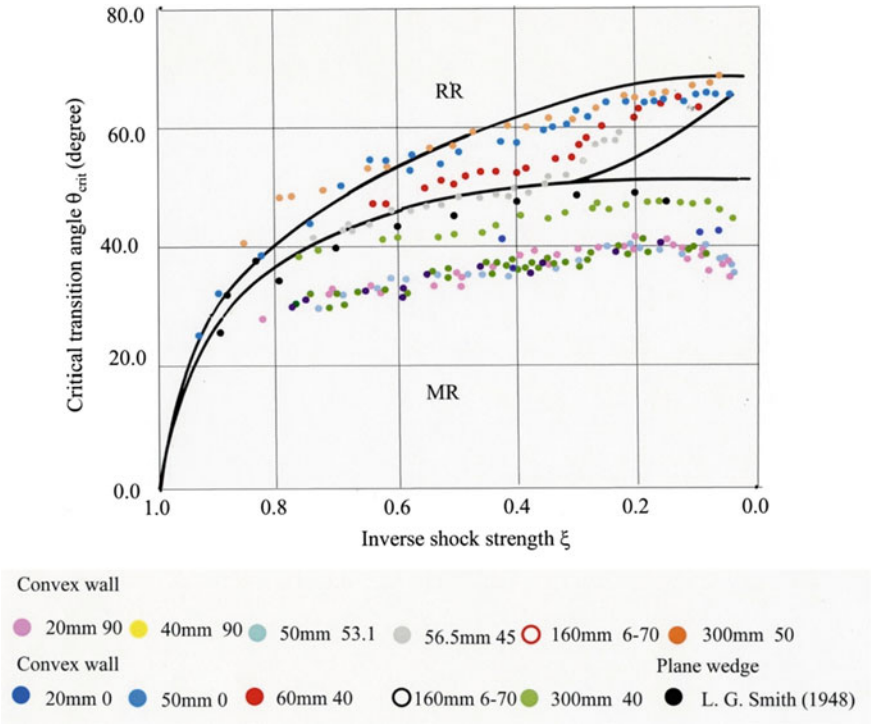

Fig. 2.4 The dependence of the critical transition angle θ_{crit} against the inverse shock strength ξ Kawamura and Saito (1956)

discussed later, along curved walls, that is, the variable wall angle with shock wave propagations, the flows are truly non-stationary; in such cases, either the transition follows the von Neumann criterion or the detachment criterion (Ben-Dor 1979; Takayama and Sasaki 1983; Courant and Friedrichs 1948).

However, the transition in stationary flows occurs at either the detachment criterion or the von Neumann criterion. Hornung et al. reported that, for a given strong shock, depending upon the operational condition of the wind tunnel or the setup of the wedge models, either MR or RR occurs in the region between the detachment and von Neumann criteria. People believe that the wind tunnels create stationary flows but it is not always true. The starting flow in wind tunnels or insertions of models into the wind tunnel flows always create the transitional flows which disturbs the stationary flows.

Another definition is that IS is weak, when the flow behind IS in MR is subsonic. Then, the I- and the R-polars intersect on the lower branch of the R-polar in Fig. 1.7. It is strong when the flow behind RS is supersonic, which occurs when the I- and the R-polars intersect on the upper branch of the R-polar. This implies that the weak and the strong boundary is at the sonic condition. However, these two definitions differ only slightly Ben-Dor (1979).

2.1.3 Wedges

2.1.3.1 Shock Wave Reflection Over Straight Wedges in a 40 mm × 80 mm Shock Tube

The transition of reflected shock waves between RR and MR is one of fundamental topics of shock wave research. In the late 1970, for shock wave reflection experiments, a 40 mm × 80 mm conventional shock tube was used by rupturing Mylar diaphragms in a double diaphragm system. At that time, the repeatability in terms of the scatter of shock Mach number ΔMs was ±2% for Ms ranging from 1.1 to 4.0 in air. Figure 2.5 shows the test section of the 40 mm × 80 mm conventional shock tube made of a single piece of carbon steel. The design and manufacturing were made in house. The parts of the shock tube were manufactured in the machine shop of the Institute of High Speed Mechanics of Tohoku University. In order to avoid thermal distortions of metal pieces, welding was not used at all. The wedge was placed on a movable stage. The wedge angle was controlled precisely ranging from 0° to 60°. As seen in Fig. 2.5, by adjusting the height of vertical shaft which sustained the height of movable stage with micrometer from outside the shock tube (Takayama and Sasaki 1983). At first, shock tube flows were visualized using conventional shadowgraph and schlieren methods. Its light source was a Q-switched ruby laser, the first product of ruby laser made in Japan. In 1980 a Q-switched ruby laser, manufactured in Apollo Laser Co. Ltd, was introduced. Then the previous optical arrangement of shadowgraph was combined with a double exposure holographic interferometry. Since then all the shock tube flow visualizations were conducted by double exposure holographic interferometry.

Figure 2.6a–j show shock wave reflections for Ms = 2.00 in air at 550 hPa and 295.6 K, at wedge angle ranging from θ_w = 0.0° and 3.0°. At small wedge angles the IS is reflected very slightly by passing along the wedge. Then this wedge angle is named as the so-called glancing incidence angle, χ_{glance}. The χ_{glance} is defined as

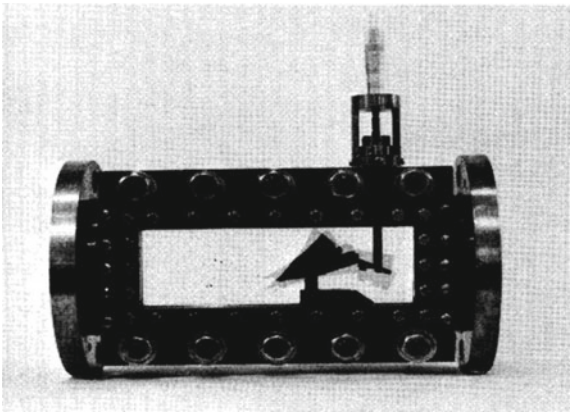

Fig. 2.5 Test section of a 40 mm × 80 mm shock tube (Takayama and Sasaki 1983)

following: the corner signal is transmitted at the particle velocity u and toward the IS at the local sound speed a. Therefore, the χ_{glance} is written as;

$$\tan\chi_{glance}. = \left\{a^2 - (Ms - u)^2\right\}^{1/2}/Ms, \tag{2.10}$$

where a is the local sound speed normalized by the sound speed in front of the shock wave a_o and u is the local particle velocity u normalized by a_0. In Fig. 2.6a, the RS intersects with the MS and lies on the MS is not observable, the trajectory of glancing incidence angle and intersect and form a triple point agrees with of $\chi_{glance} = 27.6°$ for Ms = 2.0. In Fig. 2.6b, the trajectory angle of the TP is about 24.0° for $\theta_w = 3.0°$. SL is not visible in Fig. 2.5b, so that the pattern of the reflected shock wave is von Neumann Mach reflection, vNMR. Figure 2.6a–j shows shock wave reflections for Ms = 3.00 in nitrogen at in nitrogen at 200 hPa and 295.6 K. Figure 2.5c–f shows SMR, whereas in Fig. 2.6g, h, the RS has a kink point and hence the reflection patterns are TMR. In Fig. 2.6i, with increasing the wedge angle, the kink point transits to a secondary triple point and hence the reflection pattern becomes a DMR. In Fig. 2.6j, at $\theta_w = 60.0°$, the pattern of the regular reflection is straight at the reflection point, which eventually indicates the flow behind the RS is supersonic. Hence, the reflection pattern is defined as a "supersonic regular reflection", or in short, SPRR.

Figure 2.7 shows direct shadowgraphs of DMR over $\theta_w = 45.0°$ and 50.0° wedges for Ms = 4.90 in air at 15 hPa and their enlargements. The triple points emitted luminosity. When performing for stronger shock wave at reduced initial pressures, the entire test fields were filled with intense luminosity and hence the film was totally over exposed. In performing shock tube experiments as shown Fig. 2.7, the films were covered with neutral density filters and the incident shock wave Mach number was Ms = 4.90; this shock wave was a lowest Ms we succeeded to visualize.

2.1.3.2 Shock Wave Reflection Over Straight Wedges in a 60 mm × 150 mm Diaphragm-Less Shock Tube

A 60 mm × 150 mm conventional shock tube made of standard high tensile strength carbon steel was designed and manufactured in a machine shop of the Institute. To minimize the deformation of steel plates, without using heavy machine works, the shock tube and its test section were carefully manufactured. Although it took time but their tolerance was 10 μm.

A diaphragm-less operation system was developed (Yang 1995). Figure 2.8a shows the diaphragm section. The high pressure chamber and the low pressure channel had a co-axial structure and separated by a rubber membrane as seen in Fig. 2.8b. It was bulged by pressurized helium gas from behind in an auxiliary high pressure chamber and tightly sealed the driver gas and test gas. The bulged

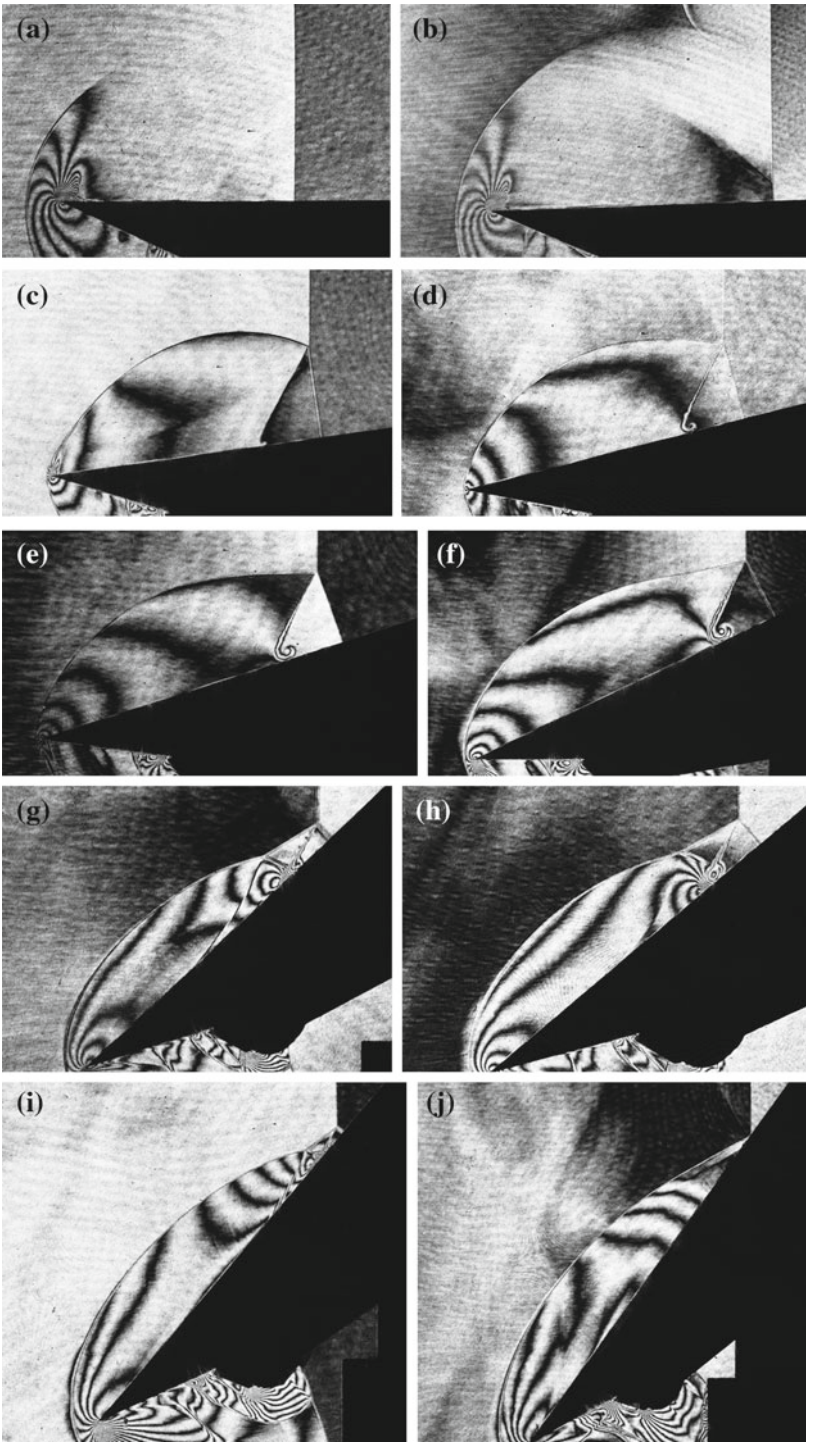
(a)
(b)
(c)
(d)
(e)
(f)
(g)
(h)
(i)
(j)

◂**Fig. 2.6** Evolution of shock wave reflection for Ms = 3.0 in nitrogen at 200 hPa and 295.6 K: **a** #81092917, Ms = 2.00 at 550 hPa and 295.6 K, θ_w = 0.0°; **b** #81092920, Ms = 2.00 at 550 hPa and 295.6 K, θ_w = 3.0°; **c** #81100219, θ_w = 11.0°; **d** #81100218, θ_w = 18.0°; **e** #81100218, θ_w = 18.0°; **f** #81100225, θ_w = 23.0°; **g** #81100305, θ_w = 40.0°; **h** #81100304, θ_w = 45.0°; **i** #81100505, θ_w = 50.0°; **j** #81100307, θ_w = 60.0° (Takayama and Sasaki 1983)

membrane was supported by a grid B. The high pressure helium was separated by a Mylar diaphragm. Upon rupturing it, the rubber membrane quickly receded and the driver gas drove a shock wave into the test section as shown in Fig. 2.8c. The rubber membrane was sustained by a grid A, when it receded.

With such a simple arrangement, shock waves were generated ranging from Ms = 1.1 up to 5.0 in air. The scatter in shock wave Mach number ΔMs was ±0.2%. The merit of diaphragm-less operation system is not only its higher degree of repeatability and but also no diaphragm fragments are generated. The diaphragm-less shock tube was operational continuously without exposing the shock tube to ambient air. As ambient air contaminated the shock tube wall so that the degree purity of the test gas was maintained high if the test gas was a foreign gas other than air.

In conventional shock tubes, diaphragm fragments are always shattered, so far as Mylar diaphragms were used. If a cellophane diaphragm is used, its fragments spread out every where inside shock tubes. Soon after the shock tube run, the inside the test section was cleaned.

Using this shock tube, the evolution of moderately strong shock waves ranging from Ms = 2.585 to 2.654 in air at 100 hPa and 289 K was shown for the wedge angle from 2° to 60°. Selective interferograms are shown in Fig. 2.9a–z. In Fig. 2.9a, in the case of the wedge angle of 2°, a three- shock confluence, that is TP is observed but a slip line, SL is not visible. The three shock wave confluence lies on a trajectory of glancing incidence angle χ_{glance}, which indicates the outer boundary of the corner signal to reach. The MS is not straight but is curved in the vicinity of the TP. This pattern shows a typical vNMR.

The measured $\chi_{glance} = \theta_w$ in Fig. 2.9a is about 23° and θ_w = 2°, whereas the predicted χ_{glance} in Eq. (2.10) being 26° for Ms = 2.61, hence the predicted value of $\chi_{glance} = \theta_w$ of Fig. 2.9a is 21°. The MS is slightly curved but intersects perpendicularly with the wedge surface as seen in Fig. 2.8a, b.

A bow shock wave generated at the leading edge of the wedge merged smoothly with a curved RS emanating from the TP. This implies that the flows in the entire region is subsonic. In the regions (3) and (4) in the vicinity of the TP, particle velocities are discontinuous but their flow directions and pressures are identical across the SL but the densities are discontinuous. However, in Fig. 2.9a. the density difference across the regions (3) and (4), is so small not sufficient for creating a visible SL. With increasing θ_w in Fig. 2.9b–d, the SL became visible and stagnated on the wedge surface. For shallower wedge angles, in Fig. 2.9b–d, the SL had a smooth laminar structure, their tail stagnated on the wedge surface. With increasing θ_w, the SL was broadened and eventually had a turbulent structure. Pressures in the regions (3) and (4) are identical in the vicinity of TP but, are higher on the wedge

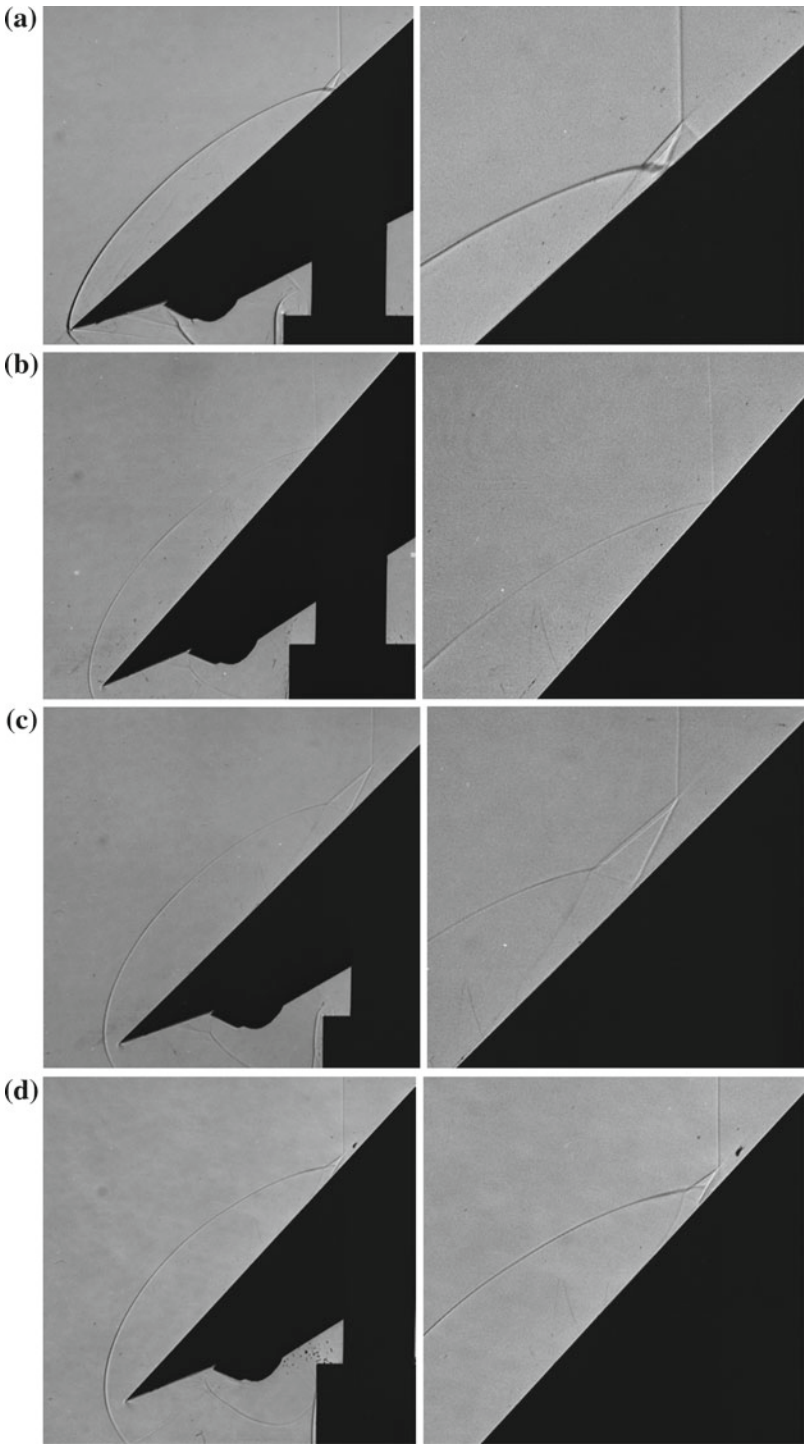
(a)
(b)
(c)
(d)

◂**Fig. 2.7** Generation of a luminous spot at a triple point: **a** #80091005, Ms = 4.90 in air at 15 hPa, 295.7 K, θ_w = 45° (Ben-Dor et al. 1983); enlargement of (**a**); **b** #80091006, Ms = 4.90, θ_w = 50°; enlargement of (**b**); **e** #80090926, Ms = 4.10 in air at 25 hPa and 297.0 K, θ_w = 45°; enlargement of (**c**); **d** #80090916, Ms = 3.10 in air at 40 hPa and 299.5 K, θ_w = 50°; enlargement of (**d**)

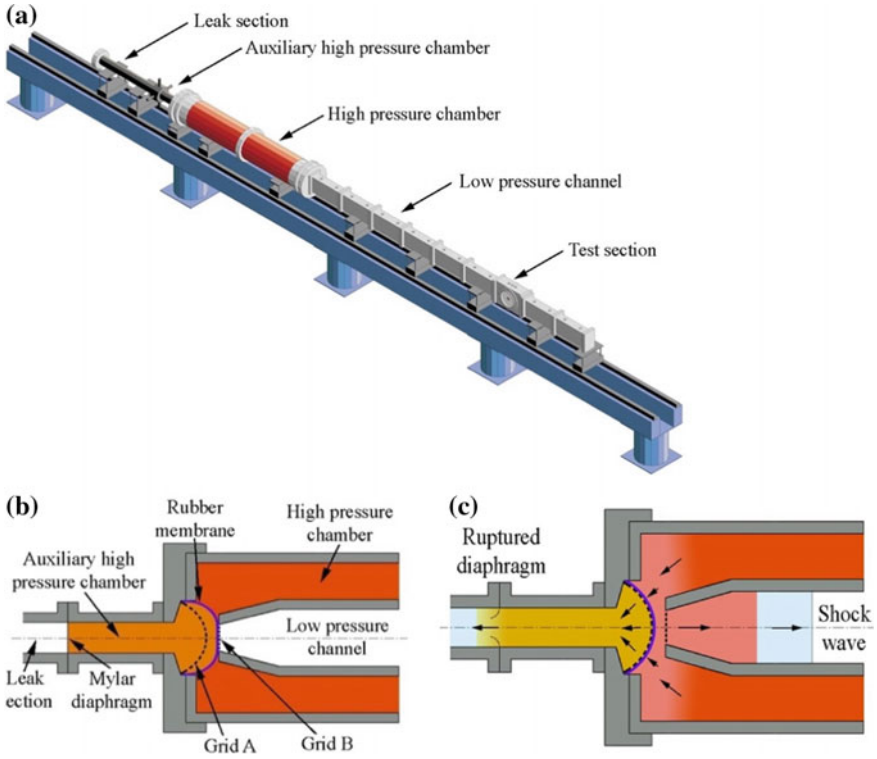

Fig. 2.8 A 60 mm 150 mm shock tube: **a** 60 mm × 150 mm diaphragm-less shock tube; **b** setup for operation; and **c** initiate to drive

surface in the region (3) than that in the region (4). Hence, in Fig. 2.9e, f, the SL rolled up forward as seen in Fig. 2.9g, h.

With increasing θ_w, the RS emanating from the TP was straightened in the vicinity of TP as seen in Fig. 2.9g, h. The straight RS implies that the flow behind the BS is transonic or supersonic. On shallow wedges, the straight RS and the curved RS intersect. This implies that the subsonic flow region and transonic flow region co-exist side by side and hence a kink point is formed and compression waves generated along the curved RS are going to coalesce if the wedge angle further increased.

The trend of dark fringe distributions indicates the assemblage of compression waves toward the kink point and then the TMR is formed. However, as observed in Fig. 2.9k–m, the TMR is not formed suddenly but takes a slightly long transient

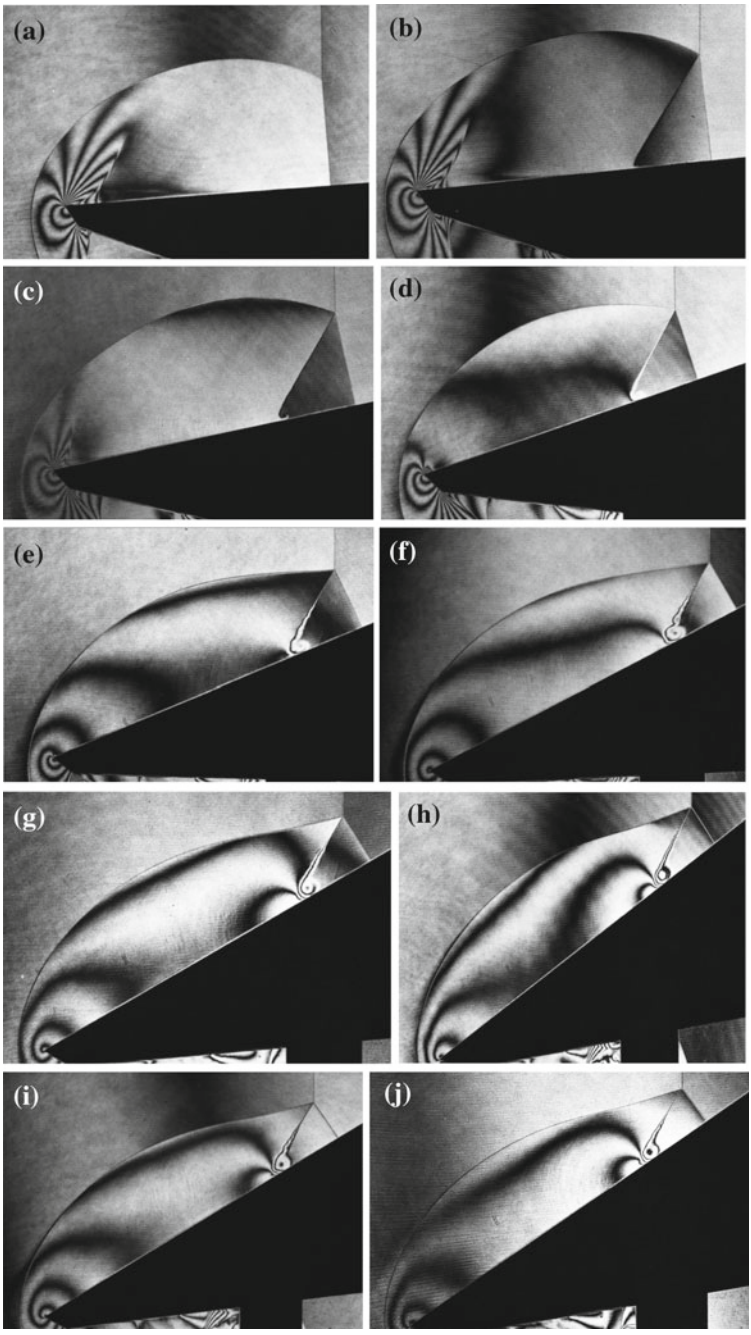
(a)
(b)
(c)
(d)
(e)
(f)
(g)
(h)
(i)
(j)

◂**Fig. 2.9** Sequential interferograms of shock wave reflection over movable wedge for Ms = 2.6 at 100 hPa, 298 K in air: **a** #83110516, Ms = 2.612, θ_w = 2°, vNMR; **b** #83110515, Ms = 2.642, θ_w = 5°, SMR; **c** #83110514, Ms = 2.653, θ_w = 11°, SMR; **d** # 83110513, Ms = 2.632, θ_w = 17°, SMR; **e** #83110512, Ms = 2.615, θ_w = 25°, SMR; **f** #83110511, Ms = 2.606, θ_w = 29°, reflected shock shows a sign of TRM; **g**#83110510, Ms = 2.602, θ_w = 31°, SMR with a sign of TRM; **h** #83110508, Ms = 2.631, θ_w = 33°, SMR with a sign of TMR; **i** #83110509, Ms = 2.631, θ_w = 34°, SMR with a sign of TMR; **j** # 83110506, Ms = 2.605, θ_w = 35°, SMR with a sign of TMR; **k** #83110505, Ms = 2.611, θ_w = 37°, a kink point is initiated; **l** #83110504, Ms = 2.648, θ_w = 39°, formation of TMR; **m** #83110503 Ms = 2.589, θ_w = 41°, TRM; **n** #83110502, Ms = 2.613, θ_w = 43°, termination of TMR; **o** #83110507, Ms = 2.599, θ_w = 46°, transition from TMR to DMR; **p** #83110423, Ms = 2.611, θ_w = 47°, DMR; **q** enlargement of (**p**), DMR; **r** #83110421, Ms = 2.624, θ_w = 48°, DMR; **s** #83110422, Ms = 2.654, θ_w = 49.5°, DMR; **t** enlargement of (**s**); **u** #83110420, Ms = 2.625, θ_w = 51° DMR; **v** enlargement of (**t**), the second TP moves toward the first TP; **w** #83110424, Ms = 2.640. θ_w = 52° DMR is going to terminate; **x** enlargement of (**w**), the second TP merges to the first TP, the termination of DMR; **y** #83110417, Ms = 2.628, θ_w = 54°, SPRR; **z** #83110415, Ms = 2.585, θ_w = 60°, SPRR

process. With a further increase in θ_w, the kink point becomes a triple point, TP and compression waves coalesce into a secondary shock wave. Eventually from the resulting TP, the three-shock confluence and a secondary slip line appear. It should be noticed that the initiation of double Mach reflection, DMR also takes a transient process. Figure 2.8l–m indicate the formation of TMR. In Fig. 2.9n, it is not decisively identified that a faint change in fringe patterns indicates the initiation of a SL in the region behind the curved RS. This also indicates a transition from a TMR to a DMR.

Ben-Dor (1979) analytically obtained, for the first time, the domain and boundary among a SMR, a TMR and a DMR. It is experimentally found that the SMR does not transit into TMR instantaneously at a predicted $\theta_{crit.}$ Similarly, the evolution from a TMR to a DMR also takes a transient process. The difference between the prediction and experimental findings is most probably based on the fact that in analytical predictions all the individual flow regions are assumed to be uniform while in reality these regions are non-uniform because of the presence of viscosity and the finite size of experimental facilities.

Figure 2.9p–x shows the transition from a DMR to a RR. At $\theta_w = \theta_{crit}$, the TP terminates and a supersonic region appears behind the straight RR. This RR pattern is defined as a "supersonic regular reflection", SPRR as shown in Fig. 2.9y. The curved RR has a subsonic flow behind the reflection point and is defined as a "subsonic regular reflection", or in short SbRR.

As θ_w approaches to the θ_{crit}, the length of the MS emanating from the TP of the DMR is shortened to the length barely recognizable. For example, Fig. 2.9s, u, w shows DMR at θ_w = 49.5°, 50°, and 51°, respectively and their enlarged images are presented in Fig. 2.8t, v, x. The DMR pattern in Fig. 2.9x is barely observable. Even such a localized TP accompanies a short SL which turns into a vortex on the wedge surface. As the local Reynolds number in terms of the characteristic length of the MS has an order of magnitude of a few hundreds, the flow at the TP is subjected to viscous effects, which indicates that the transition from MR to RR

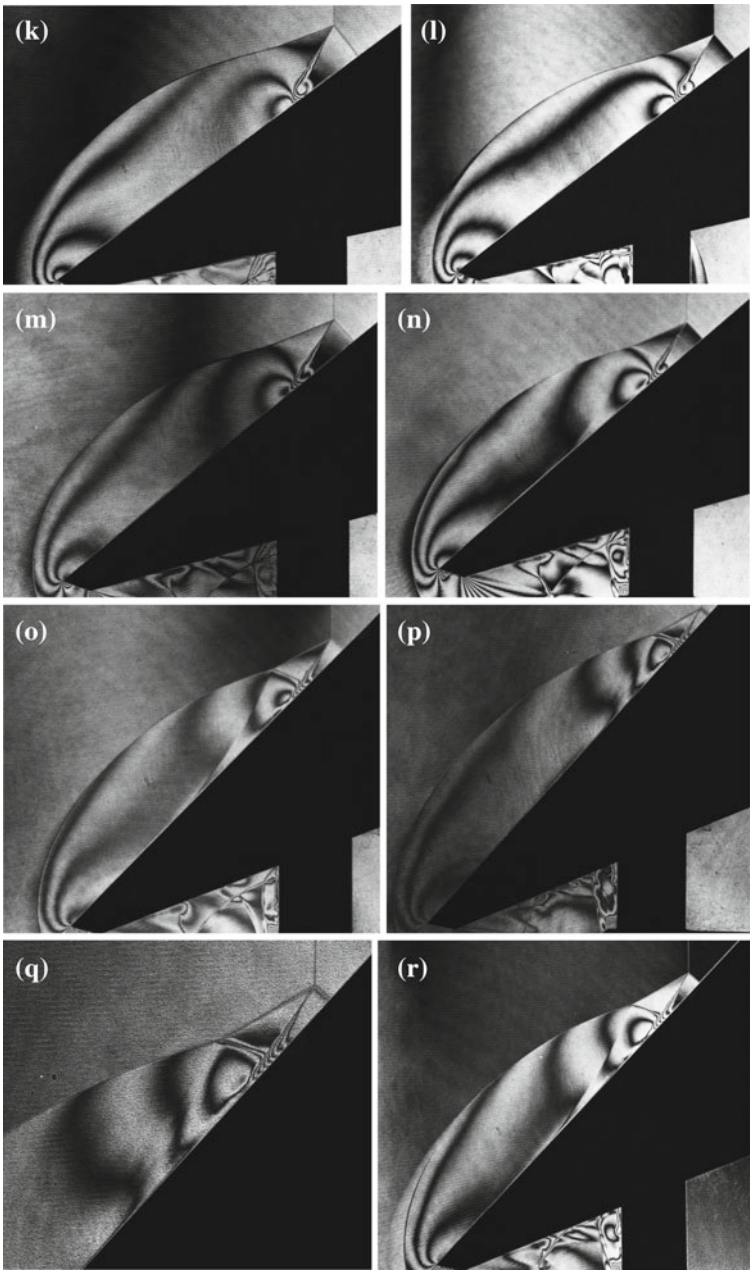

Fig. 2.9 (continued)

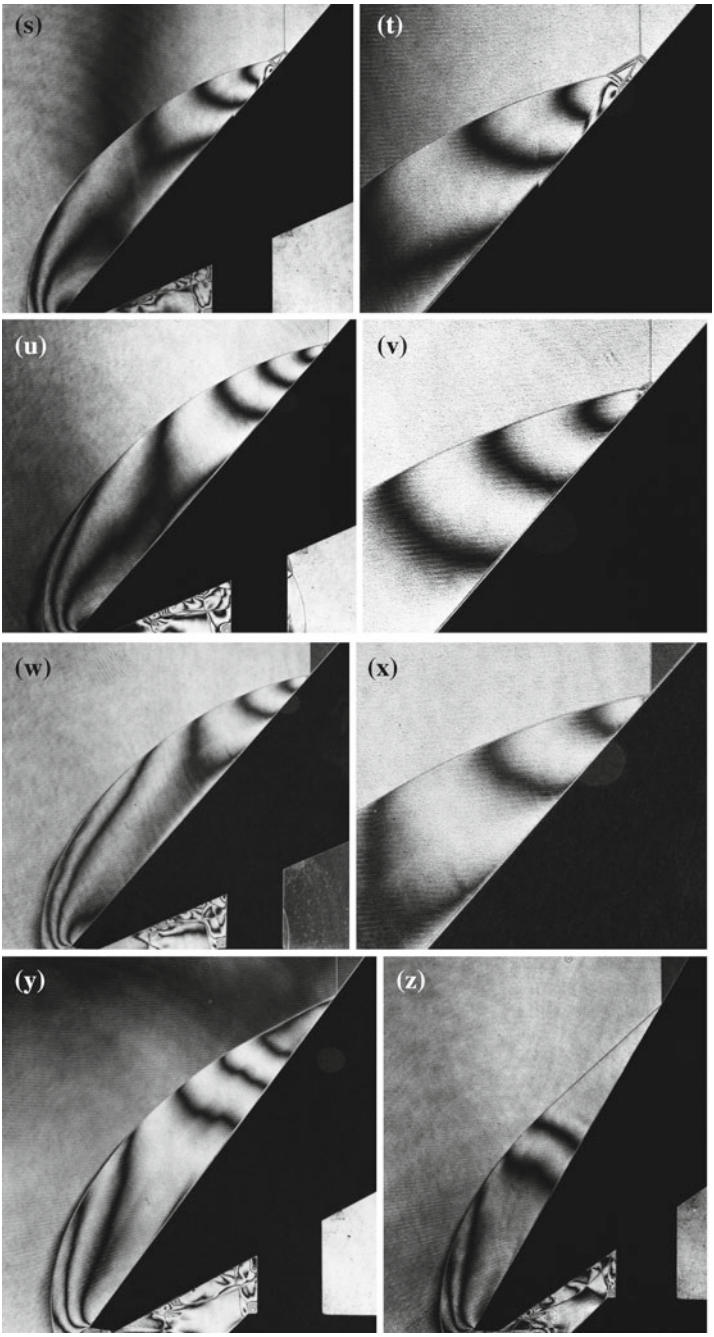

Fig. 2.9 (continued)

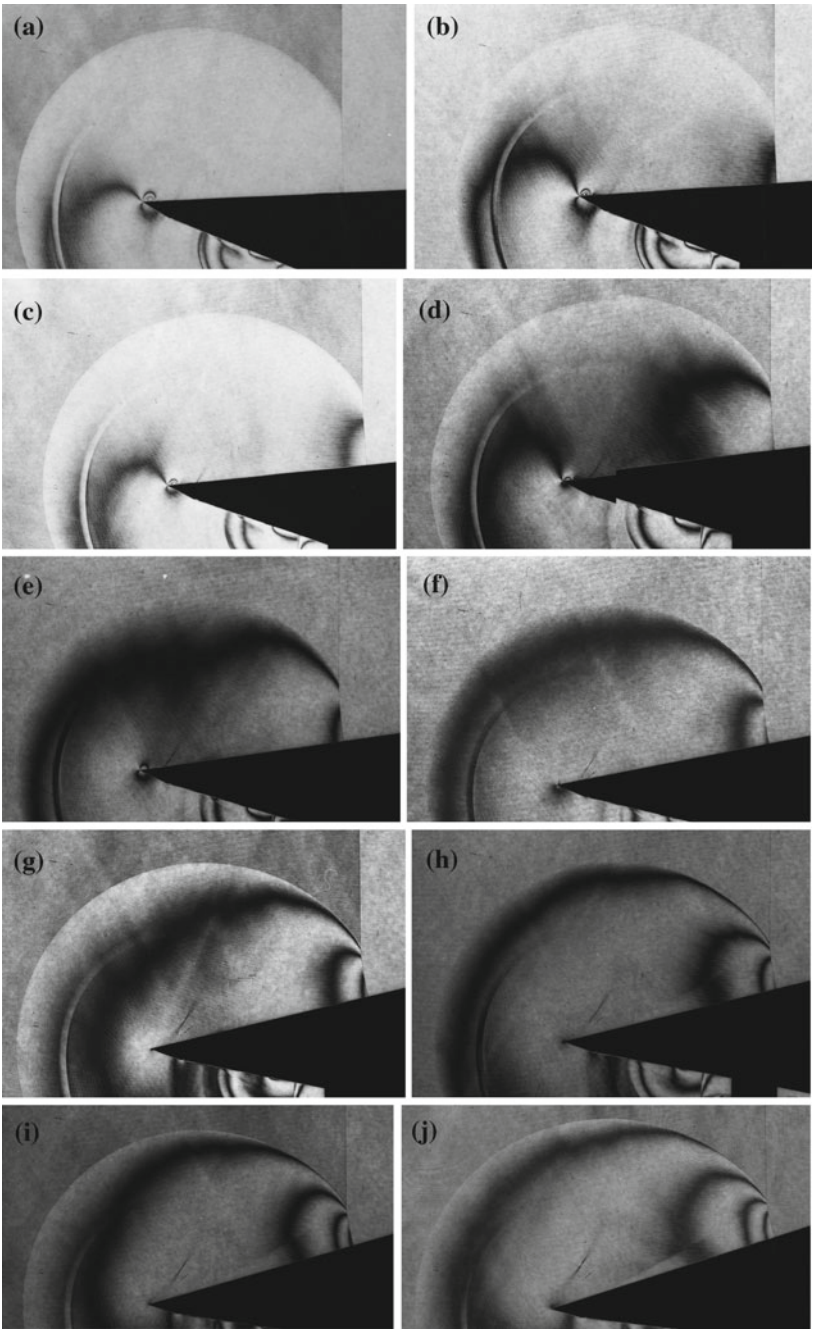
(a)
(b)
(c)
(d)
(e)
(f)
(g)
(h)
(i)
(j)

◂**Fig. 2.10** Selected images used to edit animated display of shock wave reflection over a movable wedge installed in a 60 mm × 150 mm diaphragm-less shock tube for Ms = 1.20 in air at 1013 hPa, 301 K: **a** #94100402, θ_w = 2.0°; **b** #94100404, θ_w = 4.5°; **c** #94100406, θ_w = 5.9°; **d** #94100409, θ_w = 7.4°; **e** #94100411, θ_w = 8.9°; **f** #94100414, θ_w = 11.1°; **g** #94100417, θ_w = 13.4°; **h** #94100419, θ_w = 14.8°; **i** #94100421, θ_w = 16.3°; **j** #94100423, θ_w = 17.8°; **k** #94100501, θ_w = 19.3°; **l** #94100503, θ_w = 20.8°; **m** #94100505, θ_w = 22.2°; **n** #94100507, θ_w = 23.7°; **o** #94100509, θ_w = 25.2°; **p** #94100511, θ_w = 26.7°; **q** #94100512, θ_w = 27.4°; **r** #94100514,θ_w = 28.9°; **s** #94100516, θ_w = 30.4°; **t** #94100518, θ_w = 31.8°; **u** #94100520, θ_w = 33.2°; **v** #94100522, θ_w = 34.6°; **w** #94100524, θ_w = 36.1°; **x** #94100526, θ_w = 37.6°; **y** #94100528, θ_w = 39.1°; **z** #94100530, θ_w = 40.6°; **A** #94100532, θ_w = 42.1°; **B** #94100534, θ_w = 43.5°; **C** #94100535, θ_w = 44.2°; **D** #94100540, θ_w = 48.0°; **E** #94100542, θ_w = 49.4°; **F** #94100544, θ_w = 50.9°; **G** #94100546, θ_w = 52.4°; **H** #94100544, θ_w = 54.5°

would be affected by the initial pressure. However, the effect of initial pressure on the transition of reflected shock waves from wedges were hardly detectable in conventional shock tubes.

When experiments are conducted in a shock tube having a higher degree of reproducibility, the viscous effect on the shock wave transitions would be resolved more clearly. It would be more straightforward to conduct numerical analysts for reproducing interferometric images.

2.1.3.3 Animated Display of Shock Wave Reflection from a Movable Wedge

A wedge was placed on a movable stand installed in the 60 mm × 150 mm shock tube. The movable stand had a similar structure to that shown in Fig. 2.5. The wedge angle was variable from 0° to 60°. The reflected shock waves were visualized by double exposure holographic interferometry for Ms = 1.20 in air at the atmospheric pressure and 301 K. The reconstructed holograms were edited in the form of animated display, in which the wedge surface was positioned horizontally on the bottom of the animated display and the reflection point was positioned at the center of the individual frames. Therefore, the IS was at first vertical to the center of horizontal wedge and started continuously tilting. The MS was also tilting and the TP was moving. The animated display only allowed such a unique evolution of shock wave reflection patterns. Figure 2.10 shows selective images taken from the interferometric images.

In the animation, the density variation around the TP and the growth of the MS are observed through the variation of fringes. When the IS is vertical to the wedge surface, the TP doesn't exist. However, when the MS appears over a shallow wedge surface. With the increase in the wedge angle θ_w. the MS was slightly curved, the TP lies on the trajectory angle of the glancing incidence angle. The MS, however, is not uniformly curved but has a minimal radius of curvature in a position slightly below the TP. With further increasing the wedge angle θ_w, the point of the minimal radius of curvature is gradually approaching toward the TP. At the same time, fringes appear behind the MS and increase their number. Fringes tend to merge

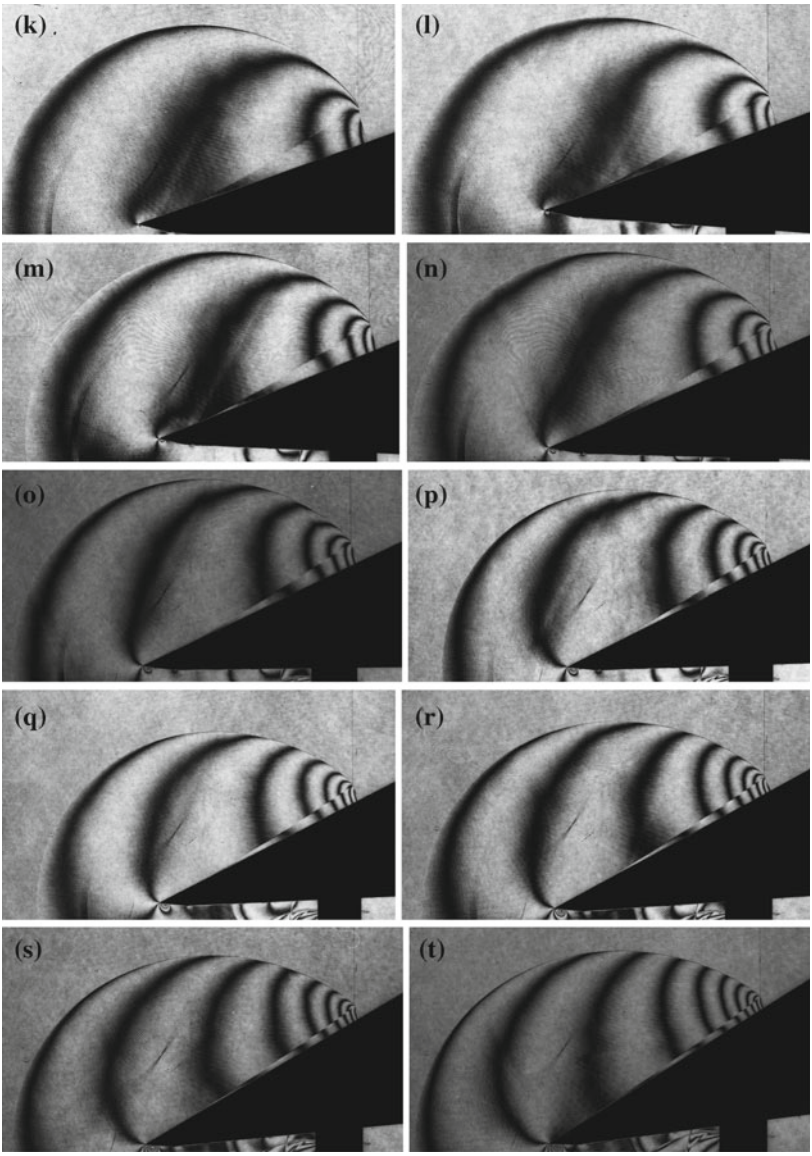

Fig. 2.10 (continued)

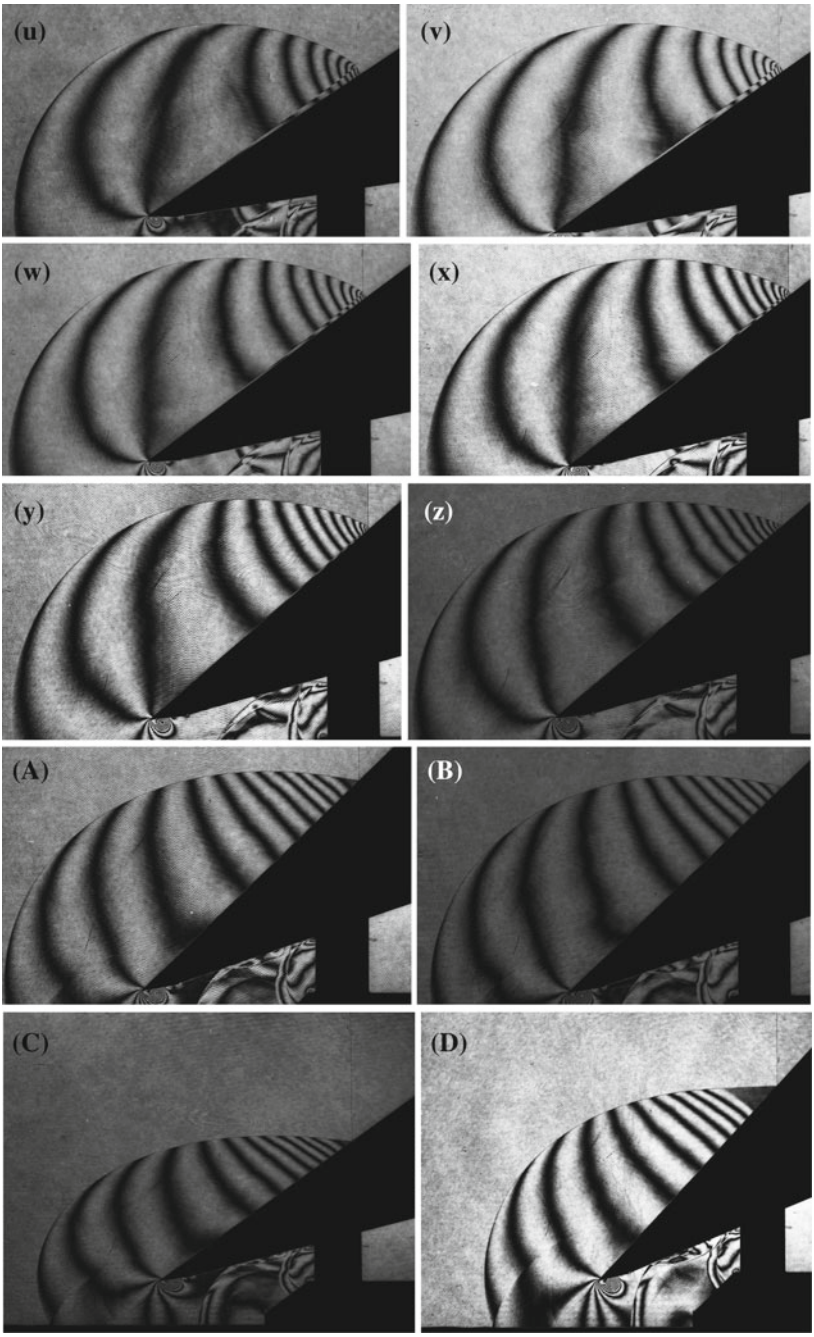

Fig. 2.10 (continued)

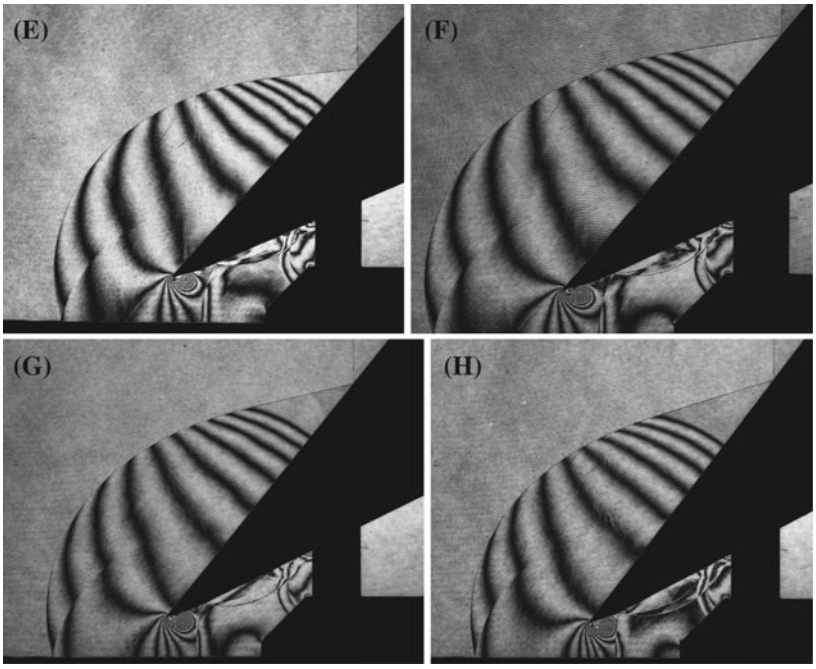

Fig. 2.10 (continued)

toward apparent TP. The fringes merged with the SL, was very vaguely visible in Fig. 2.10h, and was slightly clearly observed in Fig. 2.10i. The transition to a MR took place in Fig. 2.10y at $\theta_w = 39.1°$.

Figure 2.11 shows sequential images of very weak shock wave reflected from a wedge mounted on a movable stand installed in the 60 mm × 150 mm diaphragm-less shock tube. In Fig. 2.11a–h, the reflection patters are the vNMR so that the SL is missing. In Fig. 2.11i, the transition to the SbRR takes place.

2.1.3.4 Weak Reflected Shock Wave in a 150 mm × 60 mm Shock Tube

The density variation $\Delta\rho$ behind the shock wave in the double exposure holographic interferogram is related to the fringe number N in Eq. (1.9) as $N = \Delta\rho L/K\lambda$. This means that in an optical arrangement having a longer *OB* path, the sensitivity becomes higher. Then the 60 mm × 150 mm shock tube was turned 90° sideway forming a 150 mm × 60 mm cross sectional shock tube. Its optical sensitivity was as high as 2.5 times than the former shock tube. A 150 mm wide wedge model with a 60° edge angle was sandwiched between 150 mm diameter and 20 mm thick acrylic plates and installed into the test section of the shock tube.

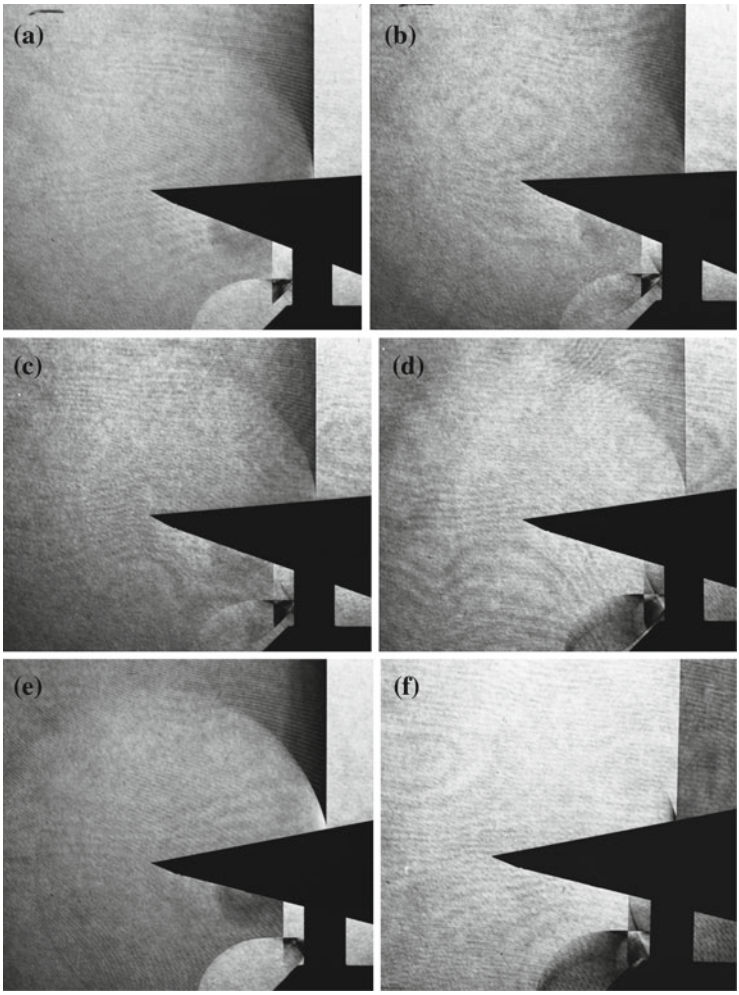

Fig. 2.11 Shock wave reflection over wedges mounted on a movable stage in a 60 mm × 150 mm diaphragm-less shock tube for Ms = 1.032 in atmospheric air, 299.5 K: **a** #94061102, $\theta_w = 3.0°$; **b** #94061101, $\theta_w = 5.0°$; **c** #94061103, $\theta_w = 6.0°$; **d** #94061105, $\theta_w = 7.5°$; **e** #94061107, $\theta_w = 10.0°$; **f** #94061108, $\theta_w = 12.0°$; **g** #94061110, $\theta_w = 14.5°$; **h** #94061111, $\theta_w = 16.0°$; **i** #94061114, $\theta_w = 17.5°$; **j** #94061115, $\theta_w = 18.5°$; **k** #94061117, $\theta_w = 20.0°$; **l** #94061120, $\theta_w = 21.5°$

Wedge angles were adjusted by rotating the observation windows and the whole wedge. Figure 2.12a–r shows sequential results for Ms = 1.20 in air at 800 hPa, taken at 80 μs after the IS passed the leading edge of the wedge. In Fig. 2.12a at $\theta_w = 2.0°$, no fringe is observed behind the MS, whereas a dark fringe appears behind the RS and the IS. In Fig. 2.12b at $\theta_w = 4.0°$ and in Fig. 2.12c at $\theta_w = 6.0°$, a dark broadened fringe appears behind the MS. In Fig. 2.12b, c, the MS is curved not uniformly but its radius of curvature varies. Two dark fringes intersect with the

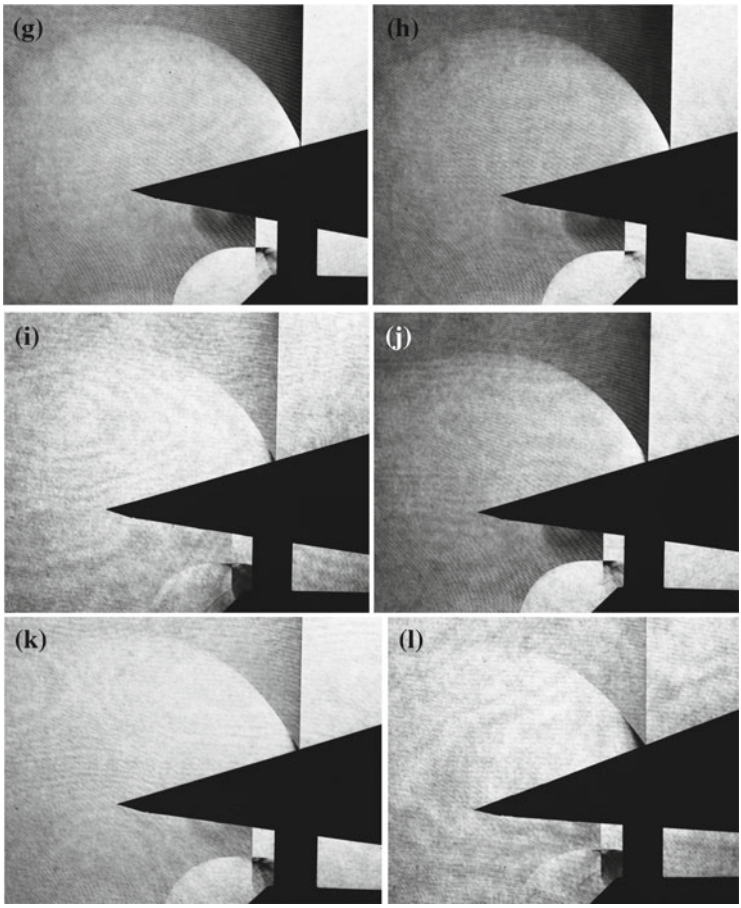

Fig. 2.11 (continued)

MS at which the radius of curvature becomes a minimum. In shallower wedge angles, the IS, RS, and MS merge at a point forming a three-shock confluence, or TP. However, the SL is not emanating from the TP as no density discontinuity exists behind the MS. Dark fringes running downward along the RS intersect with the MS, whereas other dark fringes starting from the wedge surface upward eventually intersect with the MS. These downward shifting fringes and upward shifting fringes intersect with the MS forming just like dividing stream lines. Such a fringe distribution is a typical pattern of a vNMR. Eventually, the radius of curvature along the MS becomes minimal at the point at which the fringe distribution looks like a dividing stream line. Then with the increase in the wedge angle, the fringes gradually converge into the TP and the MS becomes straight and is shortened. The shock wave reflection pattern eventually becomes a SMR. In Fig. 2.12s at $\theta_w = 34°$, the SMR transits to a RR.

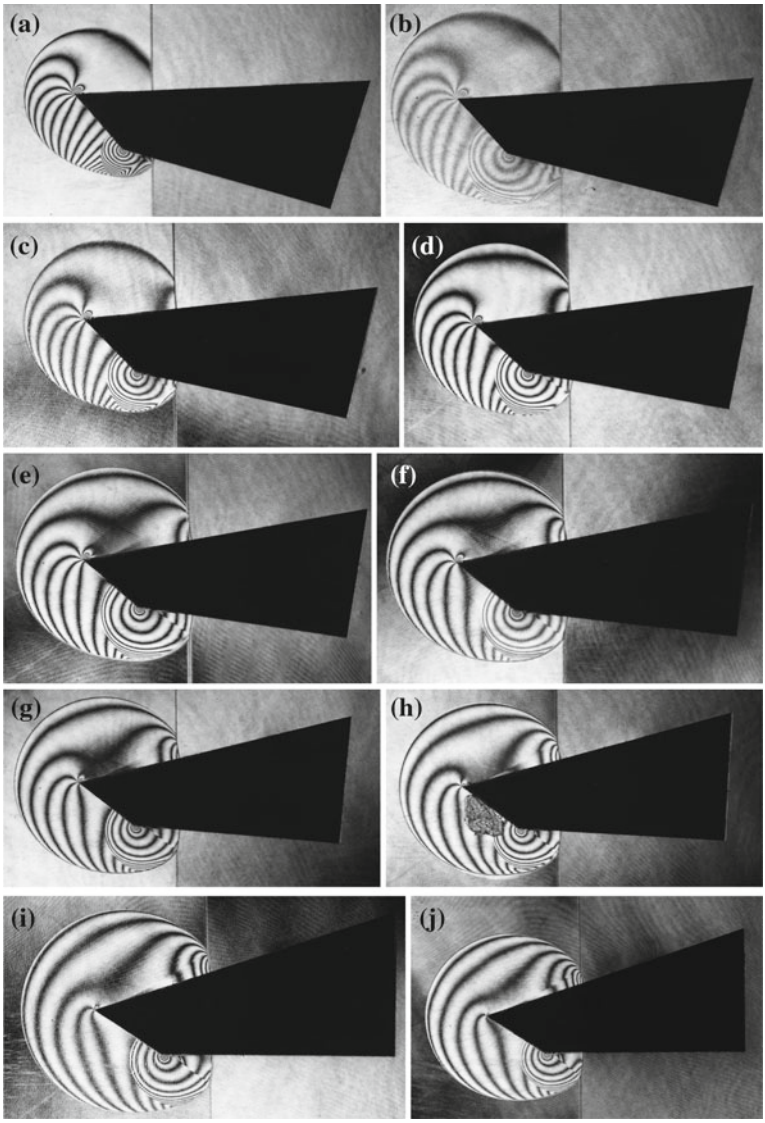

Fig. 2.12 Evolution of reflected shock wave over a 150 mm wide wedge for Ms = 1.20 in air at 800 hPa, 290.4 K in a 150 mm × 60 mm shock tube at 80 μs from the leading edge: **a** #88031004, Ms = 1.204, θ = 2°; **b** #88031006, Ms = 1.203, θ = 4°; **c** #88031101, Ms = 1.200, θ = 6°; **d** #88031103, Ms = 1.206, θ = 8°; **e** #88031105, Ms = 1.213, θ = 10°; **f** #88031107, Ms = 1.207, θ = 12°; **g** #88031111, Ms = 1.201, θ = 14°; **h** #88031113, Ms = 1.206, θ = 16°; **i** #88031115, Ms = 1.198, θ = 18°; **j** #88031103, Ms = 1.206, θ = 20°; **k** #88031118, Ms = 1.207, θ = 21°; **l** #88031119, Ms = 1.211, θ = 22°; **m** #88031123, Ms = 1.180, θ = 26°; **n** #88031125, Ms = 1.186, θ = 27°; **o** #88031126, Ms = 1.187, θ = 28°; **p** #88031129, Ms = 1.198, θ = 31°; **q** #88031130, Ms = 1.197, θ = 32°; **r** #88031132, Ms = 1.180, θ = 34°; **s** #88031133, Ms = 1.172, θ = 35°

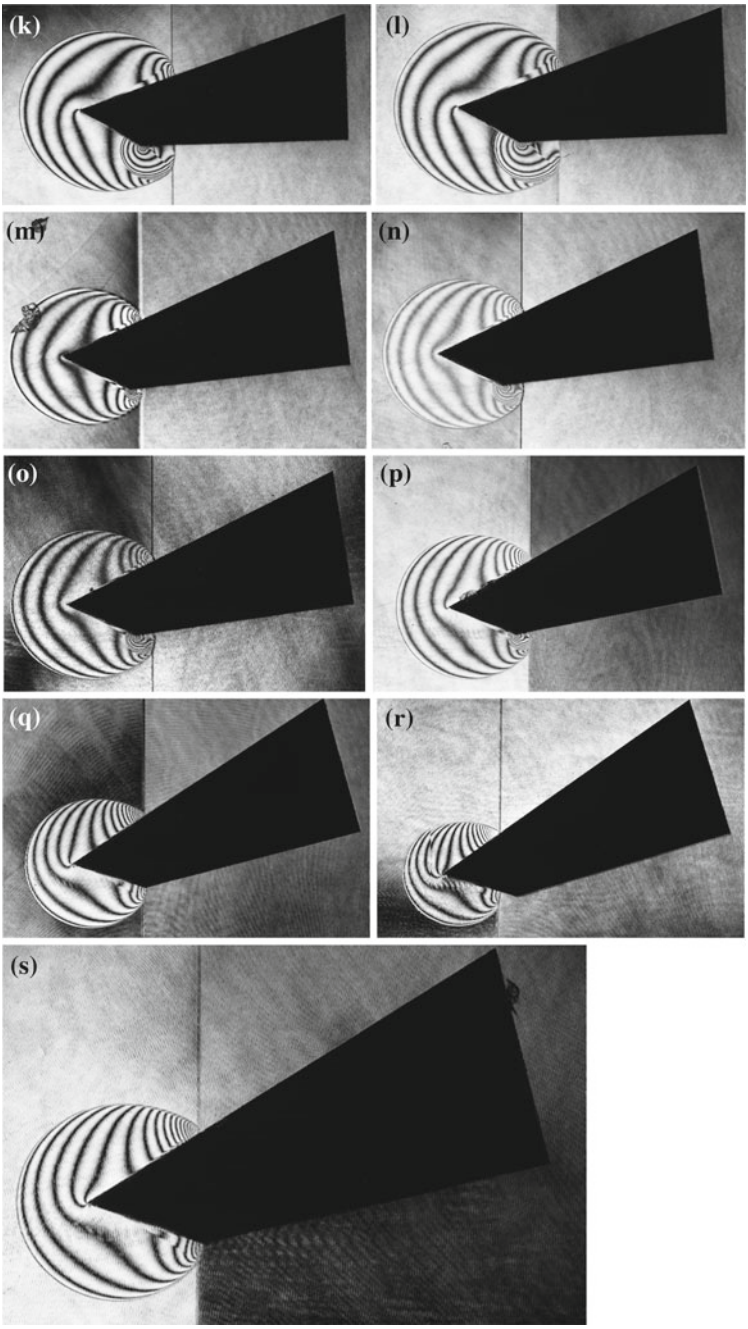

Fig. 2.12 (continued)

Figure 2.13 summarizes the variation of the TP trajectory for the shock wave of Ms = 1.20 reflected from wedges of variable angles as shown in Figs. 2.10 and 2.12. The ordinate denotes the triple point trajectory angle χ in degree and the abscissa denotes the wedge angle θ_w in degree. The glancing incidence angle of the shock wave of Ms = 1.20 in air is 25.47°; and red circles denotes the TP as shown in Fig. 2.10 and blue circles denotes the TP as shown in Fig. 2.12. At smaller θ_w, the TPs lie on the line of $\chi_{glance} - \theta_w$. Such TPs have the curved MS and intersected perpendicularly to the wedge surface. The radius of curvature is not constant but has a minimal radius along the MS. The point of the minimal radius of curvature along the MS can be experimentally estimated. In Fig. 2.13, the grey circles denote the minimal radii of curvature or the kink points shown in Fig. 2.10 and faint pink circles denote these points shown in Fig. 2.12. The grey circles and faint pink circles are distributed below the line of $\chi_{glance} - \theta_w$ and typically show the pattern of vNMR. In increasing θ_w, the MS becomes straight and the reflected shock wave pattern becomes SMR. A further increase in the wedge angles causes the transition from the SMR to the RR.

In the case of very shallow edges and for weak shock waves, the points of the merger of an IS with a RS always lie on the trajectory of $\chi_{glance} - \theta_w$, which means that pressure variations $\Delta p = \varepsilon$ are so small that the isentropic condition of Δs $(\Delta p)^3 = \varepsilon^3$ is always satisfied. On the contrary, the shock-shock is defined by Whitham (1959) as a discontinuous front carrying the boundary condition that the MS is perpendicular to the wedge surface. Then the minimum radius of curvature or a kink point is formed in the area at which the isentropic condition is satisfied and the glancing incident condition is fulfilled. Figure 2.14 show reflection of shock wave for Ms = 1.05 in air over a movable wedge ranging from 2° to 30°. It should be noticed that the reflection patters are vNMR for the wedge angle up to the critical

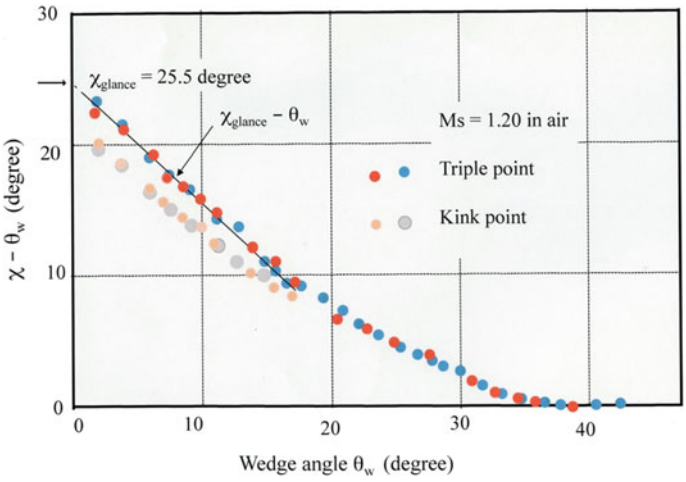

Fig. 2.13 Summary of variations of the triple point trajectory angle χ versus the wedge angle θ_w shown in Figs. 2.10 and 2.12

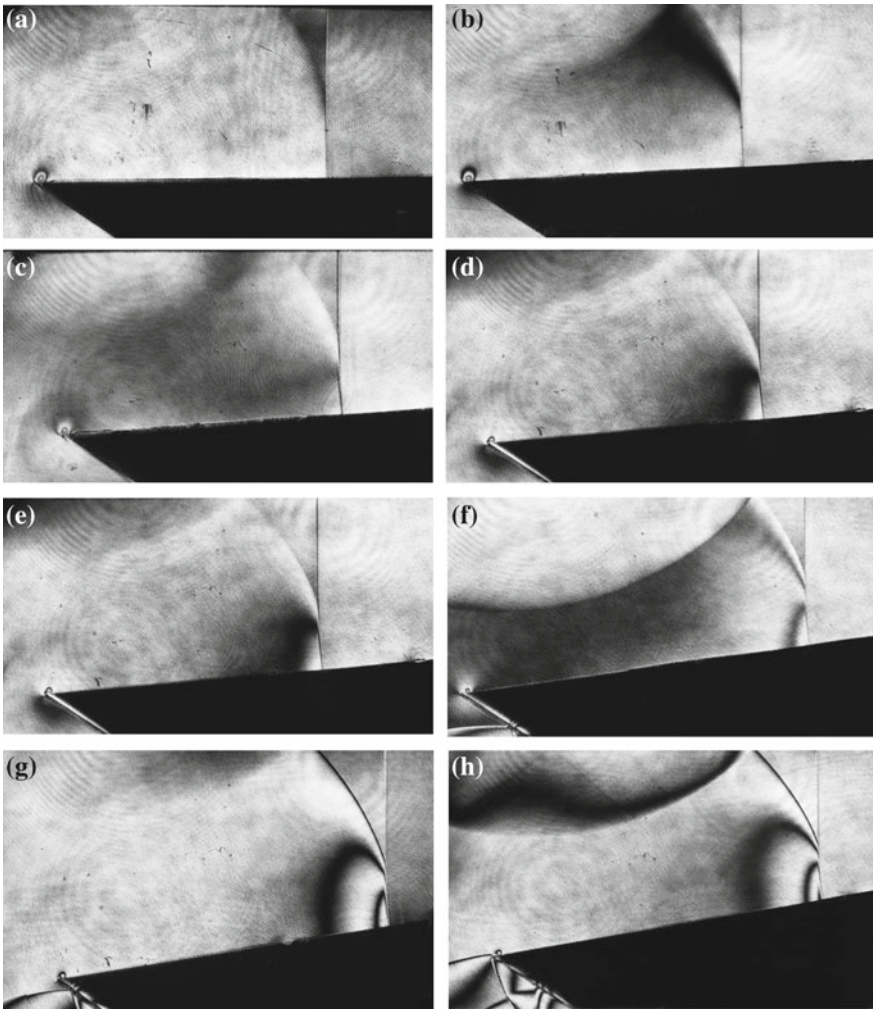

Fig. 2.14 Evolution of reflection of weak shock waves in a 150 mm × 60 mm shock tube for Ms = 1.05 in air at 1013 hPa, 290 K: **a** #88011108, Ms = 1.056, $\theta_w = 2.0°$; **b** #88011104, Ms = 1.051, $\theta_w = 3.0°$; **c** #88011102, Ms = 1.037, $\theta_w = 4.0°$; **d** #88010905, Ms = 1.050, $\theta_w = 5.0°$; **e** #88010903, Ms = 1.053, $\theta_w = 6.0°$; **f** #88010812, Ms = 1.049, $\theta_w = 8.0°$; **g** #88010810, Ms = 1.049, $\theta_w = 9.0°$; **h** #88010807, Ms = 1.061, $\theta_w = 10.0°$; **i** enlargement of (**h**); **j** #88010801, Ms = 1.058, $\theta_w = 12.0°$: **k** #88010716, Ms = 1.049, $\theta_w = 13.0°$; **l** #8801071, Ms = 1.058, $\theta_w = 14.0°$; **m** #88010711, Ms = 1.060, θw = 15.0°; **n** #88010707, Ms = 1.051, θw = 16.0°; **o** #88010704, Ms = 1.051, θw = 17.0°; **p** #87113005, Ms = 1.075, $\theta_w = 18.0°$, in a shock tube L = 60 mm; **q** #88010601, Ms = 1.072, $\theta_w = 20.0°$; **r** #87120106, Ms = 1.070, $\theta_w = 21.0°$ in a shock tube L = 60 mm; **s** #87120110, Ms = 1.073, $\theta_w = 23.0°$ in a shock tube L = 60 mm; **t** #87120118, Ms = 1.068, $\theta_w = 27.0°$ in a shock tube L = 60 mm; **u** #87120201, Ms = 1.071, $\theta_w = 29.0°$ in a shock tube L = 60 mm; **v** #87120203, Ms = 1.062, $\theta_w = 30.0°$ in a shock tube L = 60 mm

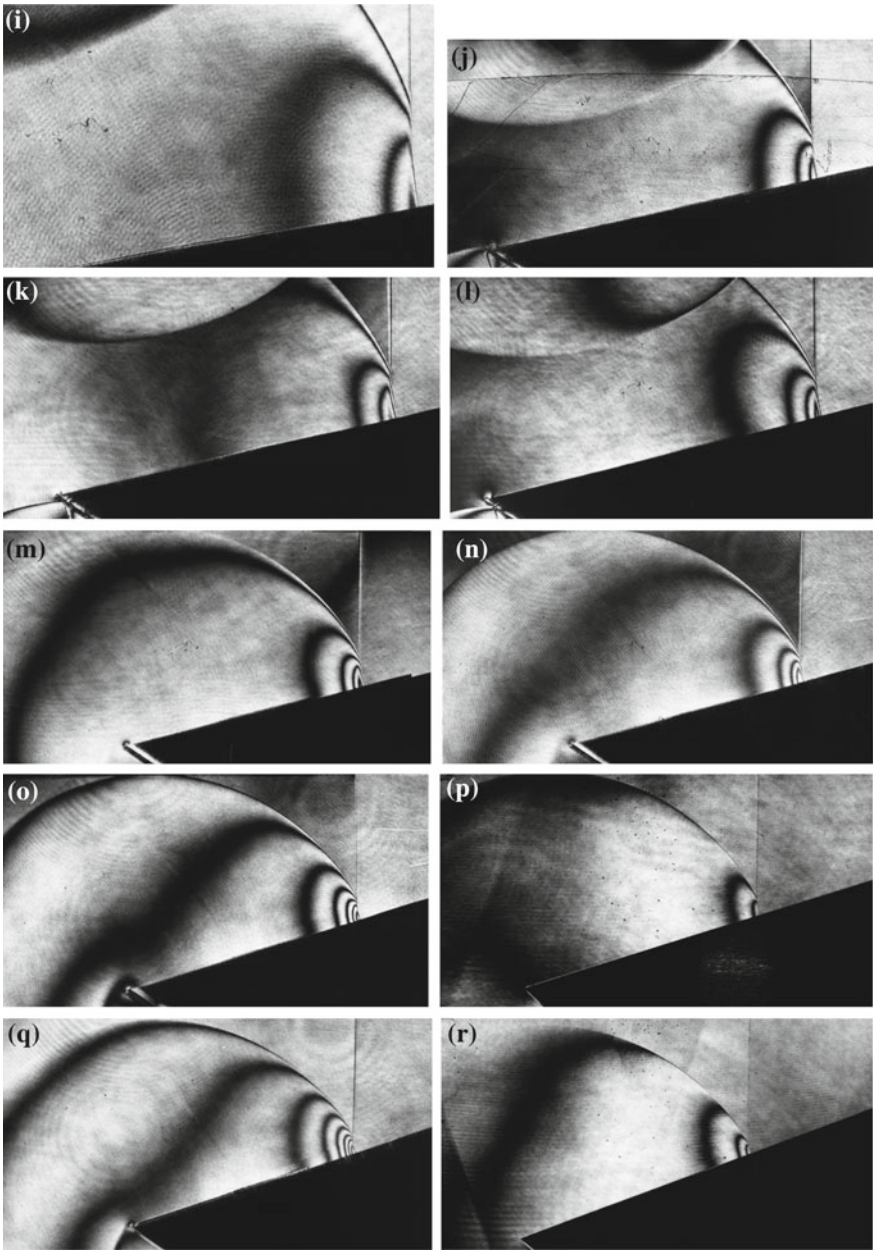

Fig. 2.14 (continued)

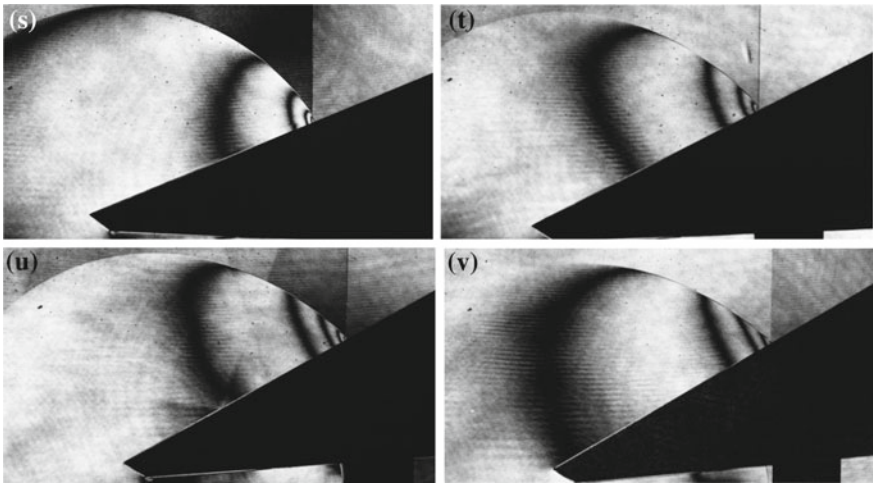

Fig. 2.14 (continued)

transition at about 29°. It is also noticed that the minimum radius of curvature point consistently appears just below the TP.

2.1.3.5 Shock Wave Reflection from Wedges in Dusty Gas

Figure 2.15 shows experimental arrangement composed of a 50 mm diameter conventional shock tube that was connected to a 30 mm × 40 mm shock tube test section. Almost spherically shaped fly ash were used as dust particles of about 5 μm in diameter; they were supplied from a dust feeder carried by an air flow placed just at the diaphragm section. At the end of the shock tube, a 150 mm diameter and 1.5 m long dump tank was connected to which a vacuum pump and a dust filter were attached Suguyama et al. (1986). The dust particle so far feeding was continuously circulated and recovered. The dust particles were distributed relatively uniformly over the test section at loading ratio of 0.02. The loading ratio was

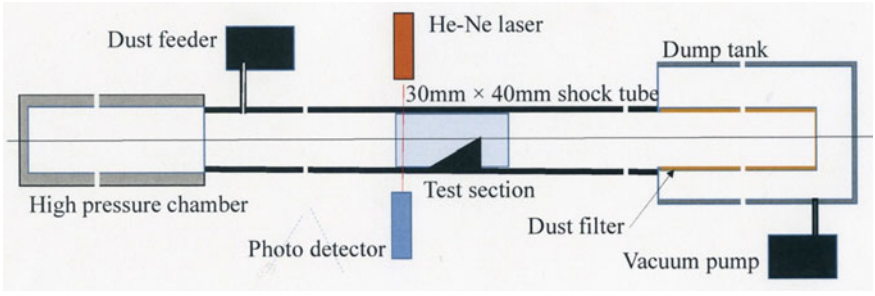

Fig. 2.15 Schematic diagram of dusty gas shock tube experiment (Suguyama et al. 1986)

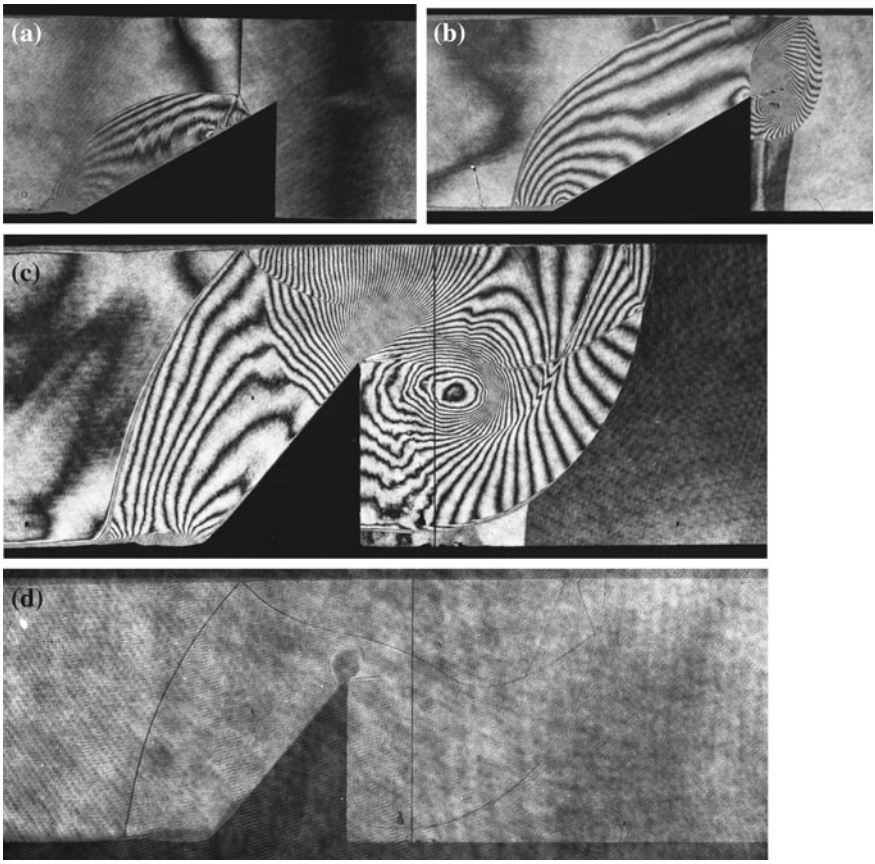

Fig. 2.16 Shock wave reflection over wedges in dusty gas for Ms = 2.05 in air at 1013 hPa, 289.5 K: **a** #87042305, Ms = 2.022, $\theta_w = 30°$; **b** #87042210, Ms = 2.044, $\theta_w = 30°$; **c** #87042215, Ms = 2.053, $\theta_w = 45°$; **d** unreconstructed hologram of (**c**)

defined as a ratio of particle mass to the mass of tested air. With this arrangement, the experiment was conducted for Ms ranging from 1.5 to 2.20 and corresponding Reynolds number ranging from 2.6×10^5 to 6.4×10^5 based on the characteristic length of the shock tube. Several different wedges in the shock tube test section. Unlike in the previously reported cases, in the present experiments, it was impossible to determine θ_{crit} as there was no movable stand for the tested wedges. In the present experiments, only shock wave reflection patterns were observed.

Figure 2.16 shows shock wave reflection patterns for Ms = 2.01. The reflection pattern seen in Fig. 2.16a is the SMR almost identical with the SMR shown in Fig. 2.9e. The boundary layer developing along the shock tube upper wall looks thicker whereas the sedimentation of dust particles on the bottom wall is observed; a layer of dust particle is blown off from the edge. In Fig. 2.16b, the transmitted shock wave was diffraction at the corner of the wedge and a vortex is formed.

The wedge was not tightly touched the observation windows and gap intervals of probably 0.05 mm existed. Then the IS leaked through this gap. The grey pattern observed at the rear corner of the wedge seen in Fig. 2.16b was the leakage of the IS. It would be a meaningful to clarify the effect of the dust loading ratio on the prevailing value of θ_{crit} of a shock wave reflection from wedges. The present experiment is a preliminary test for designing a dusty gas shock tube in which reproducible runs would produce reliable dusty shock tube flows. However, it would be appropriate to supply reliable interferometric image to support a numerical scheme for predicting the effect of dust loading ratio on θ_{crit}. Figure 2.16c, d shows the diffraction of the SMR over a 45° wedge, an interferogram and its unreconstructed image. The flow pattern is similar to shock wave diffraction over a backward facing step but it is impossible to identify the effect of dust particles on the shock wave reflection. In Fig. 2.16d, in an unreconstructed hologram, an elongated grey region just behind the bifurcated reflected shock wave at the leading edge and a circular grey region at the tip of the wedge. In such regions, the local stream lines sharply curve so that the spontaneously induced centrifugal forces would eject dust particles away from the regions. Then dust free regions are formed. However, it is a puzzle that the dust free region appears to be grey. While passing through the dusty gas shock tube flows, the collimated OB is scattered with uniformly distributed dust particles. Hence resulting *OB* were scattered due to the so-called Mie scattering Merzkirch (1974), whereas the *OB* passing the dust free regions was not affected by the light scattering. Therefore, the *OB* passing through the dust free region appears to look greyer than that through the dusty air. Then in Fig. 2.16d, the difference of light intensity is clearly distinguished. However, in the double exposures, the light scattering never contributed to the variation of the phase angle so that the dust free region did create no difference in fringe distributions.

Figure 2.17 shows the case for Ms = 1.75 and reflection patterns are similar to Fig. 2.9. In Fig. 2.17a, other than fringe distributions, as grey noises, sedimentations of dust particles on the bottom wall and on the wedge surface as well are identified. In Fig. 2.17a, b, as background noises, shadows of dust particles blown off from the corner of the wedge are observed. Figure 2.17c, d shows an interferogram and its unreconstructed image, respectively. Although the relationship between the dusty gas loading ratio and its refractive index is not known, dark fringe distribution behind the reflected shock wave in Fig. 2.17c and the grey noise distribution in Fig. 2.17d agreed with each other. The sedimentation of dust particles on the shock tube bottom wall and the wedge surface is faintly visible. The reflected shock wave is diffracted at the corner of the wedge. The transmitted shock wave forms a vortex at the corner as seen in Fig. 2.17c. Figure 2.17d shows the unreconstructed hologram of Fig. 2.17c. In Fig. 2.17d, dust free region is observed inside the region in which fringes are densely concentrated seen in Fig. 2.17c.

Figure 2.18a, b shows evolution of weak shock wave reflection of Ms = 1.40 from a wedge $\theta_w = 20°$ in dusty gas. The reflection patterns are almost identical with the reflection from a shallow wedge in a pure gas. Figure 2.18c shows a MR from a wedge of $\theta_w = 35°$. Figure 2.18d shows a RR from a wedge of $\theta_w = 45°$. So far observed, no significant difference is not observed in fringe distributions

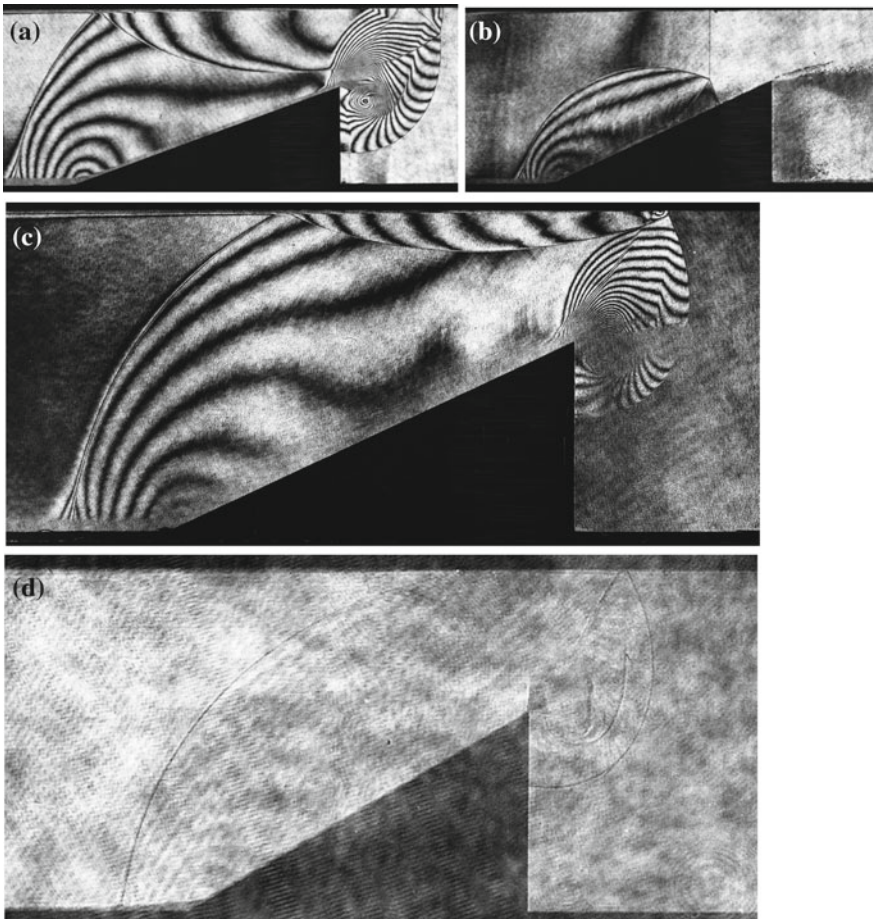

Fig. 2.17 Shock wave reflection over wedges in dusty gas for Ms = 1.75 in air at 1013 hPa, 289.5 K: **a** #87042108, Ms = 1.755, $\theta_w = 20°$; **b** #87042111, Ms = 1.718, $\theta_w = 25°$; **b** #87042305, Ms = 2.022, $\theta_w = 30°$; **c** #87042110, Ms = 1.718, $\theta_w = 25°$; **d** enlargement of (**c**)

between the present dusty gas shock tube flow and a pure air shock tube flow. These images would be useful to validate numerical schemes for reproducing dusty gas shock tube flows.

2.1.3.6 Delayed Transition in a 100 mm × 180 mm Shock Tube

In 1996, Professor Dewey organized the Mach Reflection Symposium for the second time in Victoria and reported a puzzling result of shock wave reflections over a wedge whose angle was slightly larger than θ_{crit}. in argon. Then the reflection pattern should be MR. However, Professor Dewey showed that at the leading edge of the

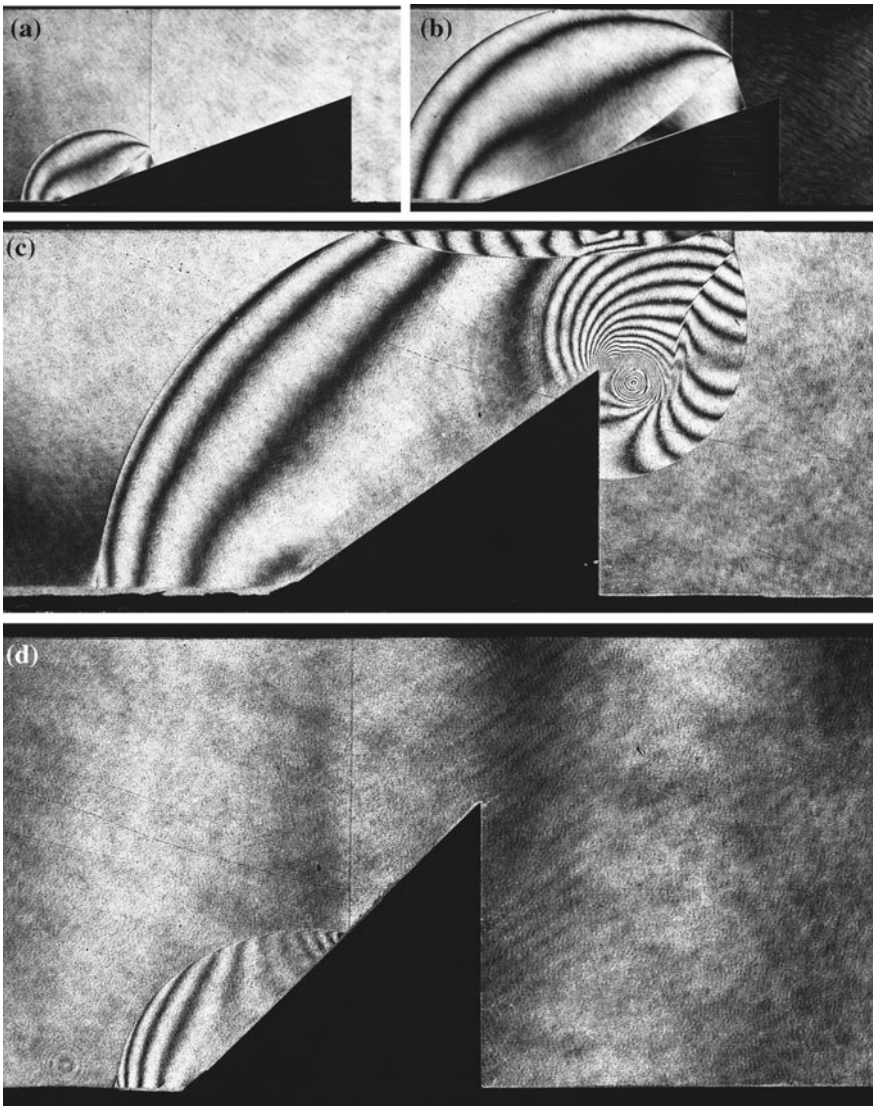

Fig. 2.18 Shock wave reflection over wedges in dusty gas for Ms = 1.44 in atmospheric air at 290.2 K: **a** #87042102, Ms = 1.432, $\theta_w = 20°$; **b** #87042103, Ms = 1.440, $\theta_w = 20°$; **c** #87042122, Ms = 1.432, $\theta_w = 35°$; **d** #87042204, Ms = 1.412, $\theta_w = 45°$

wedge, a RR appeared and it transited to a MR in the distance away from the leading edge. The audience were astonished at his lecture and expressed their own comments. No one at that time understood why delayed transitions occurred. Later Henderson proved numerically that it was the presence of the boundary layer developing along the wedge surface that caused the delayed transition (Henderson et al. 1997). In 1994, Professor Glass donated his 100 mm × 180 mm

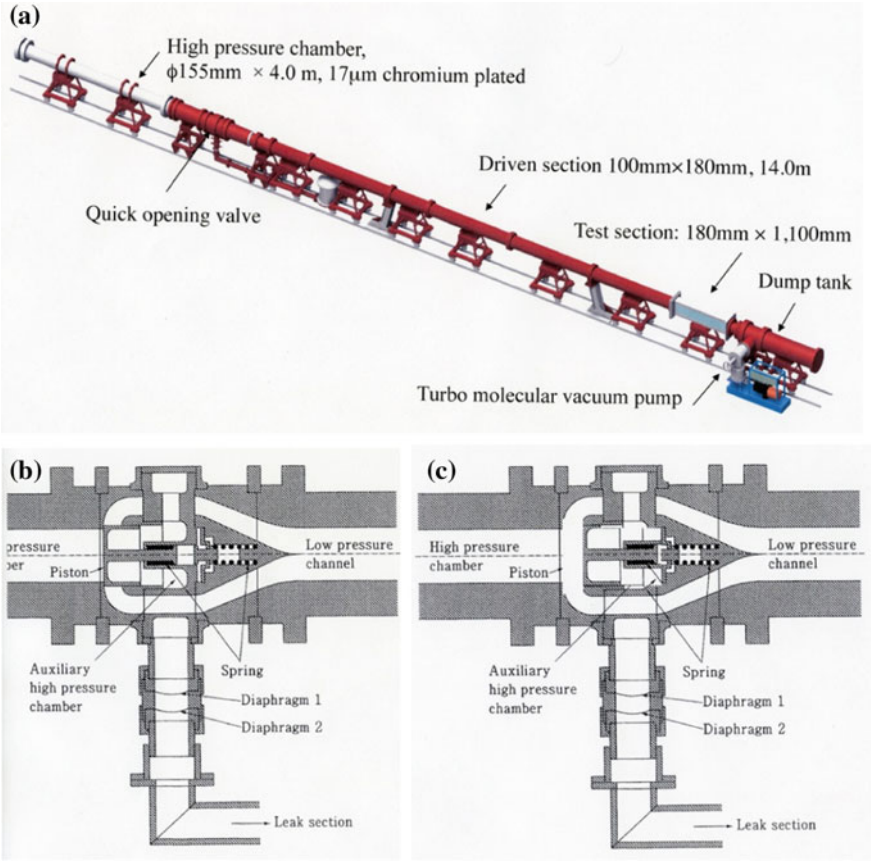

Fig. 2.19 Refurbished diaphragm-less shock tube in the SWRC of the IFS (Itabashi 1998): **a** 100 mm × 180 mm shock tube; **b** quick opening valve closed; **c** the piston was quickly stored inside the tear-drop shaped container

Hypervelocity Shock Tube of University of Toronto Institute of Aerospace Science (UTIAS) to SWRC of the Institute of Fluid Science (IFS) Tohoku University. When performing experiments in a small shock tube, results obtained in the shock tube consistently deviated from analytical predictions because of the size effect of the shock tubes. In 1994, when the UTIAS Shock Tube was delivered to SWRC, it was refurbished as shown in Fig. 2.19a. The driver chamber was manufactured at the Nippon Steel Co. Ltd., in Muroran; a single piece of high tensile strength steel of 4 m in length, 155 mm in inner diameter, 355 mm in outer diameter. The inner surface of the driver chamber was plated with chromium of 17 μm in thickness and its tolerance of the diameter was 3 μm. The test section was replaced with a stainless steel test section of the field of view of a 180 mm × 1,100 mm. Its length was wide enough to visualize shock tube flows with a 1000 mm diameter collimated *OB*. Glass (1975) stated in his book that a shock tube was a test tube of modern

aerodynamics. Indeed, the shock tube contributed immensely to the development of high speed gas-dynamics and supported the atmospheric reentry technology. However, this shock tube was not repeatable. The UTIAS shock tube adopted a diaphragm-less operational system. A high-pressure driver gas was separated by an aluminum piston from the downstream side as shown in Fig. 2.19b. The piston was supported by high-pressure helium from behind. A Mylar diaphragm was ruptured by using a double diaphragm system. Then the piston receded very quickly and neatly fit into a tear-drop shaped container as shown in Fig. 2.19c. At the same time, a shock wave moved around the container's outer boundary. A higher degree of reproducibility was achieved by this system but the planar shock formation distance became slightly longer. The piston moved very quickly from its initial position to its recovery position at 75 mm distance. It was relatively easy to accelerate the piston but it was hard to safely attenuate the piston. The piston should be repeatedly operated at least for about 300 times. Hence, a spring and a damper mechanism were used inside the container. The spring and damper were regularly maintained and after about 300 runs the parts were repaired.

Figure 2.20 shows characteristic diagram of Ms against the pressure ratio in air and nitrogen. The ordinate denotes shock wave Mach number Ms and the abscissa denotes the pressure ratio of a driver gas pressure to a test gas pressure, p_4/p_1. In a simple shock tube theory, the ratio of the driver gas pressure p_4 and the test gas pressure p_1 is given by

$$p_4/p_1 = p_4/p_2 \cdot p_2/p_1, \tag{2.11}$$

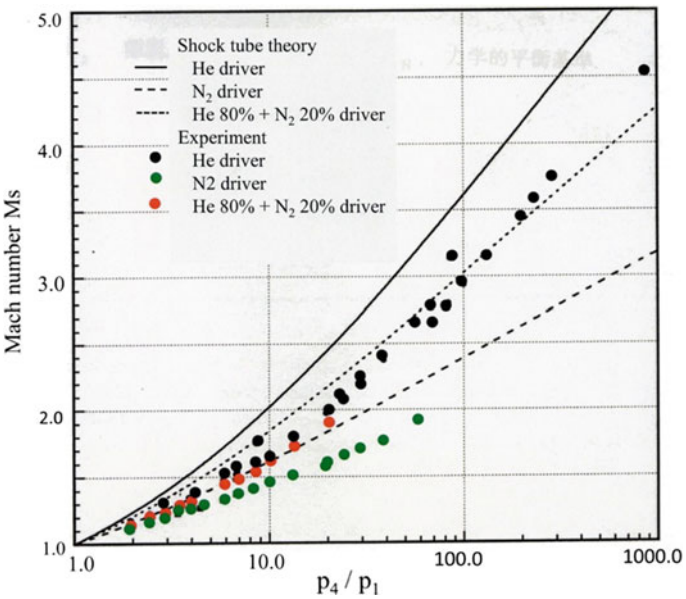

Fig. 2.20 Characteristics of the present refurbished shock tube (Itabashi 1998)

where $p_2/p_1 = (2\gamma_1 Ms^2 - \gamma_1 + 1)/(\gamma_1 + 1)$, $p_4/p_2 = \{1 - (\gamma_4 - 1)a_{41}(Ms - 1/Ms)/(\gamma_1 + 1)\}^{-m}$, $a_{41} = a_4/a_1$, and $m = 2\ \gamma_4/(\gamma_4 - 1)$. a_4 and a_1 are sound speeds of the driver and test gases, respectively. γ_4 and γ_1 are the specific heats ratio of the diver and test gases, respectively.

Experimental results were compared with a simple shock tube theory given by Eq. (2.11) (Gaydon and Hurle 1963) for high-pressure helium and nitrogen driver and a mixture of 80% helium and 20% nitrogen in volume ratio. Experimental results and the individual predictions lie neatly on lines. But in conventional diaphragm rupturing systems, experimental results scatter relatively widely. Helium drivers were contaminated with 80% helium and 20% nitrogen in volume and had a fair agreement between the prediction and experiments. Fine broken lines denote the driver of gas mixtures. The scatter of Ms obtained under the identical initial condition ΔMs is $\pm 0.3\%$ for Ms ranging from 1.5 to 5.0 in air. When the shock tube experiments are conducted continuously in a day, the ΔMs even decreases to $\pm 0.1\%$. Conventional rupturing diaphragm system could achieve the reproducibility $\Delta Ms = \pm 1.0\%$ at best.

Professor Dewy's lecture inspired Professor Henderson, who encouraged numerical analysts to simulate the delayed transition in argon (Henderson et al. 1997). To confirm their numerical results, experiments were conducted using the diaphragm-less shock tube (Henderson et al. 2001). Figure 2.21 shows delayed transition over wedges installed in the 100 mm × 180 mm shock tube for wedge angles of 34.6°, 44.0°, 50.5° and 52.0° and at initial pressures ranging from 37 to 282 hPa in argon, for the Reynolds numbers, Re, ranging from 3×10^5 to 5×10^6. where the Re was defined referring the hydraulic radius of the shock tube and the shock tube flows. For double exposure holographic interferometric observation, the first exposure was performed when the IS reached close to the leading edge and the second exposure was performed as seen in Fig. 2.21a at $\Delta t = 120$ μs after the first exposure. At the second exposure, the IS reached at the center of the wedge surface. Images of reflected shock waves observed during the double exposures are superimposed. Even in these interferograms, the density contours so far recorded are normalized by the density of the air ahead of the IS. Hence the fringes are more densely distributed at enhancing the initial pressure.

Figure 2.21a, b shows the SMR over a 34.6° wedge and at the initial pressure of $p_0 = 144$ hPa. Figure 2.21c, d shows the SMR over a 38.6° wedge and at the initial pressure of $p_0 = 288$ hPa. In Fig. 2.21a–d, the RS emanating from the TP looks straight in the vicinity of TP but a kink point is not clearly identified. In Fig. 2.9, the evolution of shock wave reflection patterns for Ms = 2.60 in air was observed sequentially over the wedges of θ_w which varied from 0° to θ_w much larger than θ_{crit}. The reflected shock wave patterns are supposed to be self-similar. However, on a hologram seen in Fig. 2.21, the two shock wave patterns are not necessarily self-similar. The reflected shock wave patterns varied slightly with the distance away from the leading edge. This implies that the boundary layer developing along the wedge surface varied the local boundary conditions. Figure 2.21e, f shows the TMR over a 44.0° wedge and at $p_0 = 144$ hPa.

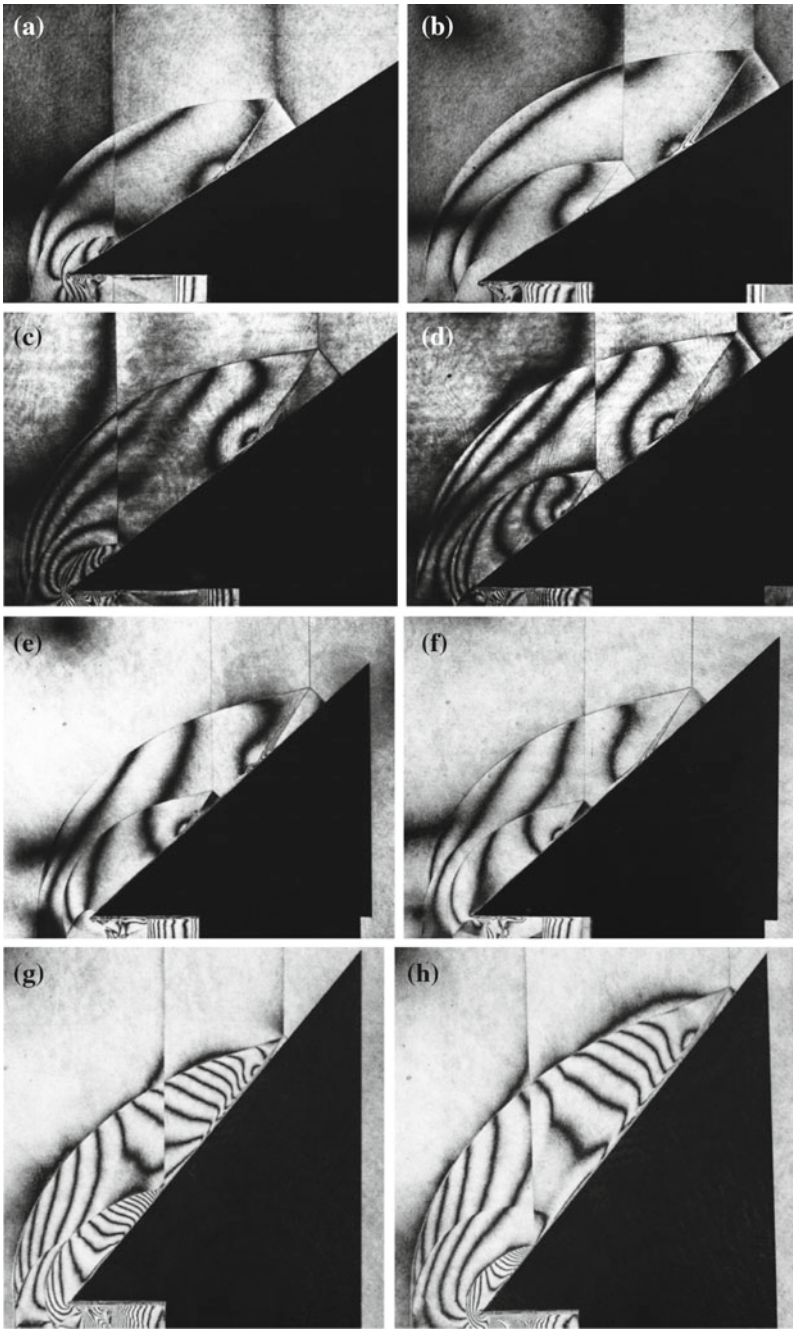
(a)
(b)
(c)
(d)
(e)
(f)
(g)
(h)

◂**Fig. 2.21** Delayed transition over wedges in 100 mm × 180 mm shock tube in argon: **a** #96091003, interval of double exposures of $\Delta t = 120$ μs, for Ms = 2.326 at 144 hPa and 295.9 K, wedge angle of $\theta_w = 34.6°$; **b** #96090905, 80 μs, for Ms = 2.333 at 144 hPa and 296.4 K, $\theta_w = 34.6°$; **c** #98112508 120 μs for Ms = 2.320 at 288 hPa and 291.6 K, $\theta_w = 38.6°$; **d** #98112509, 80 μs, for Ms = 2.328 at 288 hPa and 291.5 K, $\theta_w = 38.6°$; **e** #97040502, 60 μs, Ms = 2.315 at 144 hPa, 290.3 K, $\theta_w = 44.0°$; **f** #97041501, 60 μs, for Ms = 2.334 at 144 hPa and 289.0 K, $\theta_w = 44.0°$; **g** #97040409, 80 μs, Ms = 2.338 at 288 hPa and 291.3 K, $\theta_w = 52°$; **h** #97040404, 80 μs, Ms = 2.329 at 288 hPa and 290.9 K, $\theta_w = 52°$; **i** #97031007, 80 μs, Ms = 2.330 at 72 hPa and 289.4 K, $\theta_w = 52.0°$; **j** #97031016, 60 μs, Ms = 2.329 at 72 hPa and 289.0 K, $\theta_w = 52.0°$: **k** #97031109, 30 μs, Ms = 2.327 at 38 hPa and 291.3 K, $\theta_w = 52.0°$; **l** #97031110, 30 μs, Ms = 2.331 at 38 hPa and 291.2 K, $\theta_w = 52.0°$; **m** enlargement of (**k**)

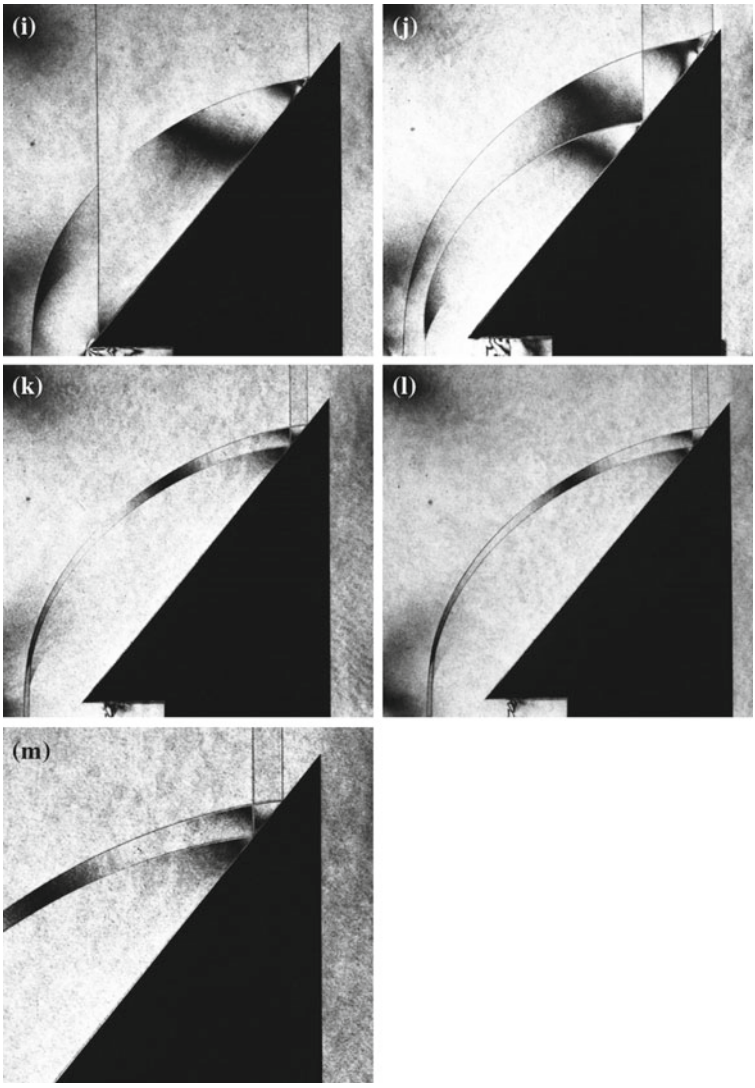

Fig. 2.21 (continued)

Figure 2.21g, h shows the DMR over a 52.0° wedge and at p_0 = 288 hPa. The two reflected shock wave patterns on a 52.0° wedge and at p_0 = 72 hPa seen in Fig. 2.21i shows a small DMR near the trailing edge of the wedge and RR close to the leading edge. In Fig. 2.21j, the reflection patterns show both small DMR near the trailing edge. When keeping the wedge angle identical and reducing the initial pressure to 38 hPa, the reflected shock wave patterns seen in Fig. 2.21k, l are supersonic RR or in short SuRR near the trailing edge of the wedge and later transits to the DMR. The initiation of MR was retarded. We now confirmed that the MR appeared delayed, the distance at which MR appeared was elongated, as the initial pressure decreased.

In shock tube flows, the IS are followed by the boundary layers, which satisfy the isothermal and non slip condition on the wedge surface. In shock fixed co-ordinates, the boundary layer displacement thickness modified the apparent contour of the shock tube wall and hence the ISs lean forward at their foot on the wall. In the neighborhood of the leading edge, apparently due to the effect of the boundary layer displacement thickness, the wedge angle θ_w exceeds θ_{crit}, and hence the reflected shock wave would be RR. When the IS moves away from the leading edge, the flow on the wedge surface satisfies the real boundary condition of $\theta_w <$ $_{crit}$. Then this information is transmitted to the reflection point through the boundary layer so that the reflection pattern reverts to MR. It is the boundary layer displacement thickness, δ, which causes delay in the RR transition. In the laminar boundary layer, the δ is inversely proportional to the Reynolds number, Re = $\rho uL/\mu$, where ρ, μ, u, and L are the density, viscosity, particle speed behind the IS, and hydraulic radius of the shock tube, respectively. The thickness effect of the boundary layer was enhanced if the initial pressure is reduced and a shock tube geometry is smaller. The interferometric images collected in a 40 mm × 80 mm shock tube as shown in Fig. 2.5 are slightly deviated from those collected in a 100 mm × 180 mm shock tube.

Figure 2.22 summarize results of visualizations (Itabashi 1998). In Fig. 2.22a, co-ordinates of triple points along a 52° wedge are presented at the initial pressures p_0 of 37, 60, 95, 141 and 282 hPa. The ordinate shows the height y of triple point in mm and the abscissa shows the distance x along the wedge in mm. Hence the intersections of estimated triple point trajectories at y = 0 mm give $x_{int,}$ the point at which the delayed transition starts. Figure 2.22b summarized the relationship between x_{int} and Re at 52° wedge which is close to θ_{crit}. The ordinate shows x_{int} in mm and the abscissa shows the Re. The x_{int} is inversely proportional to Re. It is shown that in a shock wave reflection from a wedge angle relatively closer to θ_{crit} and at very low initial pressure, the RR might have been dominant and MR wouldn't be observable even in a shock tube of, for example, a characteristic length of 100 mm. It is often reported that shock tube experiments conducted under the identical Ms and wedge angle never produce any consistent θ_{crit}. Results obtained in small shock tubes and in large shock tubes scatter widely. As seen in Fig. 2.22b, the x_{int} varies over 100 mm, which means it was tested with a shorter wedge installed in a small shock tube, and the reflection pattern is always RR, whereas with a long wedge installed in a large shock tube, it can be MR. Results of the Euler

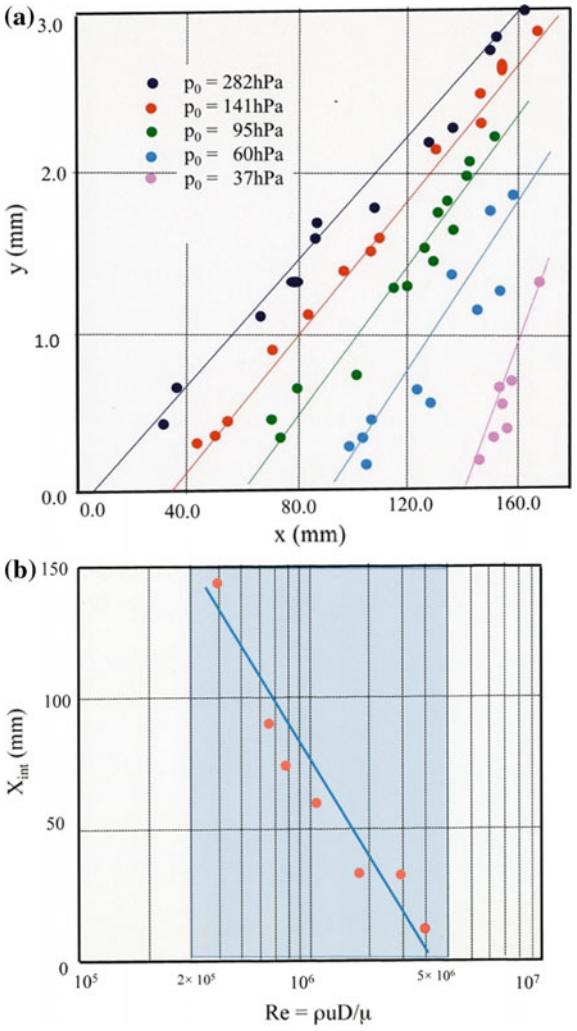

Fig. 2.22 A summary of delayed transitions in argon for Ms = 2.33. Parts of the data appeared Fig. 2.20. Dependence of delayed transition on the Reynold number, Re: **a** triple point position along 52° wedge at various initial pressures; **b** the x_{int} versus the Re; **c** triple point positions along wedges at 144 hPa

solvers disagree with experiments because inviscid solutions agree with shock tube flows of infinitely large Reynolds number. Hence to have a better agreement between numerical solutions and interferograms, for example, as shown in Fig. 2.22, Navier-Stokes solvers with a fine mesh zoning should be compared with experiments of appropriate Re. The effect of the boundary layer on the delayed transition appears not necessarily over wedge angles closer to the θ_{crit}. Figure 2.22c shows triple point trajectories of wedge angles 34.6°, 44.0°, 50.5°, and 52.0° at p_0 = 144 hPa in the x-y plane: the ordinate shows triple point height, y in mm and the abscissa shows the distance, x from the leading edge in mm. The numerical results are cited from Henderson et al. (1997). As the simulations agree well with experiments, we extraporated the trajectory lines. The intersection of the trajectories

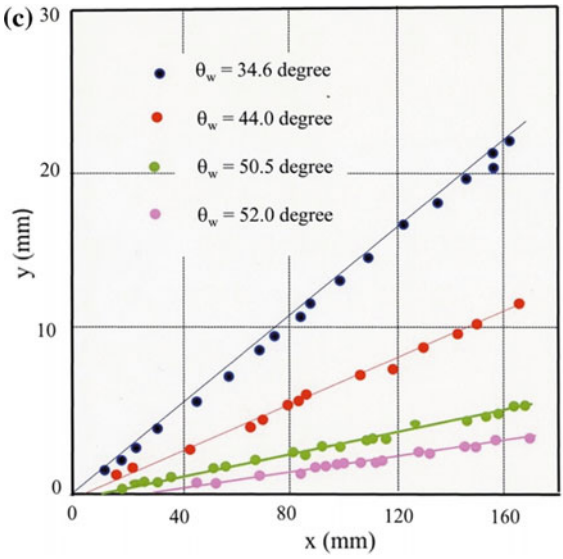

Fig. 2.22 (continued)

with the x-axis gives delayed transition distance, $x_{int.}$ For individual wedge angles, we estimated x_{int} of wedge angles 34.6°, 44.0°, 50.5°, and 52.0° to be 0 mm, about 5, 15, and about 30 mm, respectively.

Figure 2.23 shows the reflection of shock wave of Ms = 2.33 in nitrogen over wedges of 49° and 52° at different initial pressures. Figure 2.23a shows reflection patterns for Ms = 2.33 from a 49.0° wedge at 144 hPa and the double exposure interval is $\Delta t = 80$ μs. Although the reflection patterns at the first and second exposures are both DMR. These DMR patterns are not self-similar but DMR at the first exposure is much smaller than one at the second exposure. In Fig. 2.23b, at $\Delta t = 120$ μs, the reflection pattern at the first exposure is a RR near the leading edge, whereas that at the second exposure is a DMR near the rear edge. Figure 2.23b clearly shows the delayed transition. In Fig. 2.23c–f reducing the initial pressure to 72 hPa, the difference of the reflection patterns during the double exposures is observed. In Fig. 2.23g, h, the initial pressure is $p_0 = 29$ hPa. In Fig. 2.23i, j, $p_0 = 15$ hPa, the reflection pattern observed at the first exposure is RR, whereas the reflection pattern observed at the second exposure is DMR.

Figure 2.24 summarize results of visualizations: **a** triple point trajectories over a 49° wedge at 14.1, 28.2, 70.5 and 141.0 hPa displayed in the x, y-plane; **b** triple point trajectories over 34.6° wedge, 38.6° wedge, 44.0° wedge, and 49.0° wedge displayed in the x-y plane and comparison with numerical simulation offered by Professor Hatanaka of Muroran Institute of Technology. Similarly to argon, the transition distance x_{int} increases with the reduction of the initial pressures.

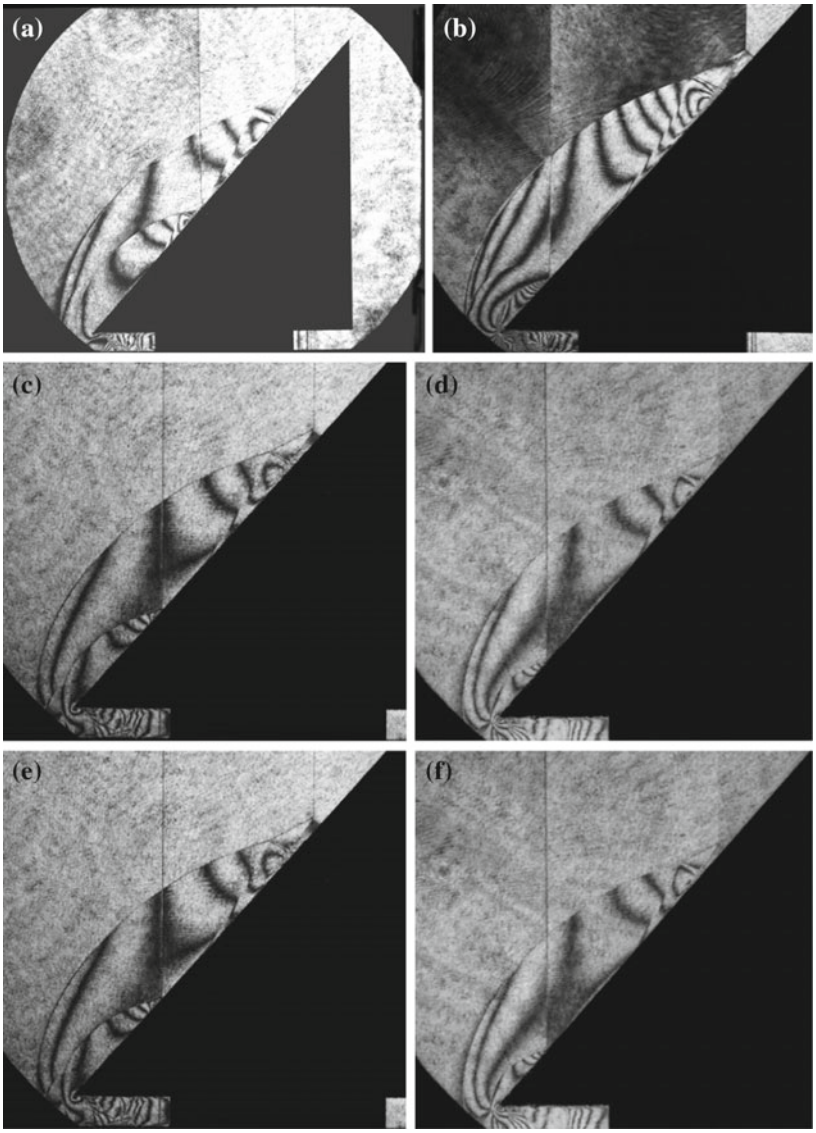

Fig. 2.23 Delayed transition over wedges in 100 mm × 180 mm shock tube in nitrogen: **a** #98090102, Δt = 80 μs, Ms = 2.328 at 144 hPa and 295.0 K, θ_w = 49.0°; **b** #98090104, 120 μs, Ms = 2.326 at 144 hPa and 295.0 K, θ_w = 49.0°; **c** #98091701, 80 μs, Ms = 2.324 at 72 hPa and 295.2 K, θ_w = 49.0°; **d** #98091702, 80 μs, Ms = 2.330, at 72 hPa and 296.2 K, θ_w = 49.0°; **e** #98091701, 80 μs, Ms = 2.324 72 hPa 22.2C θ_w = 49.0°; **f** #98091702, 80 μs, Ms = 2.330 at 72 hPa and 290.2 K, θ_w = 49.0°; **g** #98091823, 60 μs, Ms = 2.333 at 29 hPa and 301.2 K, θ_w = 49.0°; **h** #98091825, 60 μs, Ms = 2.327 at 28.2 hPa and 296.3 K, θ_w = 49.0°; **i** #98092413, 40 μs, Ms = 2.327 at 15 hPa and 296.6 K, θ_w = 49.0°; **j** #98092408, 60 μs, Ms = 2.327 at 15 hPa and 290.5 K, θ_w = 49.0° (Itabashi 1998; Henderson et al. 2001)

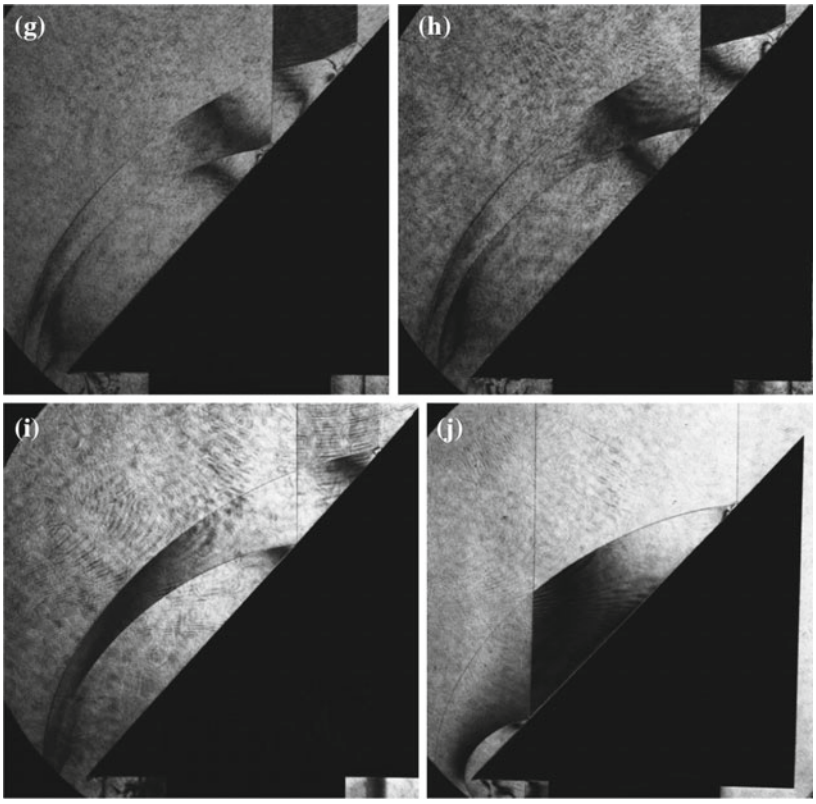

Fig. 2.23 (continued)

2.1.3.7 Evolution of Shock Wave Reflection Over Wedges in CO_2

Figure 2.25 shows the evolution of reflected shock waves over wedges for Ms = 2.0 in CO_2 at 400 hPa and 296 K in the 40 mm × 80 mm shock tube. Figure 2.25a shows a $\theta_w = 0°$ wedge and the predicted glancing incidence angle θ_{glance} is 27.0°, whereas the measured θ_{glance} is about 28°. Although in Fig. 2.25b the pattern of reflected shock wave is a SMR, the SL is only vaguely visible, whereas in Fig. 2.25c, the SL is clearly visible. However, a point from which the SL starts is not identical to the point at which the IS and the RS intersect. Figure 2.25d shows a SMR. Figure 2.25e–h shows earlier stages of TMR and its transition to DMR. Figure 2.25i shows a DMR at $\theta_w = 48°$. Figure 2.25j is a SuRR at $\theta_w = 51°$. Argon is a monatomic gas and has three translational degrees of freedom only. Nitrogen and air are diatomic gases and have three translational degrees of freedom, two rotational and one vibrational degrees of freedom, while CO_2 has, in addition to these degrees of freedom, two more vibrational degrees of freedom which are readily excited even at energy levels of modestly strong shock

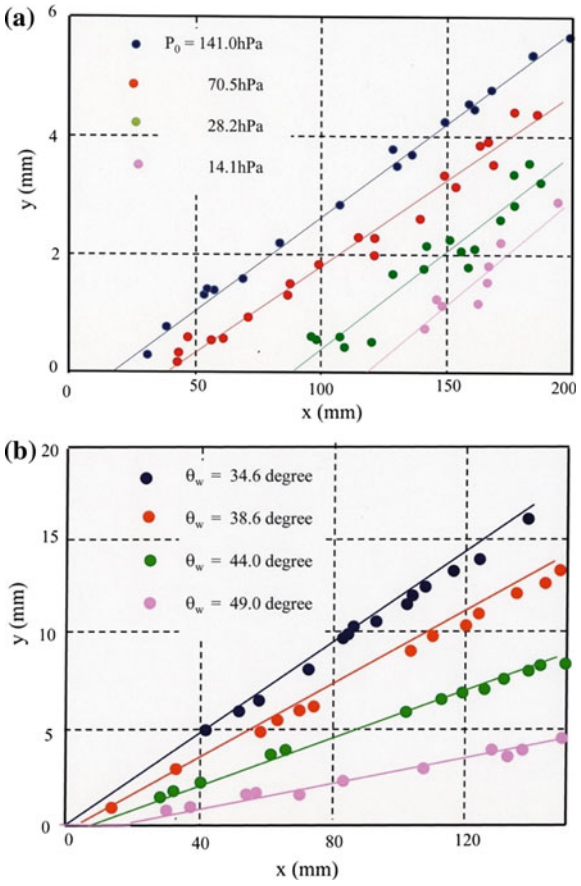

Fig. 2.24 A summary of delayed transitions for Ms = 2.33 in nitrogen. Parts of data appeared Fig. 2.17 indicating the dependence of delayed transition on the Reynold number, Re: **a** triple point position along a 49° wedge at various initial pressures; **b** triple point positions along 34.6°, 38.6°, 44.0° and 49.0° wedges at 144 hPa (Kosugi 2000)

waves. Then vibrational relaxation appears at a short distance from the frozen shock waves. It should be noticed that CO_2 is a polyatomic gas exhibiting readily the so-called real gas effect. The vibrational excitation takes place even at moderate temperature behind shock wave of Ms = 2.0. The incident shock waves seen in Fig. 2.25 shows a broadened structure that exhibits vibrational relaxation. This appears not only at the IS but also along the MS and the RS.

In an ideal gas, the density ratio ρ_{22}/ρ_1 across a strong oblique shock wave can be written as

$$\begin{aligned}\rho_{22}/\rho_1 &= (\gamma+1)\mathrm{Ms}^2\sin^2\phi/\{(\gamma-1)\mathrm{Ms}^2\sin^2\phi+2\},\\ &= \tan\phi/\tan(\phi-\theta)\end{aligned} \tag{2.12}$$

where γ is the ratio of specific heats of the gas under study, θ and ϕ are the deflection angle of flow across the shock wave and the inclination angle of the oblique shock wave, respectively. Then $\mathrm{Ms}\sin\phi$ is the normal component of the oblique shock

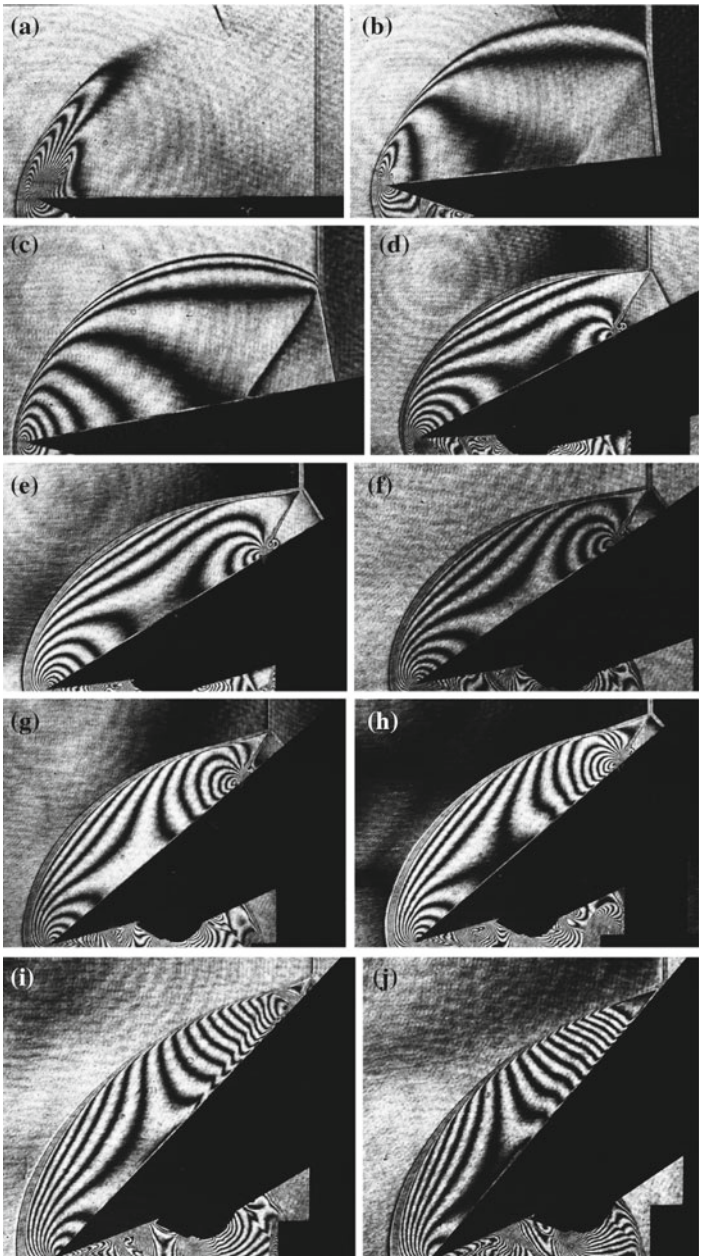

Fig. 2.25 Evolution of shock wave reflection over wedges in CO_2 at Ms = 2.0 at 400 hPa and 296 K: **a** #81100728, Ms = 1.991, $\theta_w = 0.0°$; **b** #81100726, Ms = 2.001, $\theta_w = 4.0°$; **c** #81100725, Ms = 1.955, $\theta_w = 10.0°$; **d** #81100710, Ms = 2.010, $\theta_w = 27°$; **e** #81100723, Ms = 2.001, $\theta_w = 32°$; **f** #81100722, Ms = 1.946, $\theta_w = 36°$; **g** #81100717, 130 μs Ms = 1.982, $\theta_w = 40°$ TMR; **h** #81100716, Ms = 1.991, $\theta_w = 44°$ TMR; **i** #81100713, Ms = 2.010, $\theta_w = 48°$ DMR; **j** #81100711, Ms = 1.973, $\theta_w = 51°$ SPRR

wave Mach number. For $Mssin\phi \gg 1$, $\rho_{2/}\rho_1$ is approximately $(\gamma + 1)/(\gamma - 1)$. This indicates that polytropic gases, whose ratio of specific heats is close to unity, are more compressible than monatomic or diatomic gases. Hence, at the identical oblique shock angle, $\phi - \theta$ is smaller in polytropic gases. Figure 2.26 shows a DMR over a $\theta_w = 35°$ wedge for Ms = 4.397 in CO_2 at 50 hPa. We define trajectory angles of the first and second triple points as χ_1 and χ_2. In the case of a stronger shock wave reflection in CO_2, the second triple point, is hence located closer to the wedge surface, that is, $\chi_2 < \chi_1$. The grey irregularly shaped zone attached to the RS is the remnant of bifurcated RS. The foot of the upward moving RS interacts with the side wall boundary layer and eventually bifurcates. This is a similar phenomenon which is observed when a reflected shock wave interacts with the boundary layer at the end wall of shock tubes. This phenomenon is discussed later.

Similarly to Fig. 2.25, the density distribution behind IS as observed in Fig. 2.27 shows vibrational relaxation distance. Figure 2.27a, b appeared to be a SMR over $\theta_w = 5.0°$ and 10.0° wedges, respectively, however, the RS is straightened in the vicinity of the TP. The reflection patterns look the stage of initiation of a TMR. The reflection pattern is a TMR in Fig. 2.27c and it is a DMR in Fig. 2.27d. In Fig. 2.27e–g, the reflection patterns are DMR. Figure 2.27g shows an enlargement of the DMR over a $\theta_w = 36°$ wedge in Fig. 2.27f. The secondary shock wave of the DMR interacts with a SL produces a vortex that is reversely rolling toward the MS as seen in Fig. 2.27g. In Fig. 2.27i, j, with increasing θ_w, the point of the secondary shock wave approaches to the first TP and the resulting MS is gradually shortened and at $\theta_w = \theta_{crit}$, DMR terminates and eventually transits to SPRR. An irregularly shaped grey shadow attached along the RS is the projection of the foot of the bifurcated RS. The structures of the MS, the RS, and the secondary shock wave accompanied vibrational relaxation zones. The SL turned into a vortex which moved downward. The MS tends to move downward. This trend is more enhanced when Ms increases and also in the case of SF_6 as shown later. As explained in Fig. 2.26, the secondary triple point trajectory angle χ_2 is smaller than χ_1.

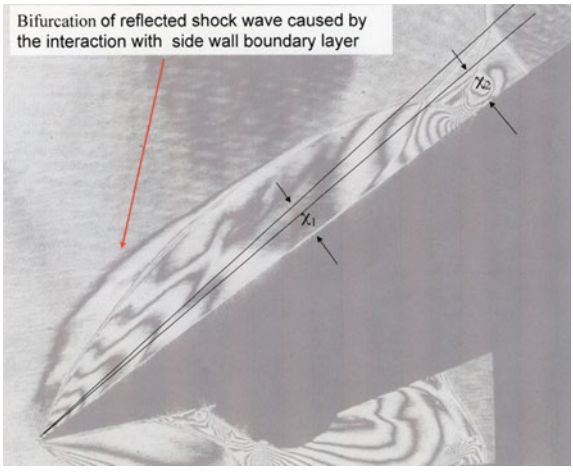

Fig. 2.26 Overeview of a shock wave reflection from a $\theta_w = 35°$ wedge for Ms = 4.397 in CO_2 at 50 hPa, #81100518

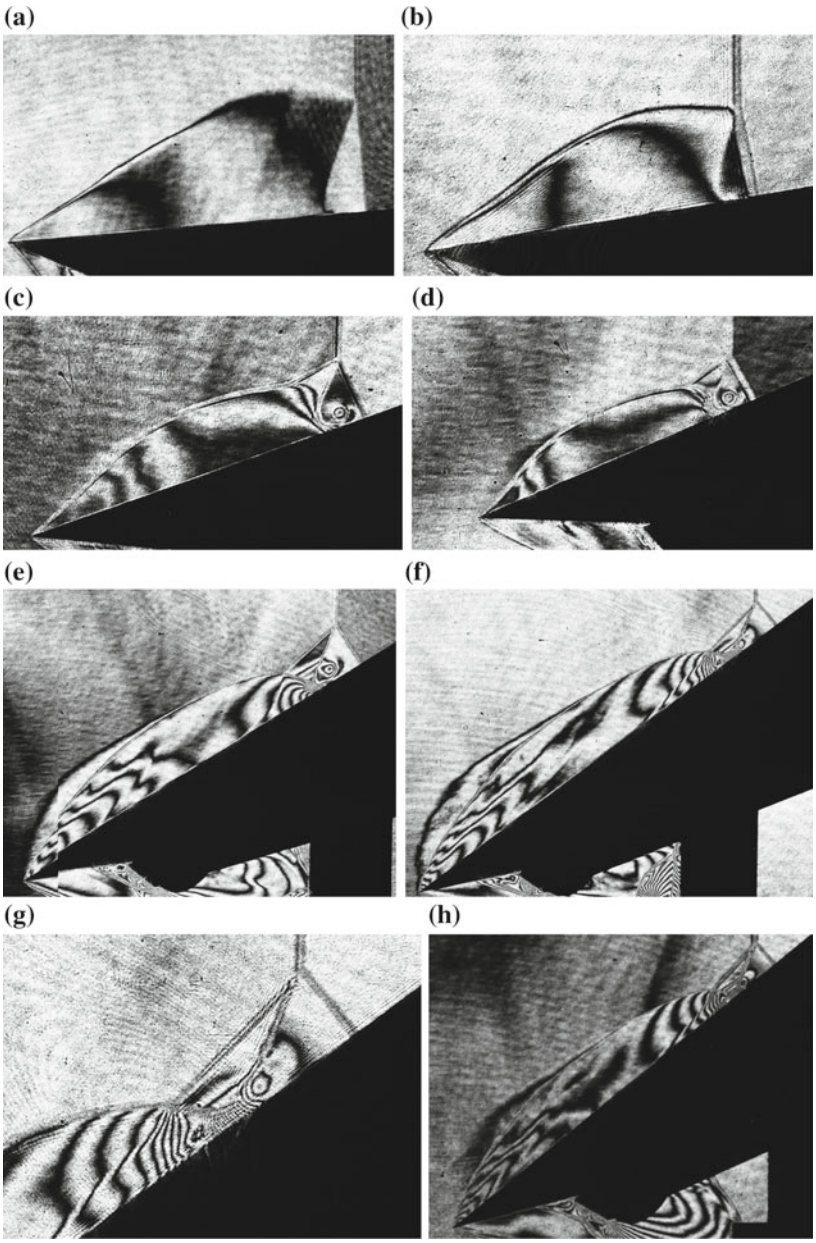

Fig. 2.27 Evolution of shock wave reflection over wedges in CO_2 for Ms = 4.3 at 50 hPa, 294.4 K: **a** #81100527, Ms = 4.307, $\theta_w = 5°$; **b** #81100526, Ms = 4.224, $\theta_w = 10°$; **c** #81100523, Ms = 4.352, $\theta_w = 21°$; **d** #81100522, Ms = 4.266, $\theta_w = 25°$; **e** #81100519, Ms = 4.396, $\theta_w = 32°$; **f** #81100517, Ms = 4.397, $\theta_w = 36°$; **g** enlargement of (**f**); **h** #81100516, Ms = 4.397, $\theta_w = 40°$; **i** #81100513, Ms = 4.352, $\theta_w = 42°$; **j** #81100512, Ms = 4.397, $\theta_w = 44°$; **k** #81100509, Ms = 4.309, $\theta_w = 50°$; **l** #81100511, Ms = 4.307, $\theta_w = 55°$

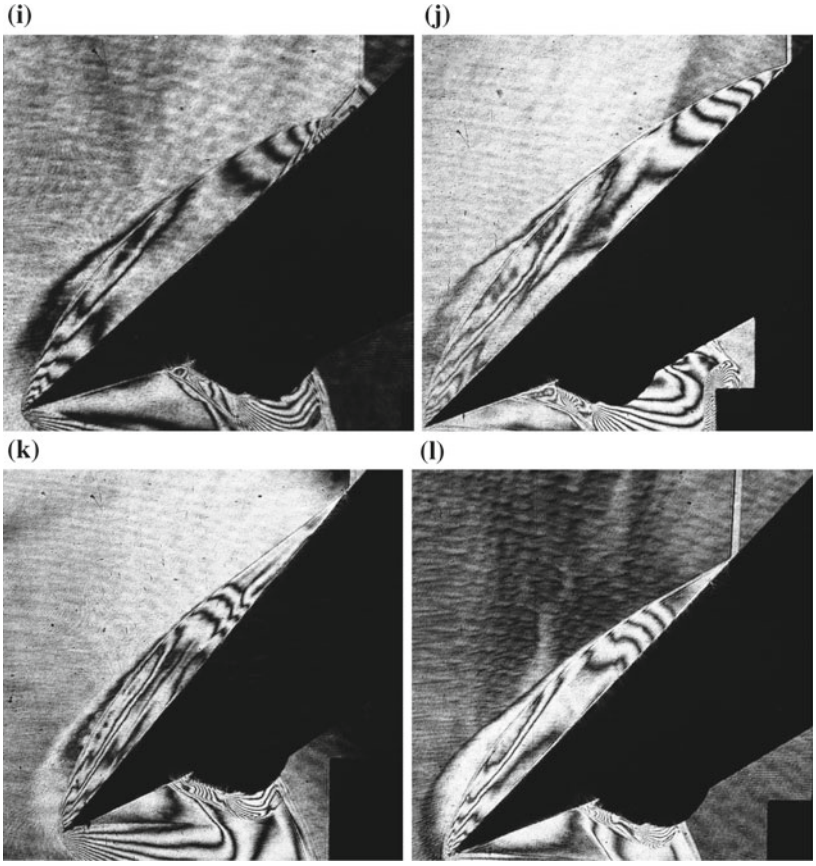

Fig. 2.27 (continued)

2.1.3.8 Evolution of Shock Wave Reflection Over Wedges in SF_6

SF_6 is frequently used for various industries such as electrical insulation etc. Regarding the basic study of isotope separation technology, SF_6 became often a replacement of radio active UF_6. The value of γ of SF_6 being 1.08, its gas dynamic behavior is unique. A shock tube experiment by using SF_6 was conducted. According to the industrial safety regulation, this gas belongs to a category of harmless gases. But after shock tube experiments, the laboratory air was contaminated with F_2 probably in a few parts per billion. Later when introducing a diaphragm-less shock tube, the shock tube was not exposed to open air and hence the contamination issue of F_2 was solved. Figure 2.28 shows direct shadowgraphs of evolution of the shock wave reflection in SF_6 in the 40 mm $\times$ 80 mm conventional shock tube. The reflection patterns are SMR seen in Fig. 2.28a–d, a TMR seen in Fig. 2.28e, f, and DMR seen in Fig. 2.28g, h.

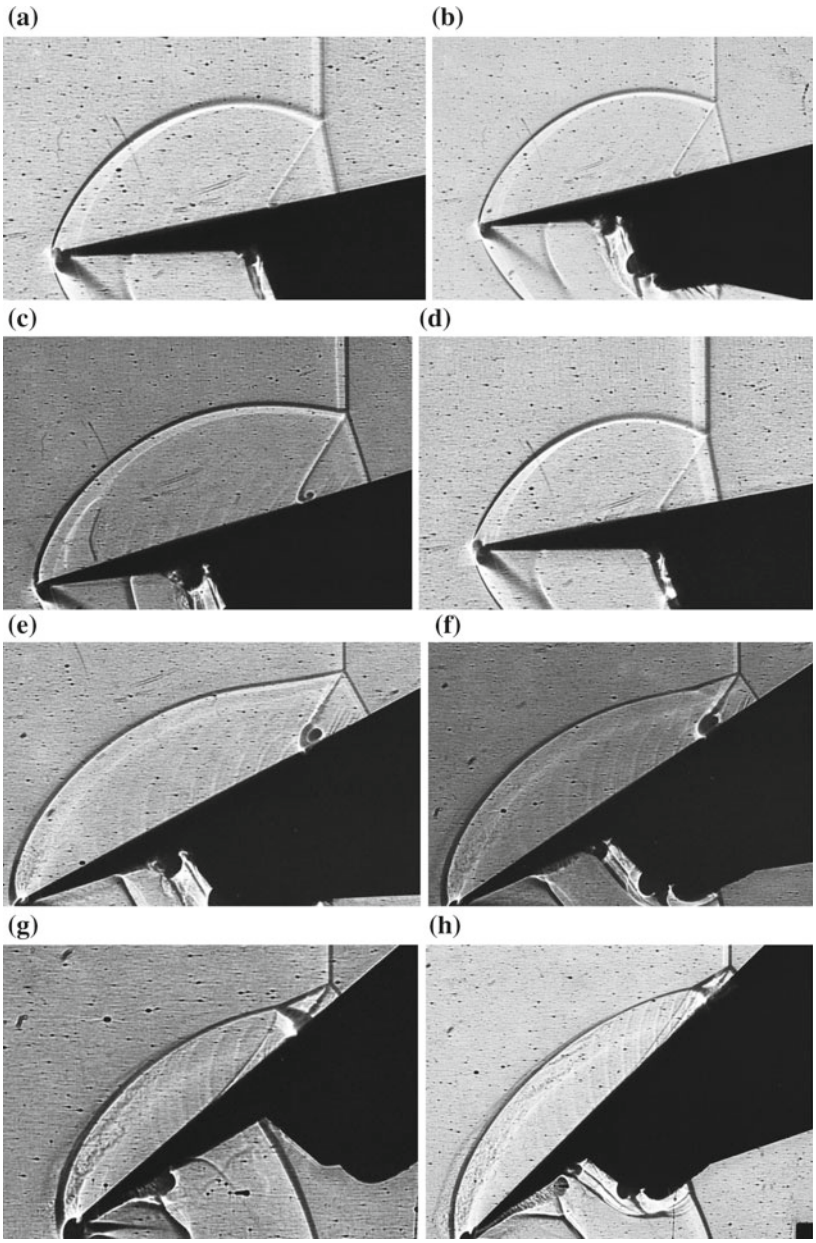

Fig. 2.28 Evolution of reflected shock wave for Ms = 2.0 in SF_6 at 240 hPa, 292.2 K: **a** #82020330, Ms = 1.940, SMR, $\theta_w = 10°$; **b** 82020329, Ms = 1.896, SMR, $\theta_w = 11°$; **c** 82020328, 880 μs, Ms = 1.903, SMR, $\theta_w = 13°$; **d** #82020324, Ms = 1.961, SMR, $\theta_w = 16°$; **e** #82020326, Ms = 1.916, TMR, $\theta_w = 27°$; **f** #82020325, Ms = 1.949, TMR, $\theta_w = 32°$; **g** #82020322, Ms = 1.985, DMR, $\theta_w = 39°$; **h** #82020321, Ms = 1.923, DMR, $\theta_w = 43°$

Figure 2.29 summarizes the triple point trajectories shown in Fig. 2.28 in SF_6 for Ms = 2.0 and shown in Fig. 2.27 in CO_2 for Ms = 4.3. The ordinate denotes the trajectory angle of the triple point $\chi - \theta_w$ in degree and the abscissa denotes the wedge angle θ_w in degree. Blue filled circles denote first triple point of CO_2 χ_1. Grey filled circles denotes the second tripe point of CO_2 χ_2. Red filled circles denote triple point of SF_6 χ_1. The glancing incidence angle χ_{glance} in SF_6 for Ms = 2.0 is about 27.0°, whereas χ_{glance} in CO_2 for Ms = 4.3 is about 22.0°. In CO_2, χ_1 is always larger than χ_2, whereas in SF_6 for Ms = 2.0, χ_1 is smaller than χ_2, the same as in diatomic and monatomic gases. However, in SF_6 for Ms = 2.0 as seen in Fig. 2.28, χ_1 is consistently larger than χ_2.

Figure 2.30a–q shows shock wave reflections from a wedge of variable wedge angles for Ms = 7.50 in SF_6 conducted in the 60 mm × 150 mm diaphragm-less shock tube. In order to generated strong shock wave in SF_6, high-pressure helium drove SF_6. A jaggedly shaped interface observed on the left of Fig. 2.30a is a contact discontinuity which drove a shock wave in SF_6. The helium/SF_6 interface is unstable due to the interfacial instability and then the interface generated obliquely running disturbances. Figure 2.30a shows the flow in the slug length. In Fig. 2.30a, b, an interferogram and its enlargement are shown. Figure 2.30c, d shows a unreconstructed hologram of Fig. 2.30a and its enlargement, respectively. It is a general trend of shock tube flows that the interface is accelerated and the shock wave is decelerated due to the presence of the boundary layer behind the shock wave developing along the sidewall. Hence, the slug length, high-pressure zone behind the shock wave is shortened with propagation.

Figure 2.30o illustrates the interfacial disturbances and the deformation of the shock wave. Figure 2.30c, d shows the un-reconstructed hologram of Fig. 2.30 and its enlargement, which is equivalent to a direct shadowgraph. The shock wave is significantly deformed in Fig. 2.30q so that the three-dimensionally distorted shock wave hardly creates a distinctly shaped first triple point. On wedges of large wedge angles, the reflected patterns are DMR and their secondary triple point trajectory

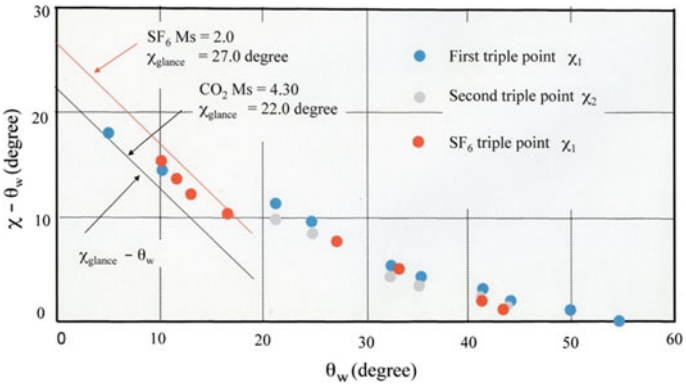

Fig. 2.29 Triple point trajectory angles χ against wedge angles θ_w. A summary of Figs. 2.26 and 2.27

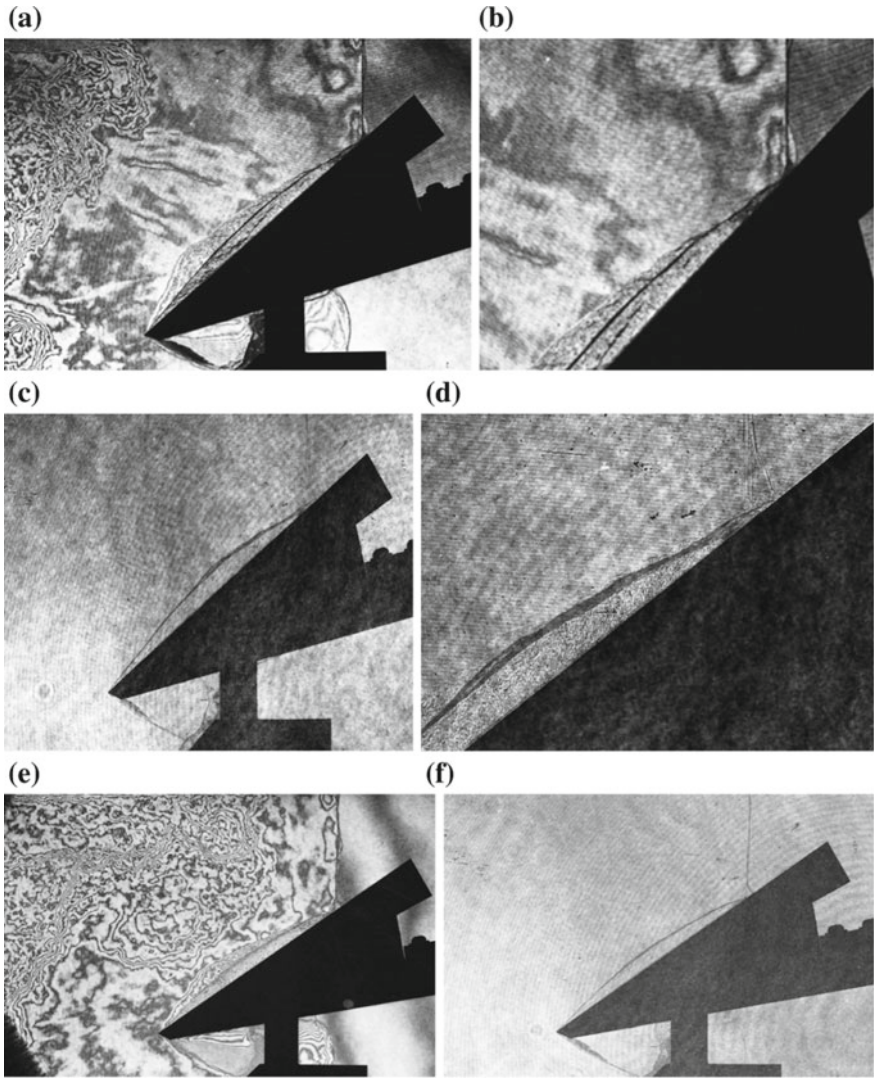

Fig. 2.30 Evolution of shock wave reflection over wedges for Ms = 7.50 in SF6 at 15 hPa and 295.5 K: **a** #91060405, Ms = 7.52, $\theta_w = 31°$; **b** enlargement of (**a**); **c** #91060405 hologram; **d** enlargement of (**c**); **e** #91060302, Ms = 7.42, $\theta_w = 32°$; **f** #91060302 hologram; **g** #91060406, Ms = 7.47, $\theta_w = 35°$; **h** #91060305, Ms = 7.62, $\theta_w = 36°$; **i** #91060404, Ms = 7.59, $\theta_w = 37°$; **j** #91060402, Ms = 7.59, $\theta_w = 37°$; **k** #91060403, Ms = 7.60, $\theta_w = 38°$; **l** #91060407, Ms = 7.47, $\theta_w = 38°$; **m** #91060407 hologram; **n** enlargement of (**m**); **o** #91060401 Ms = 7.52, $\theta_w = 41°$; **p** enlargement of (**o**); **q** #91053001, Ms = 7.36, $\theta_w = 45°$

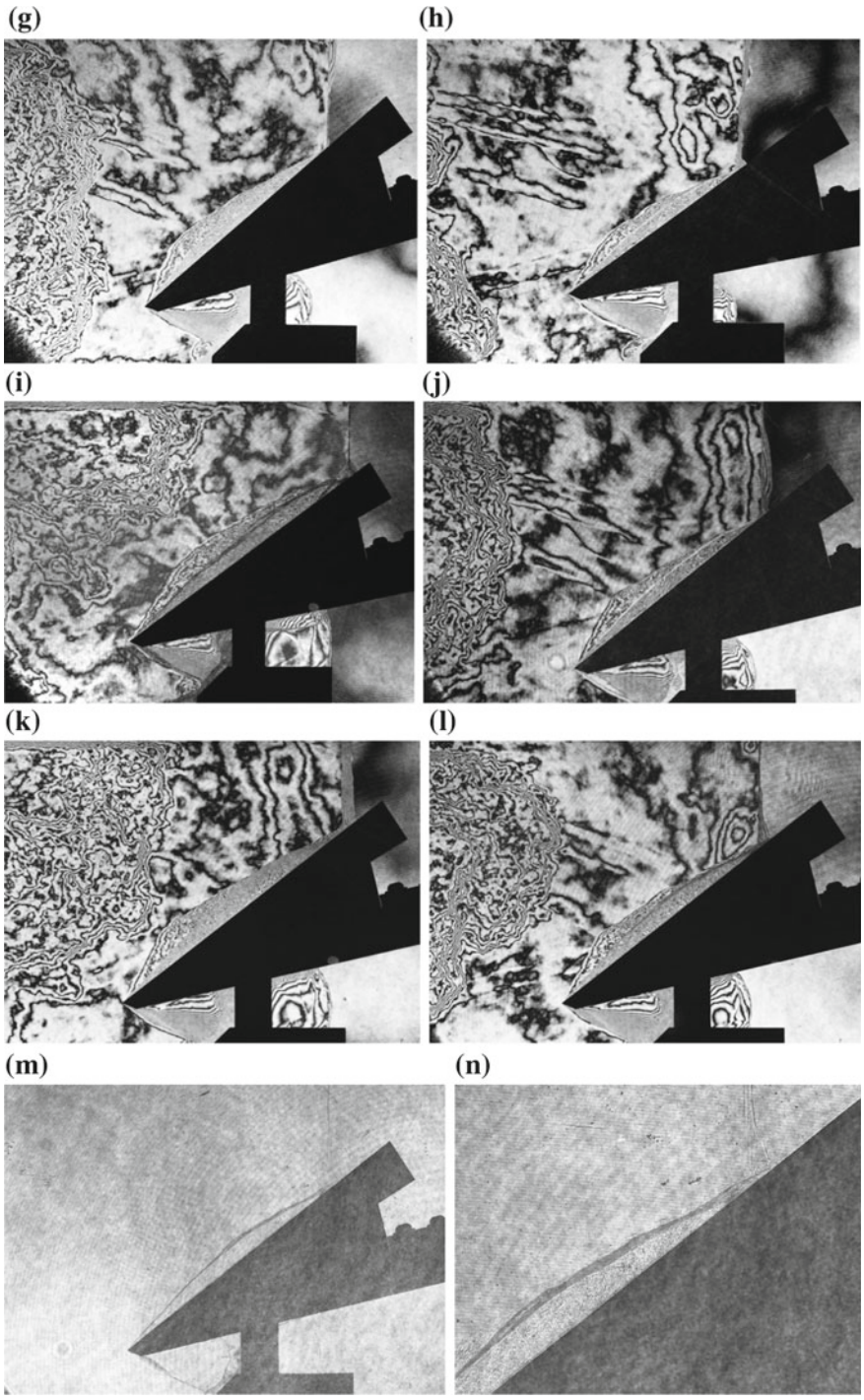

Fig. 2.30 (continued)

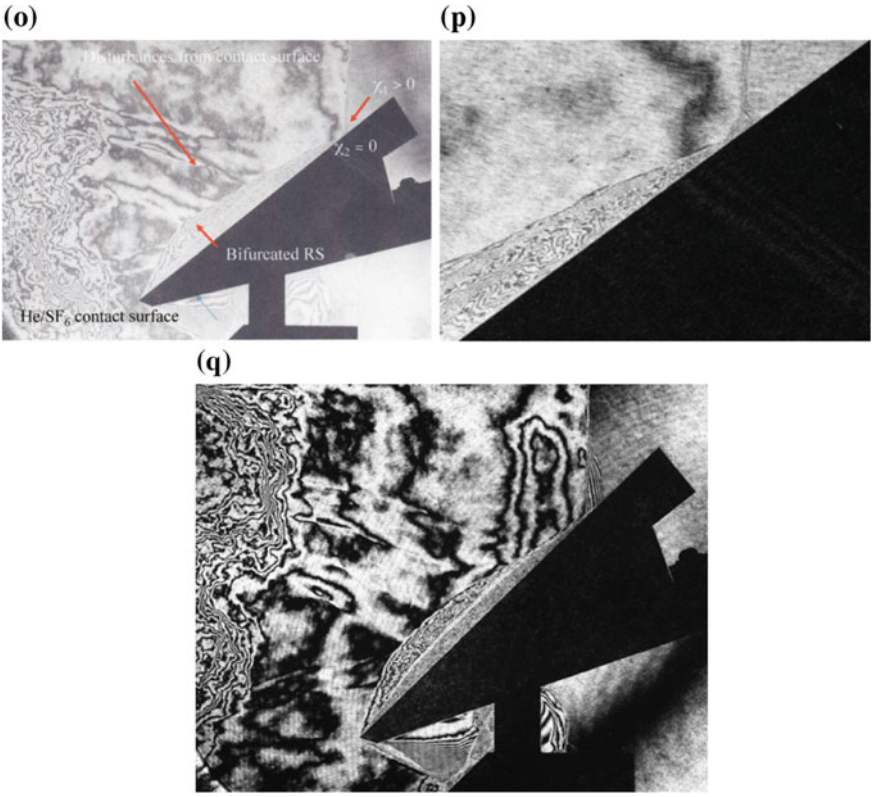

Fig. 2.30 (continued)

angle became smaller than the first triple point trajectory angle, that is, $\chi_1 > \chi_2$. With increasing the wedge angle, χ_2 tends to approach the wedge surface. In Fig. 2.30i, χ_2 is nearly lying on the wedge surface but will never stay on the wedge.

2.1.3.9 Interaction of Reflected Shock Waves Over 90° Intersecting Wedges

To simulate shock wave propagation in a rectangular supersonic air intake, three-dimensional observations of shock wave interactions from two perpendicularly intersecting wedges were conducted (Muguro 1998). Figure 2.31a illustrates the interaction of two reflected shock waves from two perpendicularly intersecting wedges. Two wedges of inclination angles 30°, 43.5°, 45° and 55° intersected perpendicularly were installed in the 60 mm × 150 mm diaphragm-less shock tube as shown in Fig. 2.31b. A reflected shock wave pattern is MR over a shallow wedge and RR over a steep wedge. Possible combinations of interaction pattern are MR-MR, MR-RR, and RR-RR. The visualization was conducted by diffuse

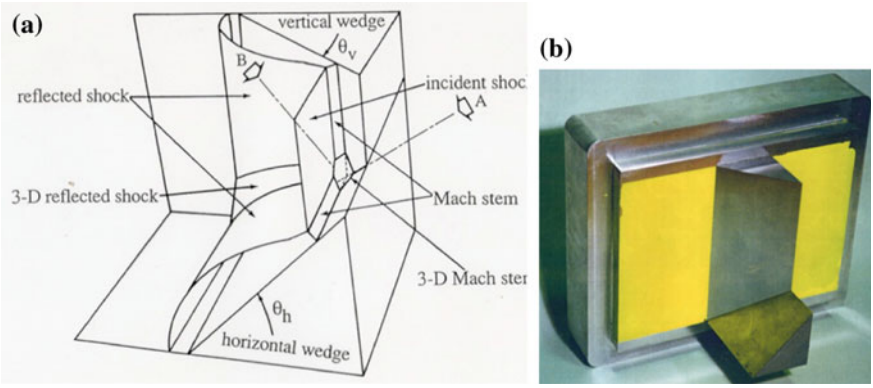

Fig. 2.31 Intersection of shock waves reflected from two intersecting wedges: **a** illustration of two shock wave interacting perpendicularly; **b** two wedge combination installed in the 60 mm × 150 mm diaphragm-less shock tube test section

holographic interferometry. The wedges and the test section were coated with a yellow fluorescent paint, which has higher degree of reflectivity to the ruby laser light (Meguro 1998). It should be noticed that as seen in Fig. 2.31a θ_h stands for the wedge angle of a vertical wedge, and θ_v that of a horizontal wedge.

A Q-switch ruby laser (Apollo Laser Co. Ltd.) has a pulse width of 25 ns and 1 J/pulse and its double pulse interval was variable from 1 μs to 1 ms. In order to visualize the shape of shock waves, the double pulse interval was selected to be 1 μs. The laser irradiation was synchronized with the shock wave motion with an appropriate delay time. Hence, the variation of phase angles occurred during the double pulse interval of 1 μs was recorded on the holographic film. As the shock wave of Ms = 2.0 moved at about 0.7 mm during 1 μs, then shock waves and their interaction over the intersecting wedges are recorded as three-dimensionally distributed thin lines. A collimated *OB* illuminated the coated wedges and was so far reflected from the coated wall. The diffused *OB* carrying holographic information irradiated a holographic film. The reconstructed images were recorded using a conventional reflex camera or a digital camera. Figure 2.32 summarize reconstructed images of interaction of the reflected shock waves from intersecting wedges. Experiments were conducted for Ms = 1.2, 1.5, 2.5 and 2.8 in air. Shock waves are described as three-dimensionally distributed thin lines having thickness of 0.5 mm to 1.0 mm, which are thin enough to explained not only the difference RR and MR but also fine reflected shock wave patterns.

Figure 2.33a shows a diagram of domain and boundary of reflection patterns for Ms from 3.0 to 1.2. The ordinate denotes the vertical wedge angle in degree and the abscissa denotes the horizontal wedge angle in degree. White circles denote MR-MR interaction accompanying 3-D MS. Black filled circles denote RR-RR. Red colored regions denote the MR-MR region, blue colored regions denote the RR-RR region, orange colored regions denote RR-MR or MR-RR region. Green colored regions denote the region outside the critical transition angles, MR-RR.

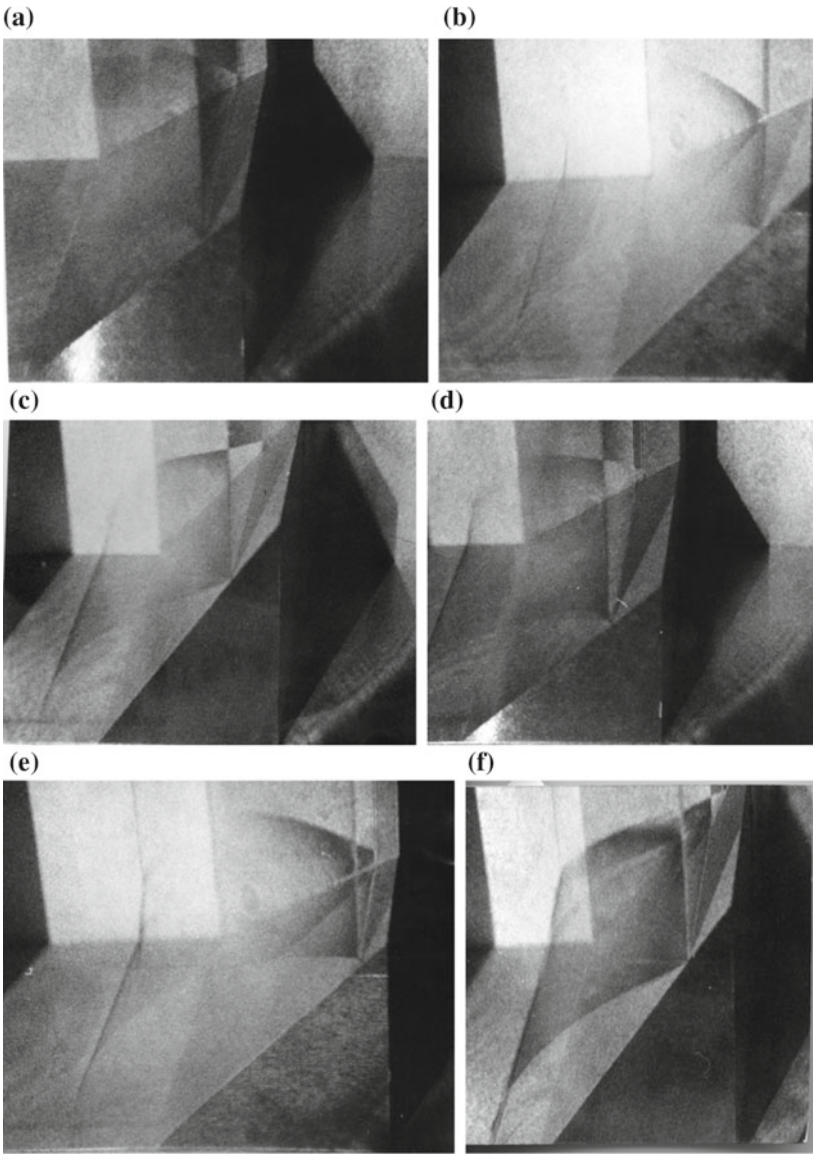

Fig. 2.32 Reconstruction of holograms: **a** #95111510, $\theta_h = 45°$, $\theta_v = 30°$, Ms = 1.201; **b** #95111201, $\theta_h = 45°$, $\theta_v = 45°$ Ms = 1.207; **c** #95111603, $\theta_h = 55°$, $\theta_v = 30°$, Ms = 1.50; **d** #95111508, $\theta_h = 43.5$, $\theta_v = 45°$ Ms = 1.500; **e** #95111406, $\theta_h = 45°$, $\theta_v = 45°$ Ms = 1.505; **f** #95111606, $\theta_h = 55°$, $\theta_v = 30°$, Ms = 2.00; **g** #95111507, $\theta_h = 43.5$, $\theta_v = 30°$ Ms = 2.000; **h** #95111503, $\theta_h = 43.5$, $\theta_v = 30°$, Ms = 2.501; **i** #95111310, $\theta_h = 45$ $\theta_v = 45°$, Ms = 2.501; **j** #95111607, $\theta_h = 55$, $\theta_v = 30°$, Ms = 2.50; **k** #95111314, $\theta_h = 45$, $\theta_v = 45°$, Ms = 2.818; **l** #95111502, $\theta_h = 43.5$, $\theta_v = 30°$, Ms = 2.845

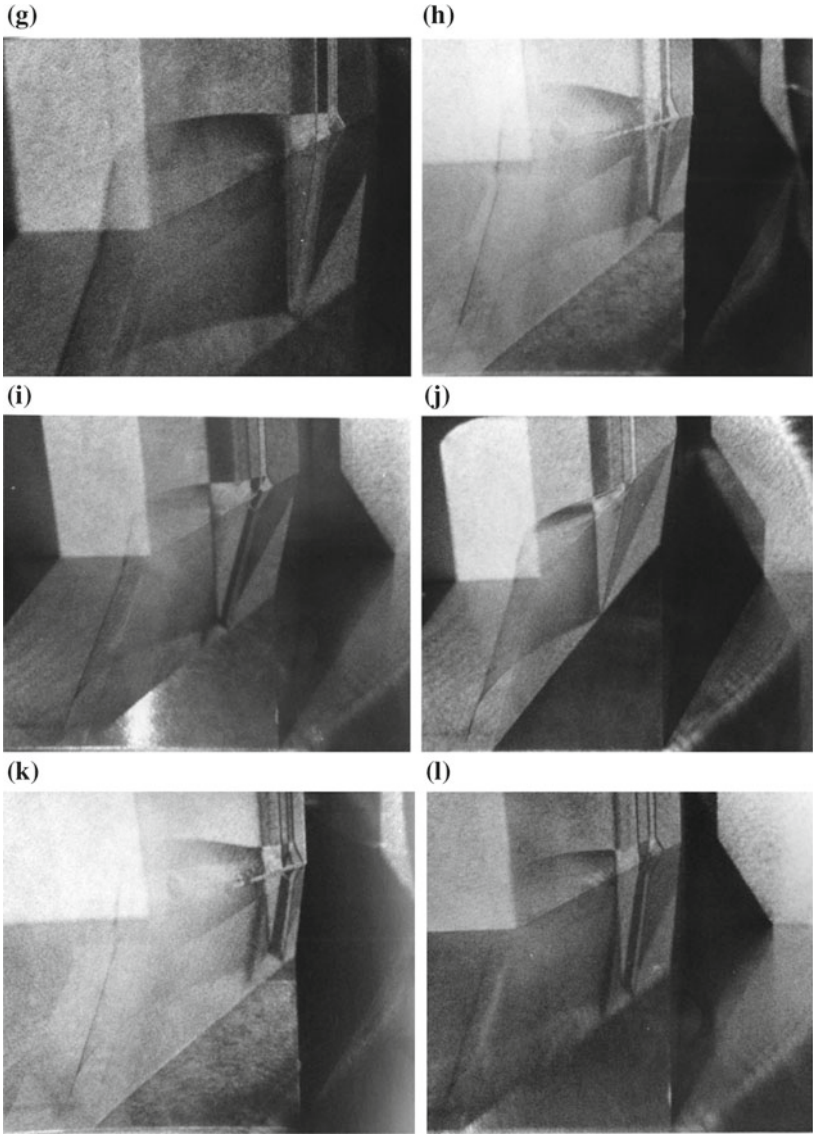

Fig. 2.32 (continued)

Figure 2.32b shows a result of numerical simulation by solving the Euler equations. The ordinate and abscissa denote vertical and horizontal wedge angles, respectively, see for details Meguro et al. (1997). The MS which is formed due to the intersection of two Mach reflections over wedges of different wedge angles, for example, over 30° and 45° wedges, has an asymmetric three-dimensional structure. Then this Mach stem can be define as a three-dimensional MS. However, the reflection

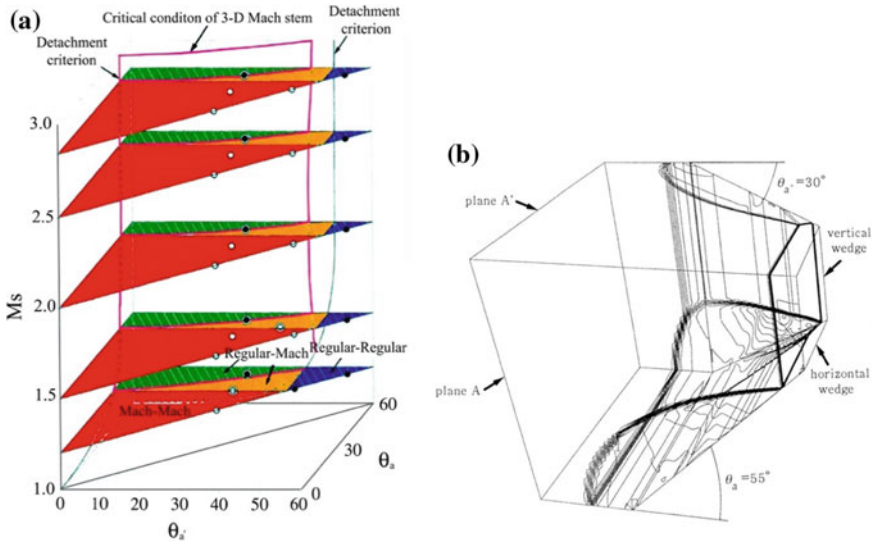

Fig. 2.33 Shock wave reflection from two intersecting wedges: **a** the domain and boundary of reflection patterns in air; **b** a numerical simulation of wedge angle 30° and 55° for Ms = 2.5 in air

patterns of RR-MR can not be identified in the present diffuse holographic observation. In conclusion, an appropriate numerical simulation may reproduce reflection patterns in wide ranges of vertical and horizontal wedge angles.

2.1.3.10 Shock Wave Reflection from a Skewed Wedge

This is a continuation of the previous subsection. If a shock wave is reflected from a three-dimensional skewed wedge whose its inclination angle varies continuously from 30° to 60°, the pattern of resulting shock wave from a 30° wedge angle will be a MR and that from a 60° wedge angle will be a RR. At a certain wedge angle, the transition from MR to RR will take place. Will this transition angle be the same as the θ_{crot} predicted by the detachment criterion reflected shock wave. The skewed wedge was installed in the 100 mm × 180 mm diaphragm-less shock tube, (Numata 2009). The shape is defined in x, y, z co-ordinates as $z = \tan\{\pi(1 + X)/6\}$, where x, y, z are normalized by the shock tube width W. This shape is so simple that it is easy to manufacture it in house. In Fig. 2.34a, the skewed wedge is placed in a 180 mm × 1100 mm test section (Numata 2009).

In order to apply the double exposure diffuse holographic interferometry of 1 μs pulse interval, the test section and the skewed wedge were coated with yellowish fluorescent spray. The collimated *OB* illuminated the test area obliquely and the reflected *OB* was collected on a 100 mm × 125 mm holo-film. Figure 2.34b shows the skewed wedge presented in x, y, z co-ordinates. The wedge is normalized by the width of the shock tube of 100 mm.

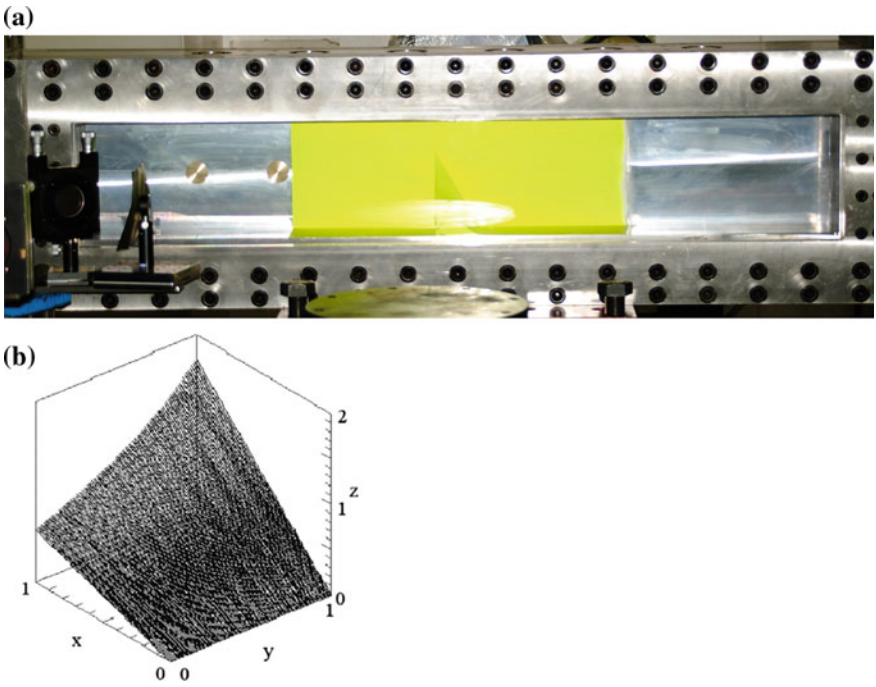

Fig. 2.34 A skewed wedge of variable inclination angles from 30° to 60° installed in a 180 mm × 1100 mm view field: **a** a skewed wedge; **b** normalized co-ordinate (Numata et al. 2009)

Figure 2.35 are reconstructed images for Ms = 1.50, 2.00, and 2.50. On the frontal side, the wedge angle was 30°, then the reflection patterns are SMR for Ms = 1.50 and 2.0 and TMR for Ms = 2.50, whereas the rear side, the wedge angle is 60° and the reflection pattern is RR. For example, when the I-polar for Ms = 1.50 is reflected from a wedge, the pressure behind its reflected shock wave readily obtained by drawing the shock polar. As seen in Fig. 2.3, the intersection point of the I-polar and the R-polar of a specified wedge angle gives the pressure behind the reflected shock wave. Then the pressure becomes higher with increase in the wedge angle. Therefore, the streamline behind the skewed wedge is not always straight along the generatrix line but move toward the shallower wedge angle. Therefore, although the transition would occur at a certain critical transition angle θ_{crit}, it is not sure whether or not this transition angle would be the same as the θ_{crit} predicted by the detachment criterion over a plane wedge.

To estimate the transition angle over the skewed wedge, the wedge surface was uniformly coated by the carbone soot. When the shock wave passed the soot covered wedge surface, the soots were removed by vortices accompanied by the slip line. Figure 2.36a shows the sooted surface exposed to a shock wave of Ms = 2.50. The soot covered surface shows the area the vortices did not scratch. A board oblique dark line shows that the transition of the reflected shock wave over

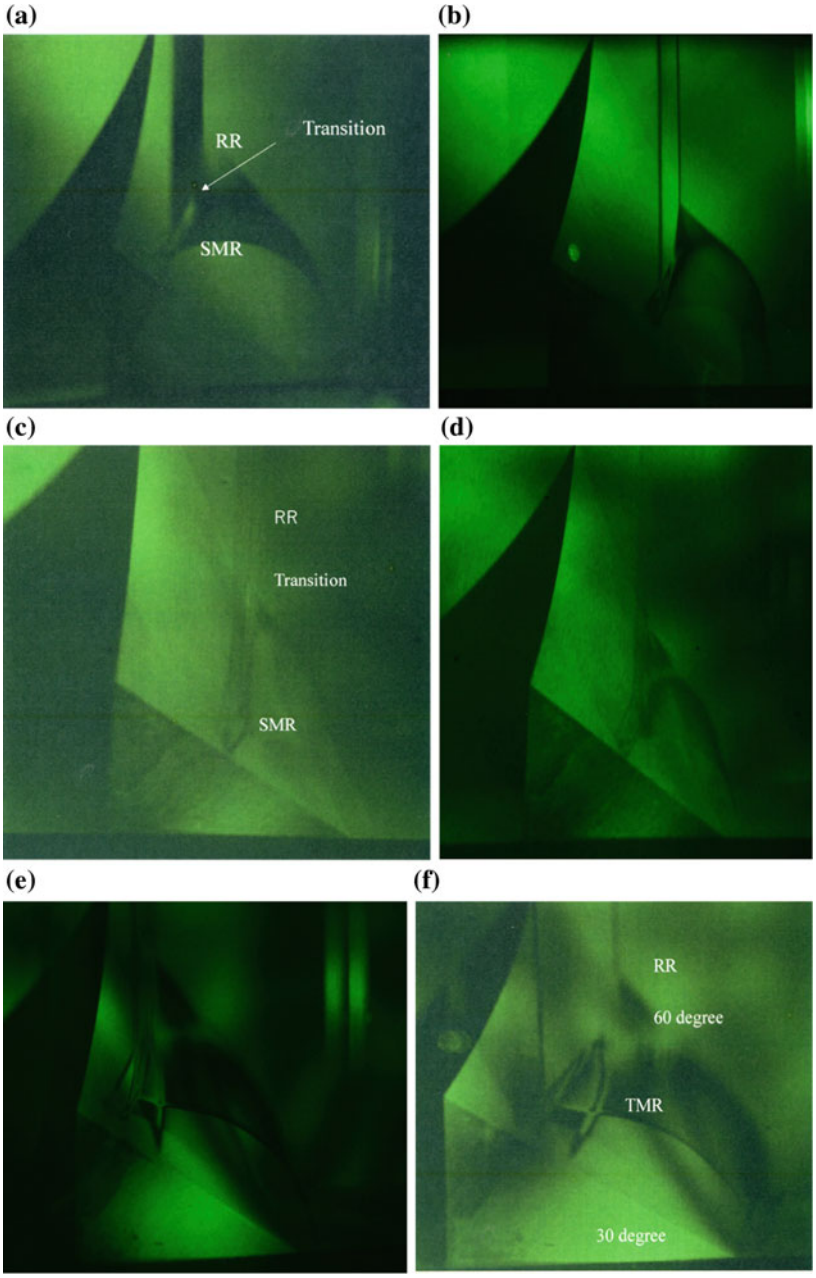

Fig. 2.35 Reconstruction of diffuse holographic interferograms: **a** #06050306, Ms = 1.55; **b** #06060101, Ms = 1.55; **c** #06051514, Ms = 2.0; **d** #06051523, Ms ∼ 2.0; **e** #06050143, Ms = 2.55; **f** #06051855. Ms = 2.55 (Numata et al. 2009)

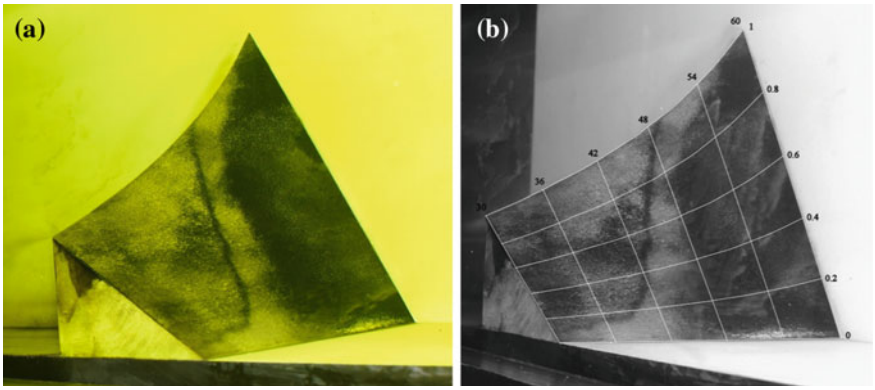

Fig. 2.36 Soot pattern created on the wedge surface for Ms = 2.5: **a** Soot pattern; **b** co-ordinate

the skewed wedge cannot be simply two-dimensional. In Fig. 2.36b, the ordinates denotes wedge angles in degree and the abscissa denotes the normalized distance along the 60° wedge surface. A black line obliquely remaining over the soot free area terminated at about 50° and indicated that the transition from TMR to RR occurred at this angle.

2.1.4 Evolution of Shock Wave Reflection from Roughened Wedges

Shock wave reflections over roughened wedges have been intensively investigated in the past. Saw tooth surface roughness was used often adopted to evaluated the effect of surface roughness on shock wave attenuations (Takayama et al. 1981). The critical transition angle θ_{crit}, in general, decreases as the degree of surface roughness increases. If the roughness is comparable to the boundary layer displacement thickness δ, it will apparently increase wedge angles. Therefore, the transition from MR to RR occurs in relatively smaller wedge angle. In the case of a very coarse surface roughness well over the boundary layer displacement thickness δ, the IS interacts separately with the roughness and creates many wavelets which promote the transition to RR. Wedges with 90° saw tooth roughnesses k = 0.1, 0.2, 0.8 and 2.0 mm are mounted on a movable stand and installed in the 40 mm × 80 mm conventional shock tube. Sequentially visualizations of shock wave reflections from these roughened wedges are carried out.

2.1.4.1 Wedges of a 0.1 mm Saw Tooth Surface Roughness

Figure 2.37 shows evolution of shock wave reflection over 0.1 mm roughness for Ms = 1.40 in air. A MR on wedges of saw tooth roughnesses, vortices are generated behind RS and MS and attenuated the transmitted shock wave. In Fig. 2.37d

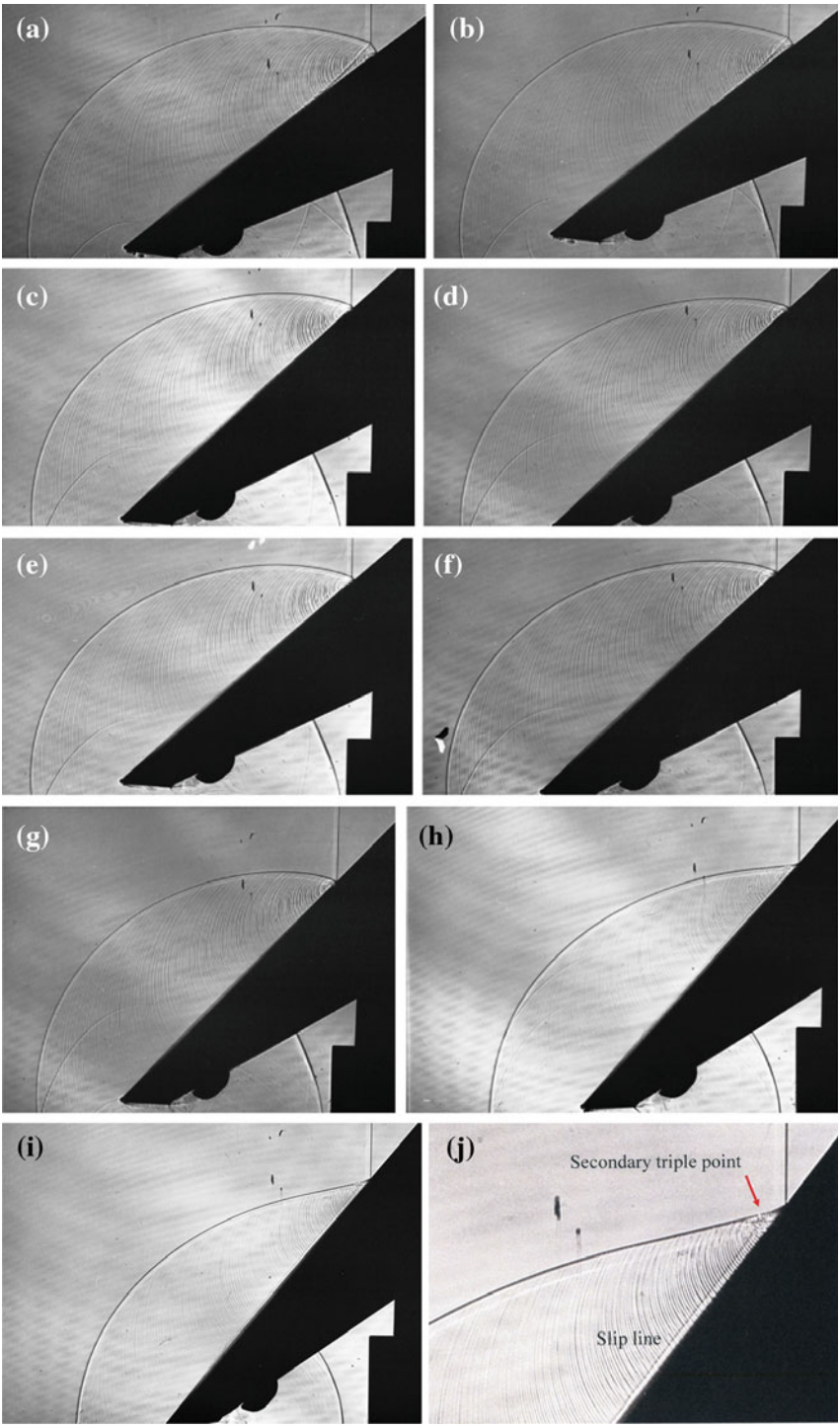
(a)
(b)
(c)
(d)
(e)
(f)
(g)
(h)
(i)
(j)
Secondary triple point
Slip line

◂**Fig. 2.37** Shock reflection over roughened wedges with a saw tooth roughness k = 0.1 mm for Ms = 1.46 in air at 500 hPa and 282.6 K: **a** #80050922, Ms = 1.463, θ_w = 38°; **b** #80050921, Ms = 1.460, θ_w = 40°; **c** #80050930, Ms = 1.465, θ_w = 41°; **d** #80050927, Ms = 1.460, θ_w = 42.5°; **e** #80050929, Ms = 1.466, θ_w = 43.0°; **f** #80050928, Ms = 1.458, θ_w = 44°; **g** #80050927, Ms = 1.460, θ_w = 45°; **h** #80050924, Ms = 1.466, θ_w = 47°; **i** #80050923, Ms = 1.463, θ_w = 49.5°; **j** enlargement of (**i**)

the slip line is directed away from the wedge surface. This reflection pattern is a so-called inverse Mach reflection, or in short IvMR (Courant and Friedrichs 1948). This will be discussed in the Chap. 3 The IvMR is a final shape of a MR and transits to a RR, as seen in Fig. 2.37g. Figure 2.37h then shows a RR which accompanies a secondary triple point. The evolution of such a transition uniquely occurs not only in a fine surface roughness but also over a coarse surface roughness.

2.1.4.2 Wedges of a 0.2 mm Saw Tooth Surface Roughness

Figure 2.38 shows evolution of shock wave reflection from wedges of a 0.2 mm saw tooth roughness for weak shock waves of Ms = 1.09 in air. In Fig. 2.38a, the wedge angle was 0° and circular co-axially shaped shock waves were reflected from each saw tooth and the MS was slightly leaned forward. Courant and Friedrichs (1948) defined this reflection pattern, as already seen in Fig. 2.38b, as an inverse Mach, vNMR. This pattern will soon transit to a RR with increasing in the wedge angle. When the TP reached on the wedge surface as seen in Fig. 2.38c, d, it is succeeded by the secondary TP on the RS as seen in Fig. 2.38f.

Figure 2.39a–j shows the evolution of reflected shock wave from 0.2 mm saw tooth roughness for Ms = 2.0 in air at p_o = 500 hPa, 293.6 K. In Fig. 2.39a, the SL was faintly observed emanating from the TP. The MS was curved and leaned forward. The boundary layer developing along the wedge surface was obscured in the region between the foot of the MS and a point at which the SL touched the wedge surface. With the increase in wedge angles as seen in Fig. 2.39f, g, the reflection patterns transited from SMR to a TMR and its kink point merged to the TP. Figure 2.39g shows that the envelop of wavelets and a SL emanating from the TP coalesce into another SL. If the wedge angle became slightly larger than the angle shown in Fig. 2.39g of θ_w = 36.0°, the TP would touch the wedge surface and eventually the RR would appear. However, the TP would not be terminated but changed to another TP on the RS. In short, the SL was maintained. As seen Fig. 2.39j, the RR accompanied a secondary TP on its RS, which resembled the pattern of a DMR. Figure 2.39k–p shows single exposure interferograms emphasizing the shock wave reflections over steeper wedges for Ms = 1.83 in air at 400 hPa, 286.5 K. Figure 2.39k shows a reflected shock pattern immediately after the transaction to a RR over an identical wedge angle of 46.0° as seen in Fig. 2.39j. Figure 2.39l shows an enlargement of the reflection pattern over a wedge θ_w = 47.0°.

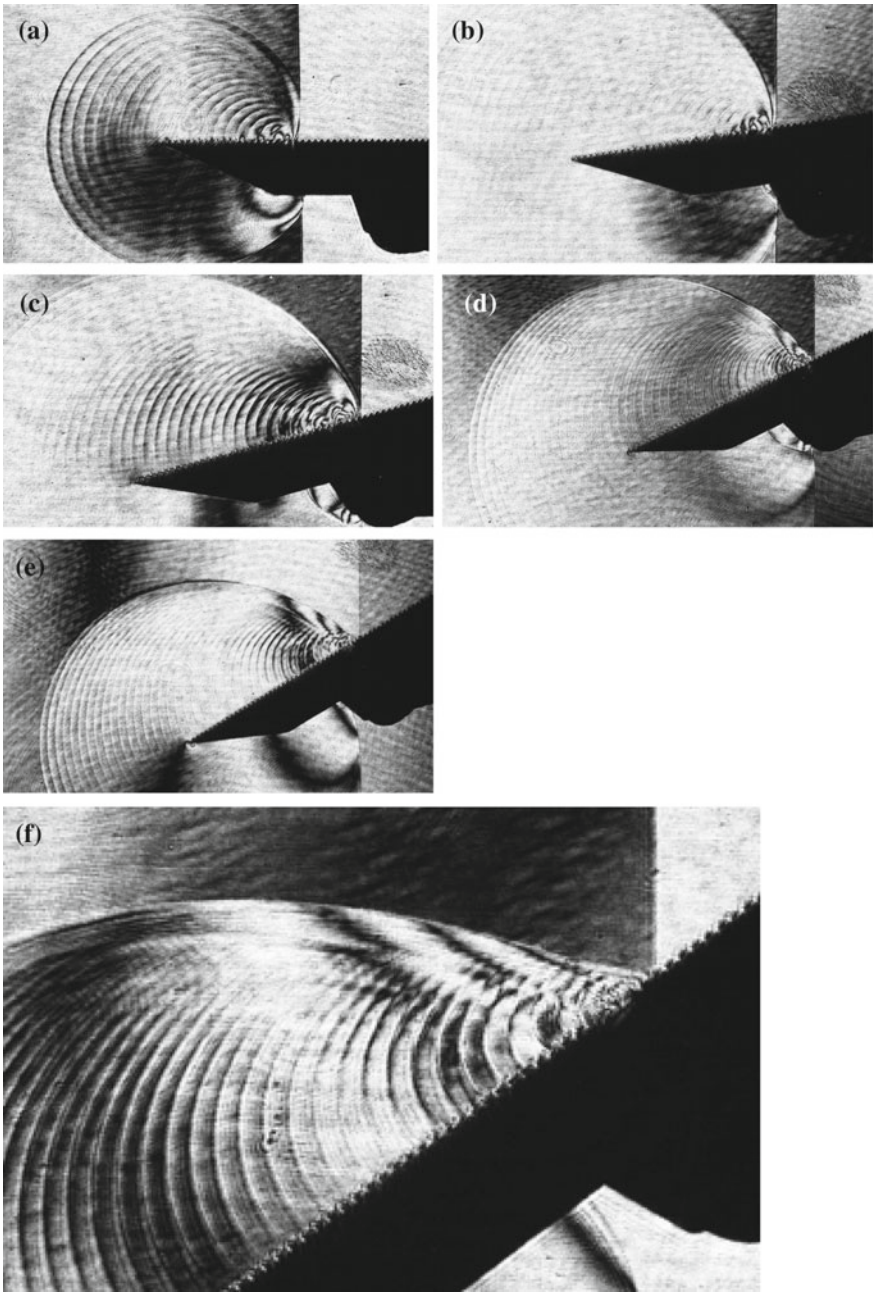

Fig. 2.38 Evolution of shock wave reflection from roughened wedges with saw tooth roughness k = 0.2 mm for Ms = 1.09: in air at 600 hPa and 293.6 K: **a** # 81101404, Ms = 1.090, $\theta_w = 0.0°$; **b** #81101407, Ms = 1.090, $\theta_w = 5°$; **c** #81101408, Ms = 1.090, $\theta_w = 17°$; **d** #81101412, Ms = 1.086, $\theta_w = 24°$; **e** #81101409, Ms = 1.093, $\theta_w = 24°$; **f** #81101411, Ms = 1.087, $\theta_w = 39°$

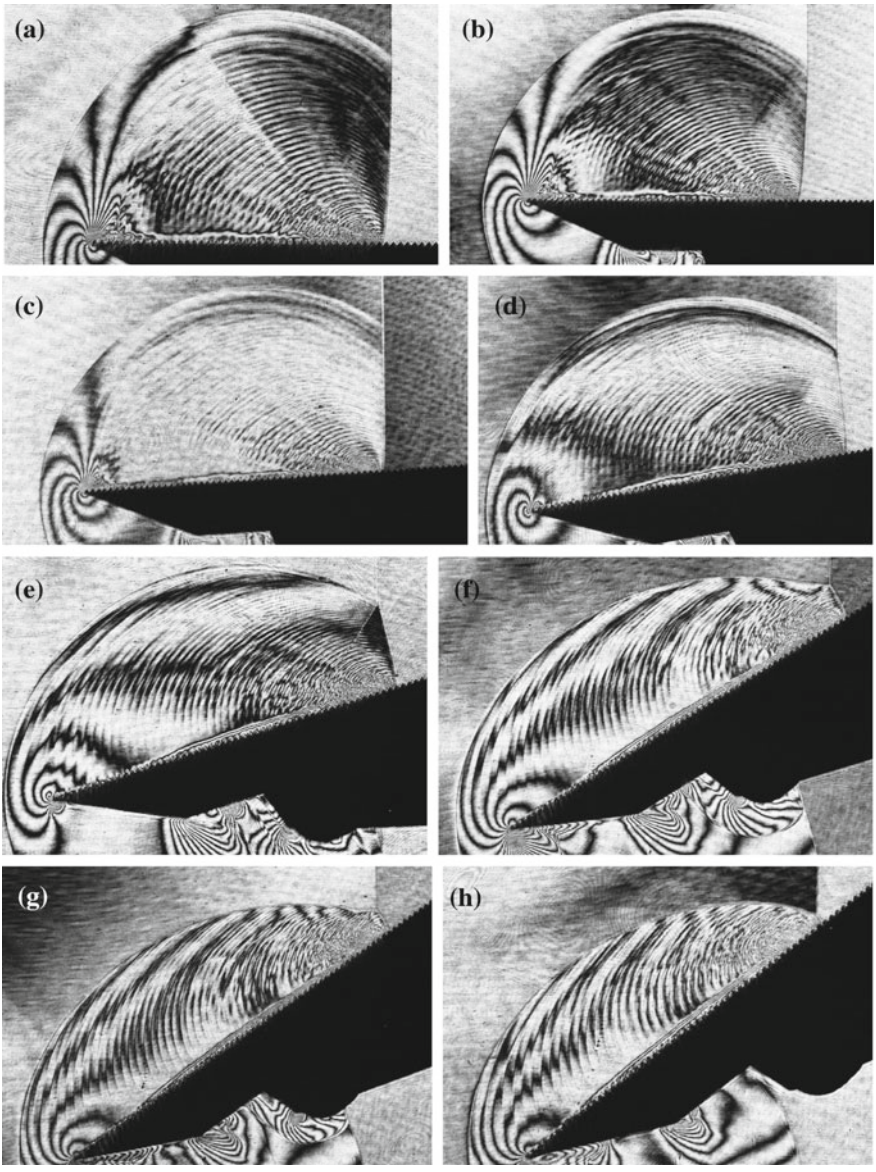

Fig. 2.39 Evolution of shock wave reflection over roughened wedges k = 0.2 mm **a–j** for Ms = 2.0 in air at 500 hPa and 293.6 K; **k–p** for Ms = 1.83 at 400 hPa, 286.5 K single exposure: **a** #81101423, Ms = 1.970, $\theta_w = 1.0°$; **b** #81101422, Ms = 2.004, $\theta_w = 2.0°$; **c** #81101421, Ms = 2.004, $\theta_w = 4.0°$; **d** #81101420, Ms = 1.993, $\theta_w = 10.0°$; **e** #81101419, Ms = 1.943, $\theta_w = 17.0°$; **f** 81101416, Ms = 2.016, $\theta_w = 31.0°$; **g** #81101418, Ms = 2.016, $\theta_w = 36.0°$; **h** #81101415, Ms = 1.981, $\theta_w = 41°$; **i** #81101414, Ms = 1.993, $\theta_w = 42.0°$; **j** #84012401, Ms = 1.862, $\theta_w = 46.0°$; **k** #84012322, Ms = 1.862, $\theta_w = 46.0°$ **l** #84012321, Ms = 1.862, $\theta_w = 47.0°$; **m** 84012320 Ms = 1.844, $\theta_w = 59.0°$; **n** 84012319, Ms = 1.884, $\theta_w = 59.0°$; **o** #84012318, Ms = 1.826, $\theta_w = 56.0°$; **p** #84012316, Ms = 1.871, $\theta_w = 59.0°$

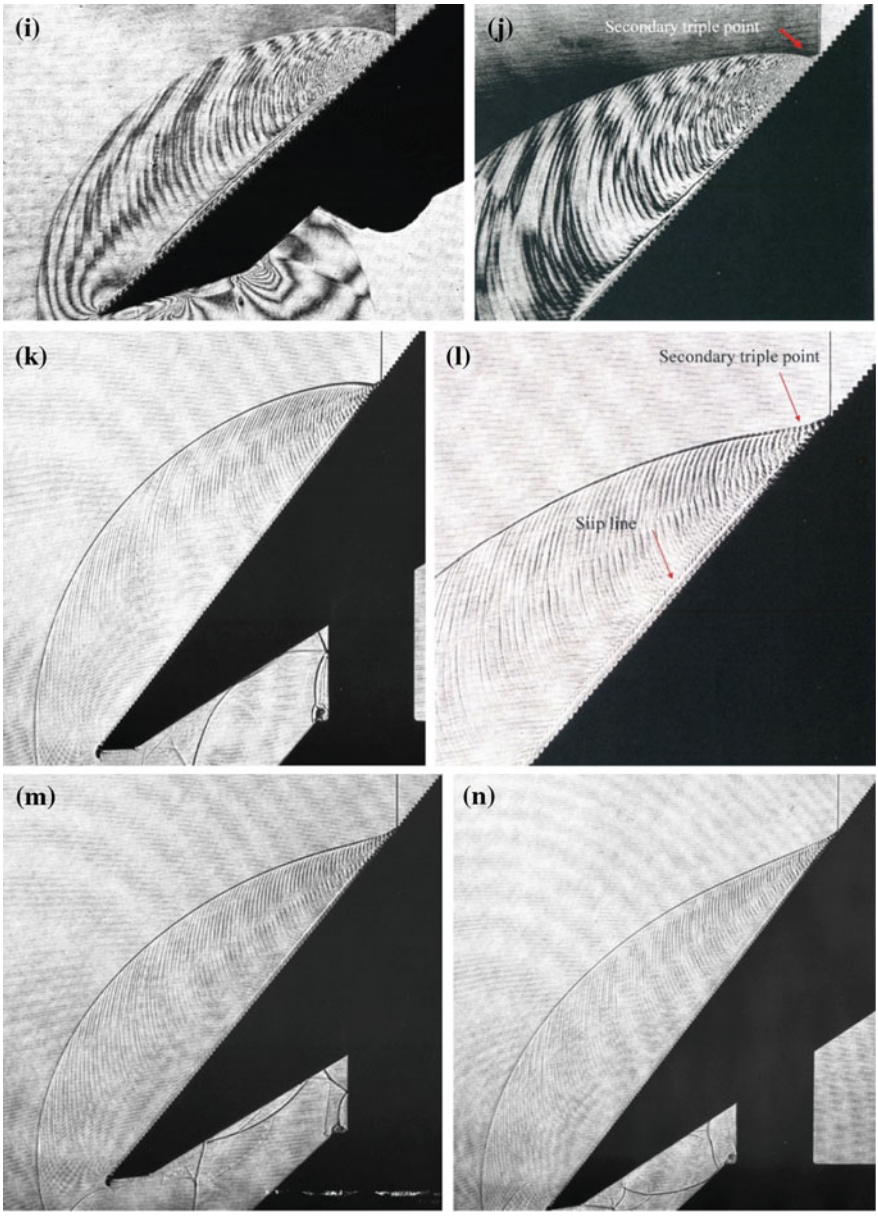

Fig. 2.39 (continued)

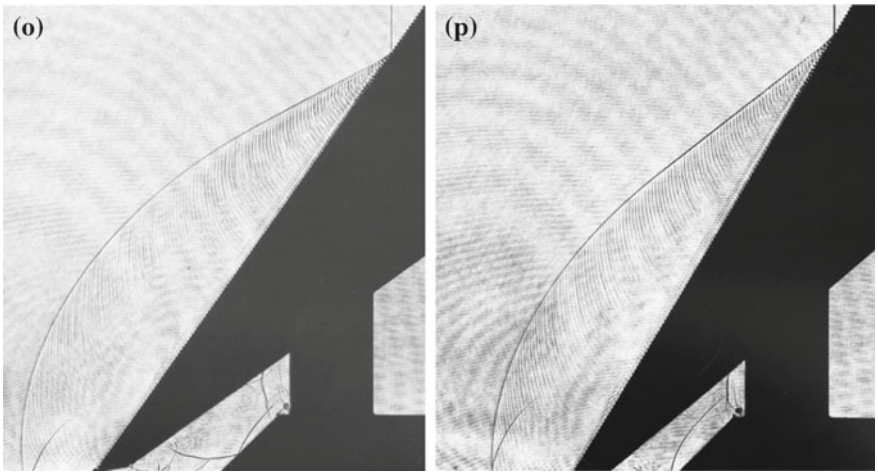

Fig. 2.39 (continued)

2.1.4.3 Wedges of a 0.8 mm Saw Tooth Surface Roughness

Figure 2.40 shows single exposure interferograms of evolution of reflected shock waves from a wedge having 0.8 mm saw tooth roughness for Ms = 1.46 in air at 500 hPa, 291.0 K. The pattern of the reflected shock wave is a SMR. Vortices were generated at the corners of the saw tooth roughness. The growth and dissipation of the vortices along the roughened wedge surface and their merger into a train of wavelets are well observed in Fig. 2.39c–g. The train of the wavelets becomes a SL emanating from the TP and is parallel to the wedge surface. Courant and Friedrichs (1948) defined this reflection pattern as a stationary Mach reflection, or in short, StMR. The shock tube flows are quasi-stationary and hence the StMR is held uniquely only for short time when the flow conditions fulfilled the presence of the StMR. Figure 2.40j shows a RR over a wedge of $\theta_w = 40.5°$. A secondary TP is seen from which the SL is emanating. The upstream flow information of the secondary TP are transmitted up to this point. Figure 2.40k shows a RR over a wedge of $\theta_w = 41.0°$. Figure 2.40l is its enlargement. The IS interacted independently with individual corners of the saw tooth.

2.1.4.4 Wedges of a 2.0 mm Saw Tooth Surface Roughness

Figure 2.41 shows later stages of single exposure interferograms of shock wave reflections from a coarse saw tooth wedge, k = 2.0 mm, for Ms = 1.47 in air at 500 hPa and 282.6 K. The saw tooth roughness is so coarse that the boundary layer displacement thickness would hardly contribute to the reflected shock wave transition. Due to interaction of IS with such a coarse roughness, the initiation, growth, and dissipation of vortices are better resolved. Analogously to the roughness of

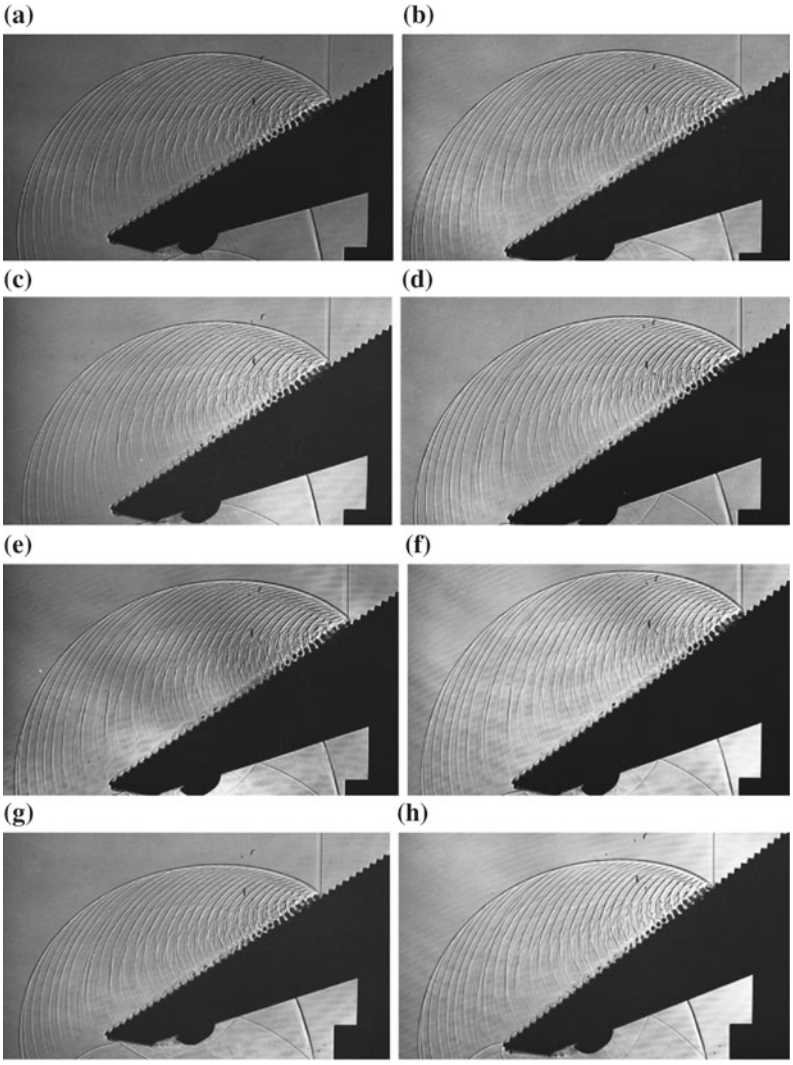

Fig. 2.40 Shock reflection over roughened wedges k = 0.8 mm for Ms = 1.45 in air at 500 hPa, 291.0 K: **a** #80050912, Ms = 1.456, $\theta_w = 32°$; **b** #80050916, Ms = 1.470, $\theta_w = 33°$; **c** #80050911, Ms = 1.456, $\theta_w = 35°$; **d** #80050913, Ms = 1.466, $\theta_w = 35.5°$; **e** #80050915, Ms = 1.473, $\theta_w = 36°$; **f** #80050914, Ms = 1.473, $\theta_w = 36°$; **g** #80050910, Ms = 1.472, $\theta_w = 36°$; **h** #80050909, Ms = 1.466, $\theta_w = 37°$; **i** #80050917, Ms = 1.472, $\theta_w = 38°$; **j** #80050907, Ms = 1.463, $\theta_w = 40.5°$; **k** #80050906, Ms = 1.466, $\theta_w = 41°$; **l** enlargement of (**k**)

0.8 mm as seen in Fig. 2.40, even in Fig. 2.41a, b, the envelop of wavelets which were created by the vortices formed a SL and merged with the TP. The SL looked parallel or was directed to the roughened wall surface. Then as already discussed in the case of k = 0.8 mm, the reflection patterns seen in Fig. 2.41a, b are StMR. With

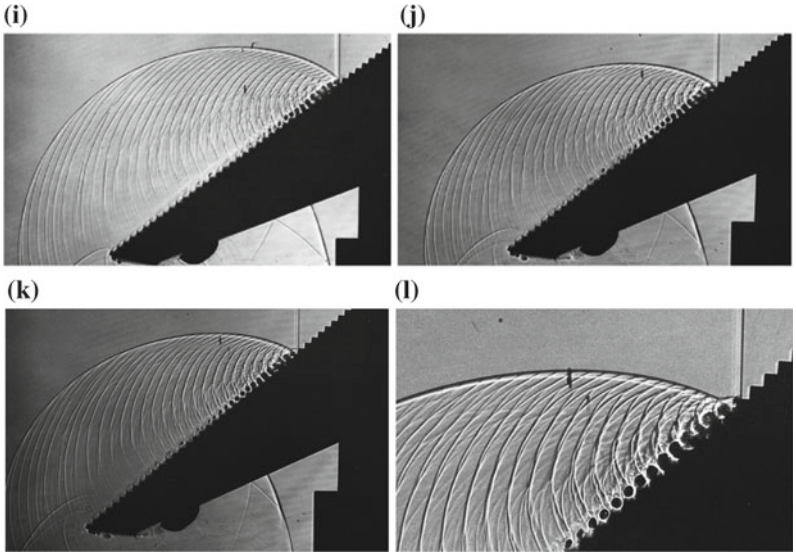

Fig. 2.40 (continued)

a slight increase in the wedge angle, the resulting reflection pattern would be an IvMR and the transition to a RR would occur. In Fig. 2.41c, a kink point which corresponds to a secondary TP is observable on the reflected shock wave. All the upstream information can reach up to the secondary TP and in the downstream region the IS interacts independently with the individual corner of the saw tooth. Figure 2.41j shows a RR and Fig. 2.41k is its enlargement. The IS interacts only locally with the individual saw tooth corners.

In order to determine the critical transition angles θ_{crit}, experiments were performed sequentially by changing in wedge angled and shock wave Mach numbers Ms. The reflection patterns were visualized by using double exposure and single exposure interferograms. Selective results of the visualizations were presented form Figs. 2.37, 2.38, 2.39, 2.40 and 2.41. The results obtained for various Ms and Re values are: Ms = 1.04, Re = 0.8×10^5, $\theta_{crit} = 27.5°$; Ms = 1.12, Re = 2.50×10^5, $\theta_{crit} = 32.5°$; Ms = 1.21, Re = 3.40×10^5, $\theta_{crit} = 40.5°$; Ms = 1.44, Re = 2.70×10^5, $\theta_{crit} = 43.7°$; Ms = 1.86, Re = 0.58×10^5, $\theta_{crit} = 45.8°$; and Ms = 3.80, Re = 0.32×10^5, $\theta_{crit} = 44.9°$.

Figure 2.42 summarized these results. The ordinate denote the θ_{crit} in degree and the abscissa denotes the inverse shock strength, the inverse pressure ratio $\xi = (\gamma + 1)/(2\gamma Ms^2 - \gamma + 1)$. Black filled circles denote θ_{crit} for smooth wedge (Smith 1948). Yellow, green, dark blue, and red filled circles denote the present results of k = 0.1, 0.2, 0.8, and 2.0 mm respectively (Takayama et al. 1981).

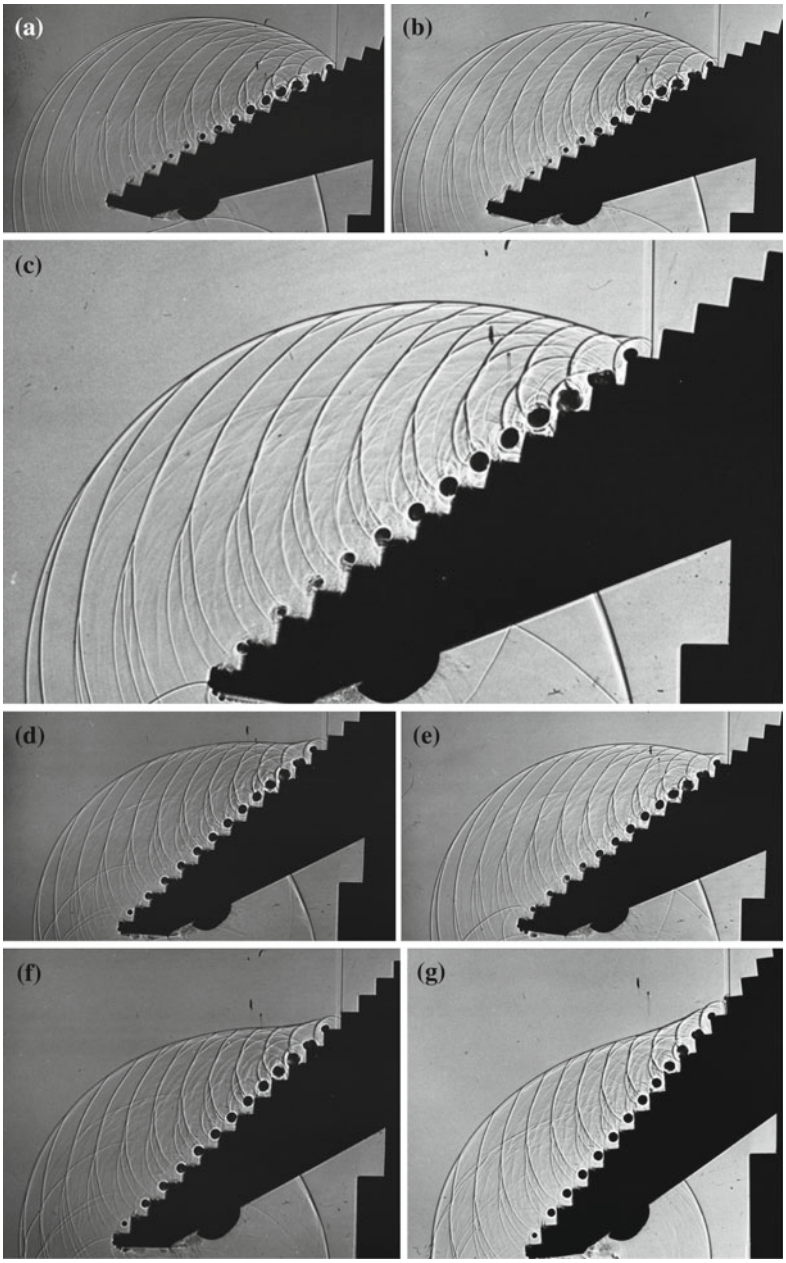

Fig. 2.41 Shock reflection over roughened wedges with saw tooth roughness k = 2.0 mm for Ms = 1.47 in air at 500 hPa and 282.6 K: **a** #80050811, Ms = 1.476, $\theta_w = 31°$; **b** #80050812, Ms = 1.470, $\theta_w = 33°$; **c** #80050839, Ms = 1.469, $\theta_w = 34°$; **d** #80050807, Ms = 1.456, $\theta_w = 37°$; **e** #80050808, Ms = 1.467, $\theta_w = 40°$; **f** #80050805, Ms = 1.473, $\theta_w = 45°$; **g** 80050802, Ms = 1.463, $\theta_w = 46°$; **h** #80050803, Ms = 1.468, $\theta_w = 47°$; **i** #80050804, Ms = 1.470, $\theta_w = 48°$; **j** #80050801, Ms = 1.456, $\theta_w = 51°$; **k** enlargement of (**j**)

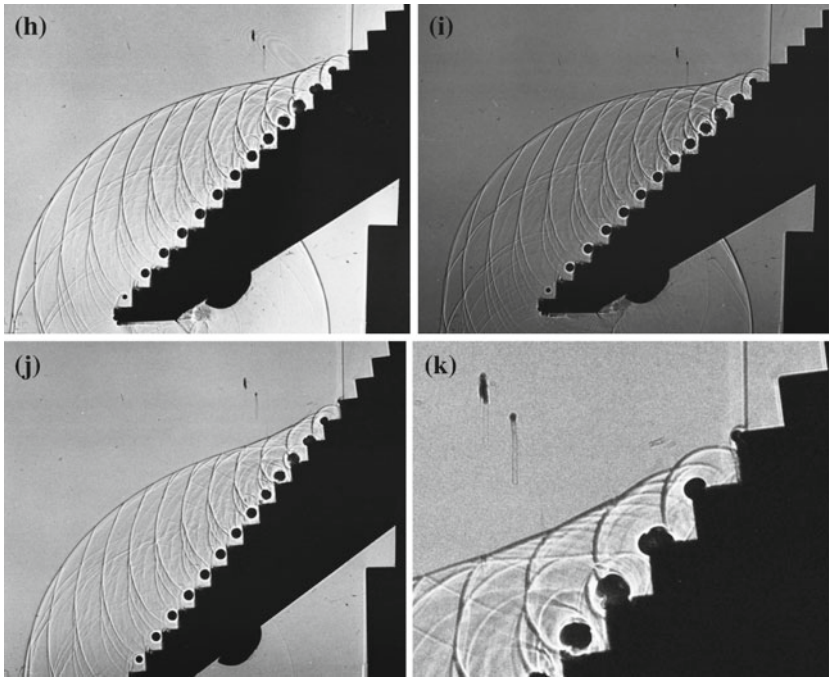

Fig. 2.41 (continued)

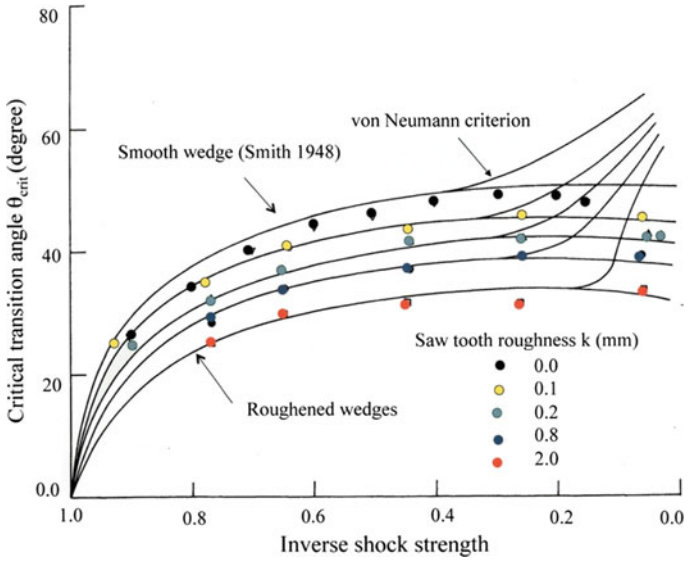

Fig. 2.42 Summary of experiments (Takayama et al. 1981)

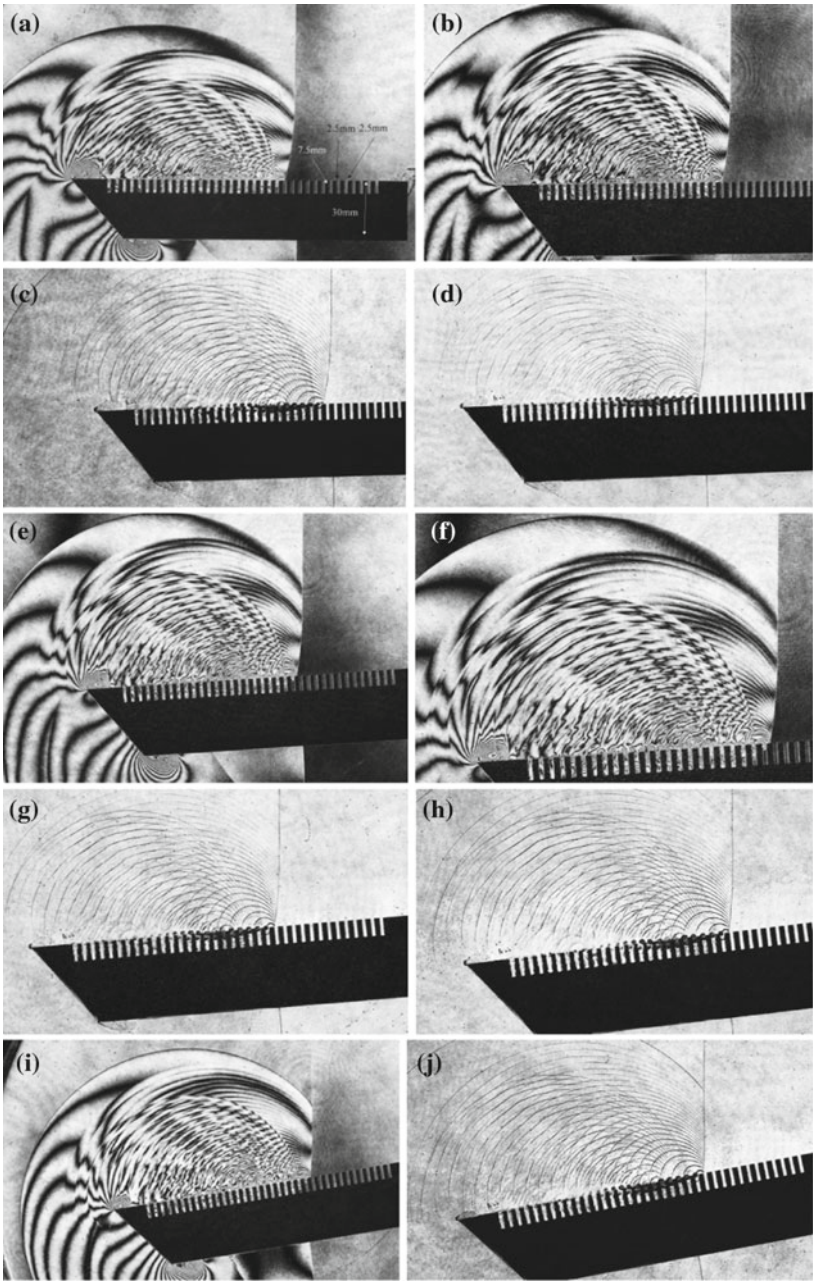
(a)
2.5mm 2.5mm
7.5mm
30mm
(b)
(c)
(d)
(e)
(f)
(g)
(h)
(i)
(j)

◂**Fig. 2.43** Evolution of reflected shock waves from a slotted wedge for Ms = 1.36 in air at atmospheric air at 295 K: **a** #86060612, Ms = 1.360, θ_w = 1.0°; **b** #86060611, Ms = 1.362, θ_w = 2.0; **c** #86060612, Ms = 1.368, θ_w = 3.0°, single exposure; **d** #86060609, Ms = 1.358, θ_w = 4.0°, single exposure; **e** #86060608, Ms = 1.358, θ_w = 5.0; **f** enlargement of (**e**); **g** #86060607, Ms = 1.367, θ_w = 6.0° single exposure; **h** #86060605, Ms = 1.370, θ_w = 8.0°, single exposure; **i** #86060603, Ms = 1.368, θ_w = 10.0°; **j** #86060601, Ms = 1.358, θ_w = 12.0° single exposure; **k** #86060517, Ms = 1.365, θ_w = 14.0°, single exposure; **l** #86060516, Ms = 1.352, θ_w = 15.0°; **m** #86060511, Ms = 1.365, θ_w = 20.0; **n** #86060510, Ms = 1.365, θ_w = 21.0°, single exposure; **o** #86060508, Ms = 1.360, θ_w = 23.0, single exposure; **p** #86060506, Ms = 1.359, θ_w = 25.0°; **q** #86060509, Ms = 1.365, θ_w = 28.0° single exposure; **r** #86053002, Ms = 1.359, θ_w = 30.0; **s** #86053004, Ms = 1.363, θ_w = 32.0; **t** #86060402, Ms = 1.349, θ_w = 34.0° single exposure; **u** #86060404, Ms = 1.344, θ_w = 36.0 single exposure; **v** #86060406, Ms = 1.346, θ_w = 38.0° single exposure; **w** #86060407, Ms = 1.346, θ_w = 39.0° single exposure

2.1.5 Evolution of Shock Wave Reflection from Slotted Wedges or Perforated Wedges

When a shock wave propagates along a roughened wedge, the critical transition angle decreases as seen in Fig. 2.42. When shock waves are reflected from slotted wedges or perforated wedges, what will happen?

2.1.5.1 Slotted Wedges

A slotted wedge was installed in the test section of the 60 mm × 150 mm diaphragm-less shock tube. The wedge was sandwiched between two acrylic disks of 200 mm in diameter and 20 mm in thickness and adjusted its angle by rotating the disks. On the tested slot is 1.5 mm wide and 7.0 mm deep and a gap between neighboring slots is 1.5 mm. 36 slits are distributed along the wedge model surface with a perforation ratio $\varepsilon = 0.4$.

Figure 2.43 shows evolution of shock wave reflected from the slotted wedge surface for Ms = 1.36 in atmospheric air at 295 K. The IS is diffracted at each slot opening, transmitted along the slot wall and reflected from its bottom. In the meantime, expansion waves are created from each slot corner coalescing into an envelop of expansion wave (Onodera and Takayama 1990). In the case of saw tooth roughened surface, vortices are created, it dissipates energy, and thereby attenuates the IS.

As seen in Figs. 2.37, 2.38, 2.39, 2.40 and 2.41, wavelets reflected from individual saw tooth roughness formed an envelop of a SL which interacted with the TP and eventually formed the IvMR. In the final reflection pattern, the SL emanating from the TP is directed away from the wedge surface, which is a typical wave pattern observed in an IvMR. When it transits to RR, the resulting RS has a secondary TP. However, over the slotted wedges, the flow is deflected at the individual slots and their reflections are expansion waves. As seen in Fig. 2.43r–t, a slip line emanating from the TP is directed toward the wedge surface. Therefore, the resulting reflection pattern is a direct Mach reflection or in short, DiMR. Hence with

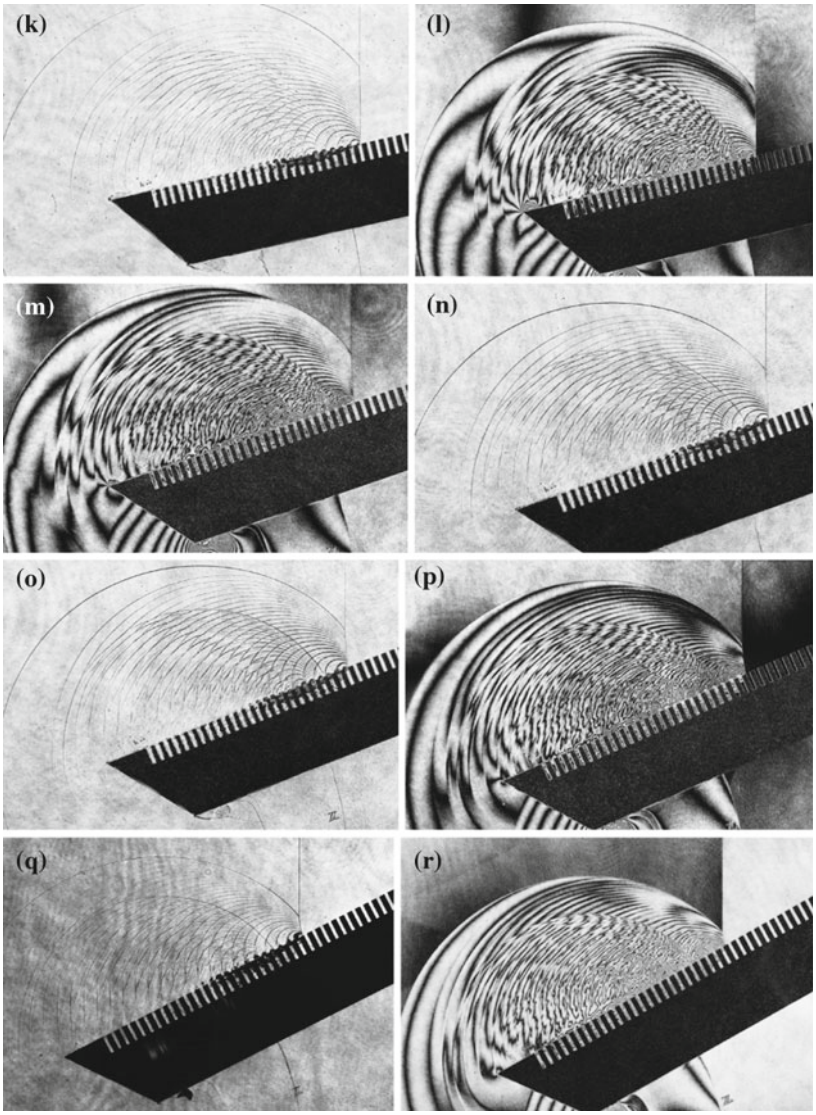

Fig. 2.43 (continued)

increase in wedge angles, MR transits to RR, without causing any complicated reflection patterns, as seen in Fig. 2.42v, w.

Figure 2.42w shows an enlargement of a RR at $\theta_w = 39°$. The transmitted shock wave propagates along the individual slots and reflected. Reflected waves from the bottom of slots released in the area behind the RS formed an envelop of compression wavelets.

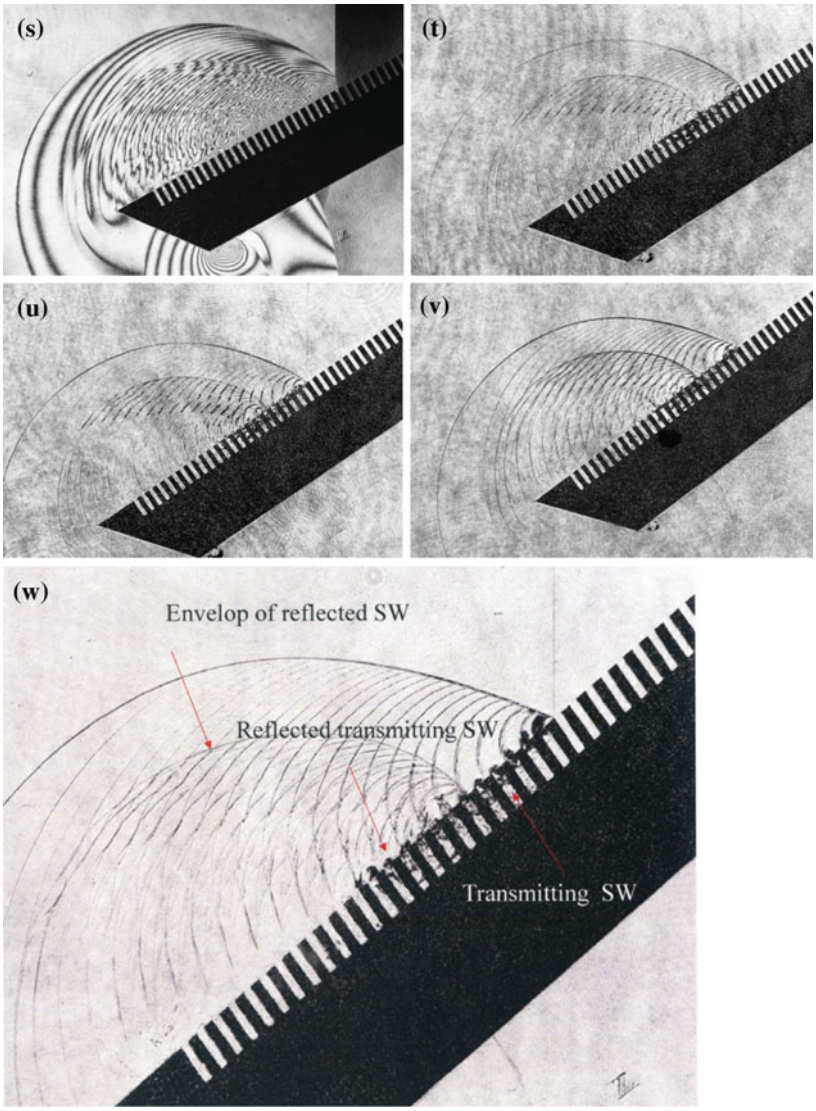

Fig. 2.43 (continued)

To assure whether or not the transition over slotted wedges occurs similarly to that seen in a case of the smooth and solid wedges, we performed the transition was checked for stronger shock waves and for wedge angles close to the θ_{crit}. In Fig. 2.43, the reflection pattern is DMR for Ms = 3.0 and the wedge angle was increased step by step over up to and over θ_{crit}. In Fig. 2.44a. a DMR pattern is seen and with increasing in the wedge angle, although the reflection pattern is maintained, it becomes smaller and eventually transits straightforwardly to RR.

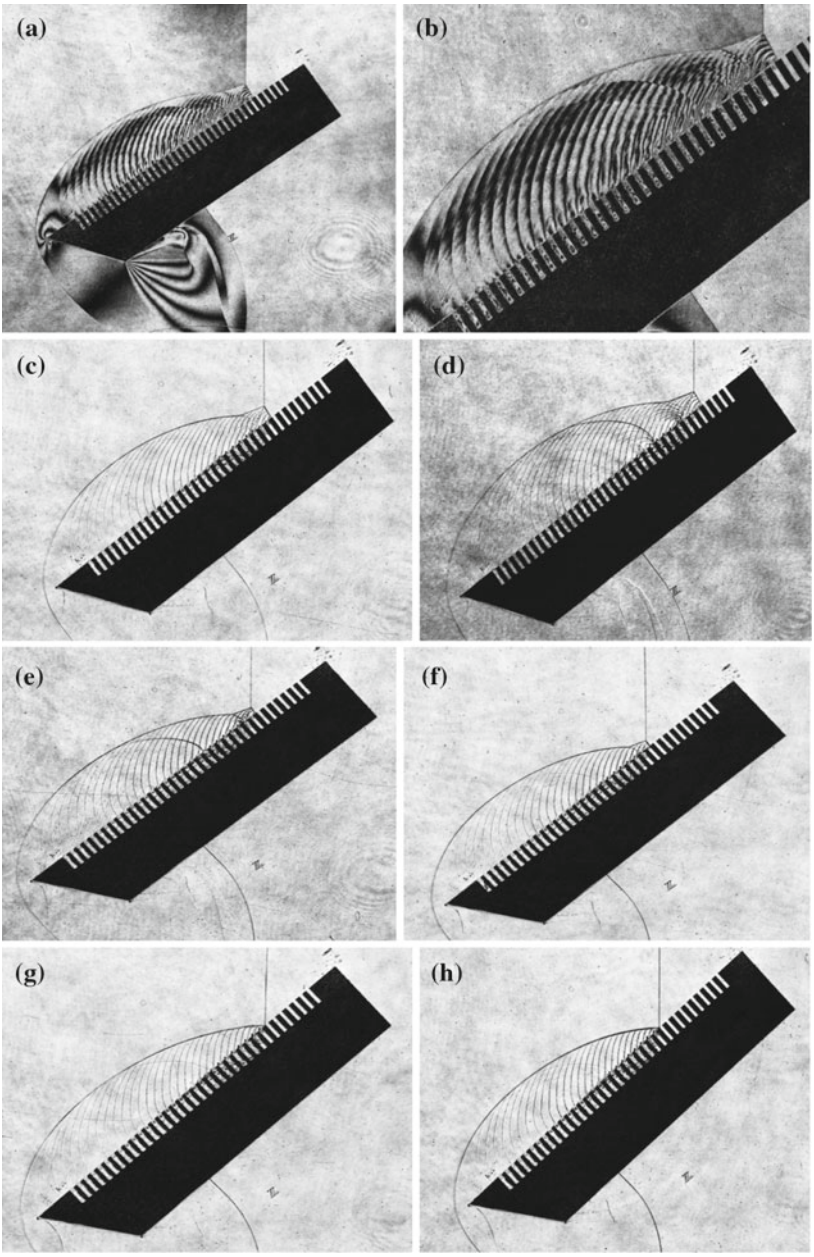

Fig. 2.44 Evolution of reflected shock waves from a slotted wedge, at 120 μs from trigger point, for Ms = 3.0 in air at 60 hPa, 2942.0 K: **a** #86060710, Ms = 3.065, θ_w = 37.0°; **b** enlargement of (**a**); **c** #86060704, Ms = 3.038, θ_w = 40.0°, single exposure; **d** #86060703, Ms = 3.016, θ_w = 40.0°, single exposure; **e** #86060706, Ms = 3.049, θ_w = 41.0°, single exposure; **f** #86060707. Ms = 3.037, θ_w = 42.0°, single exposure; **g** #86060708, Ms = 3.025, a = 43.0, single exposure; **h** #86060709, Ms = 3.025, a = 44.0, single exposure

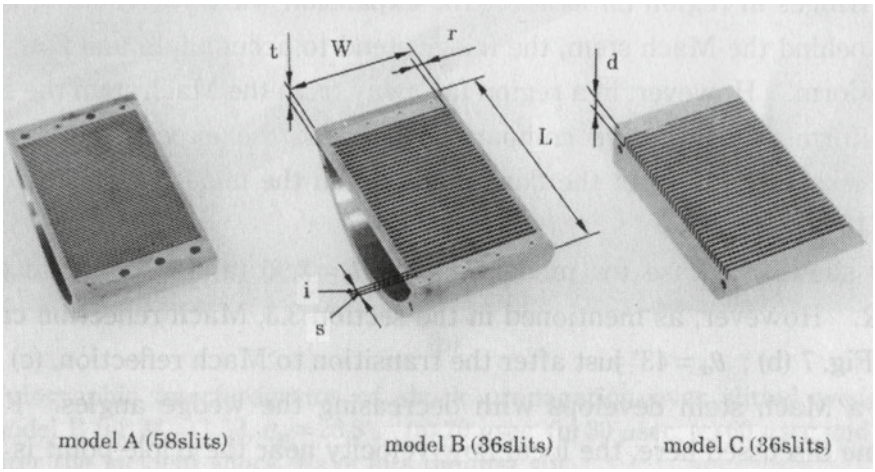

Fig. 2.45 Perforated and slotted wall Models (Onodera and Takayama 1990)

2.1.5.2 Perforated Wedges

Figure 2.45a shows slotted wall Models: Model C had the following dimensions: L = 110 mm, d = 7 mm, s = 1.5 mm, i = 1.5 mm and perforation ratio ε = 0.4. Model A hag s = 0.5 mm, i = 1.0 mm, ε = 0.34; and Model B had ε = 0.4, s = 1.5 mm, i = 1.5 mm, L = 100 mm, t = 5 mm, r = 3.0 mm.

In the early 1970s, many shock wave researchers investigated shock wave propagation over perforated walls. In the proceedings of the 8th International Symposium on Shock Tubes, papers were presented on this topic. At that time, researchers tried to Model the mass flow through the wedge perforations. For correctly measuring the mass flow through the perforations, Model A and Model B were constructed. Using these Models, it was possible to monitor mass flows leaked from the perforations. Hence it was possible to correctly estimate the deflection velocity, which would be a boundary condition in drawing shock polar.

Shock wave reflection from perforated wedges or slotted wedges is one of basic research topics of shock wave dynamics. Many reports were presented on the shock wave propagation over perforated walls (for example Szumowski 1972). A perforated plate with perforation ratio of 0.40 was manufacture in our machine shop, was sandwiched between 200 mm diameter and 20 mm thick PMMA plates, was installed in the test section of the 60 mm × 150 mm diaphragm-less shock tube. The wedge angles were arbitrarily adjusted by rotating the PMMA plates.

Figure 2.46 shows sequential observation of the shock wave reflection for Ms = 1.17 in air at 930 hPa, 290.8 K over the Model B as shown Fig. 2.45. The perforated wedges were supported by a half-cur cylinder which was fixed on the side wall. With this arrangement, it was observed that an oblique shock wave was driven by the gas flow which leaked out through the perforation behind the IS. The evolution of the inclination angle of the oblique shock wave indicates the attenuation of the transmitting shock wave along the perforated wall.

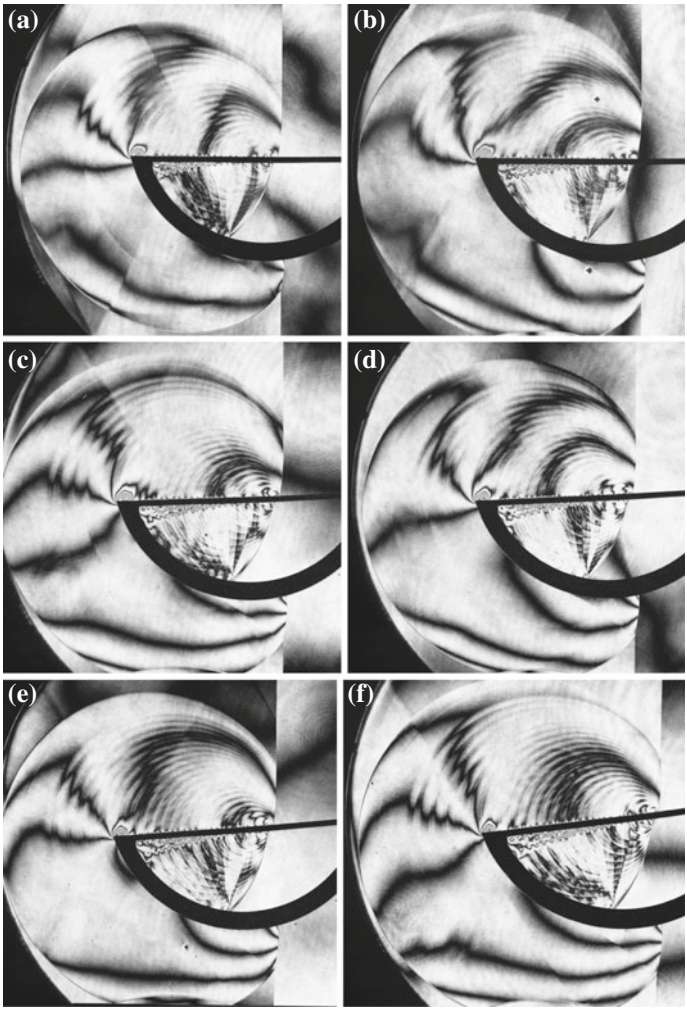

Fig. 2.46 Evolution of reflected shock waves over a perforated wall of Model B shown in Fig. 2.44 for Ms = 1.17 in air at 930 hPa, 290.8 K: **a** #86030320, Ms = 1.152, $\theta_w = 0.0°$; **b** #86030321, Ms = 1.169, $\theta_w = 1.0°$; **c** #86030318, Ms = 1.170, $\theta_w = 3.0°$; **d** #86030317, Ms = 1.170, $\theta_w = 4.0°$; **e** #86030316, Ms = 1.171, $\theta_w = 6.0°$; **f** #86030315, Ms = 1.169, $\theta_w = 9.0°$; **g** #86030314, Ms = 1.163, $\theta_w = 13.0°$; **h** #86030313, Ms = 1.163, $\theta_w = 17.0°$; **i** #86030312 Ms = 1.169, $\theta_w = 21.0°$; **j** #86030310, Ms = 1.172, $\theta_w = 27.0°$; **k** #86030307, Ms = 1.174, $\theta_w = 28.0°$; **l** #86030308, Ms = 1.170, $\theta_w = 29.0°$; **m** #86030307, Ms = 1.170, $\theta_w = 30.0°$; **n** #86030305, Ms = 1.165, $\theta_w = 32.0°$; **o** #86030304, Ms = 1.172, $\theta_w = 33.0°$; **p** #86030301, Ms = 1.173, $\theta_w = 34.0°$; **q** #86030302, Ms = 1.173, $\theta_w = 35.0°$; **r** #86030301, Ms = 1.162, $\theta_w = 36.0°$

Figure 2.46a shows the shock wave propagation along the perforated wedge at $\theta_w = 0.0°$, hence the triple point lies on the trajectory of the glancing incidence angle. Figure 2.46b–k shows the shock wave propagation along the perforated

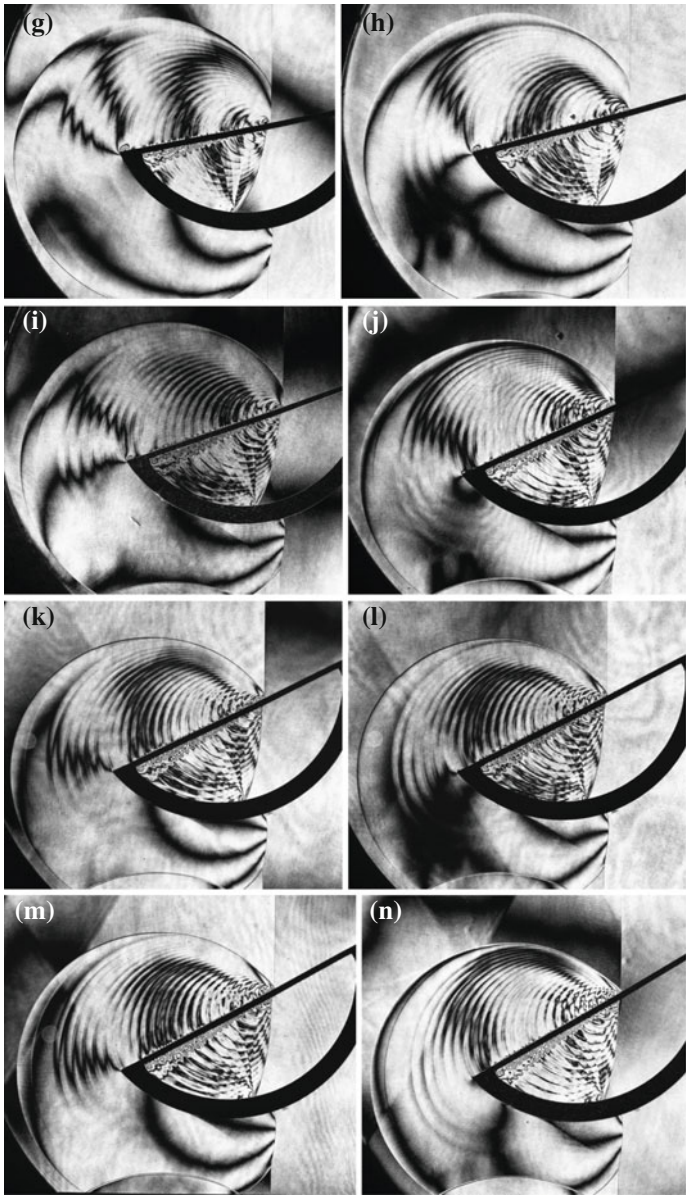

Fig. 2.46 (continued)

wedge at from $\theta_w = 1.0°$ to and 28.0°. The patterns of all the reflected shock waves show the MR but the triple points don't show any slip lines. Therefore, the reflection patterns are vNMR. In Fig. 2.46m at the wedge angle of $\theta_w = 30.0°$, the reflected shock wave misses a MS. Then the transition to a RR occurred indicating that the θ_{crit} would be about 30.0°.

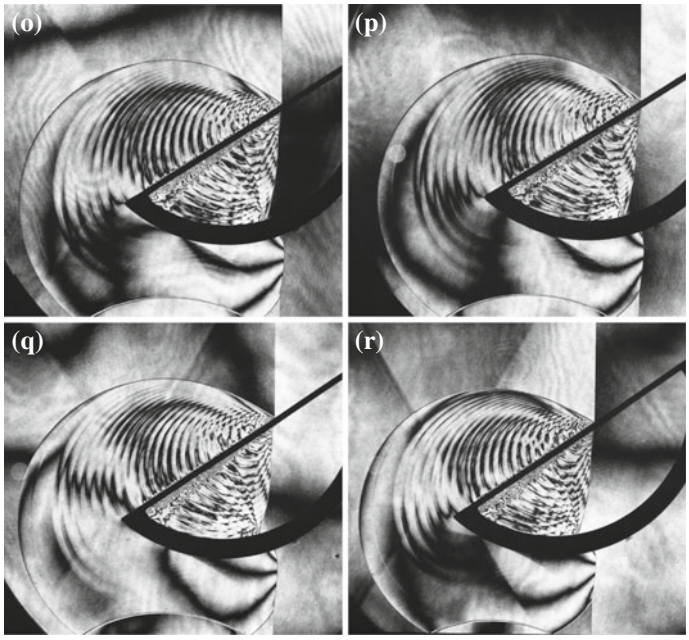

Fig. 2.46 (continued)

Figure 2.42 summarized the dependence of the critical transition angles θ_{crit} on the inverse shock strength, that is, the inverse of the pressure ratio ξ over wedges with the saw tooth surface roughness. In the case of the saw tooth roughness k = 0.8 mm, the critical transition angle θ_{crit} was about 30.0° for inverse shock strength of $\xi - 0.7$ which corresponds to Ms = 1.17. This result agreed with the result of the observation shown in Fig. 2.46.

Figure 2.47 shows the evolution of reflected shock waves over the perforated wedge of Model B for Ms = 1.56 in air or at the inverse shock strength of $\xi = 0.375$ at 755 hPa, 301 K. The wedge angle is increased from $\theta_w = 0°$ to $\theta_w = 90.0°$ by every 10.0°. Figure 2.47a shows the reflection from a wedge of the glancing incidence. In Fig. 2.47b–j, the reflection pattern is a SMR but the SL emanating from the TP is just visible, whereas in Fig. 2.46 the reflection pattern is a vNMR. The transition occurs at an angle slightly larger than $\theta_w = 40.0°$. The critical transition angle for Ms = 1.56; $\xi = 0.375$ is comparable to the value of θ_{crit} of the wedge with saw tooth roughness k = 0.2 mm as shown in Fig. 2.42. Figure 2.47j shows a symmetrical shock wave reflection from $\theta_w = 90.0°$.

Figure 2.48 shows the evolution of a shock wave reflection over a perforated wedge of the Model B for Ms = 2.90 or at the inverse shock strength of $\xi = 0.104$ in air at 40 hPa, 297.0 K. The reflection pattern is a SMR in Fig. 2.48a–c. However, with the increase in the wedge angle, it is a TMR in Fig. 2.48d–f and the transition to a RR takes place. As seen in Fig. 2.45, the Model B has wide flat edge

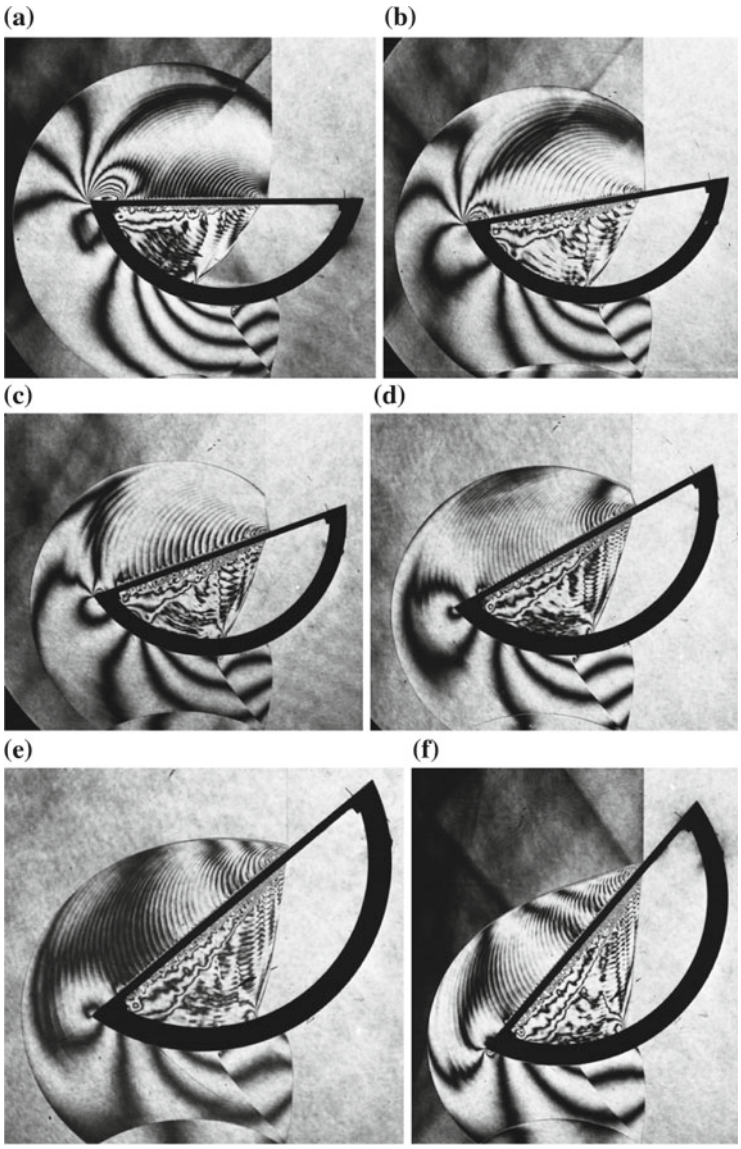

Fig. 2.47 Evolution of reflected shock waves over a perforated wall for Ms = 1.56 in air at 755 hPa, 301 K: **a** #94072801, Ms = 1.560, $\theta_w = 0°$; **b** #94072702, Ms = 1.558, $\theta_w = 10°$; **c** #94072703, Ms = 1.558, $\theta_w = 20°$; **d** #94072804, Ms = 1.560, $\theta_w = 30°$; **e** #94072805, Ms = 1.558, $\theta_w = 40°$; **f** #94072806, Ms = 1.780, $\theta_w = 50°$; **g** #94072807, Ms = 1.780, $\theta_w = 60°$; **h** #94072808, Ms = 1.558, $\theta_w = 70°$: **i** #94072809, Ms = 1.558, $\theta_w = 80°$; **j** #94072810, Ms = 1.556, $\theta_w = 90°$

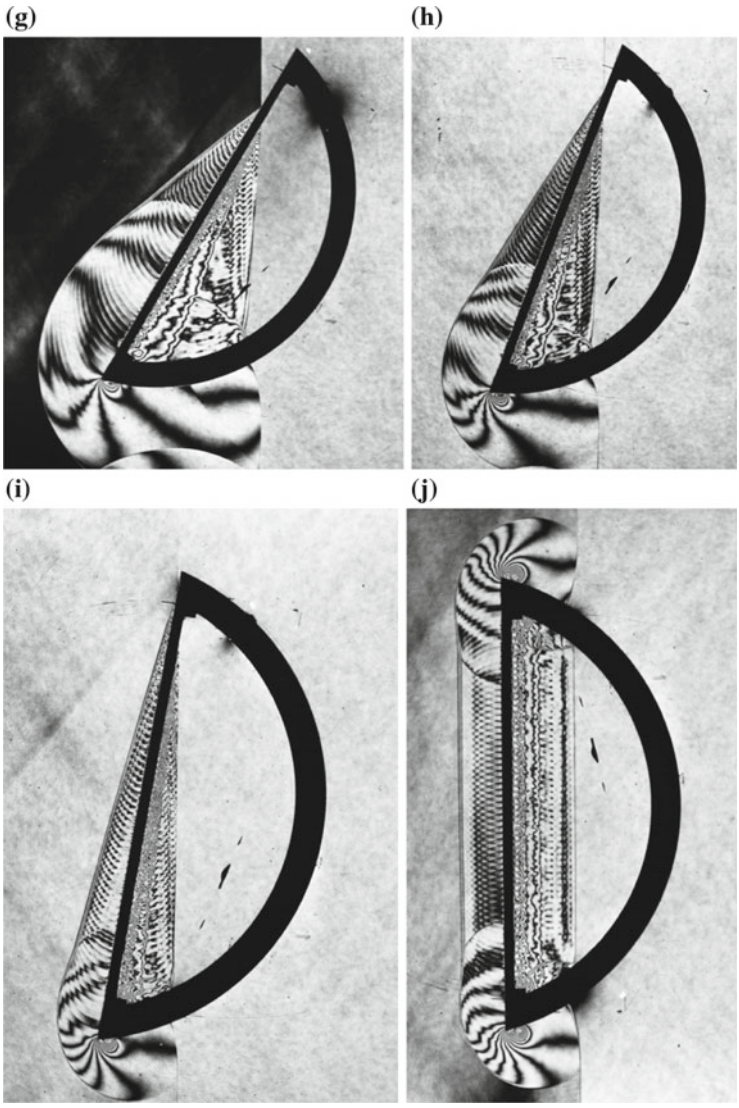

Fig. 2.47 (continued)

parts of r = 3 mm which support the perforation. It is noticed that the shock wave is reflected, at the same time, from the 54 mm wide perforated wedge and from 6 mm wide flat wedge. Then the θ_{crit} occurring over the Model B wedge would be slightly larger than the θ_{crit} occurring over a 60 mm wide perforated wedge.

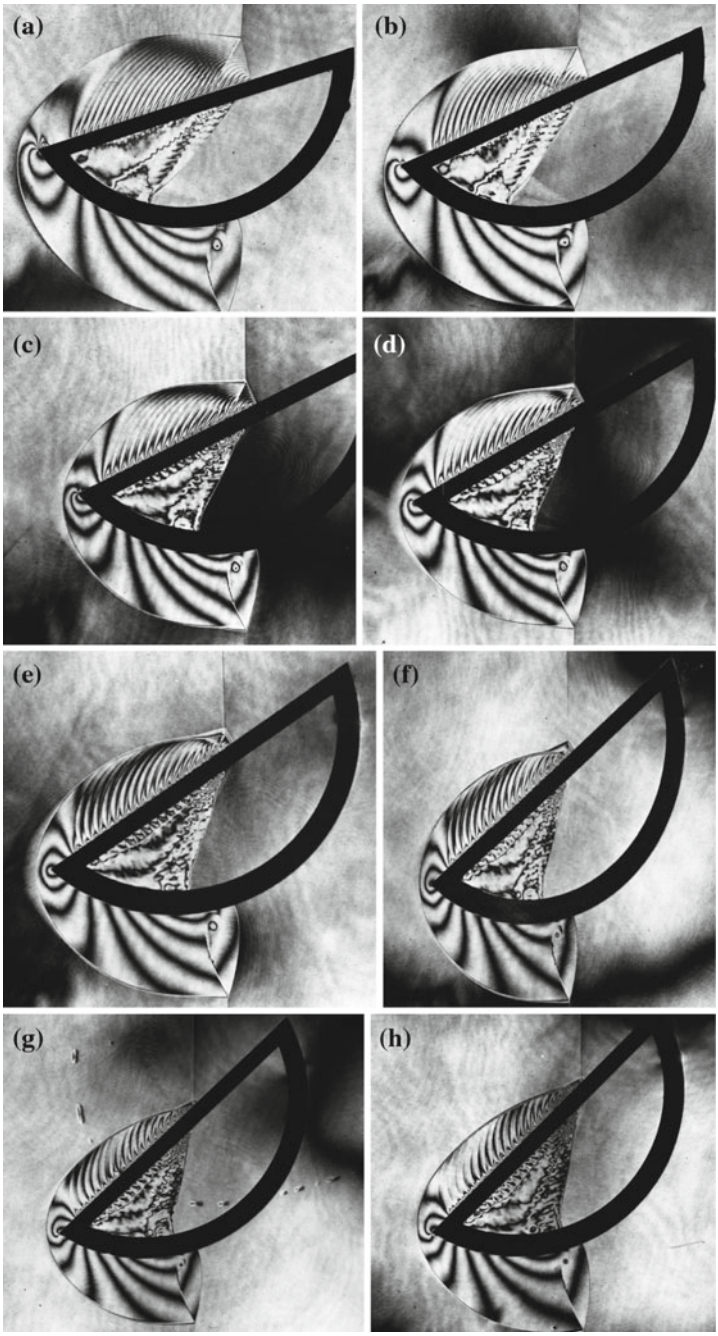

Fig. 2.48 Evolution of reflected shock waves over a perforated wall for Ms = 2.90 in air at 40 hPa, 297.0 K: **a** #86032506, Ms = 2.902, θ_w = 21.0°; **b** #86032505, Ms = 2.902, θ_w = 26.5°; **c** #86012319, Ms = 2.948, θ_w = 28.0°; **d** #86012318, Ms = 2.931, θ_w = 31.0°; **e** #86012315, Ms = 2.971, θ_w = 38.0°; **f** #86012301, Ms = 2.967, θ_w = 40.0°; **g** #86012306, Ms = 2.920, θ_w = 45.0°; **h** #86012308, Ms = 2.988, θ_w = 47.0°; **i** #86012310, Ms = 2.961, θ_w = 52.0°

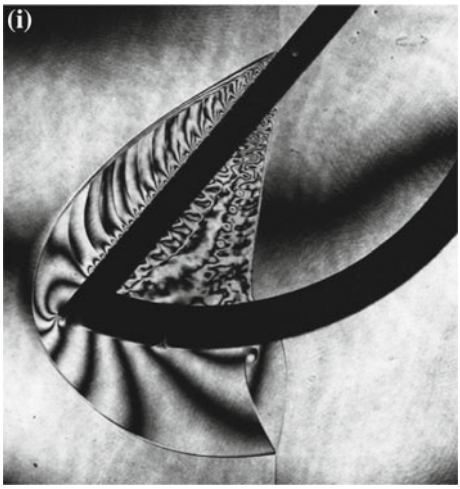

Fig. 2.48 (continued)

2.1.6 Evolution of Shock Reflection from Liquid Wedges

2.1.6.1 Water Wedges

In experiments of shock wave reflections from wedges, shock wave researchers always argue the effect of a surface roughness of wedges on the critical transition angles. It was, therefore, a motivation of shock wave reflection from water wedges. A water wedge is formed by filling water in a tilted low pressure channel of a shock tube seen in Fig. 2.49. The shock wave reflection from the water wedge is visualized in double exposure holographic interferometry (Miyoshi 1987).

A 240 mm diameter and 30 mm wide circular stainless steel test section was constructed for investigating shock wave reflection from water wedges. The test section was and connected to a 30 mm × 40 mm shock tube. The entire shock tube and the circular test section was rotated at an angle ranging from 0° up to 60° keeping the test section at the center of rotation. Water was filled and the whole shock tube was rotated at a required angle θ_w. The water wedge surface was kept perfectly flat. However, due to the surface tension in water, the water touched on the side window glasses at the wet angle forming a meniscus. The locally curved water surface working as a lens and broadened the shadow of the water surface. The pressure in the test section was reduced to the pressure slightly higher than water vapor pressure and then filled water slowly, and thereafter recovered to the desired test pressure level. Then the meniscus effect was minimized.

As the sound speed in water is much faster than that of the IS, the forward running wave is observed, in the wide range of Ms, ahead of the IS. However, the component of the IS along the water wedge surface is $u_s/\cos\theta_w$ where u_s is shock wave speed. Then, if $u_s/\cos\theta_w = a_{water}$ is valid where a_{water} is the sound speed in

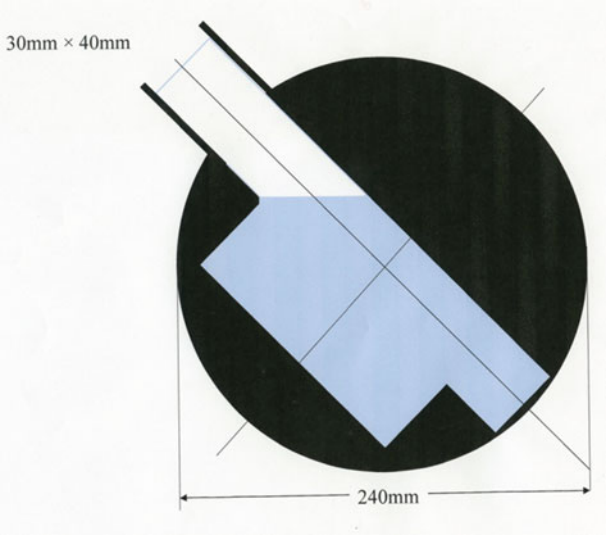

Fig. 2.49 Test section of water wedge (Miyoshi 1987)

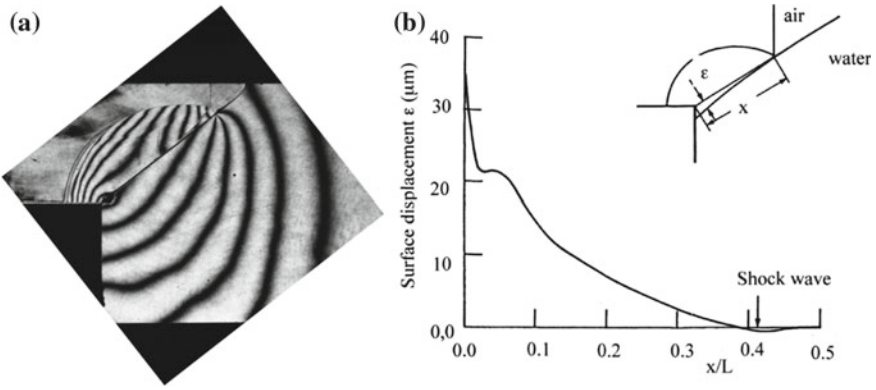

Fig. 2.50 Shock wave reflection from a water wedge for Ms = 1.666, in air at 650 hPa 294.5 K, θ_w = 37.5°: **a** #87051303; **b** deformation of water surface corresponding to (**a**) (Miyoshi 1987)

water, the precursory wave merges with the shock wave in air. Figure 2.50a shows the reflection of a shock wave of Ms = 1.67 from a 37.5° water wedge. Figure 2.50b shows a result from a numerical simulation of this experiment in which a in house code based on the TVD scheme is used (Itoh 1986). The deformation of the water wedge surface due to the shock wave loading was simulated and was maximal at the foot of the shock wave on the water wedge. Although the contact point is a singular spot, the degree of the maximal deformation predicted numerically is presumably unphysical. The deformation at the contact point would be at most about 20 μm.

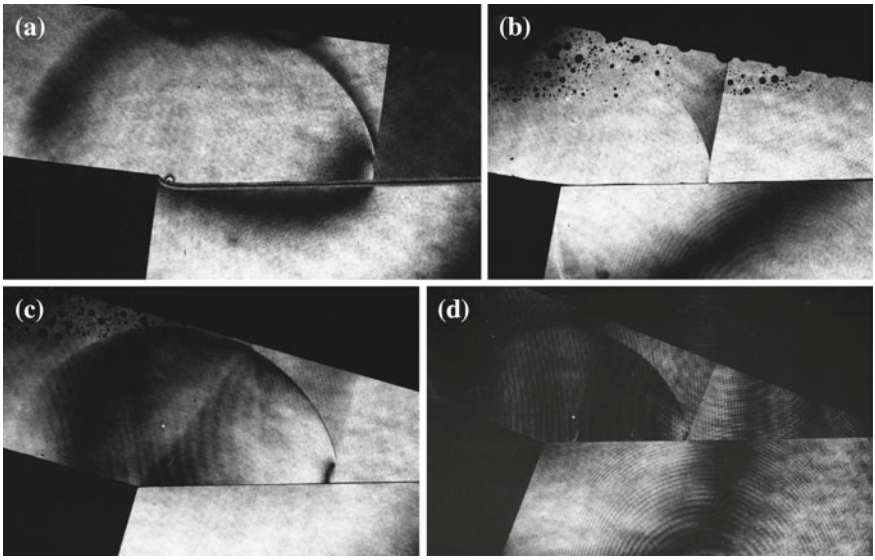

Fig. 2.51 Evolution of weak reflected shock wave over water wedges for Ms = 1.1 in air at 1013 hPa, 287.2 K: **a** #87041601, Ms = 1.148, $\theta_w = 8°$; **b** #87041602, Ms = 1.148, $\theta_w = 12°$; **c** #87041603, Ms = 1.088, $\theta_w = 17°$; **d** #87041604, Ms = 1.056, $\theta_w = 22°$

Figure 2.51 shows evolution of weak shock wave reflections over relatively shallow water wedge angles ranging from $\theta_w = 8°$ to $\theta_w = 22°$. Fringes are generated in water due to the change in phase angles during the double exposures and are converted to density variations by using the formulation given in the Chap. 1. Among quantitative optical flow visualization methods, the double exposure holographic interferometry can record only the change in phase angles during the double exposure and is insensitive to inhomogeneity of the medium or slow moving convective flows in the medium. Then the double exposure holographic interferometry is very suited for underwater shock wave experiments.

The test gas was ambient air and the test water was degassed distilled water. After shock tube runs, tested water was shattered and spread inside the shock tube. Then the water wedge experiments were not necessarily pleasant ones because it was a time wasting work to clean the inside the shock tube and to check the valve ports and pressure transducers.

Figure 2.52 shows the evolution of a weak shock wave reflection over moderately tilted and steeply tilted water wedges of $\theta_w = 30°$ to $\theta_w = 46°$. The transition occurred at an angle between $\theta_w = 30°$ as seen in Fig. 2.52c and $\theta_w = 36°$ as seen in Fig. 2.52c, d.

Figure 2.53a–h shows the evolution of reflected shock waves over water wedges from $\theta_w = 30°$ to $\theta_w = 50°$ for Ms = 1.77 in air at 650 hPa, 294.5 K. Disturbances created by the IS propagate along the water surface at the speed of Ms/cos θ_w. Then for shallow wedge angles in Fig. 2.53a, b, the disturbances propagate at subsonic speed to the the sound speed in water. Then a sonic wave appears ahead of the IS.

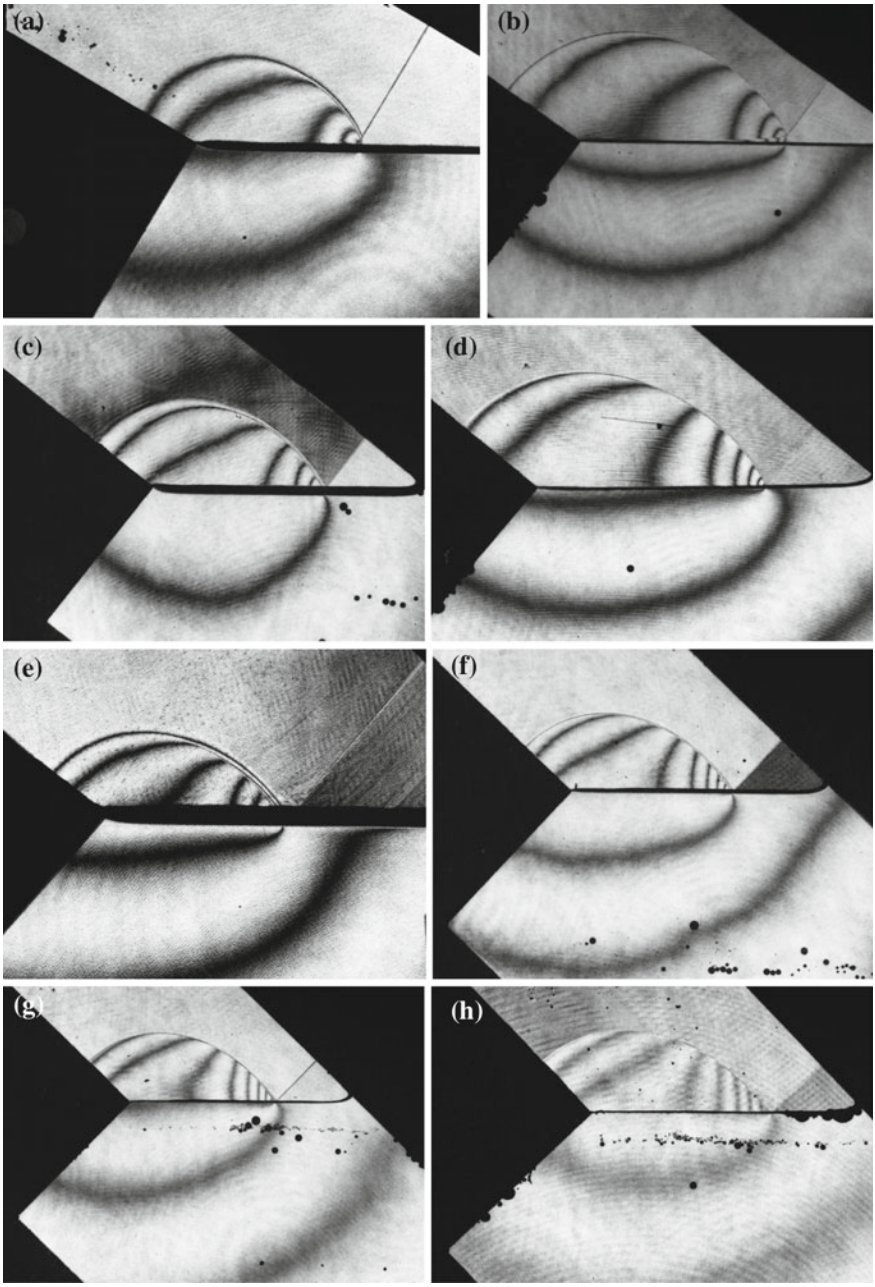

Fig. 2.52 Evolution of reflected shock wave over water wedge for Ms = 1.25 in atmospheric air at 298.0 K: **a** #87070804, Ms = 1.270, $\theta_w = 30°$; **b** #87061522 l Ms = 1.256, $\theta_w = 37.5°$; **c** #87061606, Ms = 1.243, $\theta_w = 37.5°$; **d** #87061523, Ms = 1.261, $\theta_w = 40.0°$; **e** #87070711, Ms = 1.277, $\theta_w = 40.0°$; **f** #87061601, Ms = 1.214, $\theta_w = 43.0°$; **g** #87061602, Ms = 1.214, $\theta_w = 44.0°$; **h** #87061604, Ms = 1.267, $\theta_w = 46.0°$

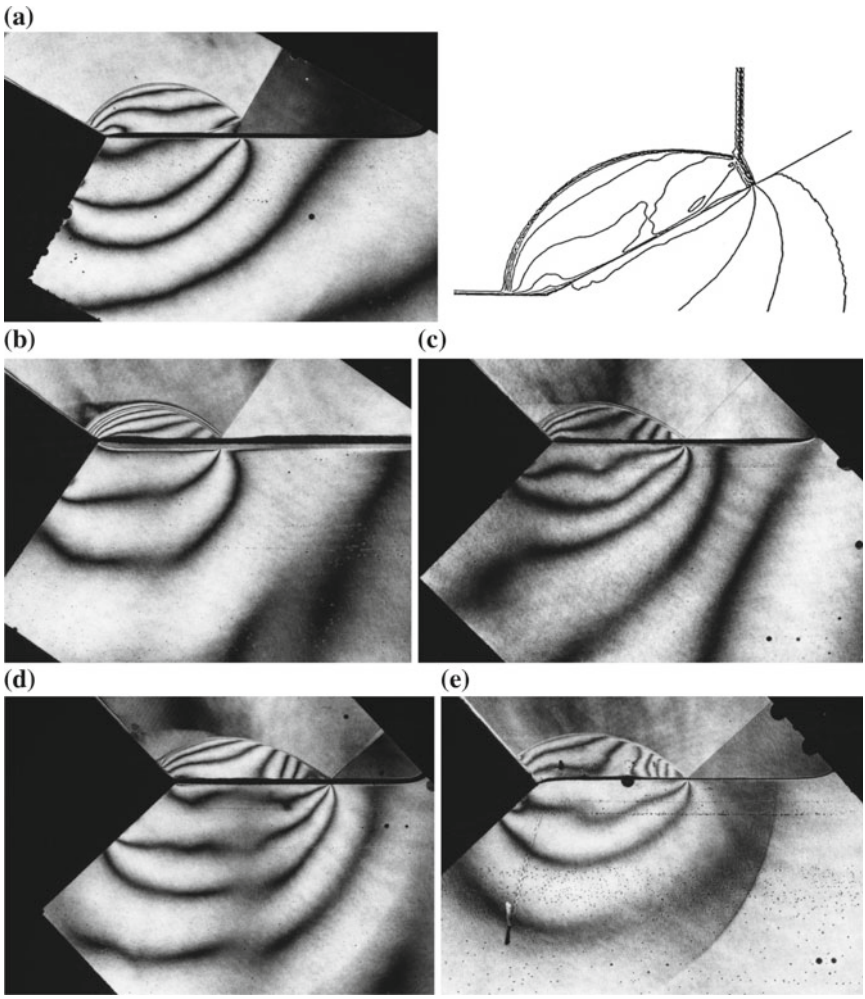

Fig. 2.53 Evolution of reflected shock wave over water wedge for Ms = 1.77 in air at 650 hPa, 294.5 K: **a** #87050705, Ms = 1.790, $\theta_w = 30°$ and numerical simulation; **b** #87050706, Ms = 1.775, $\theta_w = 35°$; **c** #87050708, Ms = 1.783, $\theta_w = 45°$; **d** #87050709, Ms = 1.778, $\theta_w = 47°$; e #87050802 343 ms Ms = 1.778, $\theta_w = 48°$; f #87051203, Ms = 1.665, $\theta_w = 49°$; **g** #87051204, Ms = 1.791, $\theta_w = 50°$; **h** #87050805, Ms = 1.787, $\theta_w = 52°$ and numerical simulation, (Miyoshi 1987)

A density distribution is obtained by solving numerically the Euler equations and displayed as a numerical fringe distribution. The numerical density is adjusted to be the same as an experimental one as shown in Fig. 2.53a. The numerical density distribution agreed well with the experimental one. Figure 2.53c shows a RR. At the foot of the IS, fringes are concentration which indicate a local pressure

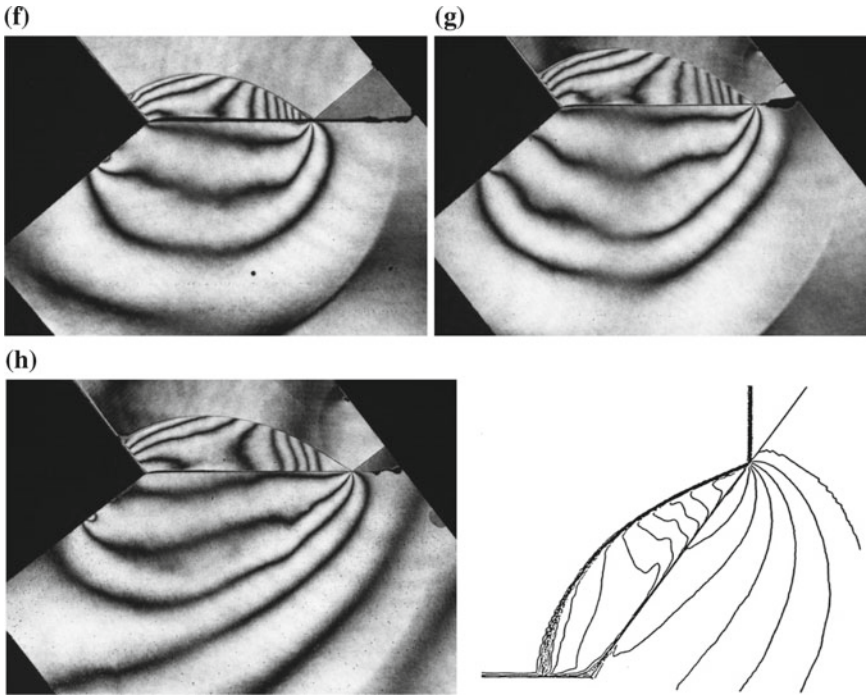

Fig. 2.53 (continued)

enhancement. Increasing θ_w, precursory wavelets form a train of compression waves and fringes are concentrated at the foot of the IS.

In Fig. 2.53d–g, a discontinuous shadow propagates at sonic speed in water. The discontinuous shadow is expected to merge with the foot of the IS, when When $\cos\theta_w = u_s/a_{water}$ where u_s and a_{water} are the shock speed in air and the sound speed in water. In Fig. 2.53h an experiment and its numerical simulation are compared for Ms = 1.787 and the wedge angle of $\theta_w = 52°$. The reflection pattern is a RR. The fringe patterns in the simulation and the interferogram agree well. The fringes in water are concentrating at the foot of the IS.

Figure 2.54a shows the evolutions of reflected shock wave propagations for Ms = 2.20 over water wedge of $\theta_w = 0.0°$. The SL is faintly visible. The IS is perfectly perpendicular to the water surface. The reflection pattern is a vNMR. In Fig. 2.54b, the reflection pattern is a SMR. In Fig. 2.54c, the fringes in water concentrate at the foot of the IS. As the shape of the RS are straight in the vicinity of the TP, which indicates that the reflection pattern is TMR. Figure 2.54d is its enlargement and the reflection pattern is a RR. With increase in the θ_w, in Fig. 2.54e, f, the reflection patterns are SPRR. It should be noticed that precursory waves are observed ahead of the foot of the IS.

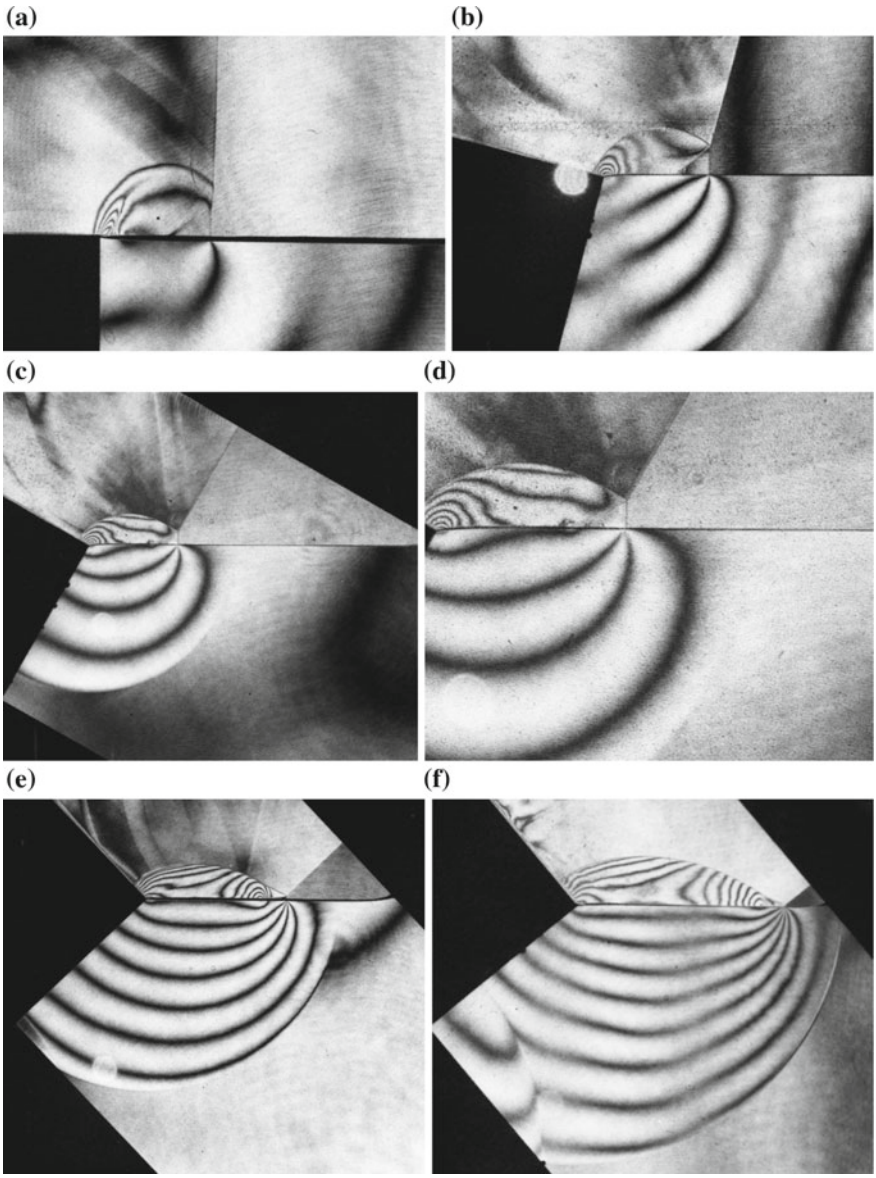

Fig. 2.54 Reflected shock wave over water wedge for Ms = 2.25 in air at 710 hPa, 294.7 K: **a** #85061901, Ms = 2.214, θ_w = 0,0°; **b** #85061705, Ms = 2.211, 14.3°, SMR; **c** #85061704, Ms = 2.217, θ_w = 29.8°, SMR; **d** enlargement of **c**; **e** #85061701, Ms = 2.217, θ_w = 46.2°, SuRR; **f** #85061407, Ms = 2.308, θ_w = 50.0°, SPRR

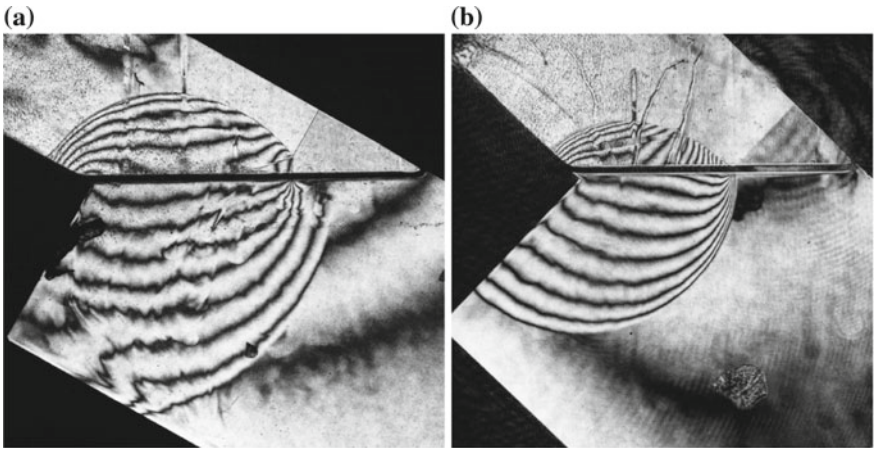

Fig. 2.55 Reflected shock wave from Aflud E10 wedge: **a** #87051810, for Ms = 1.262 in air/Aflut E10 mixture at atmospheric pressure, 289.2 K, $\theta_w = 35.0°$; **b** #87051907, Ms = 1.450 in air/Aflut E10 mixture at atmospheric pressure, 294.0 K, $\theta_w = 44.0°$

2.1.6.2 Retrograde Liquid Wedges

There are numerous combinations of gases and safe and non-toxic liquids for forming a gas/liquid interface. A retrograde liquid Aflud E10 has a retrograde medium having a peculiar character of creating condensation shock waves when the medium is exposed to expansion waves. The liquid has a high vapor pressure, stable, and non-toxic. Just for reference, a series of experiments was conducted by filling the Aflut E10 in the test section. Two images are presented here just for reference in air/Aflut E10 mixture at atmospheric pressure. In Fig. 2.55a, the reflection pattern is a SMR from the liquids wedge of $\theta_w = 35.0°$ for Ms = 1.26 in air-AfludE10 mixture and a precursory wave propagates in front of the MS. In Fig. 2.55b, the reflection pattern is a SPRR from the liquids wedge of $\theta_w = 44.0°$ for Ms = 1.45 in air-AfludE10 mixture.

2.1.7 Evolution of Shock Wave Reflection from Cones

2.1.7.1 Cones

Shock wave reflections from a wedge and a cone are self-similar phenomena. However, the reflections from cones are unique because the reflection pattern is solely affected by the cone angle and the distance from the leading edge to the foot of the shock wave. Then the cone size never affects the reflection process until it becomes the shock tube width. Figure 2.56 shows reflected shock wave

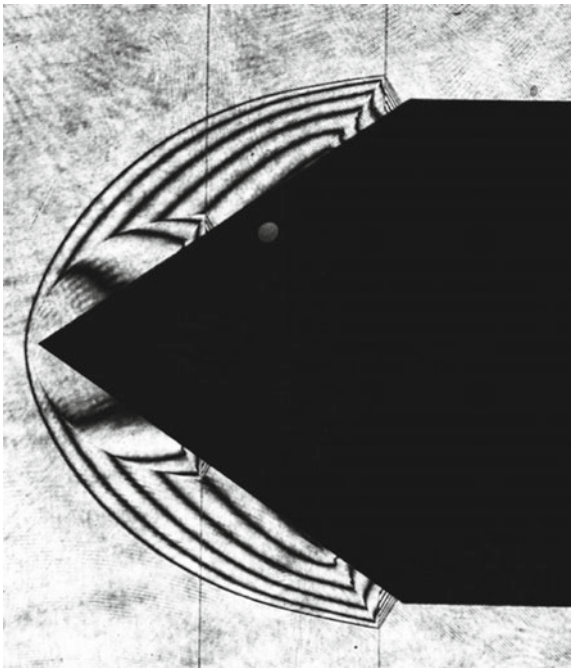

Fig. 2.56 Double exposure interferogram of shock wave reflection from a cone of apex angle is 69.2°: #98120304, Ms = 2.330, 144 hPa 292.9 K, in Argon (Kosugi 2000)

propagating over an apex angle 69.2° cone of 60 mm base diameter for Ms = 2.33 in argon. The cone was made of brass and supported rigidly from its base and was installed in the 100 mm × 180 mm diaphragm-less shock tube. This shock tube can accommodate large cones. The visualization was performed by the double exposure interferometry at 60 μs double pulse time interval. Hence two images of shock wave reflections were recorded in one hologram. When testing shock wave reflection over wedges installed in the 100 mm × 180 mm shock tube, shock wave motions along the wedge surface were affected by the presence of a boundary layer developing along the wedge surface as discussed, for example, in Fig. 2.21. The evolved flows at the foot of the IS is governed by the boundary layer displacement thickness depending on the distance from the leading edge and the shock tube sidewalls. The flows over cones are also affected by the boundary layer developing along the cone surface.

In Fig. 2.56, the superimposed reflected shock waves looked slightly different. The shock wave reflection over a cone is not necessarily self-similar.

It was decided to experimentally determine the θ_{crit} over cones. However, it was impossible to conduct experiments by continuously varying the cone apex angle. Therefore, a series of experiments were carried out in 1975 by using 50 pieces of cone models having 25 mm base diameter and apex angles ranged from 7.5° to 150° at every 2.5° step (Takayama and Sekiguchi 1977). At first, the cone models tested in a 40 mm × 80 mm conventional shock tube. In 1989, to refine the previous experiment, 88 pieces of new cone models made of brass having 25 mm base

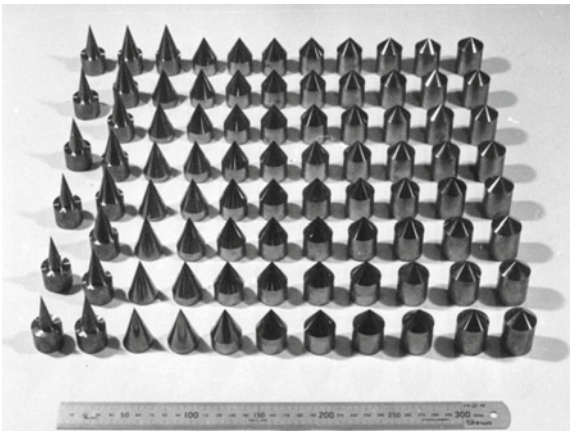

Fig. 2.57 Cone models (Yang et al. 1996)

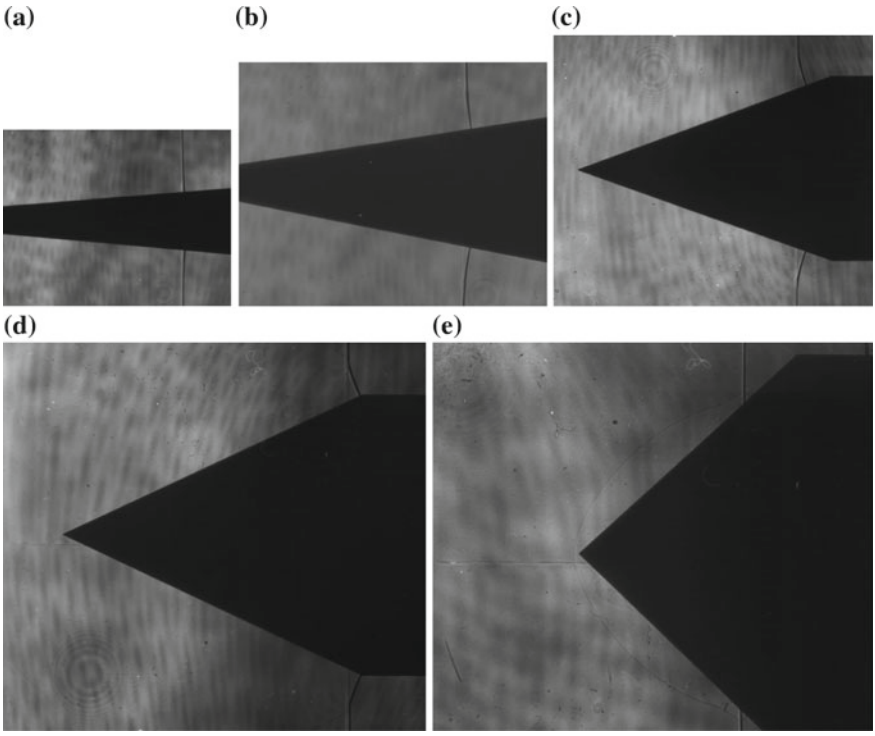

Fig. 2.58 Shock wave reflection from a cone at Ms = 1.20 in air, α apex angle of cone: **a** #75120407, $\alpha = 10°$; **b** #75120406, $\alpha = 20°$; **c** #75120404, $\alpha = 40°$; **d** #75120401 $\alpha = 55°$; **e** #75120103, $\alpha = 87.5°$

diameters and their apex angles ranging from 10° to 120° at every 2° steps were manufactured. Figure 2.57 shows the cone models used in 1989 experiments.

Four models were installed in a 60 mm × 150 mm conventional shock tube's test section and the reflection patterns were observed simultaneously. Figure 2.58 shows selected results: In axial symmetric flows, the images of IS and MS were overlapped but it was still possible to identify the position of the TP. The triple point trajectory angle χ is defined by $\tan\chi = h/L$ where h is the height of the SL and L is the distance between the cone apex and the foot of MS. The extrapolation of the angle of the trajectory abled to estimate θ_{crit} as the angle at which χ became zero.

Figure 2.59 summarizes the 1975 experiments. The triple point positions were plotted against the semi-apex angle of cones θ_c (Takayama and Sekiguchi 1977). Although time consuming and laborious εξπεριμεντσ, τηε ϖισυαλιζατιονσ ωασ περφορμεδ βψ υσινγ διρεχτ σηαδοωγραπησ. Τηε ορδινατε δενοτεσ τηε trajectory angle $\chi - \theta_c$ in degree and the abscissa denotes half apex angle of cones θ_c in degree. Filled circles denote the measured results for Ms ranging from 1.04 to 3.09. The results of Bryson and Gross (1961) agreed well with the present experiments.

In January 1989, experiments by using the cones shown in Fig. 2.57 were carried out by installing four cone models in the 60 mm × 150 mm diaphragm-less shock tube. Experiments of were repeated four times. Figure 2.60 shows results for Ms = 1.20. Figure 2.60a shows four cones of half apex angles θ_c from 39° to 42°. The reflection patterns are SMR. Figure 2.60b shows four cones of θ_c = 51°–54°. The reflection patterns are also SMR, whereas in Fig. 2.60c θ_c is between 47.5° and 49°, the reflection patterns are RR.

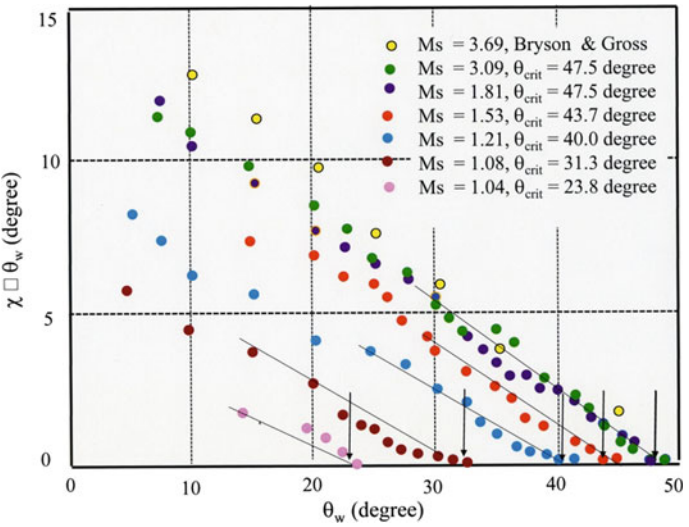

Fig. 2.59 Triple point trajectories, summary of Fig. 2.57

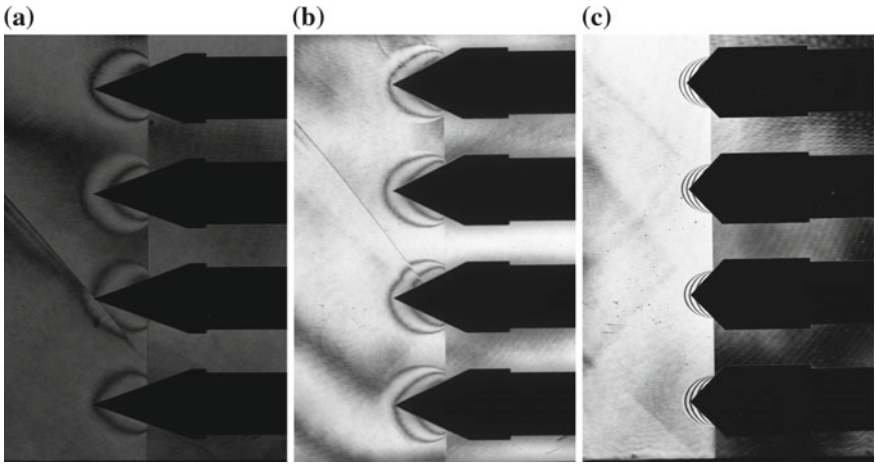

Fig. 2.60 Shock wave reflection from cones at Ms = 1.20 in atmospheric air at 291.8 K: **a** #89011304, θ_c = 19.5–21°; **b** #89011703, θ_c = 25.5–27°; **c** #89012414, θ_c = 47.5–49°

Figure 2.61a–d shows shock wave reflection for Ms = 1.17 in air from cone angles θ_c between 12° and 15°, θ_c between 21° and 24°, θ_c between 25° and 28°, θ_c between 35° and 38°, respectively. Their reflection patterns are SMR. In Fig. 2.61e, cone angles are θ_c between 43° and 46°, causing a reflection pattern RR. The transition occurred at about θ_c 40°. A question arises whether or not delayed transition may occur in the shock wave reflection from cones, similar to that witnessed in shock wave reflection from flat wedges.

In order to reply this question, cone experiments were repeated in the 100 mm × 180 mm diaphragm-less shock tube in 1995. Figure 2.62a–c shows sequential observation of shock wave reflections for Ms ≈ 1.4 in air and a cone angle of 10°. The reflection pattern is a SMR. Figure 2.62d–f, shows sequential images of shock waves obtained for Ms = 1.4 in air and a cone angle of θ_c = 15°. The reflected shock wave pattern is a SMR.

2.1.7.2 Evolution of Shock Wave Reflection from Cones Connected to Hollow Cylinders

A cone of apex angle 10° was connected to the rear part of a hollow cylinder. In order to investigate the effect of the shape of leading edge, a cylinder-cone combination having 8 mm diameter hollow cylinder, 1 mm wall thickness, and 40 mm in length was installed in the test section of the 100 mm × 180 mm diaphragm-less shock tube. In Fig. 2.63, the evolution of transmission and reflection of a shock wave for Ms = 1.40 was shown. The central part of the IS was transmitted through the hollow cylinder. The reflected shock wave is, therefore, weak and propagates along the 10° inclined conical wall. The reflected pattern is a SMR. Figure 2.63f

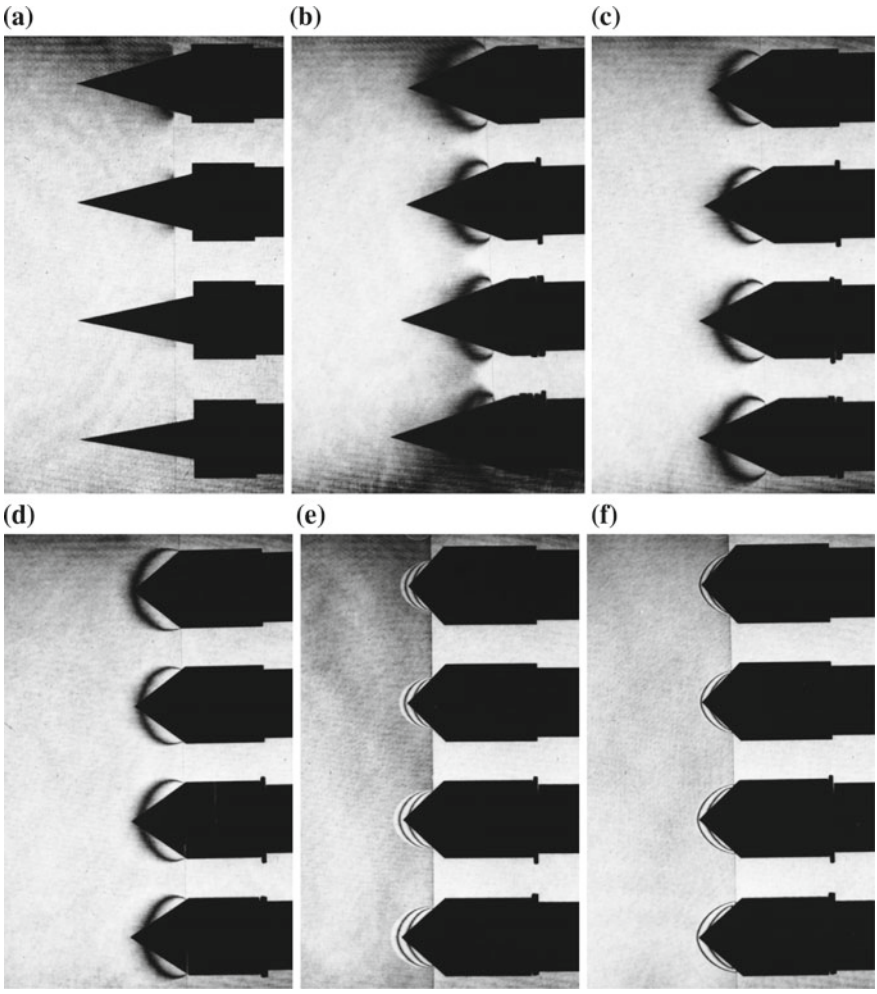

Fig. 2.61 Shock wave reflection from cones at Ms = 1.17 in atmospheric air at 290.0 K: **a** #94110503, Ms = 1.166, θ_c= 12°–15°; **b** #94110507, Ms = 1.177, θ_c = 21°–24°; **c** #94110601, Ms = 1.168, θ_c = 25°–28°; **d** #94110605, Ms = 1.168, θ_c = 35°–38°; **e** #94110609, Ms = 1.168, θ_c = 43°–46°; **f** #94110610, Ms = 1.168, θ_c = 46°–49°

was taken at the elapsed time 1060 μs and the transmitted shock wave was reflected from the bottom of the hollow cylinder and already released from the opening of the hollow cylinder. The resulting jet flow was ejected. Figure 2.64 shows evolution of reflected shock wave interaction with a 20° cone and 13 mm diameter hollow cylinder combination for Ms = 1.40. The resulted reflection pattern is a SMR.

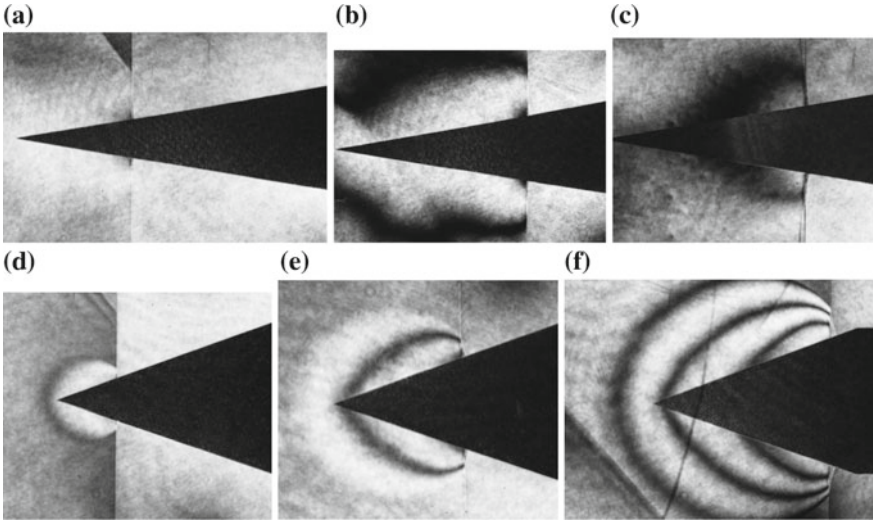

Fig. 2.62 Reflected shock wave pattern from a cone in air at 700 hPa, 290.3 K: **a** #95040601, 880 μs from trigger point, Ms = 1.389, $\theta_c = 10°$; **b** #95040602, 850 μs, Ms = 1.408, $\theta_c = 10°$; **c** #95040501, 960 μs, Ms = 1.404, $\theta_c = 10°$; **d** #95041102, 800 μs, Ms = 1.384, $\theta_c = 15°$; **e** #95041103, 900 μs, Ms = 1.411, $\theta_c = 15°$; **f** #95041105, 1000 μs, Ms = 1.400, $\theta_c = 15°$

2.1.7.3 Heat Transfer from Cones

Saito et al. (2004) distributed 16 pieces of 1.5 mm wide, 58 μm thick, and 90 mm long platinum thin film heat transfer gauges evenly along the circumference of a 40 mm diameter cylinder and measured time variations of heat flux distributions over the cylinder installed in the 100 mm × 180 mm diaphragm-less shock tube.

In order to investigate the transition of a reflected shock wave over a cone, platinum heat transfer gauges were distributed along the cone surface. Figure 2.65a shows a cone model along which 8 pieces of 1.0 mm wide, 58 μm thick, and 5.0 mm long platinum heat transfer gauges were distributed. Figure 2.65b shows the positions of the gauges and the geometry of the cone model; its base diameter is 50 mm and its apex angle α is 86°. The cone was made of ceramics, Photoveel (Sumikin Ceramics and Quartz Co. Ltd. Japan). The cone model was installed in the test section of the 100 mm × 180 mm diaphragm-less shock tube. Experiments were conducted for Ms = 2.38 in air and Re = 3×10^4 per characteristic length of 10 mm.

Figure 2.66 shows sequential interferograms. As the *OB* path lengths are so short that no dark fringes are observed and at 4 mm from the leading edge as shown in Fig. 2.66a, the reflection pattern is hardly identified but away from the leading edge at 11.6 mm. 15.3 and 23.5 mm in Fig. 2.66b–d, respectively, the reflection pattern is a TMR.

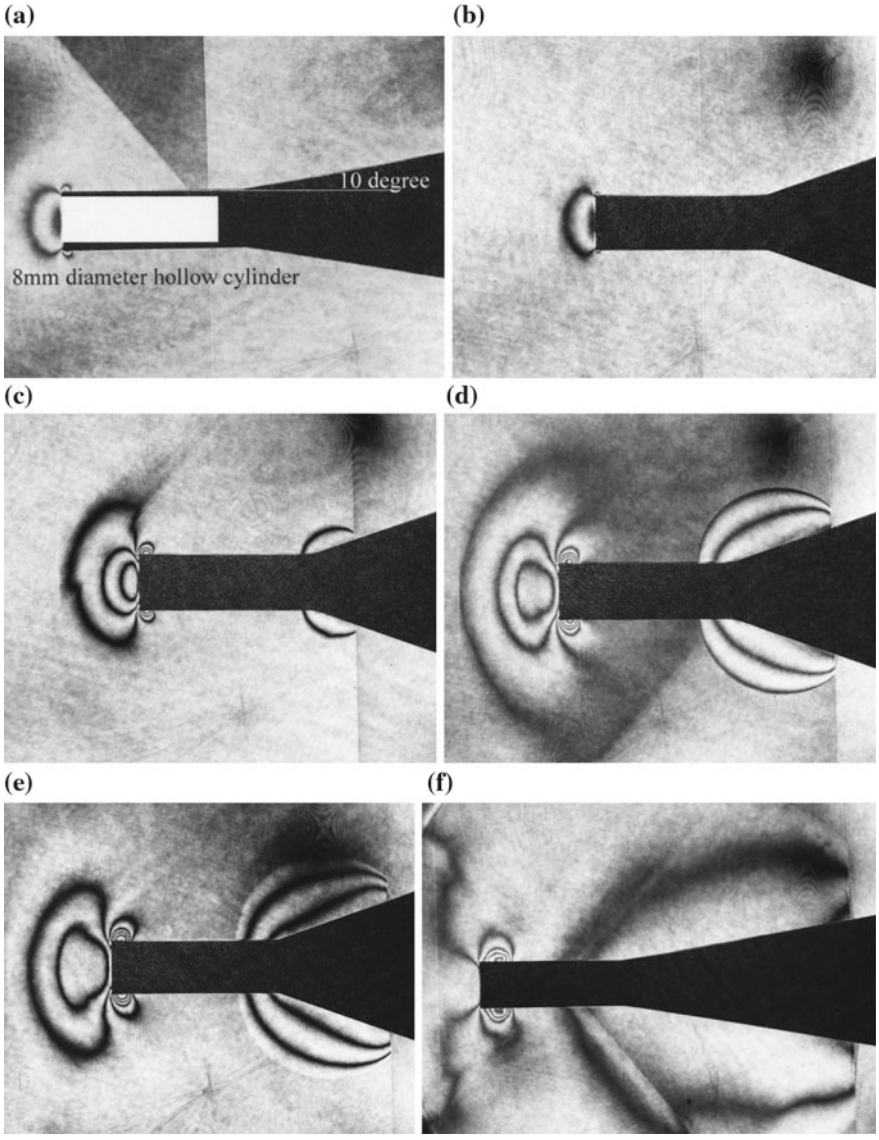

Fig. 2.63 Evolution of shock wave reflection from a 10° cone connected to a 8 mm inner diameter hollow cylinder for Ms = 1.40 in air at 700 hPa, 294.5 K: #95041404, 70 μs from trigger point, Ms = 1.380; **b** #95041409, 160 μs, Ms = 1.406; **c** #95041405, 200 μs, Ms = 1.409; **d** #95041406, 230 μs, Ms = 1.414; **e** #95041407, 250 μs Ms = 1.401; **f** #95041402, 1060 μs, Ms = 1.408

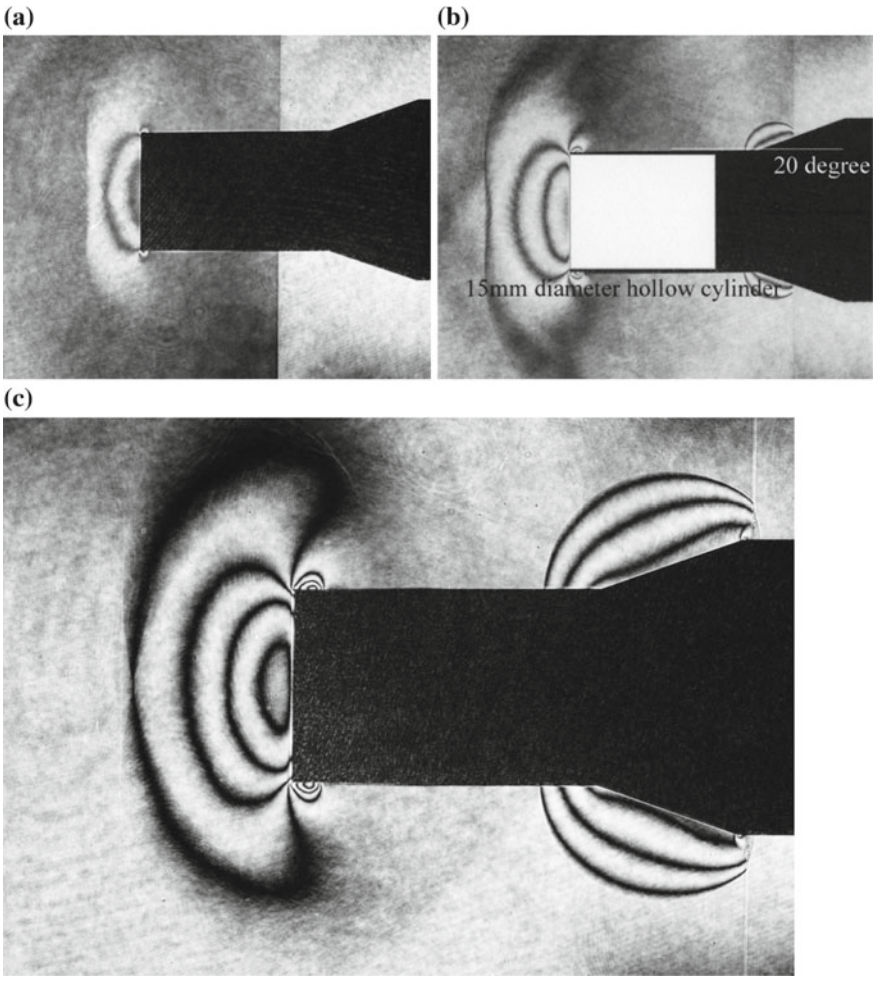

Fig. 2.64 Evolution of shock wave reflection from a 20° cone connected to a 13 mm hollow inner diameter hollow cylinder for Ms = 1.40 in air at 700 hPa, 294.5 K; **a** #95040703, 60 μs, Ms = 1.404; **b** #95041003, 100 μs, Ms = 1.400; **c** #95040705, 180 μs, Ms = 1.416

Figure 2.67a–f shows time variations of heat flux measured by platinum thin film heat transfer gauges distributed on the cone surface as shown in Fig. 2.65b: **a** 6.8 mm; **b** 10.4 mm; **c** 13.7 mm; **d** 17.0 mm; **e** 20.5 mm; **f** 23.6 mm. Dotted lines denote numerical results using in house code solving a Navier-Stokes equation. The ordinate denotes heat flux in MW/m^2 and the abscissa denotes the elapsed time in μs.

The scheme employed the following assumptions: $\gamma = 1.4$, the Sutherland formula for viscosity and heat conduction coefficients; Non-slip and isothermal

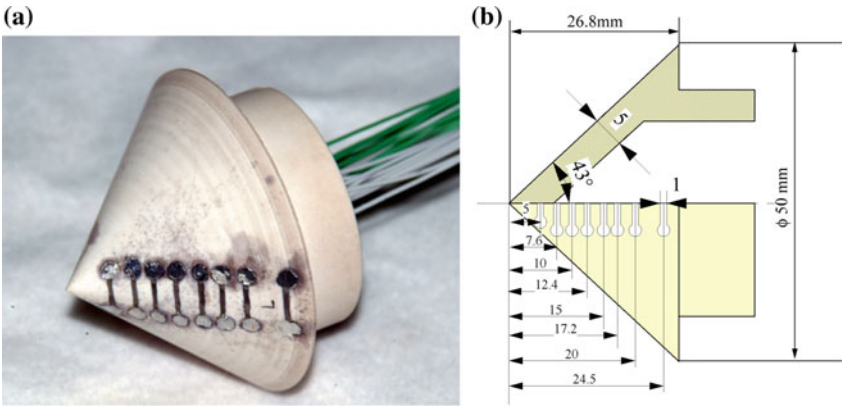

Fig. 2.65 Cone model: **a** the attachment of platinum heat transfer gauge; **b** cross section (Kuribayashi et al. 2007)

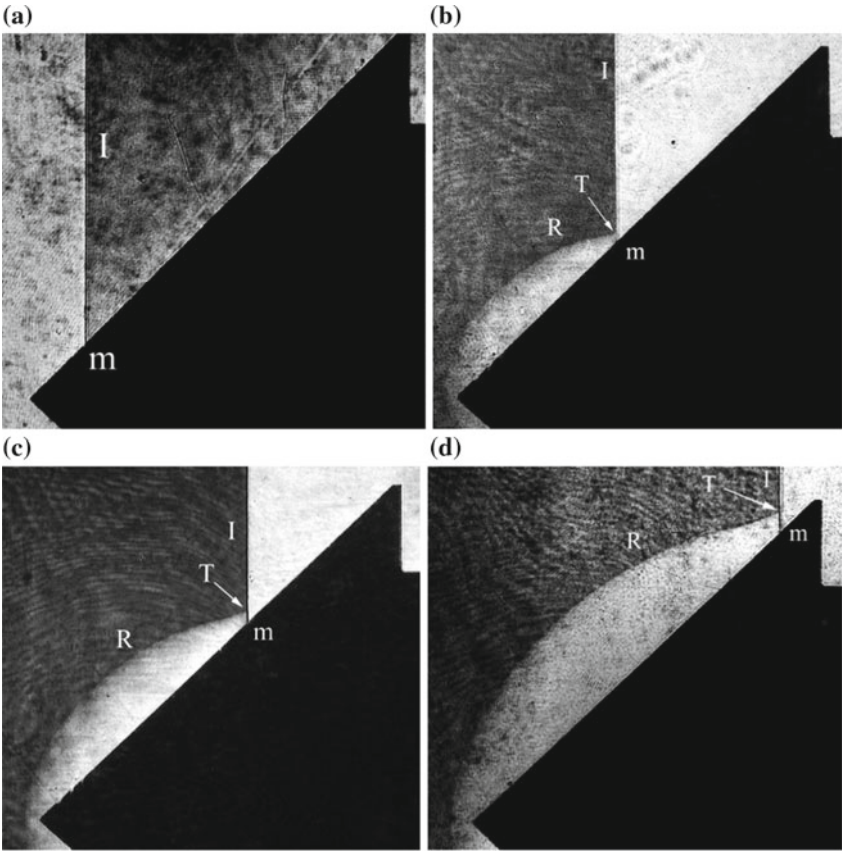

Fig. 2.66 Evolution of shock wave transition over the cone: location of the shock waves at: **a** 4.0 mm; **b** 11.6 mm; **c** 15.3 mm; **d** 23.5 mm

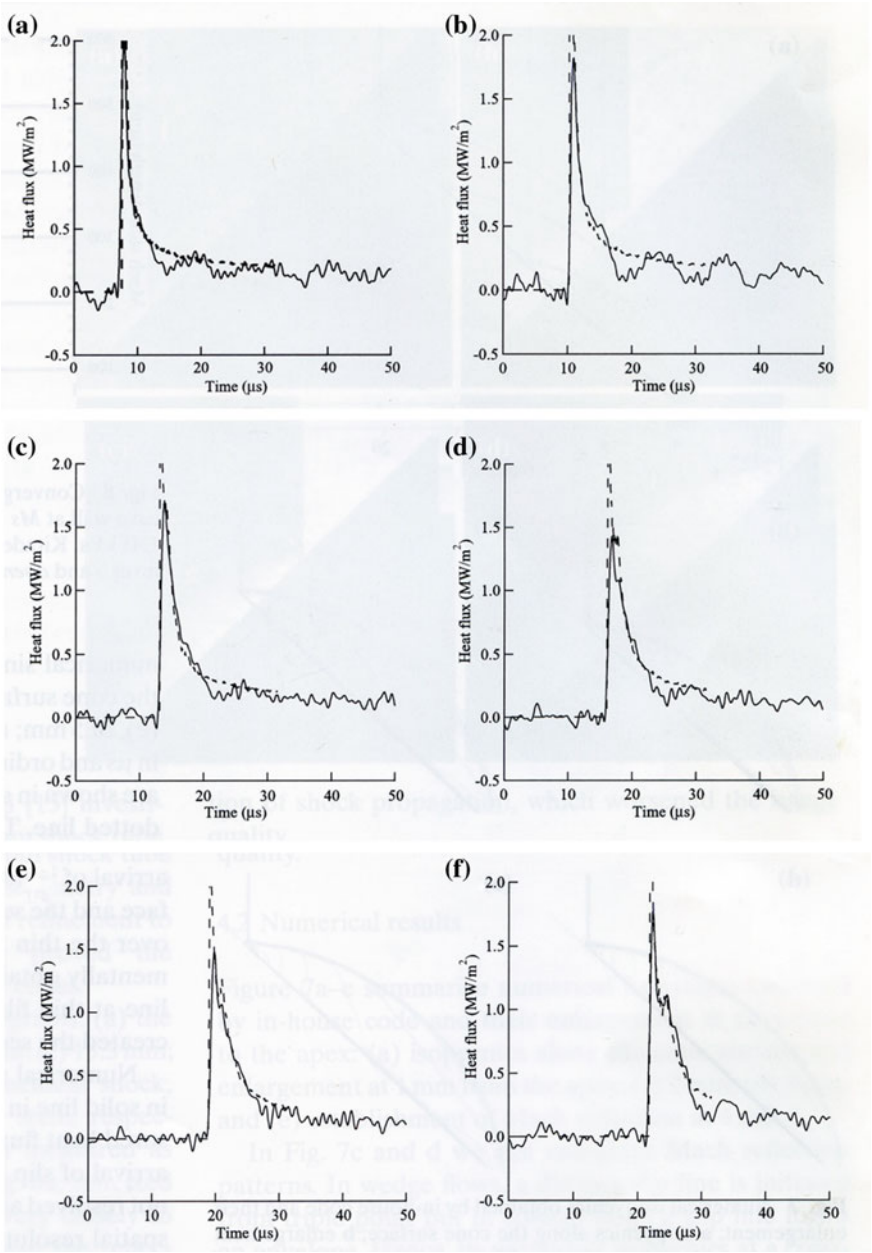

Fig. 2.67 Time variation of heat flux obtained by platinum thin film heat flux gauges shown in Fig. 2.59. Solid lines denote measured results and dotted lines denote numerical simulation: **a** 6.8 mm; **b** 10.4 mm; **c** 13.7 mm; **d** 17.0 mm; **e** 20.5 mm; **f** 23.6 mm (Saito et al. 2004)

boundary condition; Imposing quadrilateral unstructured grids. The finest grid size was a 1.5 μm around the cone surfaces. Numerical results agreed well with experimental findings.

It is clear from Fig. 2.67a that upon the arrival of shock wave, the heat flux reaches a maximum value and thereafter it decreases monotonously to appropriate steady value. Such behavior is typical to a RR reflection pattern. On the contrary, as seen in Fig. 2.67b–f, the heat flux changes its monotonous decrease in the middle. In Fig. 2.67e, f, this trend becomes eminent and the reflection pattern is SMR accompanying SL behind MS, which indicates the appearance of the delayed transition.

2.1.7.4 Effect of Initial Angle on Transition

To assure the delayed transitions over cones, 50 mm diameter cones were installed in the test section of the 100 mm × 180 mm diaphragm-less shock tube. Figure 2.68 shows a TMR over a cone whose apex angle is 34.6°. As the spatial resolution of high speed imaging was not necessarily high, it was decided to conduct double exposures at interval of 120 μs and compare directly two images recorded in one interferogram. In conclusion, the two resulting reflection never showed self-similar patterns. In Fig. 2.68e, $\theta_c = 44.0°$ the reflection pattern is a RR near the apex and transits to a TMR close to the end. In Fig. 2.68f, at $\theta_c = 49°$, the reflection pattern is a RR near the apex and transits to a DMR close to the end. In Fig. 2.68g, at $\theta_c = 50.2°$, the reflection pattern is a RR all the way along the cone surface.

The delayed transition does occur along cone surface. The ratio of the cross section of the outer boundary of the boundary layer displacement thickness to the cross section of the cones is significantly large in the vicinity of the apex but in the case of the wedge the ratio is not large in the vicinity of the leading edge. The departure of the reflected shock wave from a self-similar pattern occurs much significantly over the cones than that occurs over the wedges.

Figure 2.69 summarizes the triple point trajectories on cone surfaces having apex angle of 34.6°, 38.6°, 44.0°, 49.0°, and 50.2° at the initial pressure of 144 hPa. The ordinate denotes the TP height in mm and the abscissa the distance from the apex in mm. Dark blue, red, green, pink, and black circles denote the apex angles of 34.6°, 38.6°, 44.0°, 49.0°, and 50.2, respectively. The solid lines denote numerical results obtained by solving the Navier-Stokes Equation with fine mesh zoning (Kosugi 2000). The numerical results agree well with the experimental findings. The intersection of the solid lines with x-axis gives the length at which the transition occurs, which is the delayed transition distance as defined x_{int}. With increasing θ_c, x_{int} increases. At the cone apex angle of $\theta_c = 50.2°$ which exceeds the critical transition angle, a RR appears. Filled circles and open circles denote trajectories of upper and lower sides of the individual cone surfaces, respectively.

Figure 2.70 shows the relationship between the delayed transition distance and initial pressure for Ms = 2.327 in air. The ordinate denotes the delayed transition

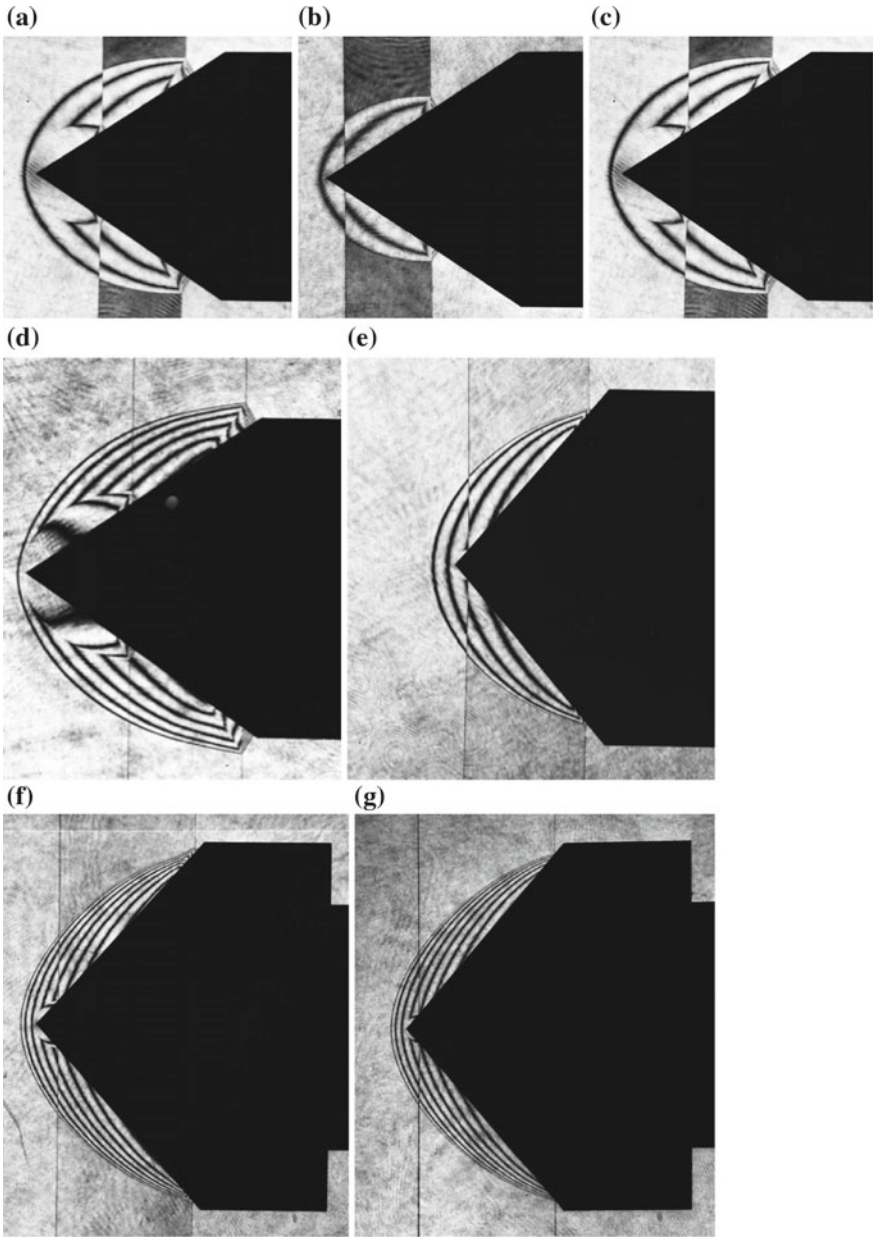

Fig. 2.68 Delayed transition of reflected shock wave over cones for Ms = 2.33 in air at 144 hPa, 293.9 K; **a** #98120103, in Argon $\theta_c = 34.6°$; **b** #98120304, Ms = 2.330 in Argon, $\theta_c = 34.6°$; **c** #98120103, Ms = 2.330 in Argon, $\theta_c = 34.6°$; **d** #98120304, Ms = 2.330, $\theta_c = 34.6°$; **e** #98120114, Ms = 2.326, $\theta_c = 44.0°$; **f** #98121102, Ms = 2.324, $\theta_c = 49.0°$; **g** #98121006, Ms = 2.327, $\theta_c = 50.2°$

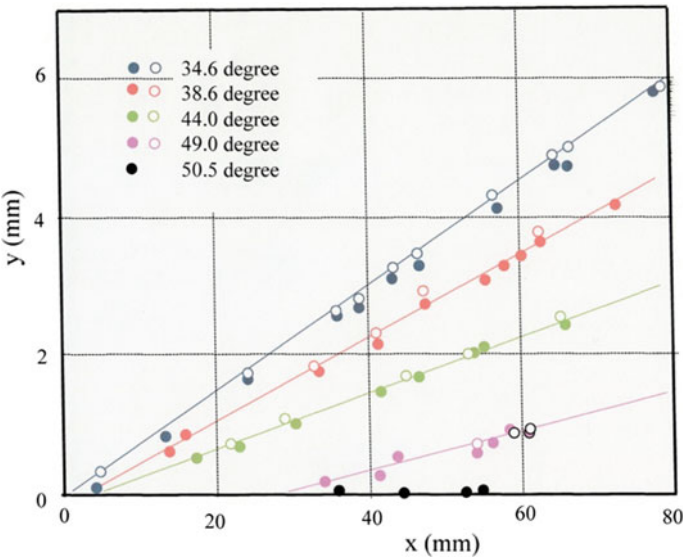

Fig. 2.69 Triple point position for Ms = 2.33 at 144 hPa

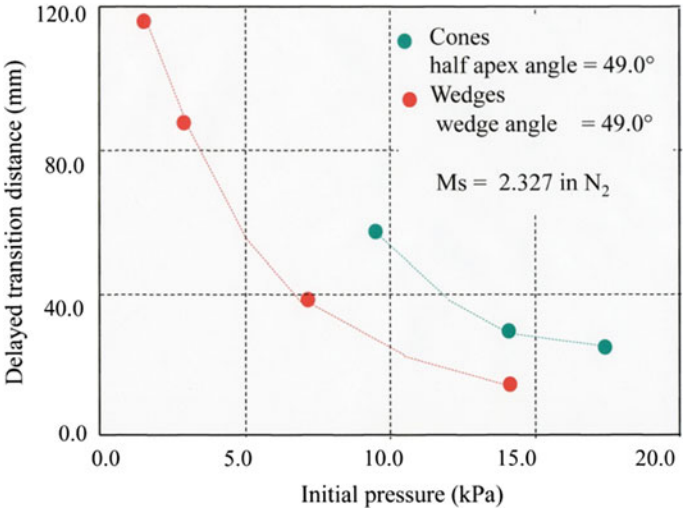

Fig. 2.70 Delayed transition distance x_{int} against initial pressure for Ms = 2.33 (Kitade 2001)

distance x_{int} in mm and the abscissa denotes the initial pressure in kPa. Green filled circles denote cone half apex angle of $\theta_c = 49°$ and red filled circles denote wedge of $\theta_w = 49°$. The delayed transition distance x_{int} increases reversely proportional to the initial pressures and this trend is more significant in cones.

Shock wave researchers often stated that shock tube experiments were not reliable, because the critical transition angles obtained by the experiments conducted under identical initial condition widely varied depending on the shock tube geometry. Figure 2.61 indicates that even if experiments are conducted for identical Ms and Re but in different shock tube geometries, although a MR is observed in a large shock tube, in a small shock tube only a RR is observed.

2.1.8 Tilted Cones

The shock wave reflection from a wedge is a two-dimensional phenomenon and that from a cone is also axial symmetric phenomenon. The shock wave reflection over a skewed wedge is a three-dimensional phenomenon. Similarly to a skewed wedge, the shock wave reflection over a tilted cone is a three-dimensional phenomenon. It is a challenge to quantitatively reconstruct three-dimensional shock wave phenomena by collections of two-dimensional images viewed from various view angles.

In order to quantitatively observe the three-dimensional interaction of a shock wave with a tilted cone interacting with a planar shock wave. Figure 2.71 shows a setup. A cone having the apex angle of 70° and the base diameter of 30 mm was tilted by 20° to the opening of a 230 mm diameter shock tube. The stand-off distance between the shock tube opening to the tip of the cone was 19 mm. The shock wave of Ms = 1.20 is diffracted at the edge of 230 mm diameter shock tube.

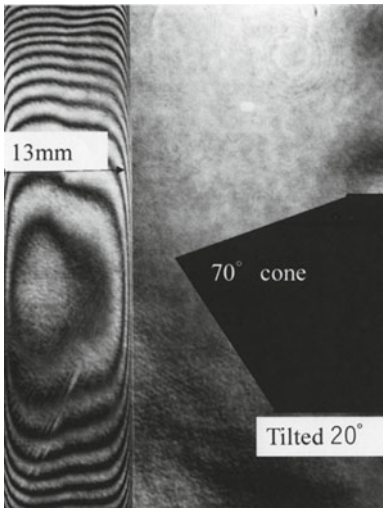

Fig. 2.71 Initial setup. The stand-off distance from the opening to the tip of tilted cone is 19 mm

The transmitted shock wave was planar when impacted the tilted cone. In Fig. 2.71, the planar shock wave reached 13 mm from the opening. Due to the diffraction at the edge of the shock tube opening, the edge part of the transmitted shock wave attenuated. The central part of the transmitted shock wave was unaffected by the diffraction so that Ms was unchanged when the shock wave interacted with the tilted cone. If the image of a three-dimensional interaction of the shock wave and the tilted cone is reconstructed, how can the initiation and the termination of RR and MR be restructures? (Fig. 2.72).

Unlike previous symmetric cone experiments, for example, as seen in Fig. 2.68, the present cone is tilted by 20° and rotated around the shock tube axis. Then the inclination angle of the cone is varied continuously from 10° to 45°.

2.2 Shock Wave Reflection Over Double Wedges

2.2.1 Concave Double Wedges

When a wedge of angle θ_2 is placed on a wedge of angle θ_1 in a staggered arrangement, such a combination of wedges would form, $\theta_1 < \theta_2$, a concave double wedge. On the contrary, when a wedge of angle θ_2 is removed from a wedge of angle θ_1 in a staggered arrangement, the resulting shape of the wedge would form, $\theta_1 > \theta_2$. a convex double wedge. In this case, if the first wedge angle is smaller than the critical transition angle, $\theta_1 1 < \theta_{crit}$, the MR would appear at first, whose MS is reflected from the corner of the second wedge. Depending on the value of $\theta_1 2$, the MS's trajectory angle χ tends to leave from the second wedge surface, $\chi > \theta_{1w}$. Courant and Friedrichs (1948) defined this reflection pattern as a direct Mach reflection, or in short, DiMR, which is locally self-similar. In the case of $\chi = \theta_{1w}$, the TP propagates parallel along the second wedge surface and the slip line SL is also parallel to the wedge surface. Therefore, the reflection pattern is locally unvaried with elapsed time. This pattern is defined as stationary Mach reflection, or in short, StMR. The StMR appears universally in steady flows, for example, in wind tunnel flows, but the presence of StMR is very unique in unsteady shock tube flows.

The SL of the MR on the second wedge surface shown in Fig. 2.73 looks locally parallel to the second wedge surface and would be, within the limitation of the length of the second wedge, parallel up to the end of the second wedge. This image does not warrant a StMR holding. If the second wedge is very long, the TP may either leave away from the wedge surface or approach toward it. When $\chi < \theta_{1w}$, the TP moves toward the second wedge surface. Courant and Friedrichs (1948) defined this reflection pattern as an inverse Mach reflection, or in short, IvMR, which belongs to a truly unsteady flow. As soon as the MS terminates and the TP touches the second wedge surface. Then, the TP was reflected from the wedge surface and formed another TP. Anyway the IvMR transited to the SPRR. However, the transition to the SPRR cannot proceed straightforwardly. The SPRR accompanies a

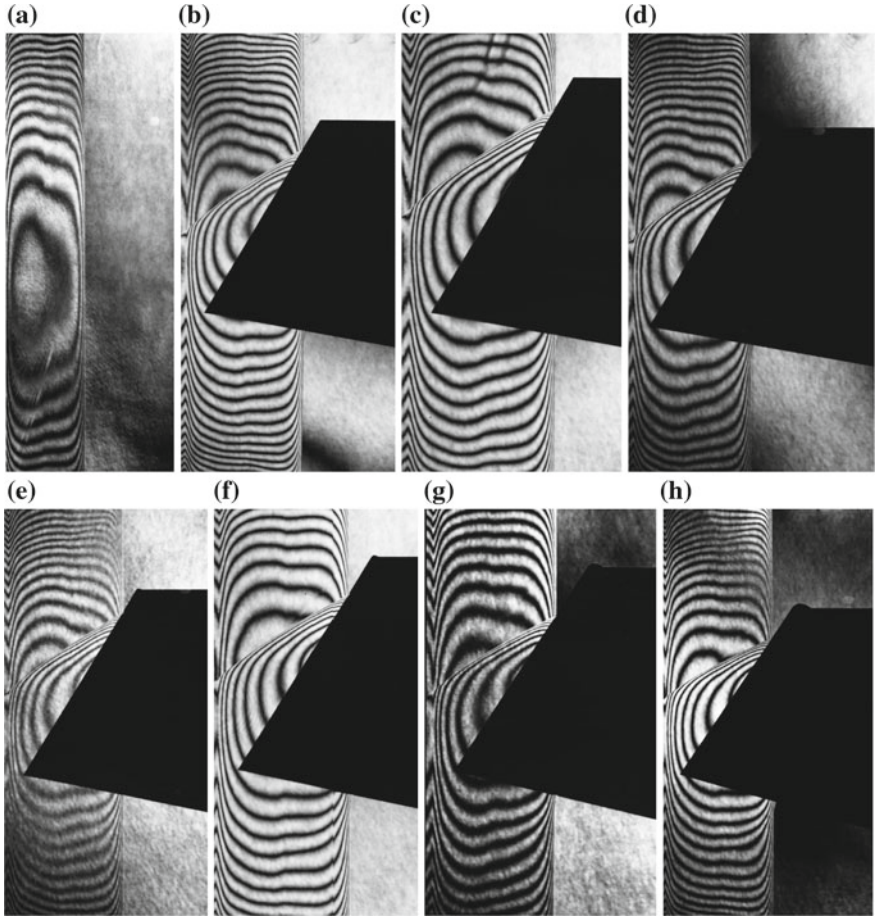

Fig. 2.72 Shock wave released from a 230 mm diameter shock tube reflected from a tilted cone for Ms = 1.20 in air at 1013 hPa. 291.8 K: **a** #92041501; **b** 92041103, Ms = 1.196, $\alpha = 4°$; **c** 92041104, Ms = 1.199, $\alpha = 8°$; **d** #92041323, Ms = 1.199, $\alpha = 10°$; **e** #92041325, Ms = 1.198, $\alpha = 18°$; **f** #92041105, Ms = 1.216, $\alpha = 20°$; **g** #92041301, Ms = 1.189, $\alpha = 30°$; **h** #92041312, Ms = 1.195, $\alpha = 38°$; **i** #92041302, Ms = 1.191, $\alpha = 40°$; **j** #92041313, Ms = 1.195, $\alpha = 44°$; **k** #92041303, Ms = 1.186, $\alpha = 50°$; **l** 92041316, Ms = 1.197, $\alpha = 58°$; **m** #92041304, Ms = 1.1962 $\alpha = 60°$; **n** #92041317, Ms = 1.197, $\alpha = 64°$; **o** #92041320, Ms = 1.193, $\alpha = 78°$; **p** #92041322, Ms = 1.194, $\alpha = 88°$; **q** #92041307, Ms = 1.153, $\alpha = 100°$

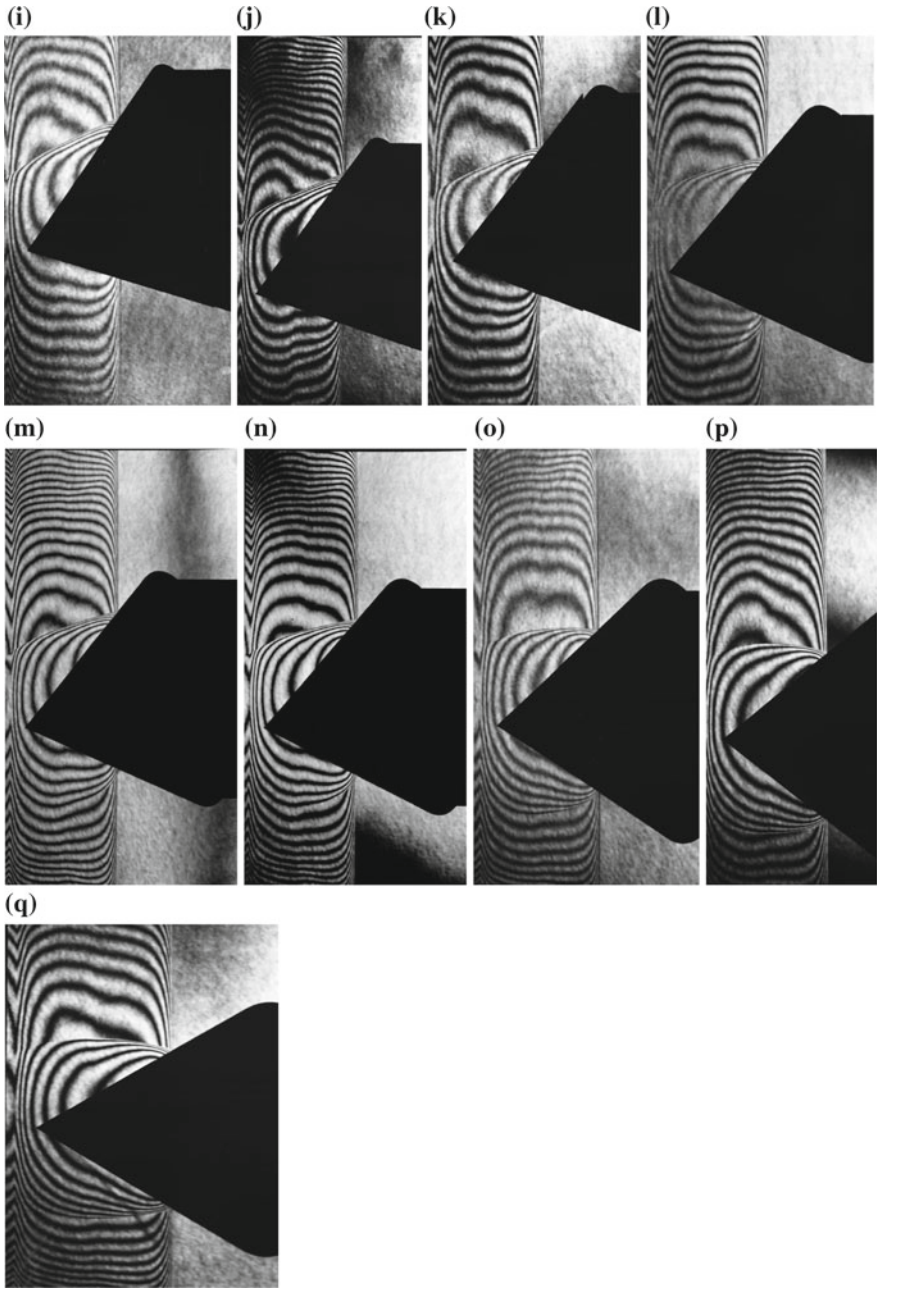

Fig. 2.72 (continued)

Fig. 2.73 Apparent StMR over a 30°/55° double wedge: #87120719, for Ms = 1.927 in air at 500 hPa 293.0 K, the first wedge length of 50 mm

distinct secondary TP on its RS. This transition proceeded in part analogously to the transition from a TMR to a DMR. The secondary TP succeeded the previous TP.

Figure 2.74 shows sequential interferograms of the reflection of shock waves for Ms = 1.50 over $\theta_1 = 15°$ and $\theta_2 = 35°$ double wedge. The allocated time to each image indicate the time of the second exposure from the triggering point. Figure 2.74b is enlargement of Fig. 2.74a. The MS interacted locally with the second wedge surface. In Fig. 2.74c, e, g, two SL interact and eventually form a DiMR as seen in Fig. 2.74h.

The shock wave transition over a concave double wedge is governed not only by the combination of wedge angles but also by first wedge length L. The height of the MS is approximately proportional to the first wedge length L. Hence the evolution of the reflection pattern on the second wedge surface is affected by L. The L can be a length scale.

Figure 2.75 compare the variation of the final reflection pattern for Ms = 1.60–1.80, wedge angles 30°/55° and 27°/52°, the first wedge lengths are L = 7, 12, 25, and 52 mm. Figure 2.75a, b shows final reflection patterns of SPRR in L = 7 mm. Figure 2.75c, d shows SPRR for Ms = 1.90 in L = 12 mm, and SPRR in L = 25 mm, respectively. Figure 2.75f shows an IvMR for Ms = 1.67 in L = 52 mm. Figure 2.75g shows StMR for Ms = 1.62 in L = 52 mm. The result indicates that the final reflection pattern is affected by the first wedge length. In Fig. 2.75e, g, the SL looks almost parallel to the wedge surface. Soon it turns into a two-dimensional array of vortices developing with elapsing time.

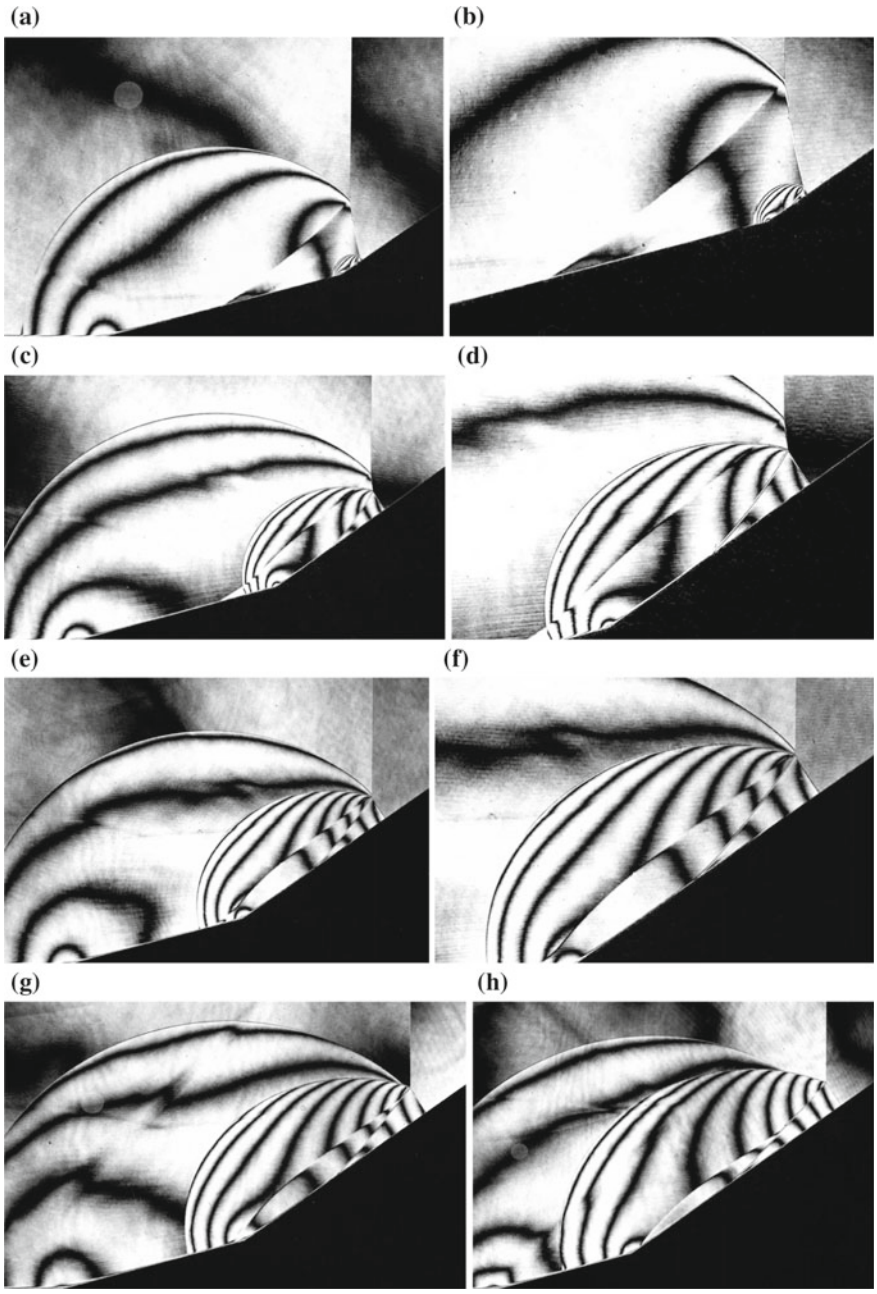

Fig. 2.74 DiMR of reflected shock wave over a $\theta_w = 15°/35°$ double wedge for Ms = 1.50 in air at 670 hPa, 290 K: **a** #86013107, 570 μs delay time from trigger point, Ms = 1.514; **b** enlargement of **a**; **c** #86013101, 620 μs, Ms = 1.506; **d** enlargement of **c**; **e** #86013104, 640 μs, Ms = 1.518; **f** enlargement of (**e**); **g** #86013106, 660 μs, Ms = 1.514; **h** #86013105, 720 μs, Ms = 1.514, DiMR

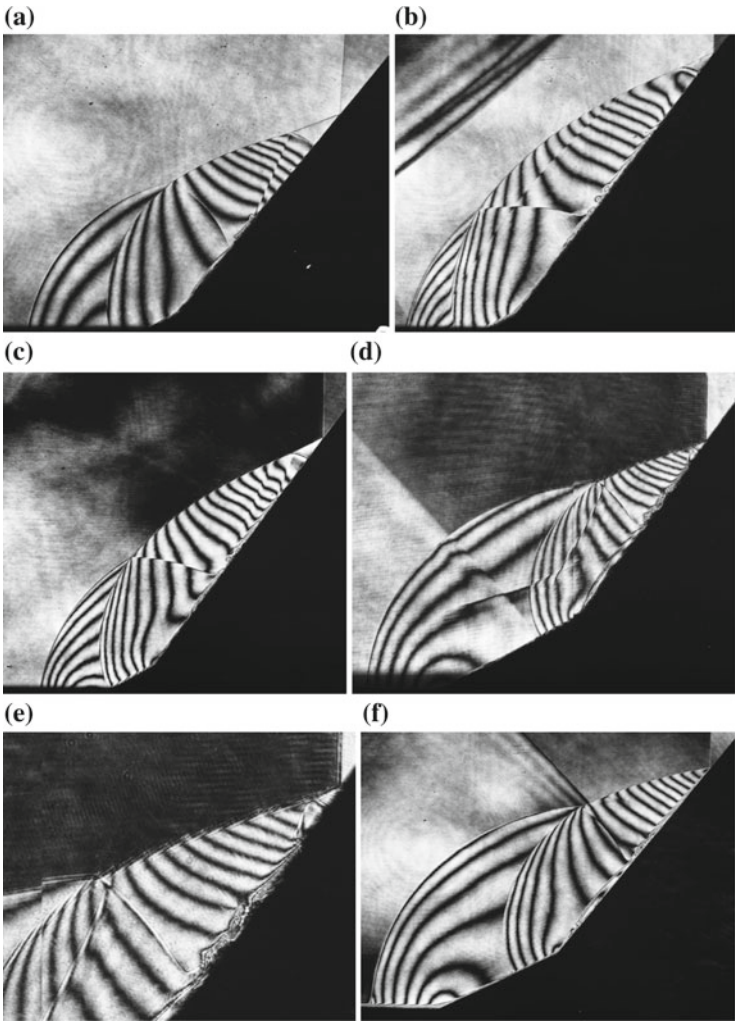

Fig. 2.75 Effect of the first wedge length on the transition for Ms = 1.5–1.9: **a** #87120715, Ms = 1.521 at 800 hPa, 293.0 K, θ_1 = 30°/55°, L = 7 mm, SPRR; **b** #87120709, Ms = 1.896 at 500 hPa, 293.0 K, θ_1 = 30°/55°, L = 7 mm, SPRR; **c** #87120708, Ms = 1.896 at 500 hPa 293.0 K, θ_1 = 30°/55°, L = 12 mm, SPRR; **d** #87120412, Ms = 1.676 at 620 hPa 293.0 K, θ_1 = 30°/55°, L = 25 mm, SPRR; **e** enlargement of (**d**); **f** #87120803, Ms = 1.639 at 680 hPa 294.1 K, θ_1 = 27°/°52, L = 52 mm, IvMR; **g** #87120801, Ms = 1.621 at 680 hPa 294.1 K, θ_1 = 27°/°52, L = 52 mm, StMR; **h** enlargement of (**g**), StMR

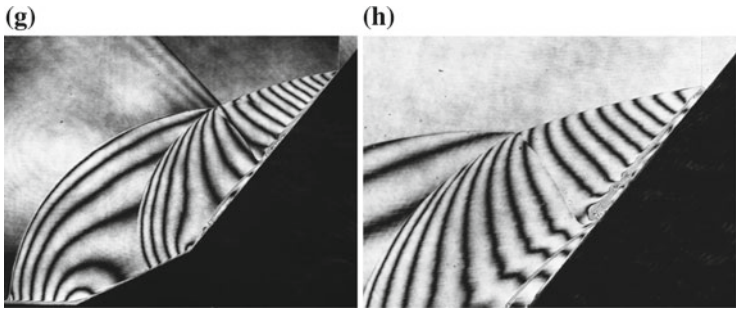

Fig. 2.75 (continued)

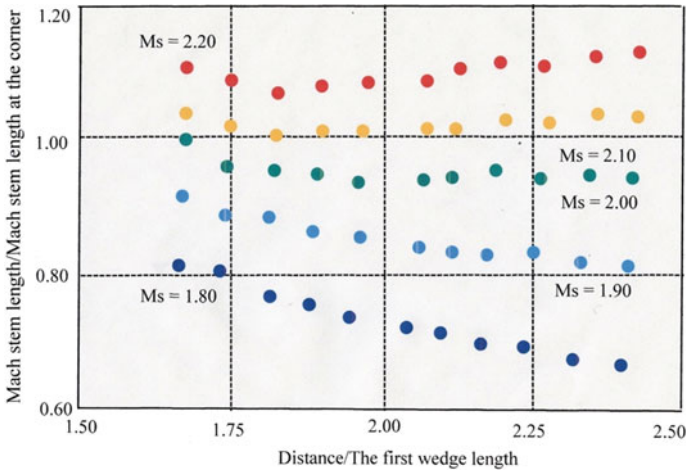

Fig. 2.76 Effect of Ms on the evolution of reflection pattern (Komuro 1990)

Figure 2.76 shows the evolution of the MS along the second wedge surface, this is a summary of numerical simulation. Komuro (1990) numerically simulated the transition of reflected shock wave along the double wedge of 27°/55° by solving the Euler Equations. The ordinate denotes the height of MS normalized by that defined at the corner of the double wedge. The abscissa denotes the distance along the second wedge surface normalized by the first wedge length. For Ms = 2.20, the height of the MS increases with it propagation, which means that the reflection pattern is a DiMR. For Ms = 2.10, the height of MS decreases, is temporarily holding as StMR, but eventually tends starts to gradually increase, which means that the reflection transits to DiMR. For Ms = 2.00, the height of MS remains constant, that is, the StMR is maintained. For Ms = 1.90 and 1.80, the height of the MS decreases monotonously, that is, the IvMR is maintained for a while and then transits to SPRR. It is known that the transition over the second wedge surface is influenced strongly depending on the first wedge length and the boundary layer

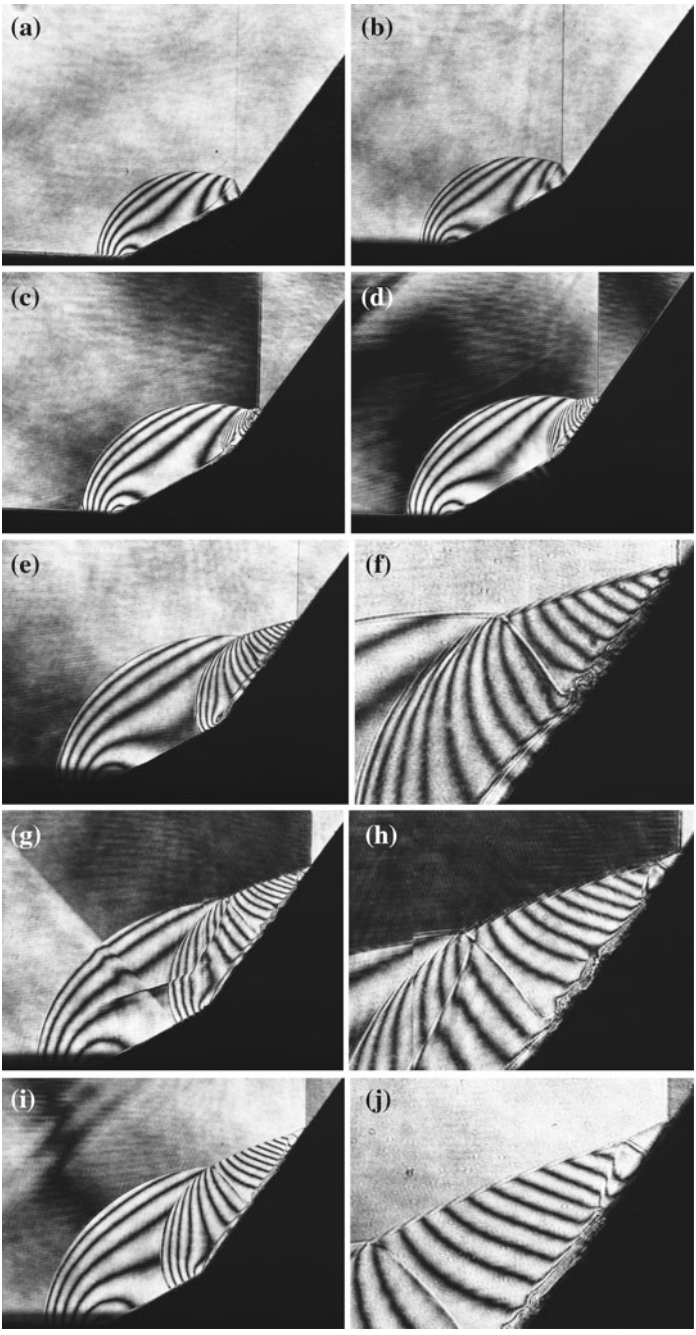

Fig. 2.77 Evolution of an IvMR over a $\theta_w = 30°/55°$ double wedge for Ms = 1.60 in air at 620 hPa, 293 K, the length of the first wedge L = 25 mm: **a** #87120404, Ms = 1.631; **b** #87120409, Ms = 1.669; **c** #87120407, Ms = 1.700; **d** #87120410, Ms = 1.676; **e** #87120411, Ms = 1.680; **f** enlargement of (**e**); **g** #87120412, Ms = 1.676; **h** enlargement of (**g**); **i** #87120413, Ms = 1.673; **j** enlargement of (**i**)

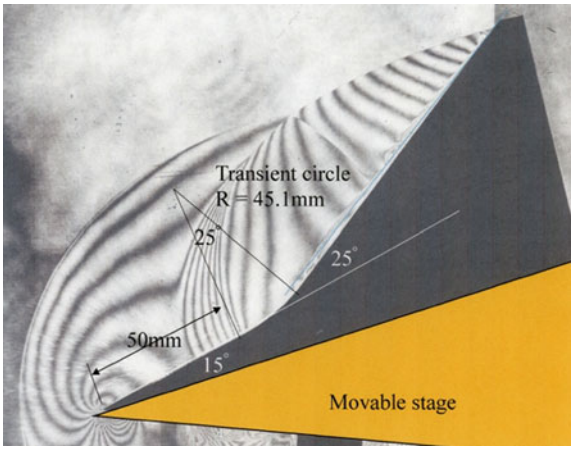

Fig. 2.78 A concave double wedge of 15°/25° installed on a movable stage #88022308, Ms = 1.764

developing on the wedges. Therefore, probably the Euler solvers shown in Fig. 2.76 may not precisely reproduce the transition over double wedges. Anyway the StMR may be present only in a special combination of parameters. Presumably this reflection pattern will not exist consistently in shock tube flows as the concept of StMR violates the unsteadiness of shock tube flows.

Figure 2.77 shows the evolution of an IvMR over a θ_w = 30°/55° double wedge for Ms = 1.60–1.80 in air at 600–650 hPa, 293 K and the first wedge length is L = 25 mm. As the second wedge angle θ_2 is larger than θ_{crit}, the reflection pattern on the second wedge is an IvMR and the transition to a SPRR would take a long distance. Figure 2.77 shows this sequence and is comparable to the numerical prediction shown in dark blue circles presented in Fig. 2.76.

The feature of the stationary Mach reflection, StMR, is that its slip line is consistently parallel to the second wedge surface. This means that the trajectory angle θ of its triple point should be $\theta = 0$. In the (p, θ)-plane of a shock polar diagram, the solution exists only on the axis of $\theta = 0$. In short, the solution of StMR is given as the intersection of R-polar with I-polar. This solution is valid only in steady flows. In Fig. 2.77, solutions suggested the existence of StMR for a specific Mach number and in a special combination of wedge angles. Then to experimentally verify the presence of StMR, a concave double wedge should be mounted on a movable stage. Figure 2.78 shows the concave double wedge mounted on a movable stage: the first wedge angle θ_1 is 15° and the second wedge angle θ_2 = 25°. The two wedges are connected smoothly with a transient circular arc of a radius of 45.1 mm.

Figure 2.79a–f shows the evolution of shock wave reflection from a 15°/25° double wedge mounted on a movable stage. As shown in Fig. 2.79c at θ_2 = 48° the reflection pattern is a StMR but in Fig. 2.79d at θ_2 = 53° the reflection pattern is an IvMR. Unlike the previous double wedge cases, the arc shaped transitional area created a band of wavelets continuously reflected via the curved area to the straight wedge of θ_2. However, the reflection pattern was not strongly affected by the circular arc.

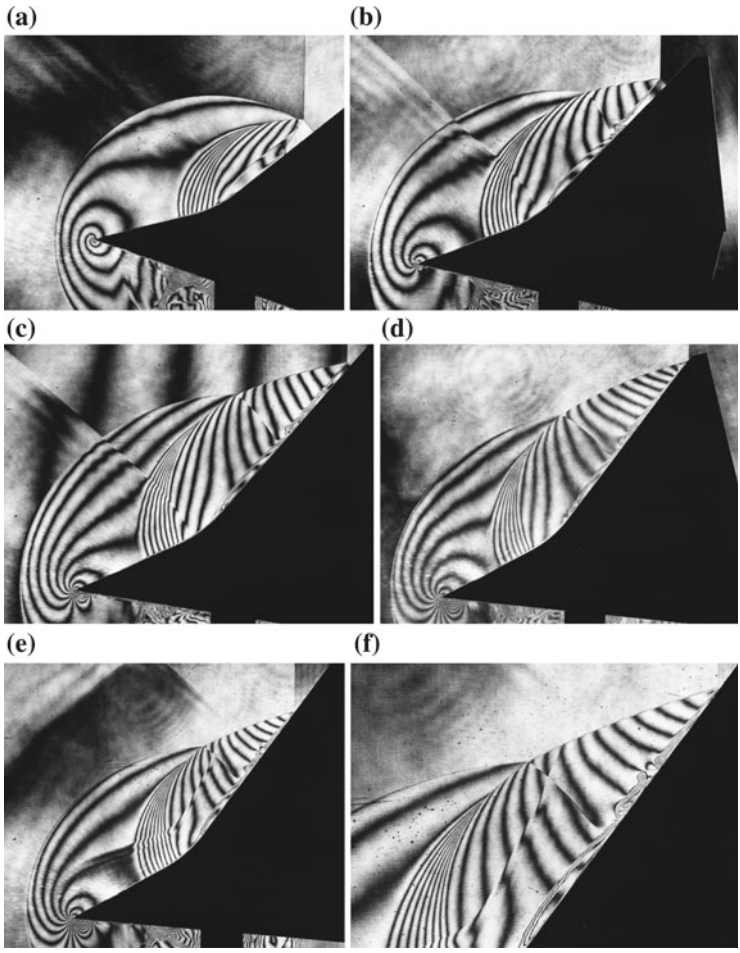

Fig. 2.79 Evolution of shock waves for Ms = 1.76 in air at 500 hPa, 288.8 K mounted on a 15°/25° movable wedge: **a** #88022402, 50 μs from the trigger point, Ms = 1.762, θ_2 = 37°; **b** #88022406. 75 μs, Ms = 1.749, θ_2 = 48°; **c** #88022407, 25 μs, Ms = 1.751, θ_2 = 48°; **d** #88022408, 70 μs, Ms = 1.764, θ_2 = 53°; **e** #88022409, 50 μs, Ms = 1.773, θ_2 = 55°; **f** enlargement of (**e**)

Figure 2.80 shows the evolution of shock wave reflection from a double wedge mounted on a movable stage for Ms = 2.35 in air. In Fig. 2.80f, at θ_2 = 55° the reflection pattern is a StMR. The SL looked parallel to the second wedge surface. In the meantime, the SL became unstable and vortices started to appear along the SL.

For collecting images of a StMR, movable wedge experiments were conducted for Ms = 2.50 by varying the wedge angles from the later stage of a DiMR to earlier stage of an IvMR. Figure 2.81a shows results for θ_1 = 43.5°, $\theta_2 - \theta_1$ = 15° for Ms = 2.521 and the final reflection pattern was DiMR. In Fig. 2.81b, for

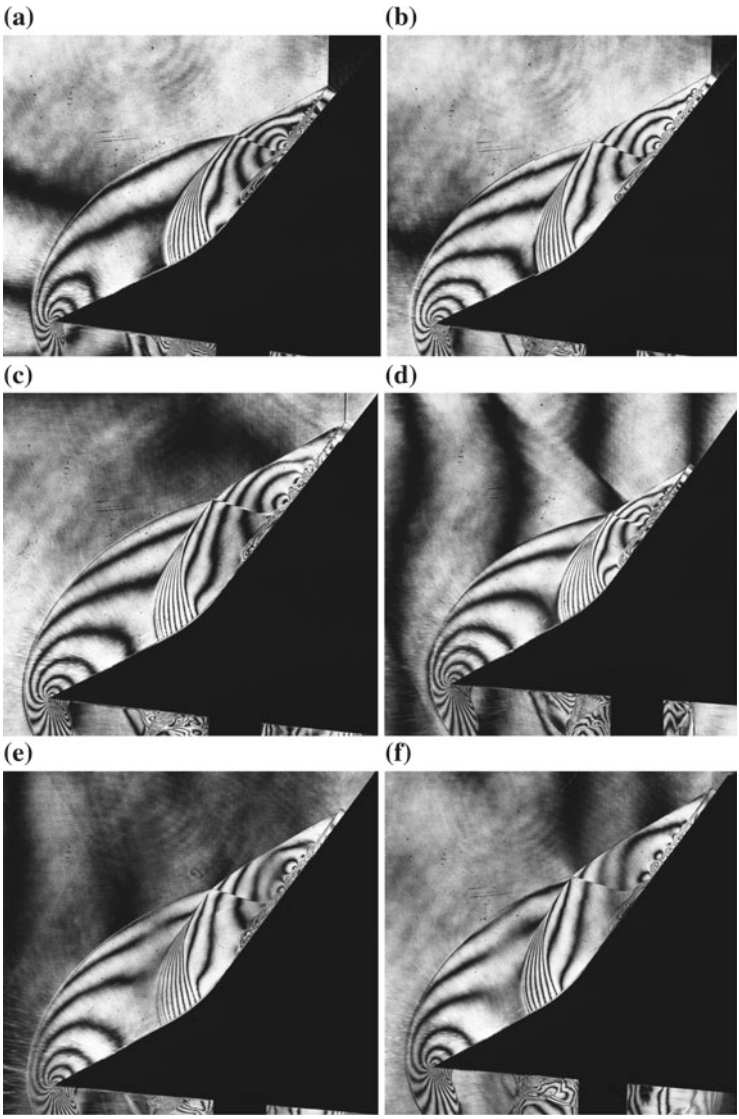

Fig. 2.80 Evolution of shock wave for Ms = 2.35 in air at 200 hPa, 288.8 K mounted on a 15°/25° movable wedge: **a** #88022504, 200 μs from the trigger point, Ms = 2.365, $\theta_2 = 50°$; **b** #88022507, 200 μs, Ms = 2.357, $\theta_2 = 50°$; **c** #88022508, 200 μs, Ms = 2.357, $\theta_2 = 50°$; **d** #88022511, 185 μs, Ms = 2.349, $\theta_2 = 55°$; **e** #88022509, 200 μs, Ms = 2.357, $\theta_2 = 55°$; **f** #88022510, 185 μs, Ms = 2.412, $\theta_2 = 55°$

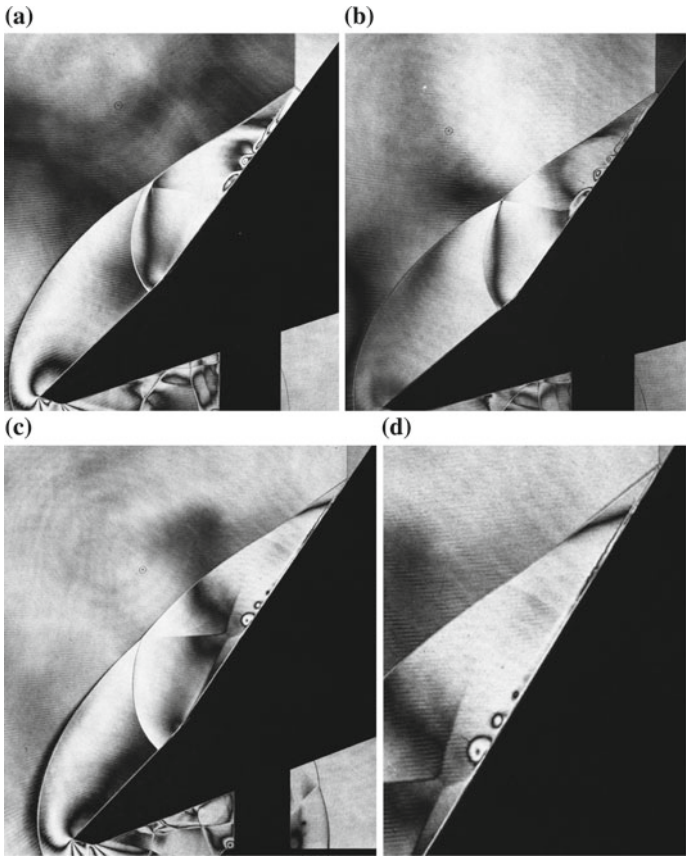

Fig. 2.81 IvMR at critical transition angles for Ms = 2.50 in air at 45 hPa, 284 K: **a** #84041906, delay time from the trigger point 40 μs, Ms = 2.521, $\theta_1 = 43.5°$, $\theta_2 - \theta_1 = 10°$, DiMR; **b** #84041909, 40 μs, Ms = 2.462, $\theta_1 = 42.0°$, $\theta_2 - \theta_1 = 15°$ StMR; **c** #84041904, 40 μs, Ms = 2.496, $\theta_1 = 42.5°$, $\theta_2 - \theta_1 = 10°$ StMR; **d** enlargement of (**c**); **e** #84041908, 40 μs, Ms = 2.521, $\theta_1 = 41.5°$, $\theta_2 - \theta_1 = 15°$ StMR; **f** enlargement of (**e**); **g** #84041913, 40 μs, Ms = 2.530, $\theta_1 = 40.0°$, $\theta_2 - \theta_1 = 20°$ StMR; **h** enlargement of (**g**); **i** #84041911, 40 μs, Ms = 2.379, $\theta_1 = 47.5°$, $\theta_2 - \theta_1 = 15°$ IvMR; **j** #84042003, 40 μs, Ms = 2.500, $\theta_1 = 47.5°$, $\theta_2 - \theta_1 = 10°$ IvMR

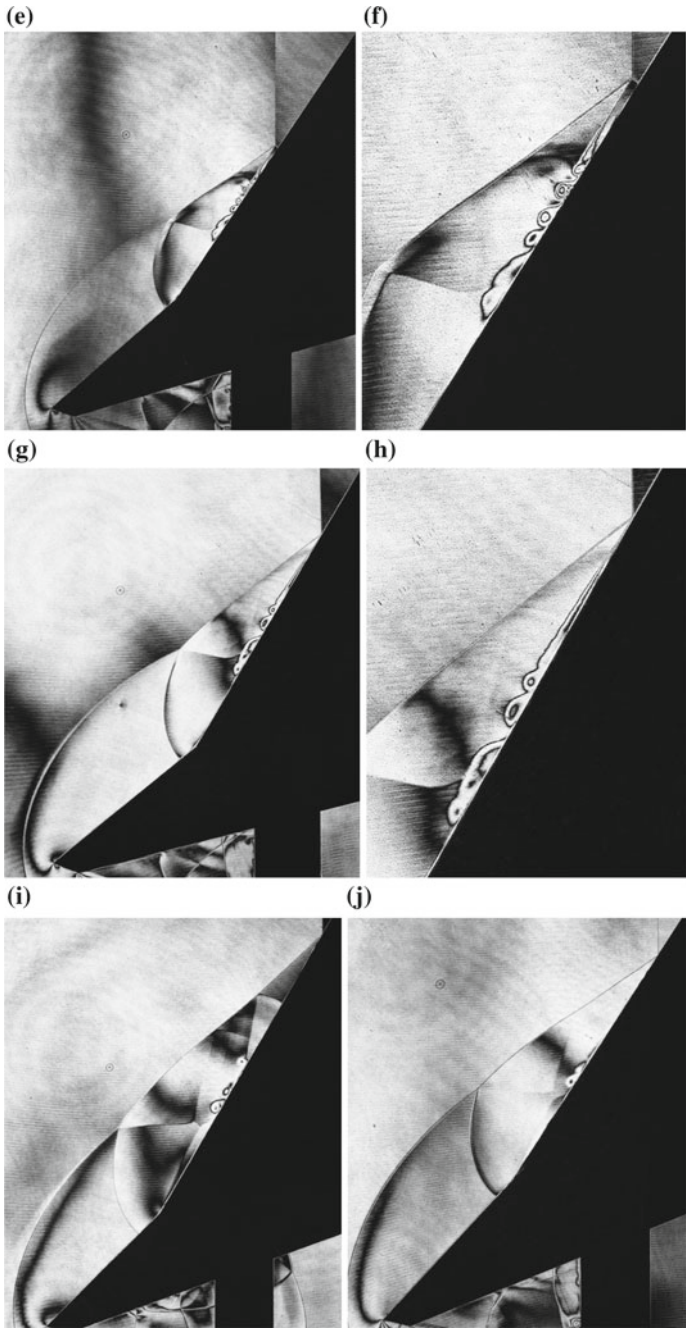

Fig. 2.81 (continued)

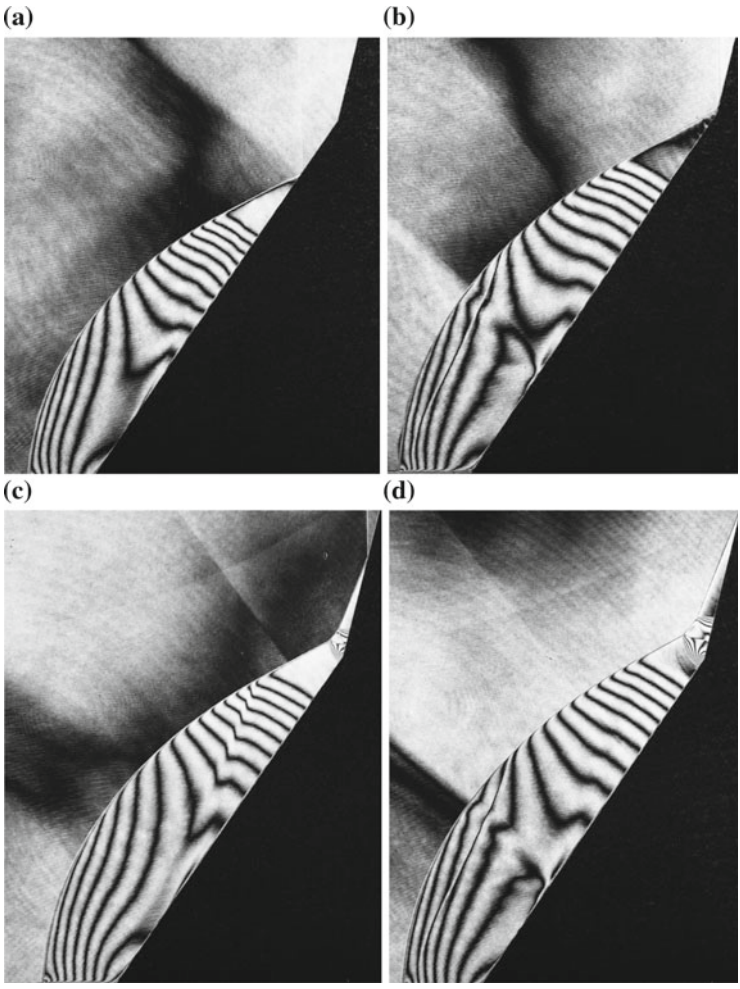

Fig. 2.82 Evolution of reflected shock wave IvMR for Ms = 2.0 over a 55°/75° concave wedge in air at 500 hPa, 298 K: **a** #86091704, 105 μs delay time from the trigger point, Ms = 1.928; **b** #86091701, 120 μs, Ms = 1.913; **c** #86091702, 130 μs, Ms = 1.922; **d** #86091703, 135 μs, Ms = 1.920

Ms = 2.462, $\theta_1 = 42.0°$, $\theta_2 - \theta_1 = 15°$, then MS is shortened but parallel to the wedge surface. Then, the reflection pattern is StMR. In Fig. 2.81c, for Ms = 2.496, $\theta_1 = 42.5°$, $\theta_2 - \theta_1 = 10°$, then the reflection pattern is StMR. Figure 2.81c is its enlargement. Ms is very shortened but looks parallel to the wedge surface. Figure 2.81e, g shows StMR. Figure 2.81f, h are their enlargements. With a slight increase in the wedge angle, the reflection pattern changed to IvMR.

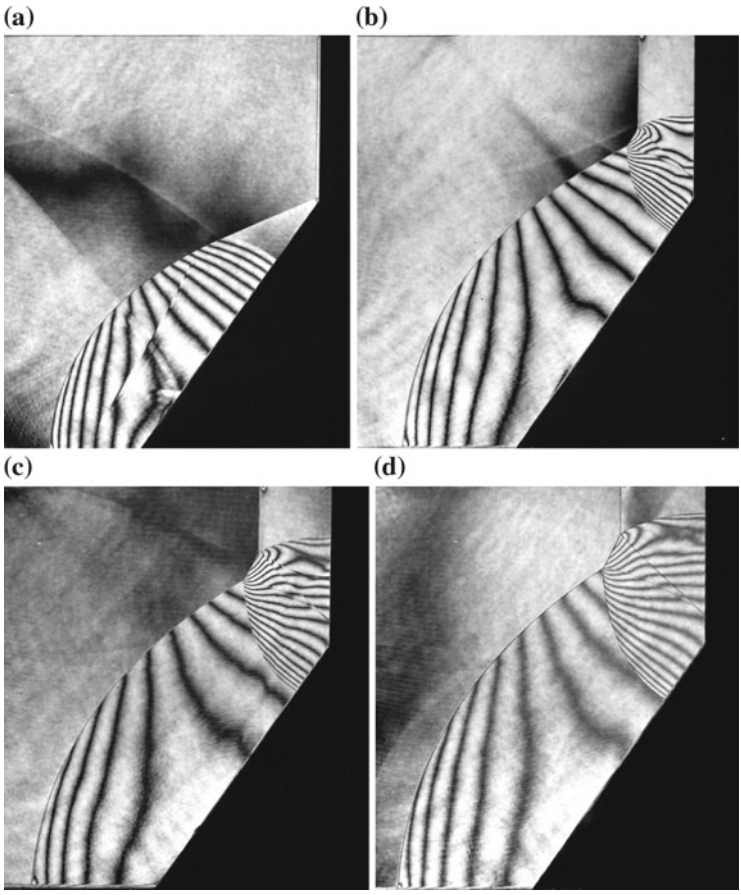

Fig. 2.83 The shock wave reflection from a 55°/90° concave double wedge for Ms = 1.470 in air at 700 hPa, 289.5 K. Experiments were conducted in 60 mm × 150 mm shock tube: **a** #92012101, delay time 610 μs, Ms = 1.468; **b** #92012005, delay time 640 μs, Ms = 1.468; **c** #92012007, 680 μs, Ms = 1.468; **d** #92012003, 700 μs, Ms = 1.470

One of the most trivial cases is the reflection from concave double wedges in which $\theta_1 > \theta_{crit}$. Figure 2.82a–d, shows the evolution of reflected shock waves for Ms = 2.0 in air from a 55°/75° concave double wedge. The reflection patterns are supersonic Mach reflections, SPRR. In the absence of triple points, the shock wave reflection patterns and their interactions are simple and straightforward.

Figure 2.83a–d shows the evolution of shock wave reflection for Ms = 1.47 from the combination of a 55°/90° wedge. The reflected shock wave pattern is SPRR already on the first wedge. At the same time, the IS is reflected from the vertical wall. Eventually, the transmitted shock wave and the reflected shock wave interacted resulting in a simple and straightforward pattern.

2.2.2 Convex Double Wedges

When the first wedge angle θ_1 is larger than that of the second wedge θ_2, it is called a convex double wedge. Then, three patterns of shock wave reflection are possible. The first case is a DiMR appearing on the first wedge. Its Mach stem is defined as MS_1. At the convex corner, it starts diffracting. At the same time, the first DiMR propagates independently on the second wedge surface. Second case is that a RR appears on the first wedge and interacts with the second wedge. MR appears on the second wedge. The third case is a trivial one. The RR is maintained on the second wedge surface, too.

Figure 2.84 shows a 60°/30° convex double wedge. A shock wave of Ms = 1.50 interacted with the wedge and eventually a MR appears. A train of expansion waves propagates reversely toward the upstream. The MR so far created at the corner continuously interacted with the reflected shock wave of the initial RR. At the corner of the convex wall, a vortex is generated.

Figure 2.85 shows the evolution of shock wave of Ms = 1.48 reflected from a 35°/15° convex wedge in air at 660 hPa and 300 K. The first wedge angle being $\theta_1 < \theta_{crit}$, a MR, appears in Fig. 2.85a. Interacting with the second wedge, the MR changes into a second MR. The SL of the first MR interacts with a vortex at the corner and its tail vanishes as seen in Fig. 2.85b. In Fig. 2.85c, d, the SL produced on the second wedge terminates with a vortex generated at the corner.

Figure 2.86 shows the evolution of shock wave of Ms = 1.50 reflected from a 60°/30° convex wedge.

Fig. 2.84 Reflection of a MR over a 60°/30° convex double wedge: #86012709 630 μs, Ms = 1.498 in air at 670 hPa, 288 K

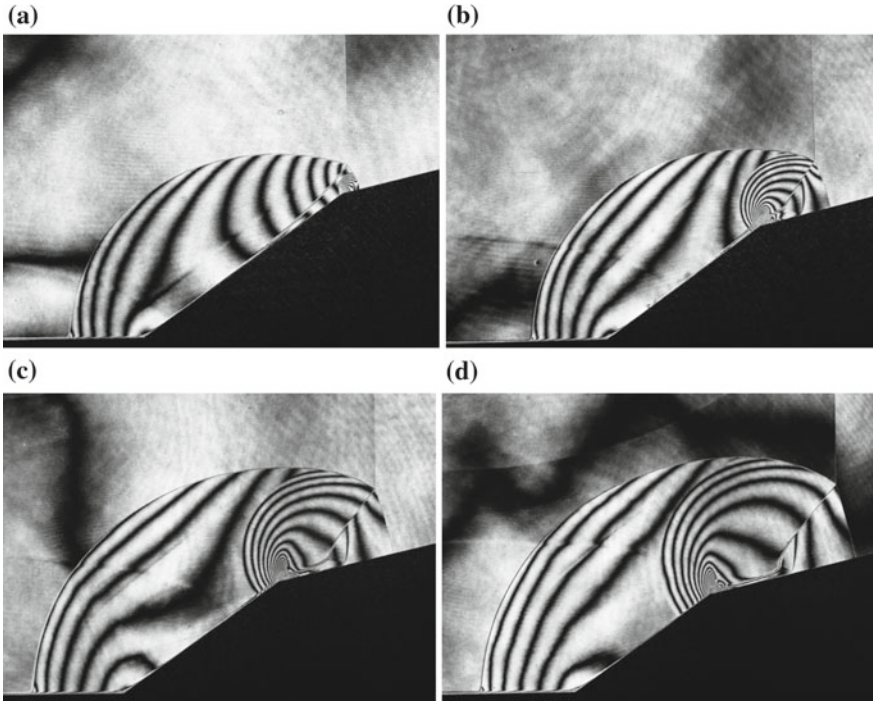

Fig. 2.85 Shock wave reflection from a 35°/15° convex wedge for Ms = 1.48 in air at 660 hPa and 300 K: **a** #86012803, 570 μs from the trigger point, Ms = 1.483; **b** #86012804, 600 μs, Ms = 1.483; **c** #86012805, 630 μs, Ms = 1.485; **d** 86012806, 640 μs, Ms = 1.489

2.3 Evolution of Shock Wave Reflection from Curved Walls

When a planar shock wave propagates over a continuously curved concave and convex walls, the main feature of the reflected shock wave transition is, in principle, similar to convex and concave double wedges. The transition from a RR to a MR occurs over a convex wedge and the transition from a MR to a RR occurs over a concave wedge (Ben-Dor et al. 1980). However, in the case of curved wedges, the critical transition angle varies significantly depending on its radius of curvature (Takayama and Sasaki 1983). The previous results of visualization regarding the dependence of the radii of curvature on the transition of reflected shock waves are summarized.

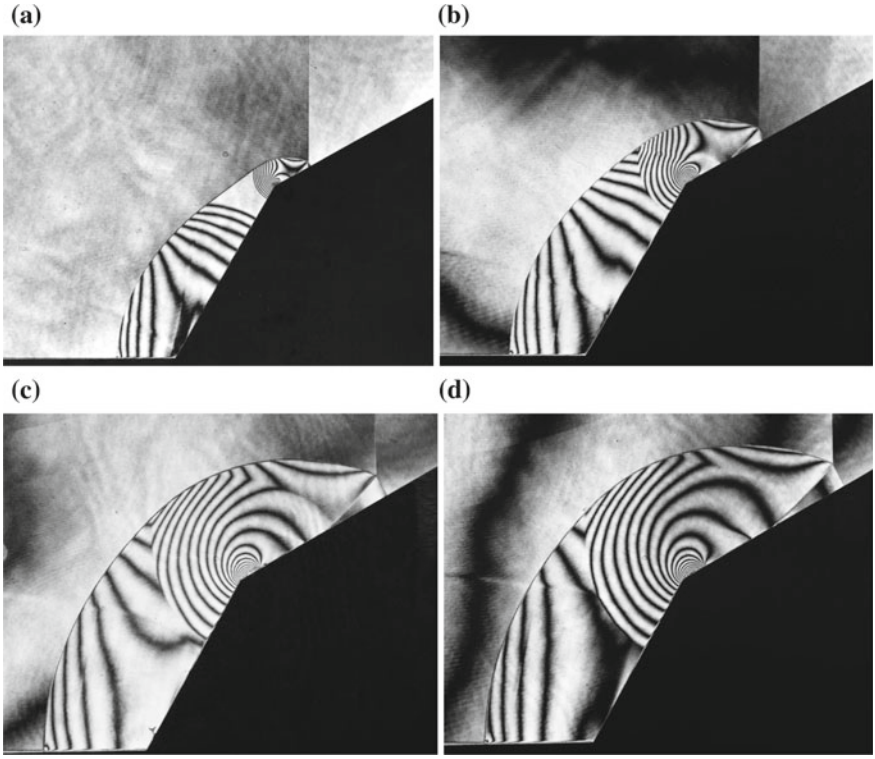

Fig. 2.86 Shock wave reflection from a 60°/30° convex wedge for Ms = 1.50 in air at 670 hPa and 288 K; **a** #86012706 570 μs, Ms = 1.496; **b** #86012707 590 μs, Ms = 1.500; **c** #86012709, 630 μs, Ms = 1.498; **d** #86012710, 650 μs, Ms = 1.490

2.3.1 Concave Walls

Unlike a concave double wedge, in a concave wall, its wall angle varies continuously from 0° to 90°. Figure 2.87 shows the sequences of reflected shock wave patterns. When the IS propagates along a shallow wall angle, the corner signal propagates along the trajectory of the glancing incidence angle as seen in Fig. 2.87a, b. Then the IS intersects with the curved MS. The MS being normal to the concave wall surface, the density behind it increases. However, at earlier stage of the reflection, although the TP is formed but not distinctly and the SL is missing. This reflection pattern is an vNMR but the trajectory angle being $\chi > 0$ so that the reflection type is DiMR as seen in Fig. 2.87c, d. With further increase in the wall angle, the TP tends to approaches toward the wall, that is $\chi < 0$. The reflection pattern becomes an IvMR as seen in Fig. 2.87e. Figure 2.87f is an enlargement of Fig. 2.87e. Figure 2.87g–j shows the termination of the IvMR and its transition to SPRR. Here the θ_{crit} is defined as a wall angle at which the IvMR transits to a

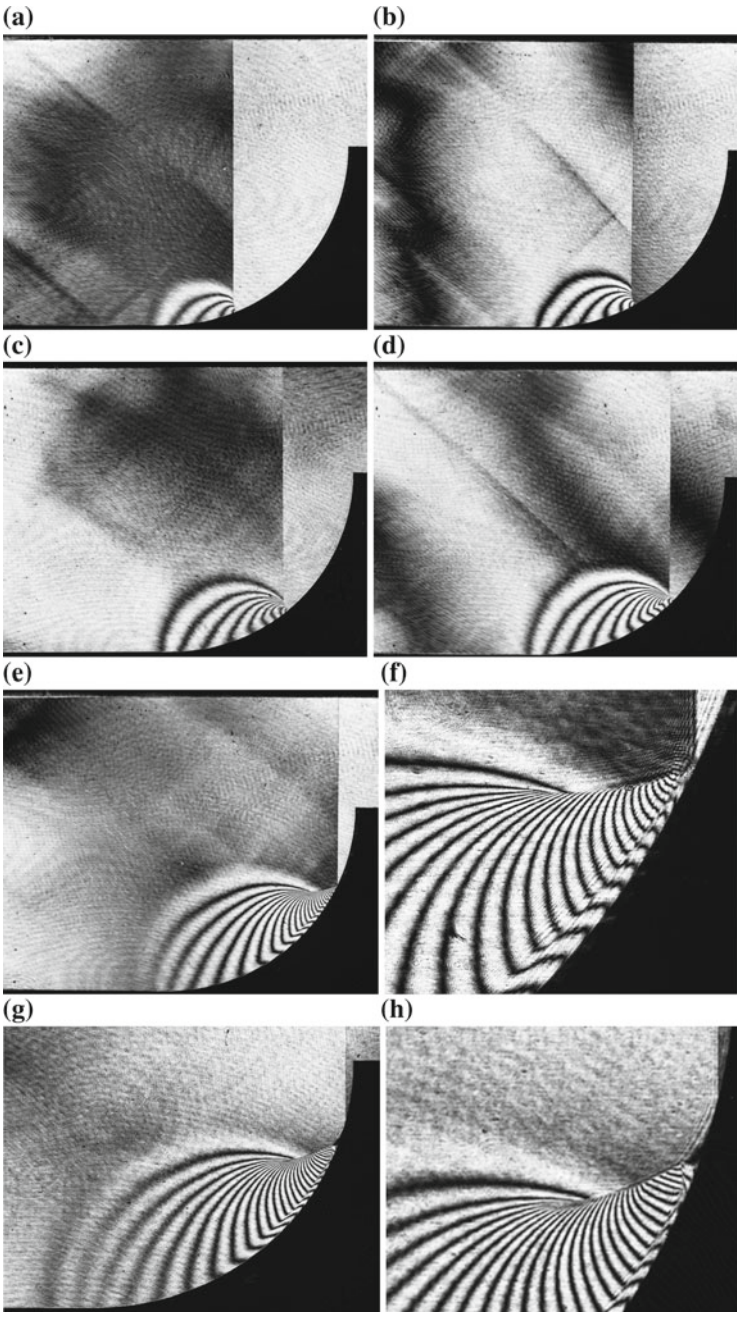

Fig. 2.87 Evolution of reflected shock wave from a 100 mm diameter circular wall for Ms = 1.53 in air at 800 hPa, 292 K conducted in the 40 mm × 80 mm conventional shock tube: **a** #81101503, 132 μs, Ms = 1.530; **b** #81101505, 142 μs, Ms = 1.530; **c** 81101507, 152 μs, Ms = 1.530; **d** #81101508, 162 μs, Ms = 1.530; **e** #81101509, us Ms = 1.530; **f** enlargement of (**e**) #81101505, 162 μs, Ms = 1.530; **g** #81101611, Ms = 1.530; **h** enlargement of (**g**); **i** #81101606, 177 μs, Ms = 1.575; **j** enlargement of (**i**)

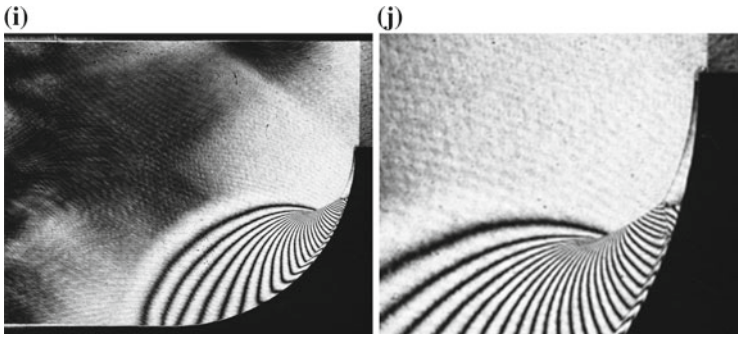

Fig. 2.87 (continued)

SPRR. As discussed later, the θ_{crit} is larger than the prediction of the Neumann criterion. In Fig. 2.87d, e, the slip lines look almost parallel or coaxial to the curved wall, but this type of reflection is analogous to StMR in the case of concave double wedges. In the present concave wall. StMR appears only transitionally and immediately transits to IvMR. As will discussed later, θ_{cri} on concave walls varied depending on the diameter of circular concave walls.

Figure 2.88 shows the evolution of shock wave reflection from a 100 mm diameter circular concave wall for Ms = 1.42 in air. Experiments were conducted in the 60 mm × 150 mm diaphragm-less shock tube having a higher degree of reproducibility. Figure 2.88a–h shows the gradual increase in fringes at earlier stage and their formation to a distinct TP. Along the concave wall, fringes increased in number with increasing the wall angle. Figure 2.88i–l shows the sequential formation of the distinct triple point. The type of reflection is a DiMR. With the further increase in the wall angle, the curved SL becomes gradually parallel to the circular wall. Such coaxial SL is maintained only for short time. The type of reflection pattern in the wedges is defined as a StMR. Along the concave walls, a similar pattern to StMR appears only temporarily as seen in Fig. 2.88k, l. When the TP touched the curved wall and the MS terminated but the entropy increase across the SL was maintained by the second TP. Therefore, at the transition from an IvMR to a SPRR, the TP carried by the IvMR became the second TP behind the SPRR. The structure of the secondary shock wave is very similar to that appearing in a DMR.

Figure 2.89 shows the initiation of an IvMR and its transition into a SPRR. Experiments were conducted in the 40 mm × 80 mm conventional shock tube. Ms scattered slightly widely but through these images the evolution of reflected shock waves was well observed. In Fig. 2.89a, b, fringe numbers increased gradually with the increase in the wall. In Fig. 2.89c–f, the formation of the TP and the transition from a StMR to an IvMR are observed. Figure 2.89g–i shows the termination of the IvMR. As soon as the TP of the IvMR reaches the wall and the MS terminate, the transition to a SPRR takes place. The value of this critical transition angle θ_{crit} is, as discussed later, larger than that predicted value by von Neumann criterion applied to straight wedges.

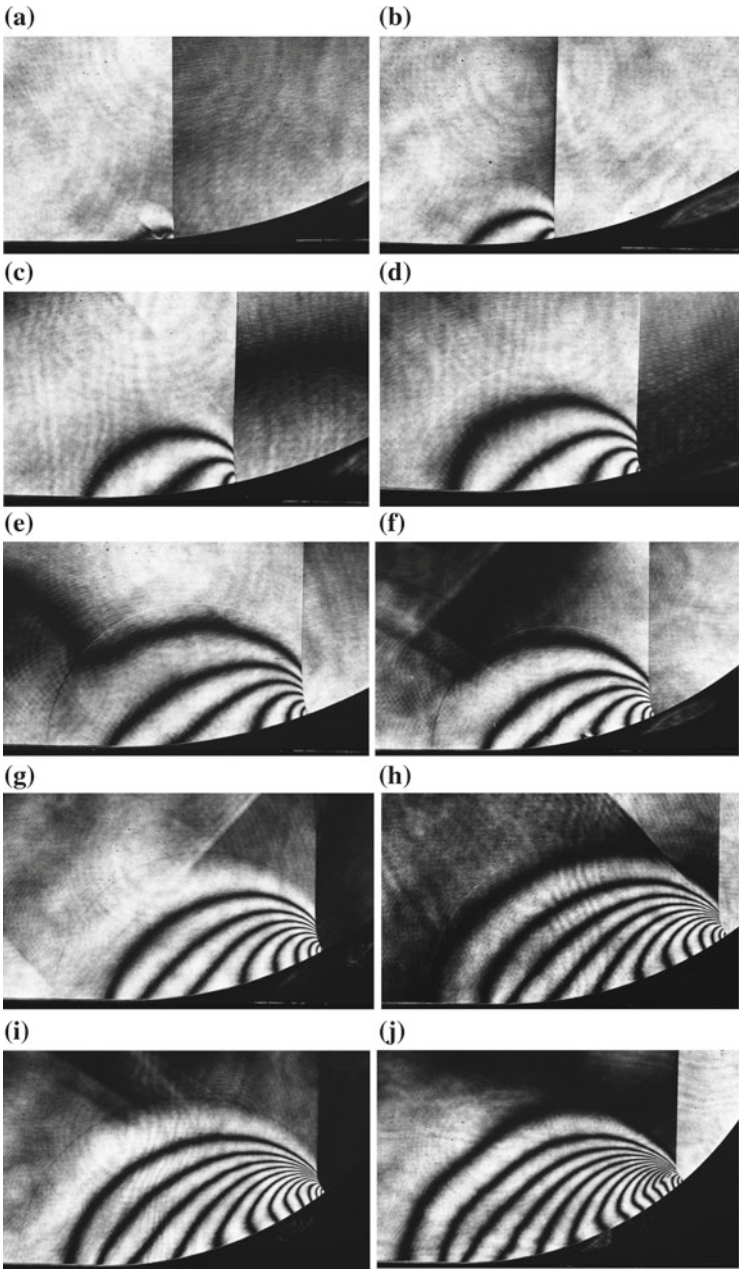

Fig. 2.88 Evolution of reflected shock wave from a 100 mm diameter circular wall for Ms = 1.42 in air at 800 hPa, 294.3 K: **a** #87111902, 240 μs delay time from the trigger point, Ms = 1.431; **b** #87111903, 260 μs, Ms = 1.432; **c** #87111904, 280 μs, Ms = 1.422; **d** #87111905, 300 μs, Ms = 1.422; **e** #87111906, 320 μs, Ms = 1.418; **f** #87111907, 340 μs, Ms = 1.410; **g** #87111908, 360 μs, Ms = 1.414; **h** #87111909, 380 μs, Ms = 1.428; **i** #87111910, 400 μs, Ms = 1.418; **j** #87112007, 415 μs, Ms = 1.422; **k** #87111912 440 μs, Ms = 1.426; **l** #87112001, 460 μs, Ms = 1.430

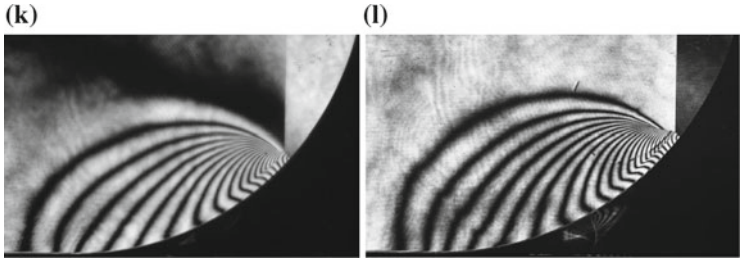

Fig. 2.88 (continued)

In propagating along a circular concave wall, the transition of a reflected shock wave from a MR to a RR occurs at the θ_{crit} at a given Ms. Its value, however, varies depending not only on Ms but also the Reynolds number, Re, that simply reflects the initial pressure and the diameter of the concave wall.

It was already observed that on the wedge having a slightly smaller wedge angle than the θ_{crit}, a RR appeared at the leading edge and the transition to a MR was delayed and that the delayed transition distance varied significantly depending on the initial pressure. Hence it is speculated that the initial pressure would affect the transition over not only concave walls but also convex walls. The θ_{crit} was obtained in the transition from an IvMR to a RR over a 100 mm diameter circular concave wall for Ms = 2.33 in air.

Figure 2.90 summarizes the experimental results: The height of MS against the concave wall angle. The ordinate denotes the height of Mach stem in mm and the abscissa shows concave wall angle in degrees. Blue and red filled circles denote initial pressures of 14.1 and 1.41 kPa, respectively. The angle at which MS vanishes is θ_{crit}. As shown in arrows on the abscissa, the detachment criterion suggests $\theta_{crit} = 51.5°$ and the mechanical equilibrium criterion offers $\theta_{crit} = 63.5°$, whereas experimentally deduced values are: $\theta_{crit} = 71.0°$ at 1.41 kPa and $\theta_{crit} = 73.0°$ at 14.1 Pa. θ_{crit} varies depending on the initial pressure, in other words, on the Reynolds number, Re. In the previous experiments, researchers paid attention mostly to Ms but were less aware of the effects of the initial pressures or Re.

2.3.2 Convex Walls

Upon the shock wave reflection from a double convex wedge whose wall angle is $\theta_w > \theta_{crit}$, the initial reflection pattern is a RR. With the decrease in the wall angle θ_w, the RR transits to a MR. This is a reverse reflection sequence from the one observed in the concave wall as discussed previously (Takayama and Sasaki 1983).

Bryson and Gross, by using shadowgraph and the schlieren methods, visualized the reflection and diffraction of shock waves over cylinders, and spheres. Shock wave reflection over the 80 mm diameter cylinder was visualized in the

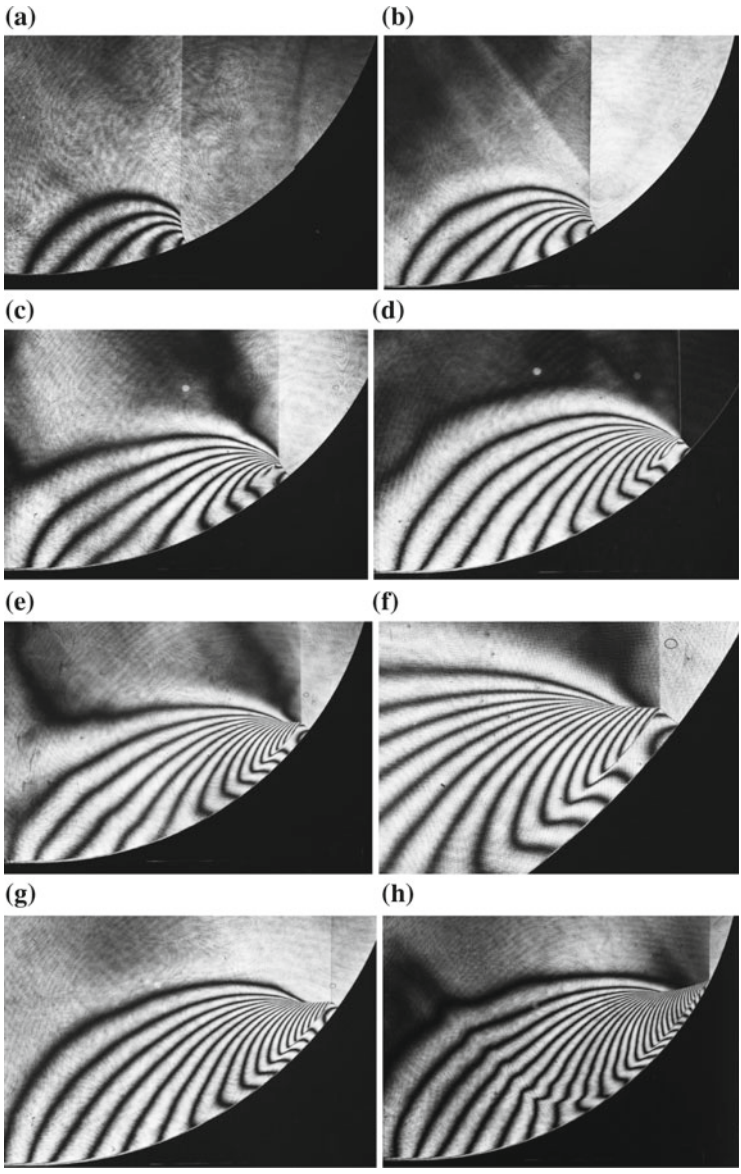

Fig. 2.89 Evolution of reflected shock wave over a 100 mm diameter concave wall for Ms = 1.60 in air at 400 hPa, 291 K: **a** #83101914, delay time from the trigger point 50 μs; **b** #83101912, 90 μs; **c** #83101911, 110 μs; **d** #83101909, 130 μs; **e** #83101902,130 μs; **f** enlargement of (**e**); **g** #83101908, 160 μs; **h** #83101904, 180 μs; **i** #83101903, 210 μs; **j** enlargement of (**i**); **k** 83101905, 210 μs; l enlargement of (**k**); **m** #83101907, 220 μs; **n** enlargement of (**m**)

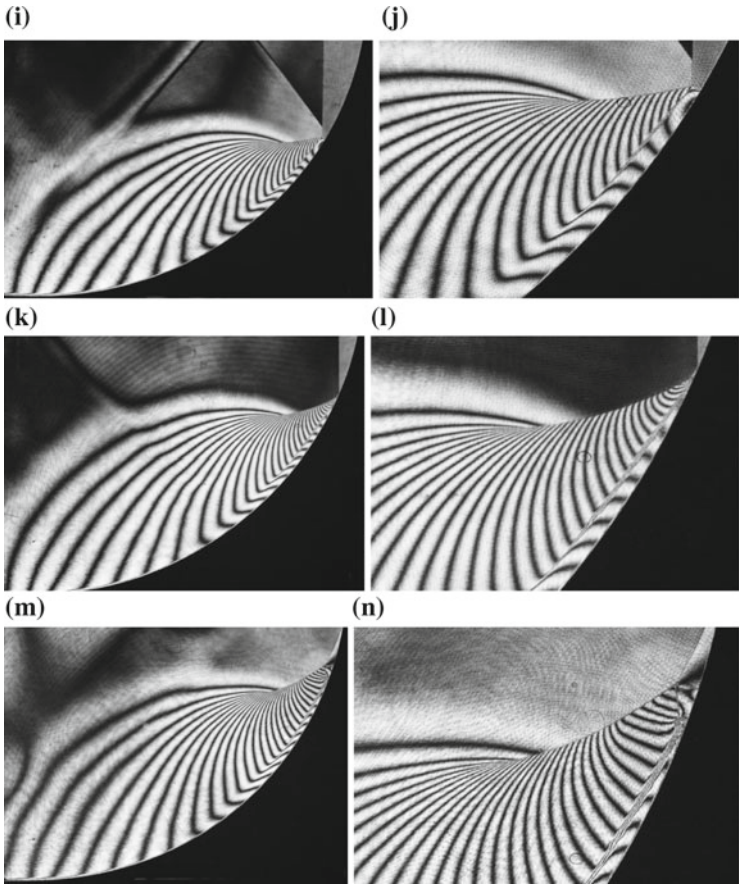

Fig. 2.89 (continued)

40 mm × 80 mm conventional shock tube for Ms = 1.035 in air Takayama and Sasaki (1983). In the present experiment, a shock wave being weak and the *OB* path length being only 40 mm, to enhance the sensitivity of interferograms at such low pressures, the initial air pressures were increased up to 1610 hPa.

Obtained interferograms are shown in Fig. 2.91. Along the frontal side of the cylinder, a RR appears as seen in Fig. 2.91a. Its enlargement is shown in Fig. 2.91b. With propagation, the RR transits to SMR as seen in Fig. 2.91c, and its enlargement in Fig. 2.91d.

Figure 2.92a–f shows reflections of stronger shock waves for Ms = 2.5. The reflection pattern shows SPRR. Hence immediately after the transition, the RR has a kink point and the reflection pattern is TMR in Fig. 2.92c.

Figure 2.93 shows direct shadowgraphs of the evolution of shock wave for Ms = 3.15 reflected from a convex wall accommodated in a 40 mm × 80 mm

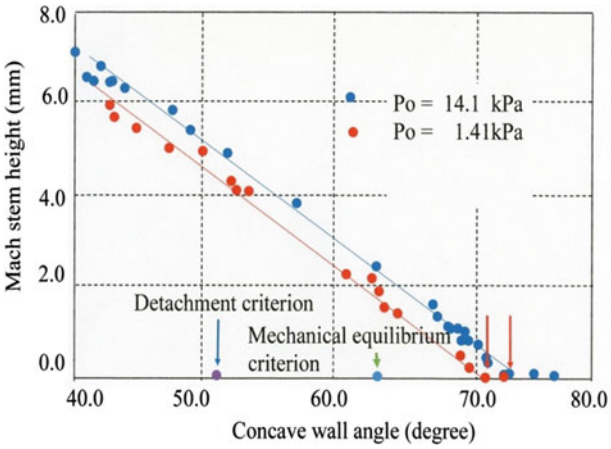

Fig. 2.90 The effect of initial pressures on θ_{crit} at Ms = 2.33 in air. The IvMR on 100 mm diameter concave wall installed in a 100 mm × 180 mm diaphragm-less shock tube (Kitade 2001)

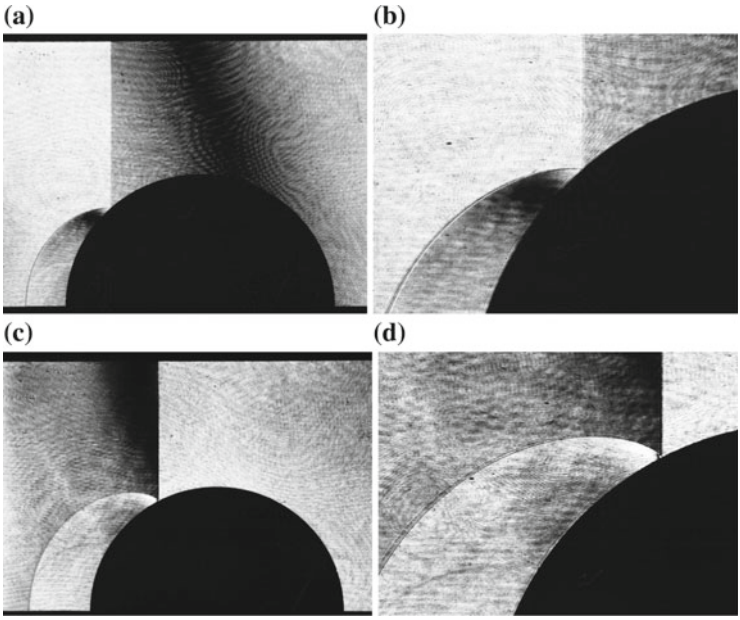

Fig. 2.91 Reflection of shock wave over a 80 mm diameter cylinder for Ms = 1.035 in air at 1610 hPa, 293.8 K: **a** #81101933, delay time from the trigger point 120 μs, RR; **b** enlargement of (**a**); **c** #81101937, 140 μs, SMR; **d** enlargement of (**c**)

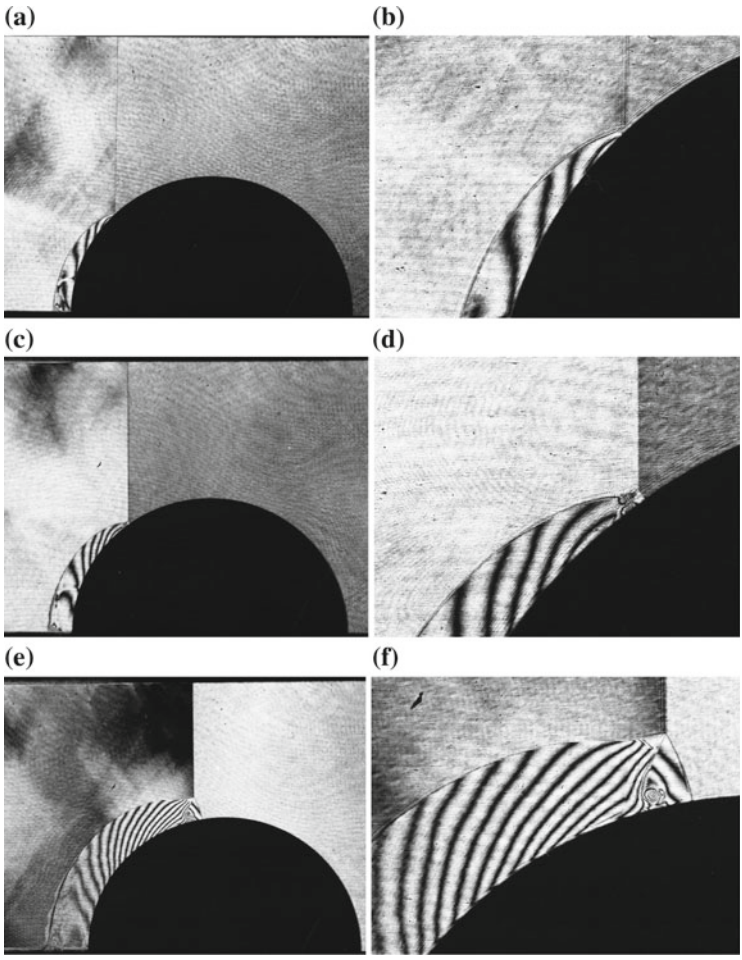

Fig. 2.92 Evolution of shock wave reflection over a 80 mm diameter cylinder for 2.50 in air at 300 hPa, 291.7 K: **a** #81102213, Ms = 2.50, RR; **b** enlargement of (**a**); **c** #81102206, Ms = 2.50, TMR; **d** enlargement of (**c**); **e** #81102208, Ms = 2.55 TMR, **f** enlargement of (**e**)

conventional shock tube. The convex wall has 300 mm diameter is mounted on a movable stage at the initial inclination angle of $\theta_w = 50°$. In Fig. 2.93a the reflection pattern at the leading edge is a RR. In Fig. 2.93b–d, reflection patterns are DMR.

Figure 2.94 shows shock wave reflection from a 100 mm diameter circular cylinder for Ms = 2.326 in air at 144 hPa, 290.2 K in a 100 mm × 180 mm diaphragm-less shock tube. Visualizations are conducted using double pulse interferogram at double pulse interval of 200 μs. The reflection pattern is a RR, with propagation, becomes a TMR, and on further propagation it turns into a SMR.

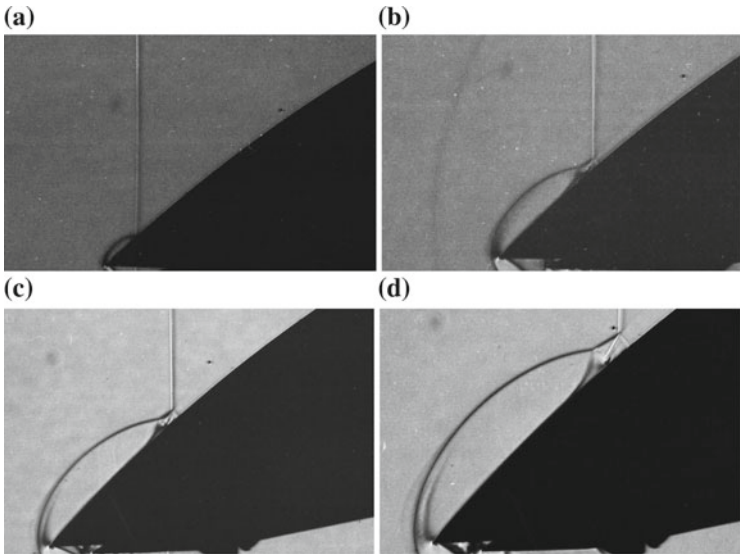

Fig. 2.93 Evolution of reflected shock wave over a 300 mm diameter convex wall mounted on a movable stage for Ms = 3.150 in air at 40 hPa, 295.1 K, at $\theta_w = 50°$, visualization was conducted by direct shadowgraph; **a** #80072529, 14 μs, Ms = 3.135, RR; **b** #80072520, 20 μs, Ms = 3.175, DMR; **c** #80072510, 24 μs; ms = 3.158, DMR; **d** #80072513, 30 μs. Ms = 3.071, DMR

In Fig. 2.95, triple point positions deduced from individual experiments are plotted. The ordinates denote the height of the MS in mm and the abscissa denotes the wall angles in degree. The blue and red filled circles denote the initial pressure 14.1 and 1.41 hPa, respectively. A filled grey circle shows θ_{crit} of detachment criterion $\theta_{crit} = 51.0°$ whereas $\theta_{crit} = 43.0°$ at $p_0 = 14.1$ hPa and $\theta_{crit} = 38.0°$ at $p_0 = 1.41$ hPa.

It is found that the initial pressure significantly affects $\theta_{crit.}$ The higher the initial pressure is, (or in other words, the higher the Reynolds number becomes) the closer the θ_{crit} approaches to the detachment criterion. For reducing the initial pressures, the larger the departure from the detachment criterion becomes.

Figure 2.96 summarizes the series of present observations. Images observed through a slit was recorded by using a streak mode of Ima-Con high speed camera (John Hadland Photonics Model 675).

Figure 2.96a shows a streak photograph and a sketch of a shock wave motion in atmospheric air. The shock wave of Ms = 1.3 was reflecting over a 100 mm diameter convex cylinder. A 0.5 mm wide slit was attached on the edge of the cylinder. The image of the shock wave viewed through the slit was visualized by direct shadowgraph and recorded in the streak mode of the Ima Con high speed camera. In order to achieve a better resolution of the streak image the slit image was rotated by 49.5° relative to the direction of the shock wave propagation. The image rotator was designed and manufactured in house. The picture in Fig. 2.96a shows

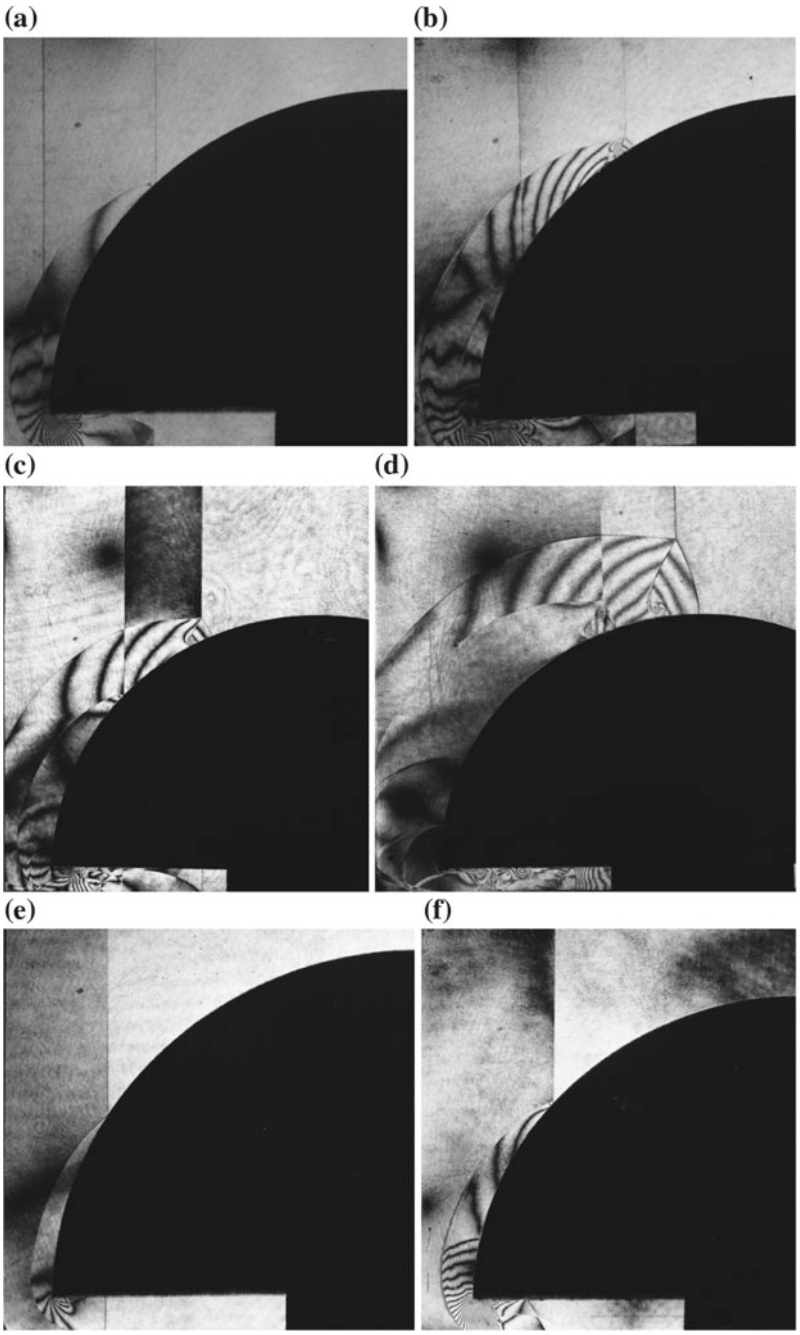

Fig. 2.94 Shock wave reflection from a 100 mm diameter circular cylinder in a 100 mm × 180 mm diaphragm-less shock tube for Ms = 2.33 in air in Fig. 2.83a–f at 144 hPa, 290.2 K, in Fig. 2.83e, f at 28.2 hPa, 291.5 K: a #98122103, Ms = 2.335; **b** #98122109, Ms = 2.326; **c** #98122104, Ms = 2.371; **d** #98122104, Ms = 2.371 144 hPa; **e** #99011909, Ms = 2.333; f #99011203, Ms = 2.330

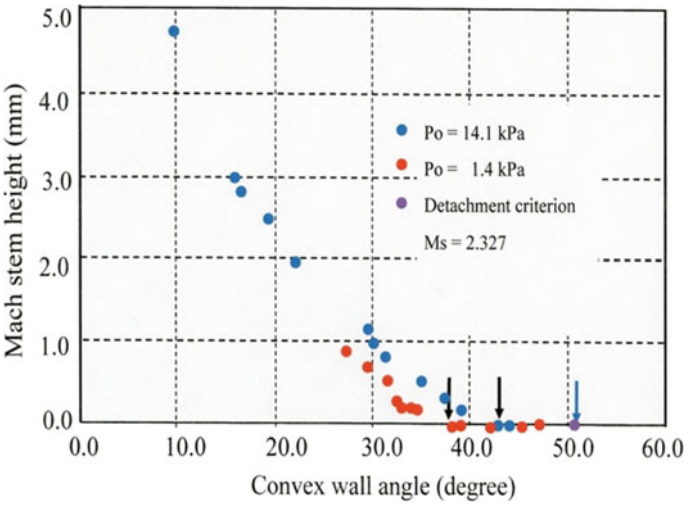

Fig. 2.95 Effect of initial pressures on θ_{crit} at Ms = 2.327 in air, 100 mm diameter convex wall in a 100 mm × 180 mm shock tube (Kitade 2001)

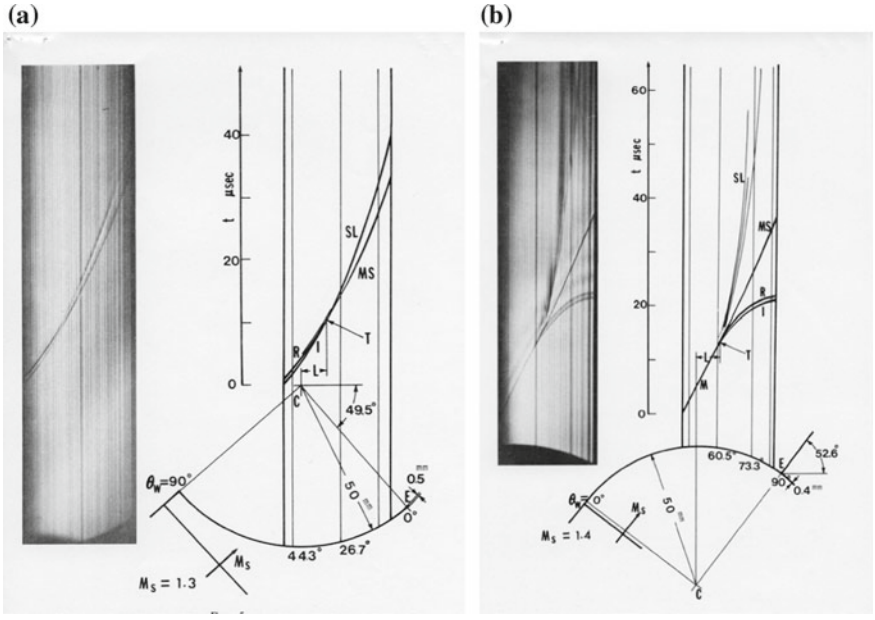

Fig. 2.96 Streak photographs applied to convex and concave walls: **a** convex wall; **b** concave wall

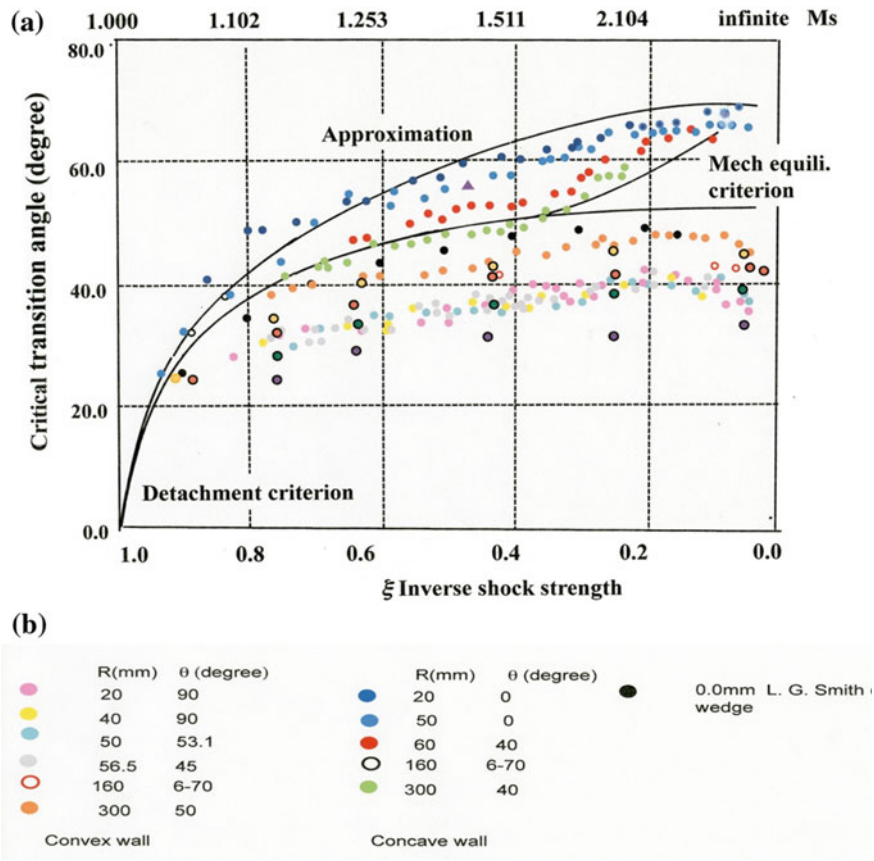

Fig. 2.97 Summary of the critical transition angle θ_{crit} versus inverse shock strength ξ: **a** summary; **b** symbols (Takayama et al. 2016)

the rotated streak image. In the streak picture, a RR in the frontal side the cylinder shows trajectories of the incident shock I and that of the reflected shock wave R. At the transition point T, the trajectories of Mach stem MS and a slip line SL appear. Interpolating the gradient change of these trajectories, the critical transition angle θ_{crit} is readily estimated.

In Fig. 2.96b, a streak photograph of the transition of a shock wave of Ms = 1.4 over a 100 mm concave wall is shown. A 0.4 mm wide slit was attached on the edge of a 100 mm diameter concave cylinder. The streak image was rotated by 52.6° in order to have the highest resolution of the images as seen in the streak picture. Along a shallow concave wall, the reflection pattern is a MR accompanying a MS. Then image through the slit was a Mach stem M. After the transition, a SPRR appears and which accompanies the incident shock wave I and a reflected shock R and later the secondary MS and a slip line SL. Then the interpolating these trajectories, their intersection provides the critical transition angle at T.

Takayama and Sasaki (1983) collected values of θ_{crit} by repeating streak recording over concave and convex walls with various radii of curvature. In addition to this, updated recent results are summarized in Fig. 2.97 (Takayama et al. 2016).

Figure 2.97a summarizes the values of θ_{crit} over concave and convex walls against the inverse strength of the shock wave ξ. The ordinate denotes the critical transition angle θ_{crit} in degree and the abscissa denotes the inverse strength of the shock wave ξ. Figure 2.79b shows the nomenclature. Data points were estimated by the above-mentioned streak recording in air. Pink. yellow, light blue, grey filled circles, red open circles, red filled circles denotes convex walls having combinations of radius and initial angle of 20 mm—90°, 40 mm—90°, 50 mm—53.1°, 160 mm—variable from 6 to 70°, and 300 mm—50°, respectively. Dark blue, blue, red filled circles, black open circles, grey filled circles indicate concave walls having combinations of radius and initial angle of 20 mm—0°, 50 mm—0°, 60 mm—40°, 160 mm—variable from 6 to 70°, and 300 mm—40°, respectively. Curve A designates the detachment criterion and curve B the von Neumann criterion. Black filled circles denote values of the critical transition angles over straight wedges measured by Smith (1948). A laminar boundary layer develops along the shock tube side wall and its displacement thickness δ grows in proportion to the square root of the inverse of the Reynolds number Re defined as $Re = (ux/\nu)^{1/2}$ where ν, u, and x is a particle speed, kinematic viscosity, and a distance from the I, respectively. Hence, the boundary layer effect appears in proportion to $x^{1/2}$.

On convex walls of a smaller radius, values of θ_{crit} significantly differ from from the detachment criterion, while on concave walls of a smaller radius, the θ_{crit} departs from the von Neumann criterion. However, for convex and concave walls of larger radii, values of θ_{crit} tend to agree with the detachment and von Neumann criteria, respectively. This implies that the larger the radii is, the less pronouncing the contribution of boundary layers to the transitions were.

References

Ben-Dor, G. (1979). *Shock wave reflection phenomena*. New York: Springer.

Ben-Dor, G., Takayama, K., & Kawa'uchi, T. (1980). The transition from regular to Mach reflection and from Mach to regular reflection in truly nonstationary flows. *Journal of Fluid Mechanics, 100,* 147–160.

Birkhoff, G. (1960). *Hydrodynamics. A study in logic, fact, and similitude*. Princeton: Princeton University Press.

Bryson, A. E., & Gross, R. W. F. (1961). Diffraction of strong shocks by cone, cylinder, and spheres. *Journal of Fluid Mechanics*, *10*, 1–16.

Courant, R., & Friedrichs, K. O. (1948). *Supersonic flows and shock waves*. NY: Wiley Inter-Science.

Gaydon, A. G., & Hurle, I. R. (1963). *The shock tube high-temperature chemical physics*. London: Chapmam and Hall Ltd.

Glass, I. I. (1975). *Shock wave and man*. Toronto: Toronto University Press.

Henderson, L. F., Crutchfield, W. Y., & Virgona, R. J. (1997). The effect of heat conductivity and viscosity of argon on shock wave diffraction over rigid ramp. *Journal of Fluid Mechanics, 331,* 1–49.

Henderson, L. F., Takayama, K., Crutchfield, W. Y., & Itabashi, S. (2001). The persistence of regular reflection during strong shock diffraction over rigid ramps. *Journal of Fluid Mechanics, 431,* 273–296.

Hornung, H. G., & Kychakoff, G. (1978). Transition from regular to Mach reflection of shock waves in relaxing gases. In: A. B. Hertzberg & D. Russell (Eds.), *Proceeding of 11th International Symposium on Shock Tubes and Waves, Shock Tube and Shock Wave Research* (pp. 296–302). Seattle.

Itabashi, S. (1998). *Effects of viscosity and heat transfer on reflected shock wave transition over wedges* (Master thesis). Faculty of Engineering, Graduate School of Tohoku University.

Itoh, K. (1986). *Study of transonic flow in a shock tube* (Master thesis). Graduate School of Engineering, Faculty of Engineering Tohoku University.

Kawamura, R., & Saito, H. (1956). Reflection of shock waves. *Journal Physics Society of Japan, 11,* 584–592.

Kitade, M. (2001). *Experimental and numerical study of effect of viscosity on reflected shock wave transition* (Master thesis). Graduate School of Engineering, Faculty of Engineering Tohoku University.

Komuro, R. (1990). *Study of shock wave reflection from concave double wedges* (Master thesis). Graduate School of Engineering, Faculty of Engineering Tohoku University.

Kosugi, T. (2000). *Experimental study of delayed transition of reflected shock wave over various bodies* (Master thesis). Graduate School of Engineering, Faculty of Engineering, Tohoku University.

Krehl, P. O. K., & van der Geest, M. (1991). The discovery of the Mach reflection effect and its demonstration in an auditorium. *Shock Waves*, *1*, 3–15.

Kuribayashi, T., Ohtani, K., Takayama, K., Menezes, V., Sun, M., & Saito, T. (2007). Heat flux measurement over a cone in a shock tube flow. *Shock Wave, 16,* 275–285.

Merzkirch, W. (1974). *Flow visualization*. New York: Academic Press.

Miyoshi, H. (1987). *Study of reflection and propagation of shock wave over water surface* (Master thesis). Graduate School of Engineering, Faculty of Engineering Tohoku University.

Meguro, T., Takayama, K., & Onodera, O. (1997). Three-dimensional shock wave reflection over a corner of two intersecting wedges. *Shock Waves*, *7*, 107–121.

Muguro, T. (1998). *Study of three-dimensional reflection of shock waves* (Ph.D. thesis). Graduate School of Engineering, Faculty of Engineering, Tohoku University.

Numata, D. (2009). *Experimental study of hypervelocity impact phenomena at low temperature in a ballistic range* (Ph.D. thesis). Graduate School of Engineering, Faculty of Engineering Tohoku University.

Numata, D., Ohtani, K., & Takayama, K. (2009). Diffuse holographic interferometric observation of shock wave reflection from a skewed wedge. *Shock Waves, 19,* 103–112.

Onodera, H., & Takayama, K. (1990). Shock wave propagation over slitted wedge. *Reports Institute of Fluid Science, Tohoku University, 1,* 45–66.

Reichenbach, H. (1983). Contribution of Ernst mach to fluid mechanics. *Annual Review Fluid Mechanics, 15,* 1–28.

Saito, T., Menezes, V., Kuribayashi, T., Sun, M., Jagadeesh, G., & Takayama, K. (2004). Unsteady convective surface heat transfer measurements on cylinder for CFD code validation. *Shock Waves, 13,* 327–337.

Smith, L. G. (1948). *Photographic investigation of the reflection of plane shocks in air*. Off Sci Res Dev OSRD Rep 6271 Washington DC USA.

Suguyama, H., Takayama, K., Shirota, R., & Doi, H. (1986). An experimental study on shock waves propagating through a dusty gas in a horizontal channel. In: D. Bershader & R. Hanson (Eds.), *Proceedings of 15th International Symposium on Shock Waves and Shock Tubes, Shock Waves and Shock Tubes* (pp. 667–673). Berkeley.

Szumowski, A. P. (1972). Attenuation of a shock wave along a perforated tube. In: L. J. Stollery, A. G. Gaydon & P. R. Owen (Eds.), *Proceedings of 8th International Shock Tube Symposium Shock Tube Research* (pp. 14/1–14/14). London.

Takayama, K., Abe, A., & Chernyshoff, M. (2016). Scale effects on the transition of reflected shock waves. In: K. Kontis (Ed.) *Proceedings of 22nd ISSI Glasgow Shock Wave Interactions* (pp. 1–29).

Takayama, K., Gotoh, J., & Ben-Dor, G. (1981). Influence of surface roughness on the shock transition in quasi stationary and truly non-stationary flows. In C. E. Treanor & J. G. Hall (Eds.), *Proceedings of 13th International Symposium on Shock Tubes and Waves Shock Tubes and Waves* (pp. 326–334). Niagara Falls.

Takayama, K., & Sasaki, M. (1983). Effects of radius of curvature and initial angle on shock wave transition over a concave or convex wall. *Reports of Institute High Speed Mechanics, Tohoku University,* (Vol. 6, pp. 238–308)

Takayama, K., & Sekiguchi, H. (1977). An experiment on shock diffraction by cones. *Reports of Institute High Speed Mechanics, Tohoku University*, *36*, 53–74.

von Neumann, J. (1963). *Collected works 6*, pp. 238–308.

Whitham, G. B. (1959). A new approach to problems of shock dynamics. Part II three dimensional problems. *Journal of Fluid Mechanics, 5*, 359–378.

Yamanaka, T. (1972). *An investigation of secondary injection of thrust vector control (in Japanese). NAL TR-286T*. Chofu, Japan.

Yang, J.-M. (1995). *Experimental and analytical study of behavior of weak shock waves* (Doctoral thesis). Graduate School of Tohoku University, Faculty of Engineering.

Yang, J. M., Sasoh, A., & Takayama, K. (1996). Reflection of a shock wave over a cone. *Shock Waves, 6,* 267–273.